THE DEFECT ENERGIES AND DEFORMATION
MECHANISMS OF SINGLE CRYSTAL
SUPERALLOYS

by

Graham Stewart Hillier, B.Met.

St. John's College
Cambridge

A dissertation submitted for the degree of

Philosophiae Doctor at the University of Cambridge

September 1984

Dedicated to my Mum and Dad

PREFACE

This dissertation describes work carried out in the Department of Metallurgy and Materials Science, Cambridge between October 1981 and September 1984 under the supervision of Dr. H.K.D.H. Bhadeshia.

The contents are, to the best of my knowledge, original except where acknowledgement has been made to the work of others, and the work has been carried out without collaboration. This dissertation contains less than 60,000 words and no part of it has been, or is being, submitted for any other degree, diploma or qualification at any other university.

Graham Hillier.

G.S. Hillier
St. John's College
September 1984

Acknowledgements

I am grateful to Dr. H.K.D.H. Bhadeshia for his advice and assistance throughout my project. I am especially indebted to Dr. Cathy Rae for many stimulating and fruitful discussions, and I would also like to thank Dr. W.M. Stobbs for his help with electron microscopical techniques. Thanks are also due to Mr. R.G. Roome and Mr. P. Doorbar for allowing me to use the JEOL 200 CX at Rolls-Royce, and for their advice on the use of TEM to study superalloy materials.

The cast single crystal superalloys were supplied by Rolls-Royce Ltd., Derby. I wish to thank Dr. R.P. Arthey and Mrs J. Hooker for looking after alloy manufacture and making stress-rupture test facilities available. In addition I wish to thank Mrs. Janet Laing for her excellent typing of this thesis, and also the technical staff, both in the department and at Rolls-Royce, for their help.

Thanks are also due to Professor R.W.K. Honeycombe, F.R.S., for the provision of laboratory facilities, and the SERC for the provision of a quota award to support this work.

Finally, I would like to thank my Mum, Dad and sister, Jacqui, for their interest and encouragement over the last three years.

The Defect Energies and Deformation Mechanisms of Single Crystal Superalloys

G.S. Hillier

Summary

The homogenisation behaviour of seven cast single crystal Ni-base superalloys with Ti contents between 1.8 and 2.7at.% has been studied using various microanalytical techniques. It is found that homogenisation for 32 hrs at 1570K is sufficient to produce reasonably uniform alloys. The γ' precipitate has been coarsened by treating the specimens for 16 hrs at 1300K and it is found that there is no perceptible change in γ/γ' misfit or composition of the specimens before and after growth.

Bright field and weak beam dark field transmission electron microscopy are used extensively to study some of the dislocation interactions in the γ' of three of the alloys after deformation at room temperature and annealing at 1170K. Hexagonal and square superdislocation networks are studied and mechanisms are proposed for the creation of such defects.

Superdislocation spacings have been measured in order to deduce the variation in the antiphase boundary (APB) energy of three of the alloys as a function of Ti content. A new technique for the evaluation of superlattice stacking fault (SSF) energy from three-fold supernode configurations is presented and used to study the dependence of SSF energy on Ti content. It seems that APB energy is essentially independent of Ti but that the intrinsic and extrinsic SSF energies decrease with increasing Ti. It is suggested that the decrease in the SSF energies is due to the stabilization of SSFs by Ti segregating to the planar faults. Such stabilization is expected since the faults involve a stacking sequence equivalent to a few layers of the Ni_3Ti structure.

A modification is proposed to the accepted superalloy deformation mechanisms by γ' shear as a result of the measured energy values. This involves a mechanism, similar to Suzuki locking, which retards γ' shearing by the passage of partial dislocations.

CONTENTS

CHAPTER 4. PLANAR DEFECTS AND HEXAGONAL DISLOCATION NETWORKS

CHAPTER 5. FURTHER DISLOCATION INTERACTIONS

CHAPTER 6. MEASUREMENT OF ANTI-PHASE BOUNDARY AND SUPERLATTICE STACKING FAULT ENERGY

CHAPTER 7. THE EFFECT OF TITANIUM ON DEFORMATION MECHANISMS IN SINGLE CRYSTAL SUPERALLOYS

CHAPTER 8. CONCLUSIONS AND SUGGESTIONS FOR FURTHER WORK

References

ABBREVIATIONS AND SYMBOLS

APB - Anti-phase boundary
FCC - Face centred cubic
FIM - Field ion microscope
SSF - Superlattice stacking fault
SESF - Superlattice extrinsic stacking fault
SISF - Superlattice intrinsic stacking fault
TEM - Transmission electron microscope
γ - Gamma matrix
γ' - Gamma prime precipitate

A - Anisotropy factor
a - Lattice parameter
$\underline{B}$ - Electron beam direction
$\underline{b}$ - Dislocation Burgers vector
c_{ij} - Elastic constants
c_x - Concentration of element x
D_x - Diffusion coefficient of element x
d - Diffusion distance
F - Force
$G(\rho)$ - Geometric function of supernode
$\underline{g}$ - Diffraction vector
M - γ/γ' misfit
m - Apparent dislocation spacing
$\underline{N}$ - APB plane normal
$\underline{R}$ - Lattice displacement vector
R - Internal dimension of supernode
r - Distance from dislocation
\- True superdislocation spacing
$\underline{s}$ - Deviation from the Bragg condition

T - Temperature

T_m - Melting point

t - Time

$\underline{u}$ - Dislocation line vector

v - Velocity

$W_{(n\underline{g},n\underline{g})}$ - Weak beam dark field condition

X - Distance

X, Y, Z - Co-ordinate axes

x_j, y_j, z_j - Co-ordinate axes of dislocation j

z - Distance

α - Phase factor

γ_A - Anti-phase boundary energy

γ_{SSF} - Superlattice stacking fault energy

$\dot{\varepsilon}$ - Secondary creep strain rate

θ - Angle between dislocation line vector and Burgers vector

\- Angle between dislocation spacing vector and electron beam direction

λ - Wavelength

μ - Isotropic shear modulus: equivalent to $[C_{44}(C_{11}-C_{12})/2]^2$ for screw dislocations

ν - Poissons ratio

$\xi_{\underline{g}}$ - Extinction distance

ρ - Dislocation density

\- $\frac{\text{True superdislocation spacing}}{\text{Internal dimension of supernode}} = \frac{r}{R}$

σ_j - Stress on a dislocation

Φ - Angular co-ordinate

ϕ - Wave amplitude

$\underline{\omega}$ - Deviation parameter ($=\underline{s}.\xi_{\underline{g}}$)

CHAPTER 1

BACKGROUND AND INTRODUCTION

1.1 The Principles of Jet Propulsion and the Working Cycle of the Gas Turbine Engine

The possibility of using the jet principle to move an aircraft through the air had interested aircraft designers for a long period but the inability of piston engines with propellers to provide the large airflows necessary to produce a 'jet' caused serious problems. In 1930 Frank Whittle was granted a patent to apply the gas turbine to jet propulsion (Whittle, 1930). Eleven years later his engine completed its first flight. Since that time gas turbine engines have been extensively developed until they have become vitally important in applications which require very high power outputs from compact power sources, particularly in the aircraft and ship industries. Recently they have also been used industrially for pumping natural gas across continents and for small scale power generation in isolated areas away from normal energy supplies.

The principal of jet propulsion is an application of Sir Isaac Newton's third law of motion which states that 'for every force acting on a body there is an equal and opposite reaction'. The earliest known example of the jet engine was produced in about A.D. 100 by the famous mechanician Hero of Alexandria (see Bernal, 1969). This engine showed how the momentum of steam issuing from a jet could cause the 'engine' to revolve by producing an equal and opposite reaction (fig. 1.1). For aircraft propulsion the fluid forming the jet is air, rather than steam. As in Hero's engine the expansion of the accelerated air has an equal and opposite effect on the engine; thus, providing propulsive power which causes the engine and the

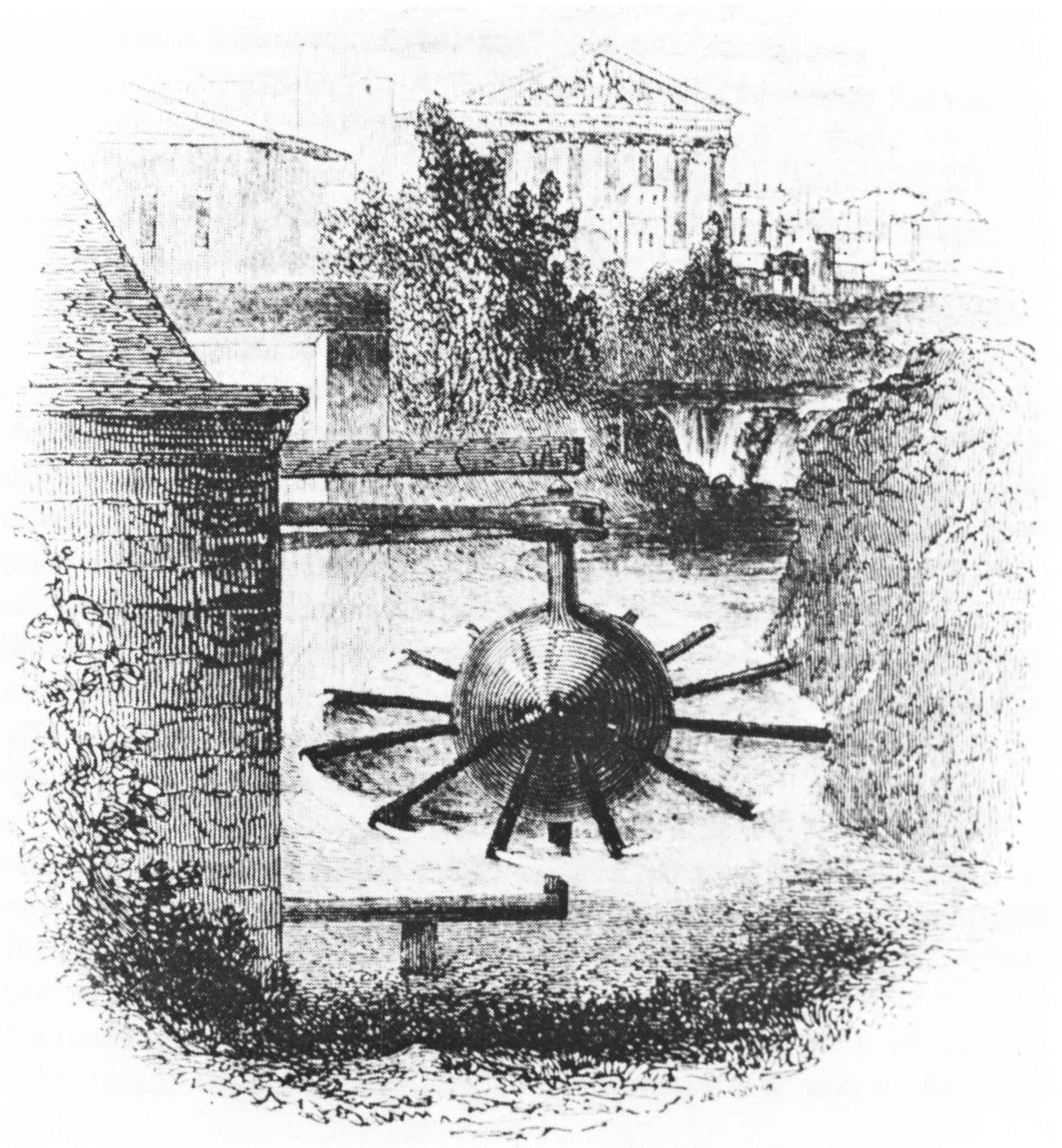

Fig. 1.1. A reproduction of the aeolipyle more commonly known as Hero's engine. The drawing is from a book by Dionysius Lardner, published in 1856, in which the principles of steam as a motive power are discussed. (Bernal, 1969.)

aircraft to which it is attached to move forward.

A section through the original Whittle engine is shown together with sections through two other more modern aircraft gas turbines in fig. 1.2. All three engines work on the same continuous induction, compression, combustion and exhaust cycle. The continuous cycle and absence of reciprocating parts gives a smooth running engine which enables higher power outputs to be gained from gas turbines, when compared with piston engines of the same size. A schematic diagram showing the working cycle of the gas turbine is shown in fig. 1.3. From A to B ambient air is compressed several times by the compressor section (fig. 1.4). From B to C it is heated in the combustion chamber by the injection of burning fuel; this causes a large increase in gas volume. From C to D the expanding gases flow through the turbine and jet pipe before being returned to the atmosphere. During the final part of the cycle some of the energy in the gas is turned into mechanical power by the turbine and this is used to maintain engine operation by driving the compressor; the rest of the gas stream provides propulsive power as it is discharged to the atmosphere. Figure 1.4 shows the typical air flow through a single-shaft axial flow turbo-jet.

Modern jet engines such as the R.B.211 (fig. 1.2c) split the airflow through the engine into two. Eighty per cent of the air is accelerated a little by the large front fan acting as a large propeller. This air is ducted out past the engine core. The 'fan' is driven by the low pressure compressor which is sited at the back of the exhaust air stream from the engine core. The other 20% of the airflow passes through the engine core. The compressor and turbine assembly is split into two, an intermediate pressure section and a high pressure section. These are totally independent from one another and can rotate at different speeds. This enables significant gains to be made in the propulsive and specific fuel efficiencies of the engine. Turbo-fan and turbo-jet engines in aircraft have their power

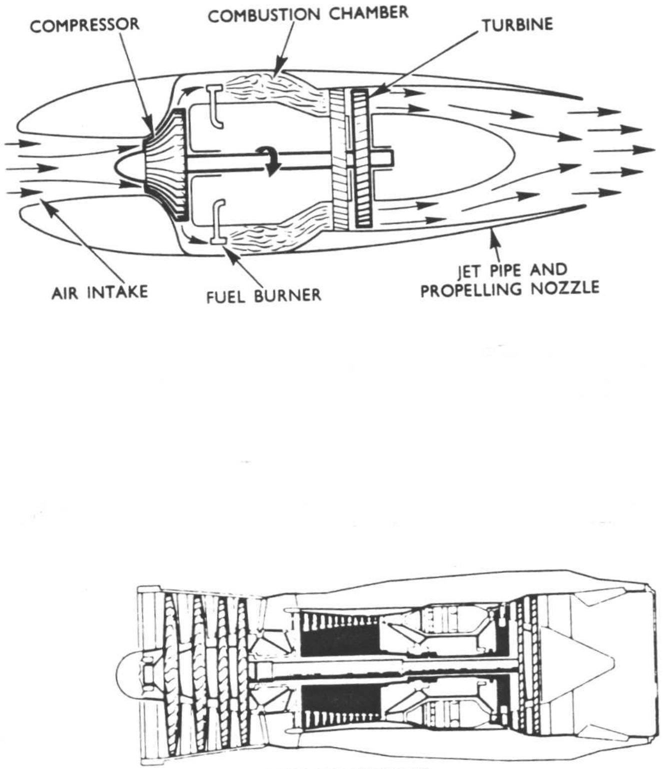

TWIN-SPOOL BY-PASS TURBO-JET

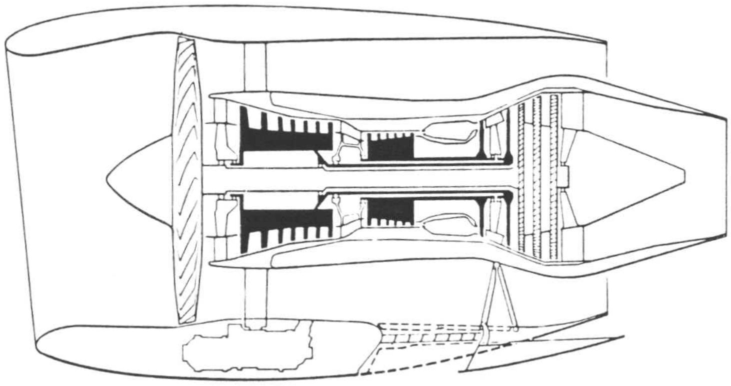

Fig. 1.2. Diagrams showing the mechanical arrangement of three typical gas turbines. The arrangements shown are (a) the single-spool Whittle engine, (b) the Rolls-Royce Spey twin-spool by-pass turbo-jet, and (c) the Rolls-Royce RB211 three shaft by-pass turbo-fan. (From The Jet Engine, 1973 and Driver, Hall and Meetham, 1981.)

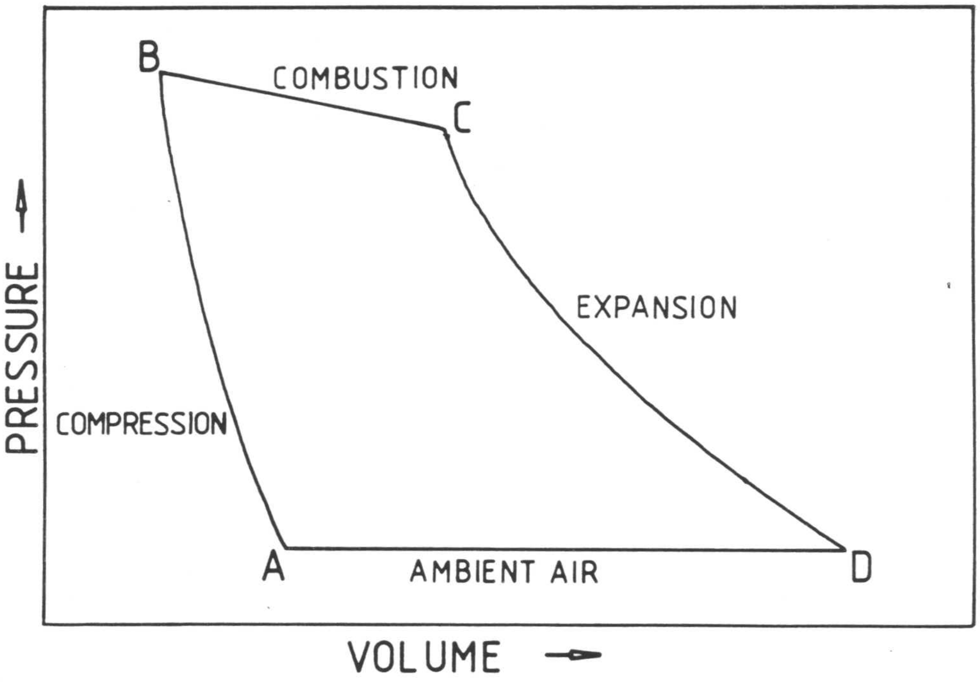

Fig. 1.3. The working cycle of the gas turbine on a pressure-volume diagram (The Jet Engine, 1973).

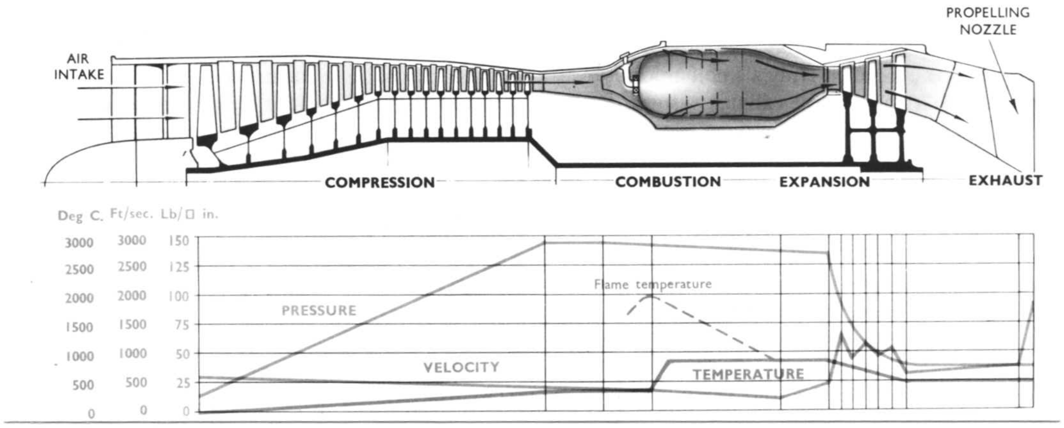

Fig. 1.4. The airflow through a typical single-spool axial flow turbo-jet engine (The Jet Engine, 1973).

ratings expressed in lbs thrust, the thrust being the force exerted by the expansion of the accelerated air on the engine after the turbines have taken their share. (The R.B.211 generates between 37,400 and 56,000 lbs thrust at sea level.) Propeller, ship and industrial gas turbines transfer power to rotate a shaft via a reduction gear. This is done by installing more turbine stages; these extract most of the energy from the exhaust gas stream and transfer it to the rotating shaft. The power output is expressed in shaft horse power. The operation of the gas turbine and detailed information about the various engine sections and assemblies mentioned above can be found in The Jet Engine (1973).

The rising cost of fuel has meant that gas turbine manufacturers have to produce increasingly efficient engines. The efficiency of any heat engine is improved by increasing the difference between the maximum and minimum temperatures of the heat cycle. The ambient temperature of the air is fixed, therefore any improvement in efficiency requires an increase in the temperature of the hot gases entering the turbine. The other major factor affecting efficiency is the compression ratio. Figure 1.5 shows the effect of compression ratio and turbine entry temperature (TET) on the specific fuel efficiency and specific thrust. It is shown that for an efficient high thrust gas turbine a high compression ratio and a high TET are required. The TET is limited by the maximum operating temperature of the materials in the turbine assembly. Consequently the major materials research effort in the gas turbine industry is directed towards improving the temperature capability of the first stage turbine blade and disc materials.

1.2 Turbine Blade Material Requirements

The high pressure turbine blades operate under the most arduous condition in the gas turbine engine. Not only do they experience gas temperatures in excess of 1500K and stresses of up to 550 MPa, which can

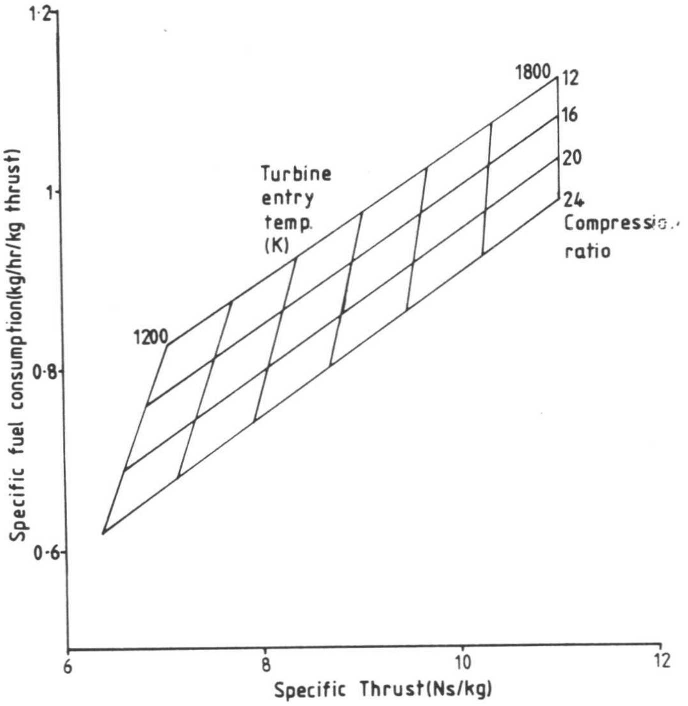

Fig. 1.5. The effect of turbine entry temperature and compression ratio on specific thrust and specific fuel consumption. (Driver et al., 1981.)

cause creep, but they also experience thermal fatigue due to temperature transients on take-off and landing. The blades are surrounded by highly oxidising gases which may contain contaminents such as chlorides and sulphates; these can cause hot corrosion. Blades may also suffer erosion by sand ingested on take-off, from the atmosphere (particles are present at up to 30,000 ft. over the world's deserts), or by particles of carbon formed during the combustion process. Creep and thermal fatigue can alter the turbine vibration characteristics so much that a resonant frequency is reached causing high cycle fatigue. This may, in time, cause a blade or part of a blade to break off in the engine where it will come into contact with other blades. The turbine assembly must, therefore, be impact resistant if disintegration of the engine is to be prevented.

To sum up, turbine blades must have high (>1200K) and intermediate (1000-1200K) temperature creep resistance; to a lesser degree they must be resistant to oxidation and hot corrosion, erosion, thermal fatigue and impact. In addition to this, to be economic, they must have service lives in excess of 7000 hrs. and be fairly easy to fabricate.

1.3 Material Choice

Austenitic stainless steel was used for the turbine blading in the first Whittle engine but this proved to have insufficient creep resistance and was soon replaced by the first two members of the 'Nimonic' series, alloys 75 and 80 (table 1.1). Since then most aircraft high pressure gas turbine blading has been made from nickel-base superalloys. Cobalt, iron and chromium-based alloys have been tried but the Ni-base group has been by far the most successful; only these will be subsequently discussed.

Successively more complex alloys have been empirically developed over the years resulting in modern polycrystalline superalloys such as Mar-M 002 and Mar-M 200 (table 1.1).

Table 1.1. Some Common Superalloy Compositions (at.%)

	Alloy				
Element	Nimonic 75	Nimonic 80A	Mar-M 002	Mar-M 200	SRR 99
Ni	76.0	70.7	60.5	59.5	66.5
Al	-	2.7	12.2	11.2	12.1
Ti	0.5	2.9	1.9	2.5	2.7
Cr	21.8	20.8	10.2	10.4	9.7
Co	-	1.1	10.0	10.2	4.6
W	-	-	3.2	4.1	3.0
Ta	-	-	0.8	-	0.9
Nb	-	-	-	0.7	-
Mn	0.1	0.1	-	-	-
Si	1.4	1.4	-	-	-
C	0.3	0.3	0.7	0.7	<0.1
B	-	-	-	0.1	-
Zr	-	-	∿0.03	∿0.03	-
Hf	-	-	0.5	0.7	-

Table 1.2. Bulk Compositions of the Alloys Studied (at.%)

	Alloy						
Element	A	B	C	D	E	F	G
Ni	67.7	68.2	67.8	68.2	68.3	68.1	68.9
Al	11.8	11.4	12.0	11.9	11.8	11.8	11.9
Ti	2.7	2.5	2.4	2.2	2.1	2.1	1.8
Cr	9.3	9.4	9.3	9.3	9.4	9.4	9.3
Co	4.8	4.8	4.8	4.7	4.8	4.8	4.8
Ta	0.9	0.9	0.9	0.9	0.9	0.9	0.9
W	2.8	2.8	2.8	2.8	2.8	2.8	2.8

These alloys are based on a Ni-Cr solid solution similar to that patented by Marsh (1906) for electrical heating elements. This heat resistant FCC matrix, γ, is strengthened by the precipitation of a high volume fraction of the $L1_2$ ordered precipitate gamma prime, γ' (fig. 4.3a). Gamma prime, chemical formula Ni_3Al, can be strengthened by additions of Ti, Ta and Nb while γ can be strengthened by Co and W. Zr and Hf can be added with C and B to strengthen the grain boundaries by the precipitation of small globular carbides and borides on the boundaries. Cr and Al also provide some corrosion protection by forming oxide films on the surface. Operating conditions are now exceeding the level of protection offered by these films and specific corrosion resistant coatings have been developed. A discussion of these is outside the scope of this thesis; a good review is that by Restall (1981).

In the late 1960's and early 1970's the rush to produce compositionally more complex alloys was reversed by the development of a process to produce single crystal turbine blades. These require no grain boundary strengthening so the alloy composition is more simple (eg. SRR99, table 1.1); they also have superior mechanical properties. The process developments leading to single crystal growth are discussed below.

1.4 Process Developments

1.4.1 Forging

In the early days of gas turbine development all turbine blades were drop-forged. This process soon gave way to press forging which enabled better control of the blade microstructure. Most low temperature, low pressure turbine blades are still manufactured by a forging route, some are manufactured by a combination of extrustion and forging processes. For an account of turbine blade forging see Wells (1981).

Greater property demands from engine designers forced the alloy manufacturers to increase the γ' content of wrought alloys. This decreased the solidus and liquidus temperatures but increased the solid solution temperature resulting in a considerable narrowing of the hot working range. Further problems arose with the introduction of air-cooled blades where the aerofoil contains intricate internal passages (see fig. 1.6) which carry cooler air to lower the blade surface temperature. The advantage gained by using cooled blades is that they can operate at higher TETs and propulsive efficiency is improved for a given material. It proved extremely difficult to successfully manufacture complex cooled blades from high strength superalloys using extrusion and forging.

An alternative fabrication route was found by investment casting which was quickly developed into a viable alternative. This process allows a much greater design freedom. It is now almost universally accepted to be the best technique for the manufacture of intricate air-cooled high performance gas turbine blades.

1.4.2 Investment casting of polycrystalline turbine blades

To produce an investment casting a wax pattern of the finished article is covered with many layers of a ceramic material until a shell is formed. The wax is then melted out in an autoclave and an induction melted charge is poured into the mould to produce an exquiaxed polycrystalline product. Product quality is improved if the process is performed under vacuum because the loss of the more volatile elements to the air or to metal-crucible interactions is reduced.

Blades cast in this way are known as conventionally cast turbine blades: an example is shown in figure 1.7(a). After casting they are heat treated to optimise γ' and carbide distributions; they are then machined, tested and installed in engines where they operate at temperatures of up to 1100K.

As stated earlier, blades must have high and intermediate temperature creep resistance. When creep occurs in polycrystalline materials the

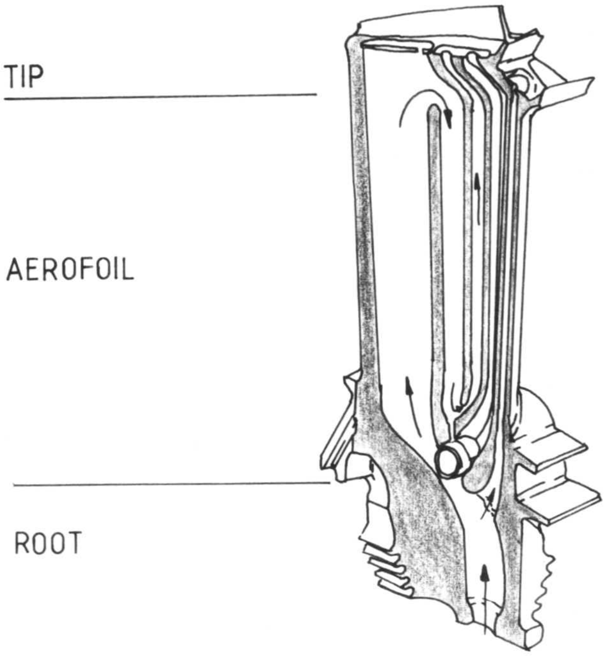

Fig. 1.6. Cut-away diagram of an air-cooled turbine blade showing the complex internal cooling passages.

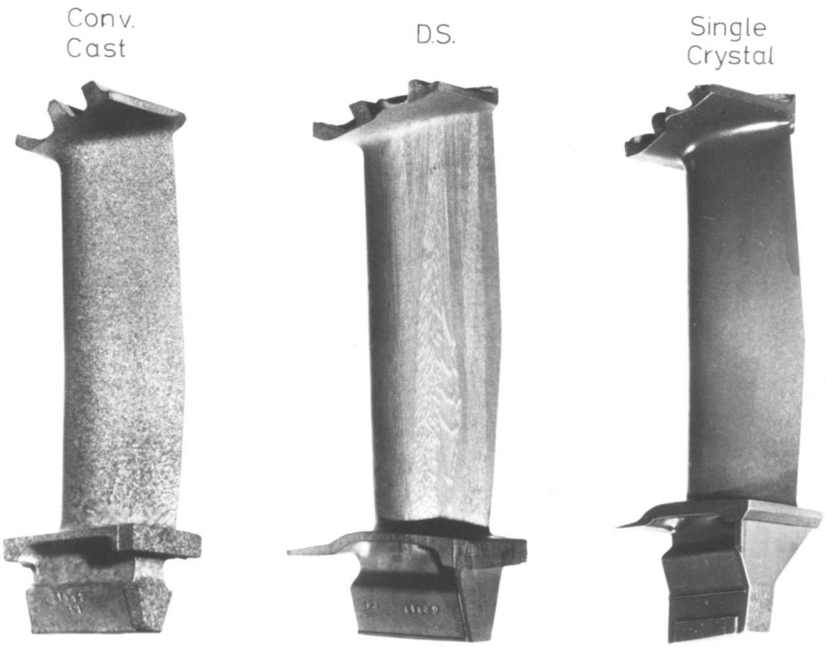

(a) (b) (c)

Fig. 1.7. Half scale photograph showing the macrostructures produced by (a) conventional casting, (b) directional solidification, and (c) single crystal casting.

major effects are grain boundary sliding, intergranular cavitation and excessive boundary precipitation. The most serious effects occur along grain boundaries perpendicular to the radial stress direction (eg Ver Snyder and Guard, 1960 and Piearcey and Terkelson, 1967). Figure 1.7(a) shows that the conventionally cast turbine structure contains small equiaxed grains with many high-angle grain boundaries. Sliding within such structures would be severe if it were not controlled by the precipitation of small globular carbides and borides along the grain boundaries.

Given that the most serious cavitation occurs along the grain boundaries perpendicular to the radial stress axis a significant increase in creep resistance can be obtained from a columnar grain structure with boundaries running from the blade root to the blade tip. Structures of this type are referred to as directionally solidified (DS) structures. The principle is to cast the molten charge automatically, under vacuum, into an open ended preheated ceramic shell mould standing on a water-cooled copper chill (fig. 1.8). Chill crystals nucleate and grow up into the head of molten metal. The mould is slowly withdrawn from the furnace to keep the solidification front at the maximum temperature gradient. This results in the growth of large dendritic columnar crystals (figure 1.7b). In DS FCC materials growth is most favourable for grains with <001> directions along the withdrawal axis. Because growth will occur at the same speed on all the close packed planes, in FCC these are {111}, the dendrite tip will be shaped like a pyramid with a <001> vertex (fig. 1.9 and Chalmers, 1954). The blade produced has a <001> orientation along the radial stress axis. The orientation of grains in other directions is not controlled. This orientation is convenient since superalloys have their best thermal fatigue resistance along this direction.

Grain boundaries are still present in the structure and these must be strengthened by the inclusion of small amounts of grain boundary

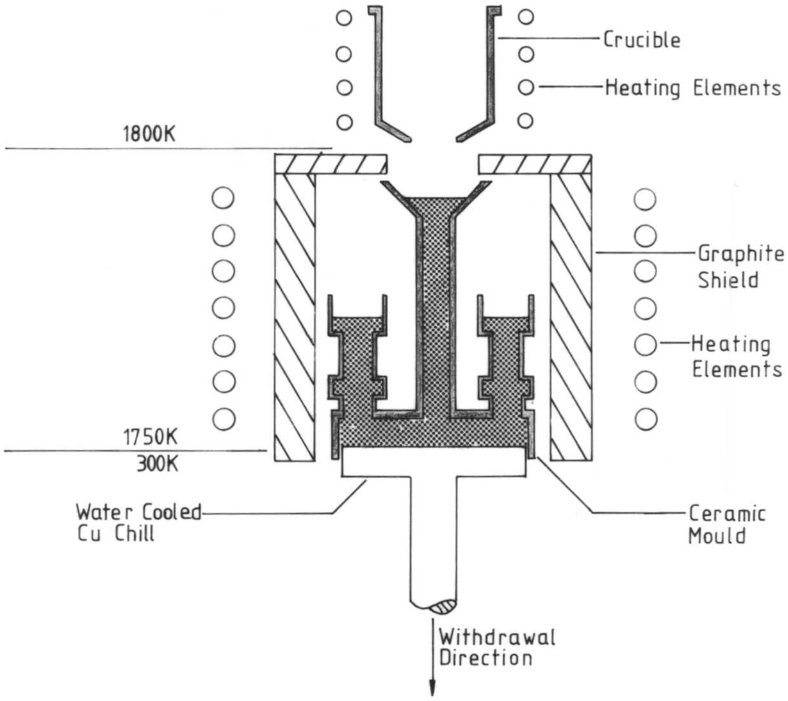

Fig. 1.8. Schematic diagram of a section through a directional solidification furnace.

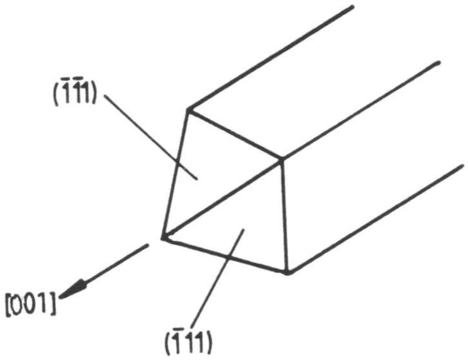

Fig. 1.9. Diagram of a fast growing dendrite tip showing how the four close packed {111} planes produce a dendrite with an [001] vertex.

strengthening elements.

To maintain columnar growth the solidification process is slow. This leads to severe segregation of some elements. This inhomogeneity prevents complete solid solution treatment of the product because small regions melt before the γ' solvus is exceeded. Local melting is known as incipient melting and in most polycrystalline superalloys the incipient melting point is below the γ' solvus. A more detailed discussion of heat treatment is presented in chapter 2.

Despite these heat treatment problems DS blades show a marked increase in ductility, thermal fatigue resistance, stress-rupture properties and intermediate temperature creep properties over their conventionally cast counterparts. Mar-M 002 and Mar-M 200 are two of the best DS superalloys available. After partial solution treatment and careful aging they can be used in gas turbine operation for long periods at temperatures of up to 1300K.

1.4.3 Investment casting of single crystal turbine blades

Most failures of DS blades originate at the grain boundaries so further improvement in properties should be gained by the exclusion of all high angle grain boundaries to form a single crystal product. Industrial 'single crystals' contain a small number of low angle boundaries. They can be grown by a small modification to the DS mould (see for instance Piearcey, 1970 and Ver Snyder and Shank, 1970) to include a helical grain selector between the base of the mould and the blade cavity as shown in figure 1.10(a). Columnar crystals are nucleated on the water cooled copper chill; they grow up into the selector. The helix gradually eliminates grains until only one enters the mould cavity. This is grown out to form the single crystal turbine blade (fig. 1.7c). A component grown in this way has a <001> crystal orientation parallel to the growth direction but the orientation perpendicular to the growth direction is not

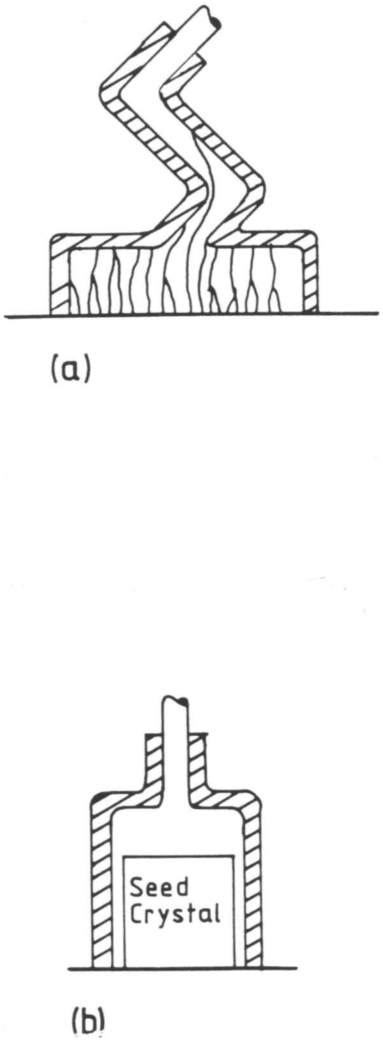

Fig. 1.10. Single crystal production methods using (a) a helical grain selector and (b) a seed crystal at the base of a ceramic shell mould.

controlled. A precisely positioned seed crystal (fig. 1.10b) can be used in the base of the mould in place of the helix if all the crystal orientations need to be precisely controlled.

Since single crystals contain only a few low angle boundaries they require no grain boundary strengthening additions. This leads to simpler alloy compositions (eg. SRR 99, table 1.1) which produce less severe segregation patterns. The γ' solvus is below the incipient melting point so it is possible to fully heat treat the structure to produce a uniform microstructure of small equiaxed γ' precipitates in a γ matrix (chapter 2).

Commercial data have shown that single crystal turbine blades have microstructural stability up to 1370K and if they are air-cooled they should be able to operate at TETs of up to 1600K. Single crystals improve on DS polycrystals by showing further increases in ductility, thermal fatigue resistance, stress-rupture life and intermediate temperature creep life. Figure 1.11 shows the stress-rupture property advantage of single crystals by comparing creep curves at 1250K and 207MPa for conventionally cast, DS and single crystals made from the same material.

1.5 Strengthening Mechanisms in Ni-base Single Crystal Superalloys

A superalloy single crystal is equivalent to one grain containing a few low-angle boundaries and many γ/γ' interfaces. Methods of alloy strengthening by pinning the boundaries with carbides are totally inapplicable; as a result, the alloys contain no grain boundary strengthening additions and the carbon content is minimised.

The most useful strengthening mechanisms are those which prevent deformation by impeding the movement of dislocations through the material; the two most potent methods being precipitation hardening and solid solution strengthening. In single crystal superalloys most of the strengthening is achieved by the γ' precipitate slowing or stopping the

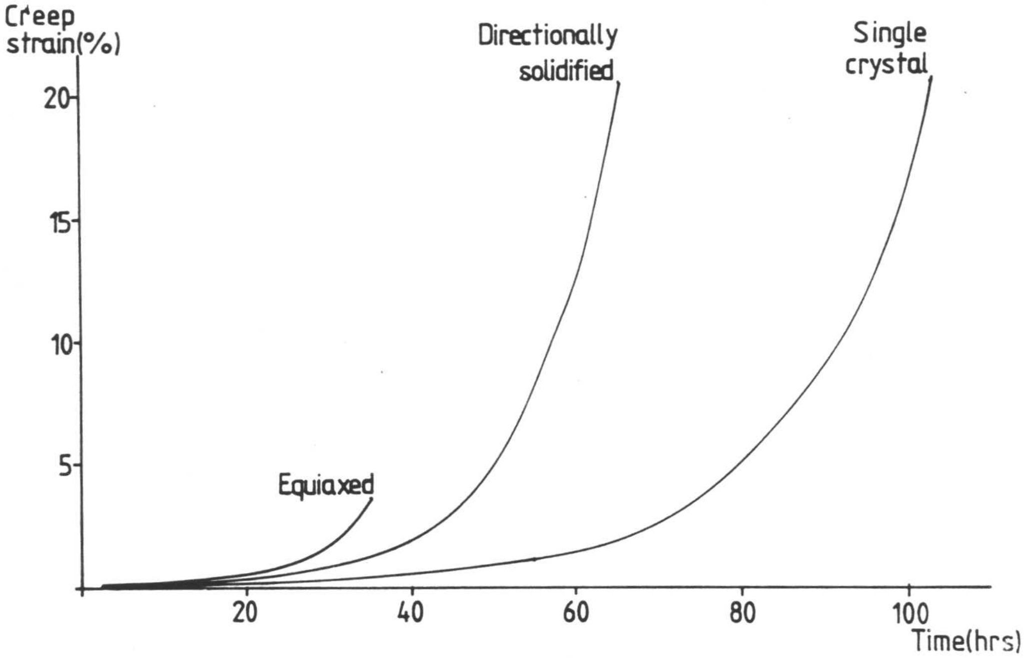

Fig. 1.11. Comparison of the creep strength of conventionally cast, directionally solidified and single crystal superalloys. (Driver et al., 1981.)

passage of dislocations either by forcing them to by-pass or shear through the particles. In addition, solid solution strengthening of the γ matrix reduces the mobility of dislocations between the γ' particles.

1.5.1 Solid solution strengthening

The requirements for solid solution strengthening are the largest possible difference in atomic size and a large range of solid solubility between solute and solvent atoms. Also, to give high temperature strengthening, the solute should have a higher melting point than the solvent and, to give creep resistance, a low diffusivity in the solvent. The γ matrix, which is essentially nickel, adequately fulfils these requirements by having a high solubility for many solute elements, most of which have a low diffusivity in nickel.

At intermediate and high temperatures ($>0.6T_m$) the likely γ deformation mechanisms involve dislocation cross-slip, climb and the diffusional relief of stress. Cross-slip can be reduced by adding elements which lower the γ stacking fault energy to produce wider dislocation dissociations. Volume diffusion rates are generally lowered by alloying with slow diffusing elements. In practice all solid solution strengthening additions are limited by the precipitation of deleterious phases, such as sigma (Decker, 1969).

The major solid solution strengtheners in the alloys under investigation are cobalt, chromium and tungsten. Titanium is also a potent solid solution strengthener but is included mainly to strengthen γ'. These elements were shown to be effective by Pelloux and Grant (1960) who studied the effect of Co, Fe, Cr, Al, Ti and V on the room temperature strength of binary solid solutions with nickel. Some of the strengthening results from the lowering of the stacking fault energy as shown by Beeston and France (1968) and Beeston, Dillamore and Smallman (1968). High temperature strength is due, in part, to the slow diffusing tungsten which also lowers the diffusivity of Ti and Cr in Ni at 1173K (Pridantsev (1967).

1.5.2 Precipitation hardening

Most of the strength of single crystal superalloys results from the precipitation of the $L1_2$ gamma prime, γ'. The similarity in structure and lattice parameter of γ and γ' allows homogeneous nucleation of coherent, reasonably ductile γ' which has extraordinary high temperature stability. γ' nucleates as coherent spheres, but often adopts a cubic morphology during growth. Havalada (1969a) showed that the shape change was, in part, due to γ/γ' misfit. He also suggested that some other factor had an effect. Figure 1.12 is a TEM micrograph taken of alloy A showing the alignment of γ' cubes along the <001> γ directions.

Like the γ matrix the γ' precipitates can accommodate varying amounts of solute elements. These can substitute on Ni and/or Al sites. Decker (1969) has schematically shown (fig. 1.13) that Co occupies Ni sites, V occupies Al sites and Mo, Cr and Fe occupy either site. Blavette and Bostel (1984) have confirmed Decker's observations using time-of-flight FIM and also shown that Ta and W occupy Al sites.

Misfit strengthening

Misfit strengthening occurs when there is a slight difference between the γ and γ' lattice parameters. The strained region will then retard the passage of dislocations through the interface. Replacement of Al in the γ' by Ti was found to increase the γ/γ' misfit (Decker and Mihalisin, 1969). They also showed that Ti raised the stress-rupture and creep life and decreased the γ' growth and coalescence rate.

Titanium is the element most easily absorbed into the Ni_3Al structure. Taylor and Floyd (1952) and Nordheim and Grant (1954) showed that up to two-thirds of the Al sites could be occupied by Ti; Havalada (1969b) showed that this proportion was increased further when W was present. Titanium is such a beneficial addition to γ' that most commercial superalloys

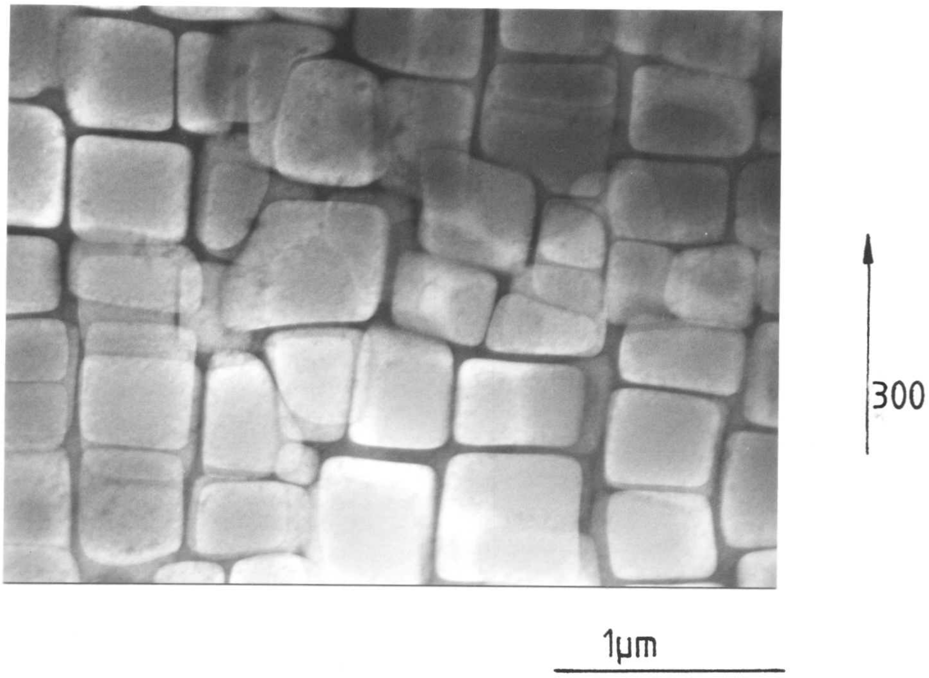

Fig. 1.12. Typical single crystal superalloy microstructure showing γ' cubes aligned in <001> directions. (Foil normal: ~[001].)

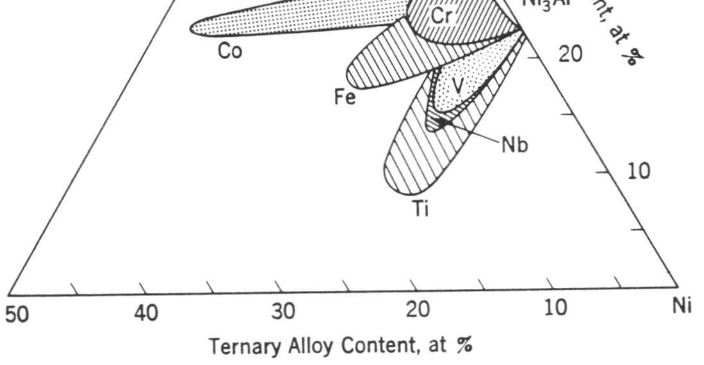

Fig. 1.13. Diagram showing the solid solution fields of various ternary elements in Ni_3Al at 1420K. (Decker, 1969.)

have γ' compositions which are referred to as $Ni_3(Al,Ti)$. In addition to Ti, Nb and Ta also increase the γ' lattice parameters, Cr, Mo and W decrease it, and Co has no effect. Misfit can also be controlled by γ alloying elements; W, Nb and Mo expand the γ lattice parameter, while Co, Cr and Fe have little effect (Decker, 1969).

γ' Particle size

Figure 1.14 shows how the hardness of a Ni, 23at.% Cr, 3.2at.% Ti, 6.4 at.% Al alloy is related to γ' particle size (Mitchell, 1966). The particles are cut by the dislocations on the ascending curve and by-passed on the descending curve. By-passing or Orowan looping (Orowan, 1948) normally only occurs at large particle sizes. Figure 1.14 shows the best properties will be obtained from an alloy which contains the largest particles which will be sheared rather than looped.

γ' Volume fraction

Alloy strength is also increased by increasing the volume fraction of γ'. This is most easily achieved by adding greater amounts of γ' forming elements. Figure 1.15 shows how strength is increased with increasing γ' volume fraction. When alloys contain high volume fractions of small γ' particles deformation occurs mainly by dislocations shearing through the γ', although under certain circumstances looping and climb of dislocations are still important.

Anti-phase boundary and superlattice stacking fault energies

It has been shown (Kear, 1974 and Kear and Oblak, 1974) that as deformation temperature is increased the shearing mode of γ' changes from superdislocation shear, producing anti-phase boundaries (APBs), at low temperatures to partial dislocation shear, producing superlattice stacking faults (SSFs), at intermediate temperatures and finally, back to super-dislocation shear at high temperatures. Different alloys have different

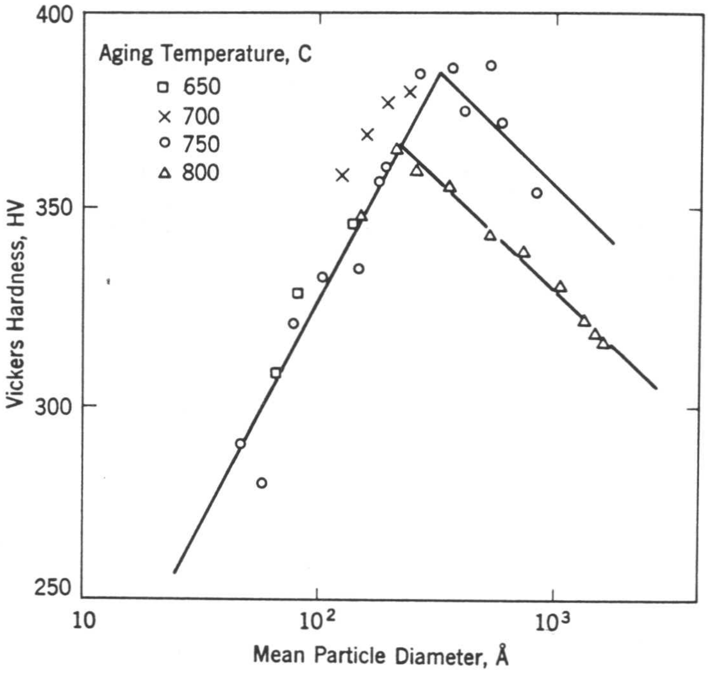

Fig. 1.14. Relationship between particle diameter and hardness for a Cr – Ti – Al alloy. (Mitchell, 1966.)

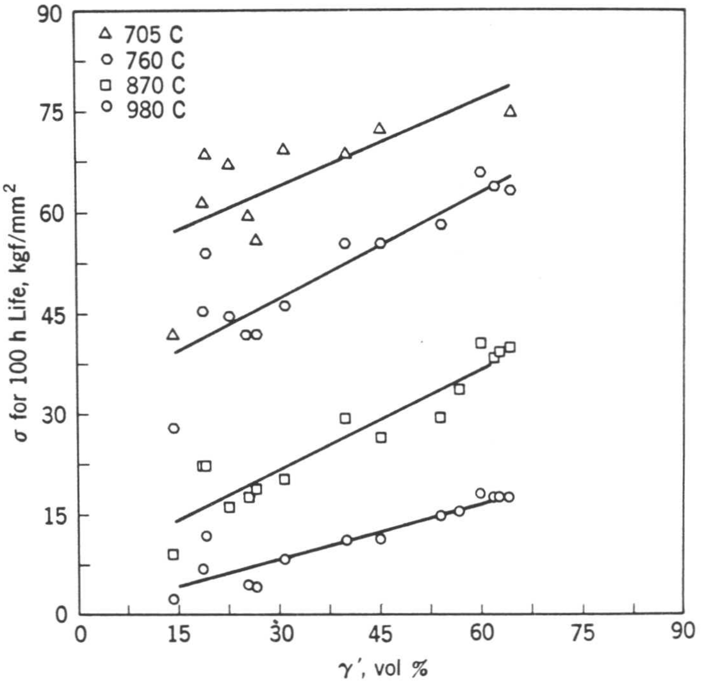

Fig. 1.15. Effect of volume percent γ' on the strength of superalloys at different temperatures.

change-over temperatures but a rough guide is for temperatures up to 1000K to be low temperatures, between 1000K and 1200K to be intermediate and those above 1200K to be high.

Kear et al. (1968) suggested that γ' shearing would take place by the dislocation configuration with the lowest energy. Kear (1974) suggested that the changes in γ' deformation mode may be due to changes in the APB and SSF energies relative to one another (fig. 1.16a). Despite these proposals little effort has been made to establish the APB energy (see 6.2.4) and no effort has been made to evaluate the SSF energies (6.3.4). The effect of γ' composition on the deformation modes of γ' has not been studied prior to this investigation.

The main γ' forming elements in the alloys studied were Al, Ti and Ta. Ti is the major γ' strengthening element and Ta is added to improve high temperature properties by raising the γ' solvus.

1.5.3 Summary

The strengthening mechanisms employed to strengthen single crystal superalloys are:

(i) Solid solution strengthening of γ.

(ii) High volume fraction of γ'.

(iii) γ' particle size.

(iv) Misfit strengthening.

(v) Superlattice stacking fault and anti-phase boundary energies.

Seven alloys (A to G, table 1.2) have been studied. The expected strengthening effect of each of the alloying elements on the Ni base is listed below:

(i) Aluminium
- major γ' forming element.
- γ solid solution strengthener.
- high temperature corrosion resistant Al_2O_3 film effective up to 1530K.

(ii) Cobalt
- γ solid solution strengthener.
- thought to lower the γ stacking fault energy.
- increases γ' stability by reducing the solubility of γ' forming elements in γ.

(iii) Chromium
- γ solid solution strengthener.
- corrosion resistant Cr_2O_3 film, effective up to 1370K.

(iv) Tantalum
- γ' strengthening element giving high temperature stability because of its high melting point.

(v) Titanium
- major γ' strengthening element.
- controls γ/γ' misfit.
- small changes in concentration are thought to have a considerable effect on alloy strength due to changes in the deformation mechanism.

(vi) Tungsten
- γ solid solution strengthener because of its low diffusivity and high melting point.

1.6 The Aim of this Investigation

In their recent review of high γ' volume fraction Ni-base superalloys Pope and Ezz (1984) concluded that although the deformation mechanisms are well understood and the tensile properties are well documented there has been little work on the creep of superalloys or on the creation of a model which links deformation mechanisms to properties. One of the most serious gaps is the lack in understanding of the effects of composition on the flow and creep properties of both single phase γ' and two-phase γ/γ' alloys.

The aim of the present work is to study the influence of titanium content on the defect energies and dislocation structures in a series of single crystal superalloys (table 1.2). No attempt has been made to verify the deformation mechanisms established by others. Attention has been focused on the influence of Ti on the APB and SSF energies of the alloys with a view to relating these parameters via the observed deformation mechanisms, to the performance of the alloys in stress-rupture tests.

It seems (Roome, 1982) that changes of the order of 0.8 at.% in the Ti content have a significant effect on the stress-rupture life of semi-homogenised superalloys. To further verify this effect tests designed by the author have recently been performed on three fully homogenised alloys

(A, D and G of table 1.2). The specimens used for these tests were carefully prepared so factors (i) to (iv) of 1.5.3 were constant. Any changes in behaviour must then be related to factor (v). The results are presented in figure 1.17 and appendix A. It is clear that the stress-rupture life is improved by small increases in the Ti content.

Roome suggested that in addition to the change in mechanism with temperature (fig. 1.16a and Kear, 1974) there was a change in APB energy with alloy titanium content, which may influence the temperature at which the change in deformation mechanism occurs; at higher titanium levels the change occurred at lower temperatures (fig. 1.16b). It was found that longer stress-rupture lives were obtained from higher Ti alloys when γ' shear was occurring by partial dislocations producing superlattice stacking faults.

Kear (1974) and Roome (1982) could not establish their ideas as no accurate values for APB energy and no values for SSF energy as a function of Ti content were available for any superalloy material.

The following chapters describe experiments performed to measure the fault energies in a series of single crystal superalloys which contain systematic variations in Ti content and then discusses the implications of these values to the creep deformation of superalloys.

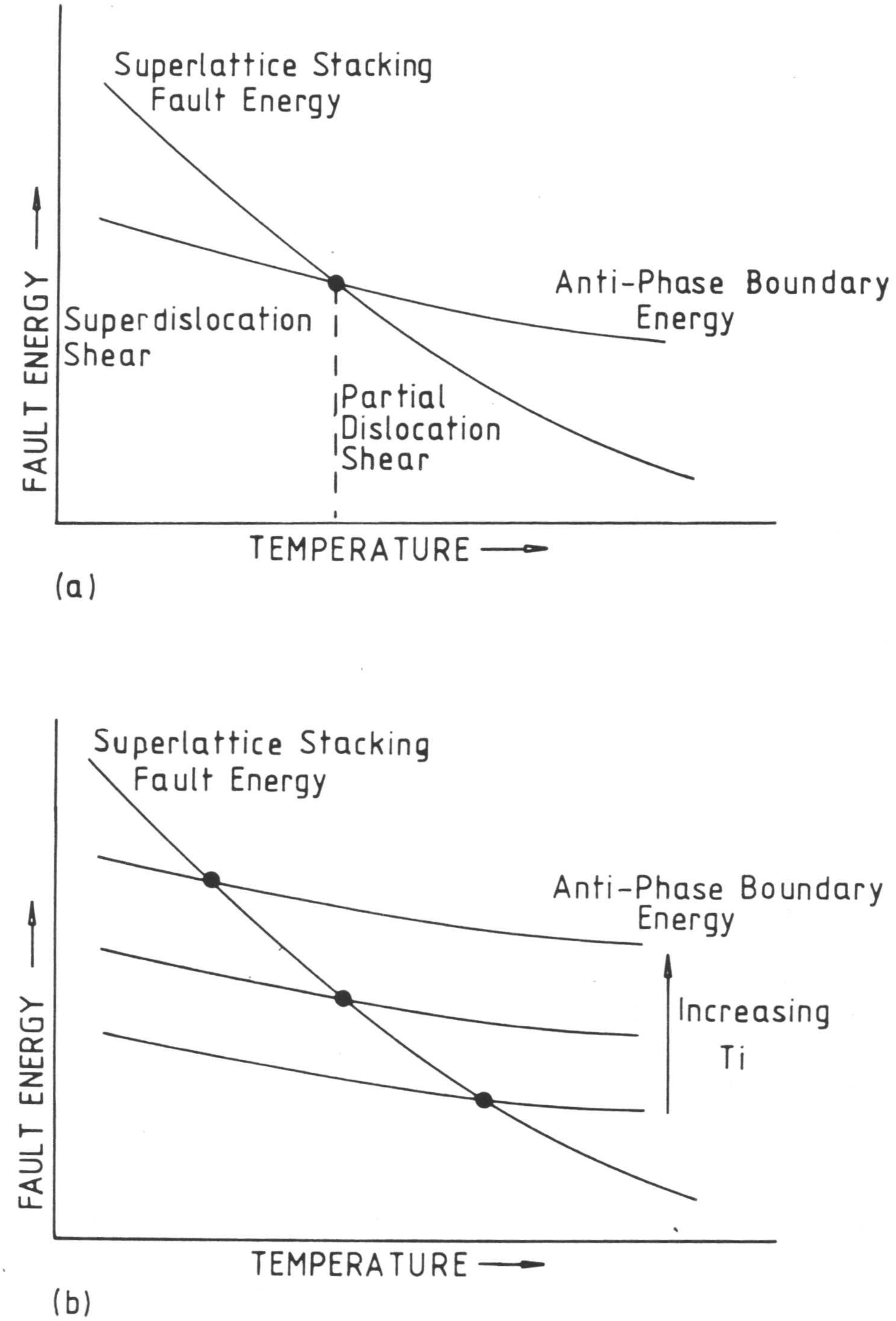

Fig. 1.16. Schematic diagram showing the relationship between deformation mechanism and fault energy (a), and the effect of titanium on fault energy and deformation mechanism proposed by Roome (1974) (b).

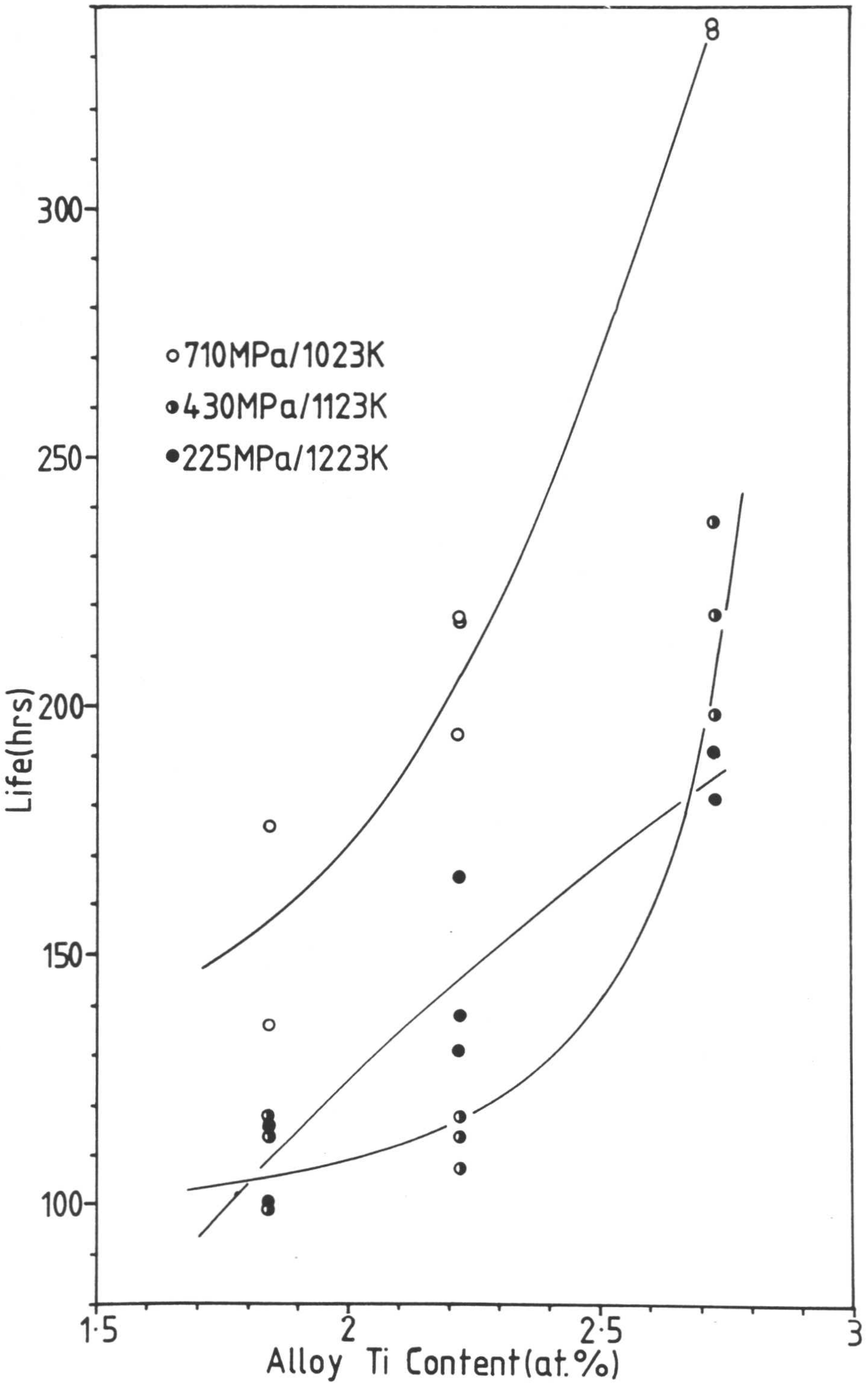

Fig. 1.17. Relationship between stress-rupture life, titanium content and test conditions for alloys A, D and G (table 1.2).

CHAPTER 2

THE HOMOGENISATION BEHAVIOUR OF SINGLE CRYSTAL SUPERALLOYS

2.1 Alloy Supply and As-cast Composition

The compositions of the as-cast alloys used in this investigation are listed in table 1.2. These bulk analyses were gained from X-ray fluorescence performed by Ross and Catherall Ltd., Sheffield. All the alloys were cast as 10mm diameter single crystal rods by Rolls-Royce Ltd., Derby using the technique described in 1.4.3. The small compositional variations were achieved by adding a highly alloyed 'button' of material to a master melt before casting.

2.2 Heat Treatment

As-cast, directionally solidified, single crystal rods of Ni-based superalloys are heavily cored due to non-equilibrium cooling caused by the slow withdrawal from the furnace. During solidification the γ' forming elements are partitioned to the liquid. The enriched interdendritic liquid ultimately solidifies by eutectic decomposition to form a coarse γ/γ' mixture (fig. 2.1b). The as-cast microstructure (fig. 2.1a) contains a fine dispersion of γ' particles in the initially γ dendrites; the coarse γ/γ' eutectic is visible in the interdendritic spaces. The severe coring causes the γ' morphology at the centre of the dendrites (fig. 2.1d) to be considerably different from that at the edge (fig. 2.1c). A small number of carbides are also visible (fig. 2.1e). These precipitate ahead of the alloy solidification front and are essentially unchanged by subsequent heat treatment.

The aim of heat treatment is to remove the inhomogeneity by taking the precipitates into FCC solid solution at high temperature, holding the

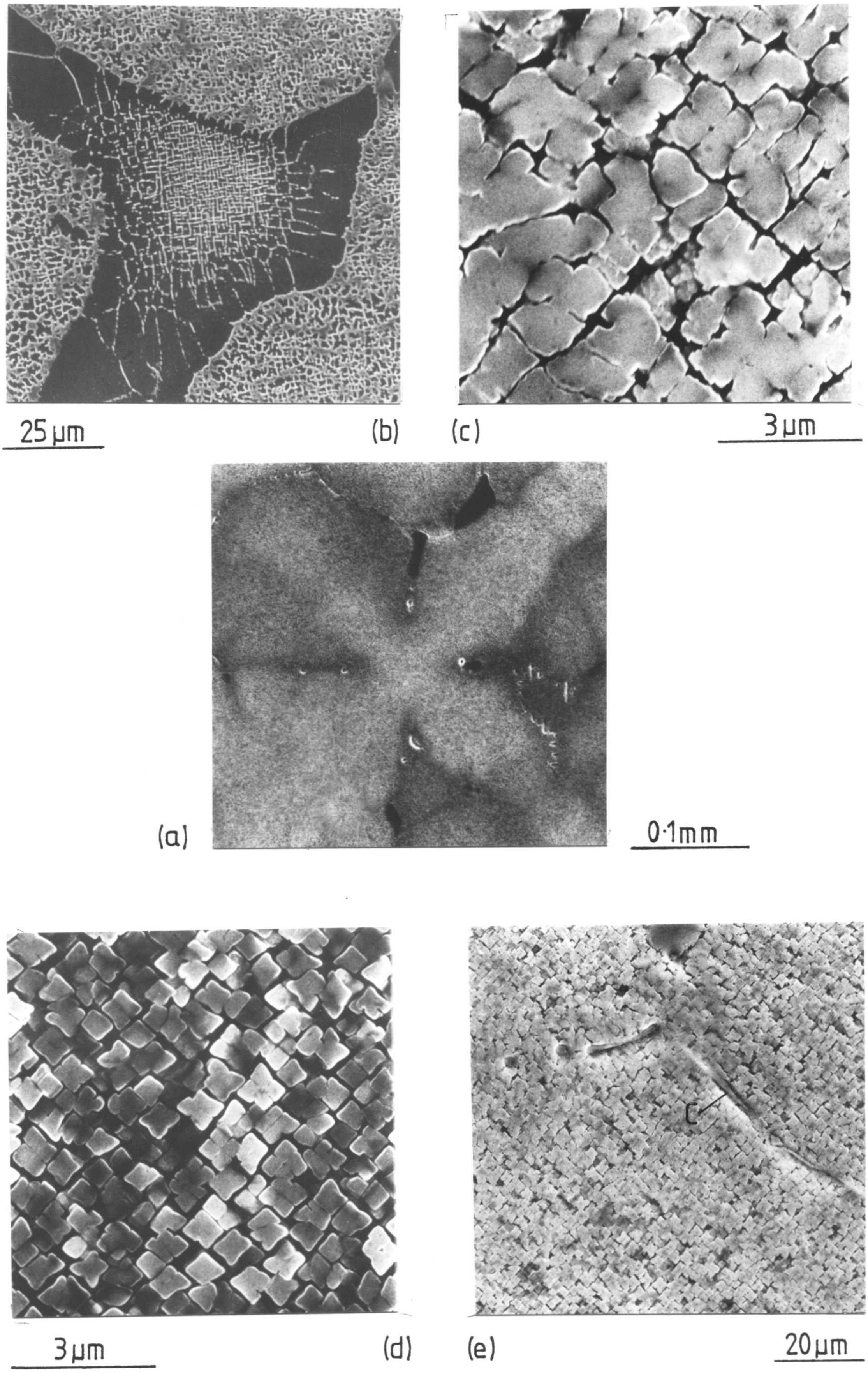

Fig. 2.1. The as-cast microstructure showing: the overall structure (a), γ/γ' eutectic (b), ragged coarse γ' at the dendrite edges (c), regular fine γ' at the centre of the dendrites (d), and dendritic carbide C (e). (Etch: electrolytic 10% phosphoric in water for (a), (c), (d) and (e); electrolytic 5% H.F., 10% glycerol and water for (b).)

material at this temperature until all the compositional waves have decayed and then rapidly cooling to precipitate fine, even γ'. Unfortunately in most commercial polycrystalline alloys the inclusion of grain boundary strengthening elements causes the γ' solvus to be higher than the incipient melting point. In these cases 'solution treatment' is undertaken at a temperature as near as possible to the incipient melting point. It is not possible to dissolve the γ' or the γ/γ' eutectic completely so these components, although much reduced, are still present in the treated microstructure. Cooling from the 'solution' temperature precipitates fine γ' between the large γ' particles to produce a dual γ' size distribution. A long aging treatment (normally 16 hrs. at 1140K) is then used to improve γ' shape and to precipitate grain boundary carbides.

Single crystal materials have much higher incipient melting points than conventional alloys; it is possible to solution treat these alloys above the γ' solvus, but below the incipient melting point. This temperature interval is known as the heat treatment window. It is typically 20K wide. At the heat treatment temperature the γ' and the γ/γ' eutectic are completely solutioned enabling complete homogenisation. Reprecipitation of γ' can be controlled to produce a morphologically and chemically homogeneous microstructure of fine equisized γ' in a γ matrix without γ/γ' eutectic.

2.3 Determination of the Heat Treatment Window

An initial attempt to determine the heat treatment window was made using the Stanton-Redcroft DTA673-4 differential thermal analysis system at Rolls-Royce Ltd. Owing to the gradual changes in heat output at the γ' solvus, γ/γ' eutectic solvus and incipient melting point it was difficult to determine accurate temperatures from the DTA traces (fig. 2.2). The errors were assessed to be of the order of ±10K. In many cases the heat treatment window was of that order so a more accurate technique was required.

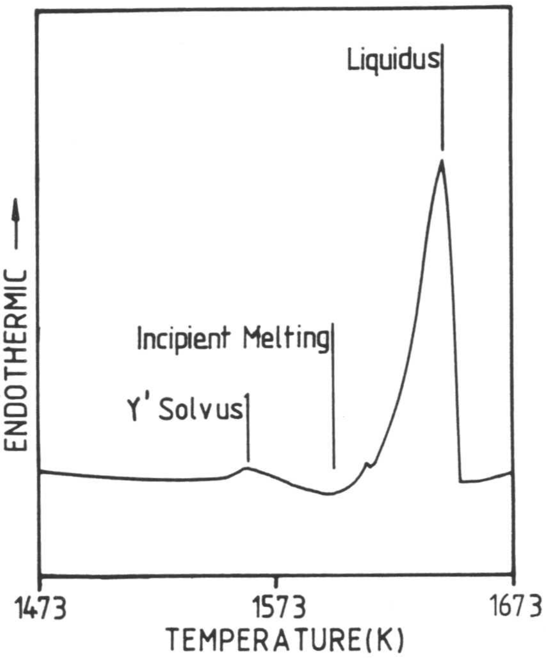

Fig. 2.2. Semi-schematic representation of a typical DTA trace gained from alloys A to G showing gradual changes in heat output.

A simple technique employing optical microscopy was chosen. 15 mm x 10 mm diameter cylinders were heated to temperatures at 10K intervals between 1550 and 1610K for one hour periods then rapidly air cooled to ambient temperature. Incipient melting locally alters the microstructure and was detected on polished and electrolytically etched samples, eg. figure 2.3(b). The temperature at which the γ/γ' eutectic entered solution was similarly determined, eg. figure 2.3(a). It is noted that this is the standard method used to determine the heat treatment windows of commercial alloys. The error in the method was of the order of ±6K.

The results are presented in figure 2.4 which shows that the incipient melting point decreased with increasing titanium content; the eutectic solvus rose and the overall effect was to narrow the heat treatment window with increasing titanium.

The effect of increasing the Ti content is to increase the volume fraction of liquid which decomposes to the γ/γ' eutectic; higher Ti levels thus lead to higher eutectic volume fractions in the as-cast alloy (0.02 in alloy A and 0.003 in alloy G). This means that for a given homogenisation temperature, high titanium alloys will require longer times for the dissolution of the eutectic. Because the heat treatment window assessment procedures were isochronal, high titanium alloys were expected to show an apparent increase in the γ/γ' solvus temperature (fig. 2.4).

In the absence of detailed phase diagram data the effect of Ti on the incipient melting point cannot be properly discussed but the observed effect is consistent with that of titanium (at levels less than 15 at.%) on the solidus temperature of Ni-Ti-Al alloys (Nash, Vejus and Laing, 1982).

2.4 Microanalysis of the As-cast Structure

Microanalysis was carried out on a Cambridge Instruments Microscan 5 electron microprobe (spot size 2μm) and an ISI 100-A SEM with a Link 860 EDS unit (spot size 1μm). The results obtained from both

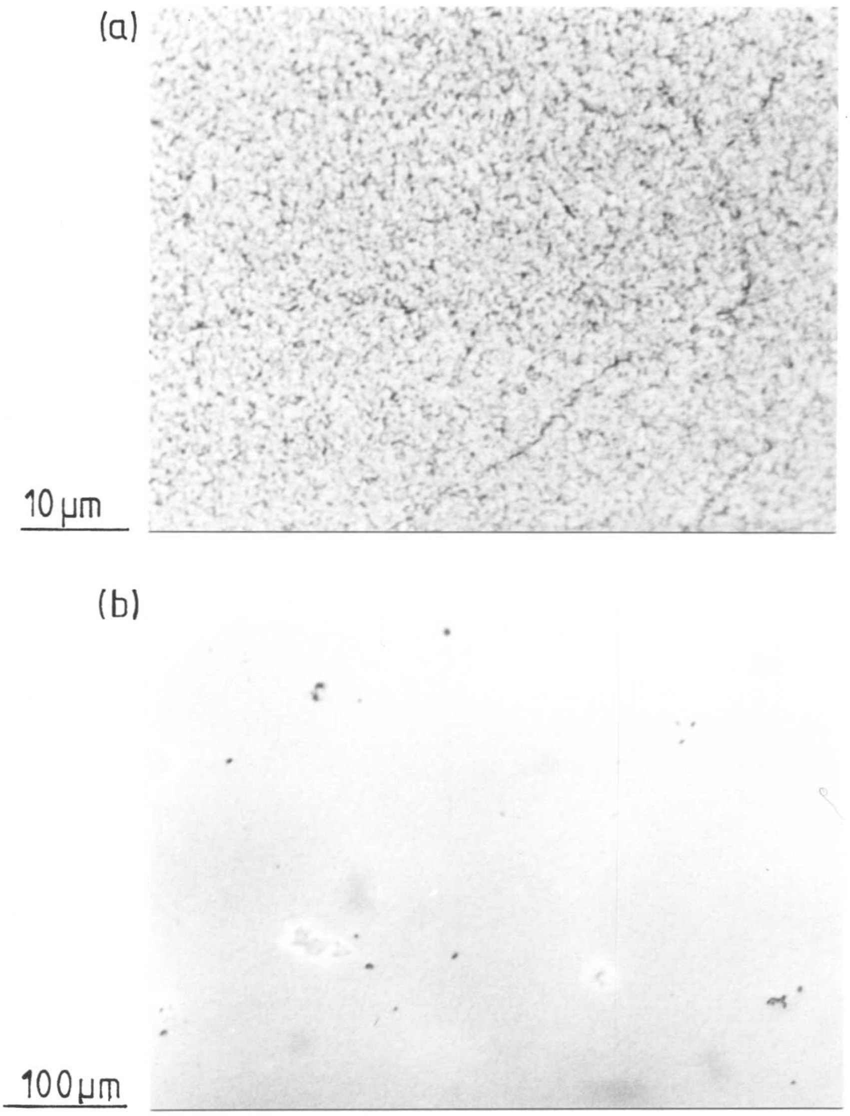

Fig. 2.3. Micrographs of the microstructures at the γ/γ' eutectic solvus (a) and the incipient melting point (b).

Etch: Electrolytic 10% Phosphoric acid in H_2O

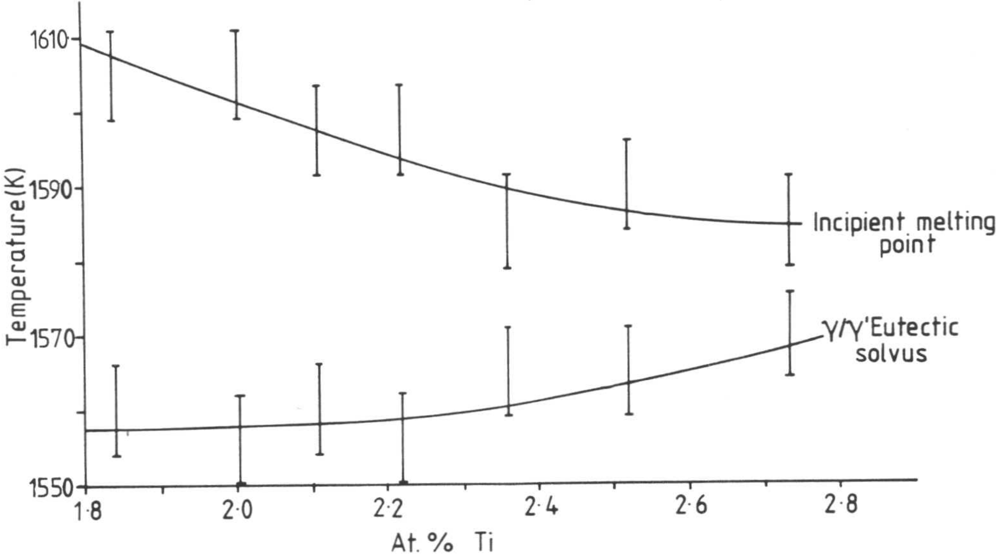

Fig. 2.4. Temperature dependence of the incipient melting point and the γ/γ' eutectic solvus on the bulk alloy titanium content.

techniques were corrected for atomic number, absorption and fluorescence.

Probe and EDS traces across dendrite arms show relatively high concentrations of Al and Ti, both strong γ' forming elements, at the edges of the dendrites, while W showed high concentrations in the central regions (fig. 2.5). Quantitative metallography on a Quantimet 720 image analysing computer showed that the γ' volume fraction at the edges of the dendrites was higher than at the centres. Alloy A (2.7 at.% Ti) contained 0.6±0.05 γ' at the edges of the dendrites and 0.55±0.05 at the centres; the corresponding results for alloy G (1.8 at.% Ti) showed 0.71±0.05 at the edge and 0.49±0.05 in the centres - see figure 2.1(c) and (d). As expected this indicates that the γ' forming elements are rejected from the solidifying alloy. The difference in γ' morphology between dendrite edges and centres may be due to soft impingement between the rapidly growing γ' particles.

Analysis of the eutectic colonies shows them to be rich in the expelled titanium and aluminium, and deficient in chromium and tungsten (fig. 2.6). Quantitative microscopy showed that the eutectic in alloy A contained 0.93 γ' and 0.17 γ. Figure 2.6 indicates that there are large concentrations of Cr and Ti near the eutectic interfaces. This segregation pattern is similar to that observed by Piearcey, Kear and Smashey (1967). However, the cause of this extreme segregation is unclear. If the solidifying eutectic were expelling non-γ' forming elements then such strong titanium segregation is unlikely. An explanation could be that the analysis spot has passed over a small Ti rich carbide although none is visible in figure 2.6.

2.5 Homogenisation

A temperature of 1573K was chosen for this experiment since it lies within the heat treatment window of all the alloys. Homogenisation was carried out on samples of alloy A sealed in a silica tube containing a

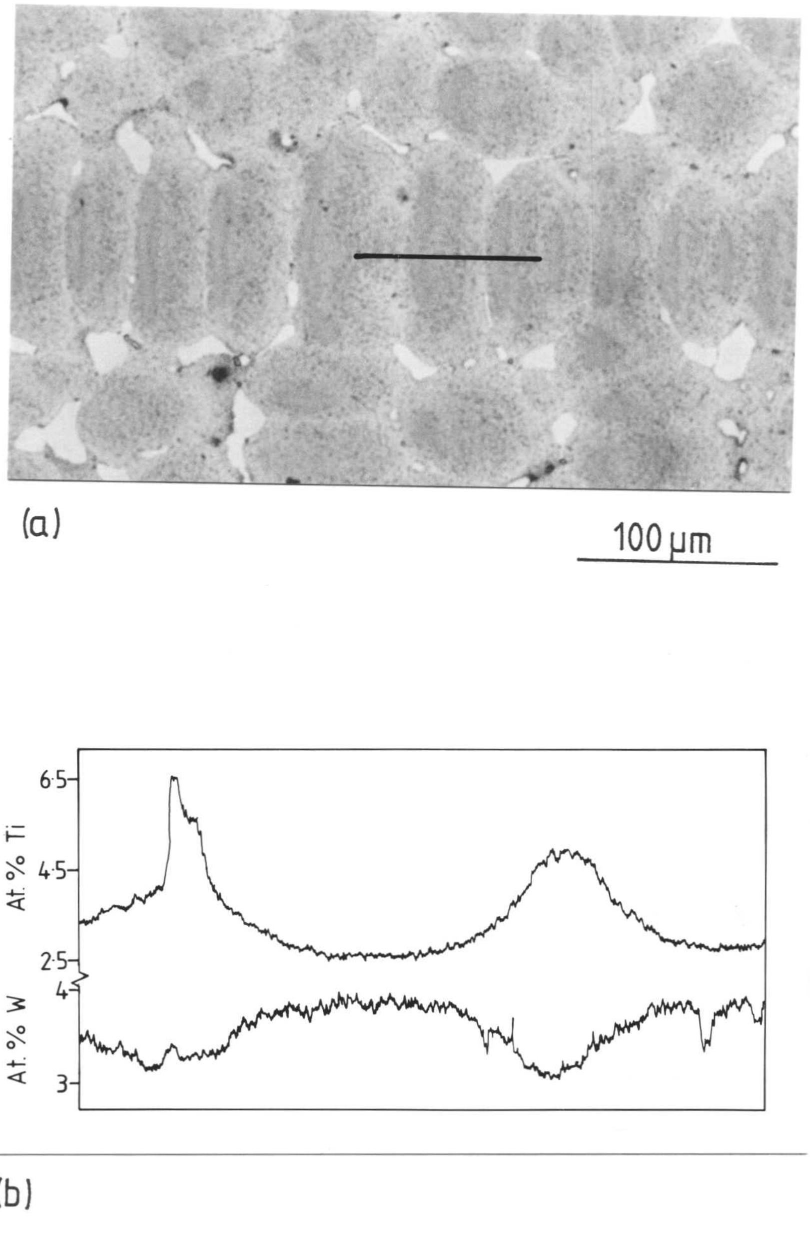

Fig. 2.5. Electron microprobe traces for Ti and W (b) across two secondary dendrites arms shown in (a).

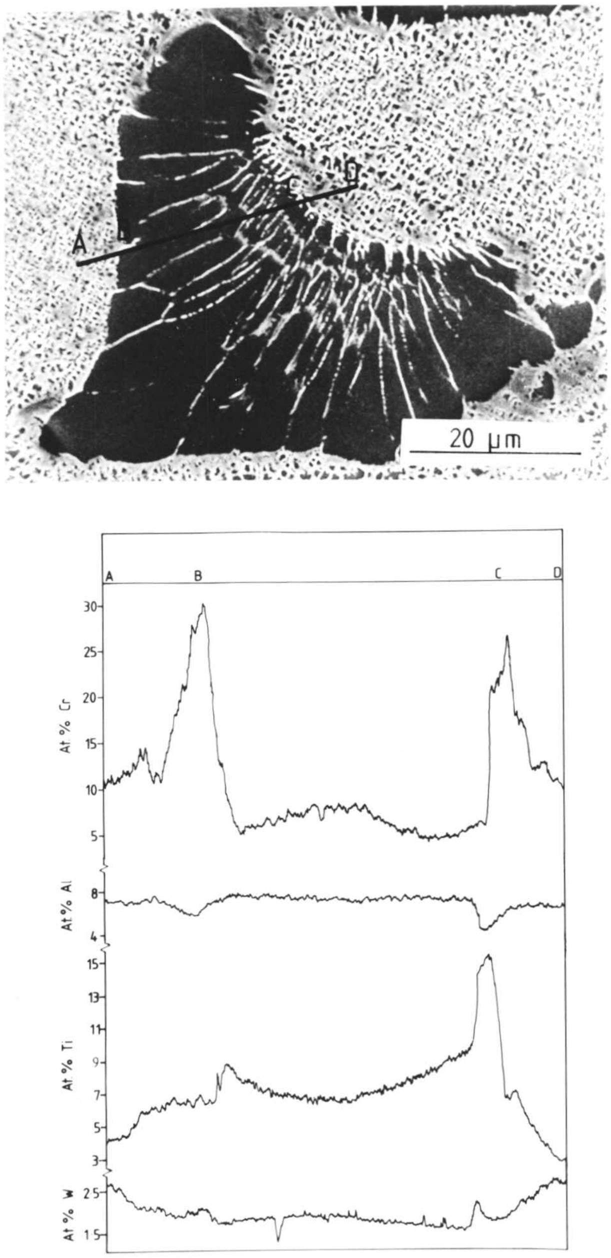

Fig. 2.6. Electron microprobe traces for Cr, Al, Ti and W across a typical γ/γ' eutectic colony.

partial pressure of Ar. The experiment was interrupted after 4, 8, 16, 32 and 64 hours at temperature for examination. A fiducial line marked on the specimen was used; after each heat treatment SEM/EDS analyses were made on this line at 10μm intervals. This experiment was only designed to show overall macroscopic composition variations.

Heat treatment for 8 hours at 1573K produced an apparently uniform microstructure, figure 2.7(a), but analysis showed that the compositional variations were still present. After 16 hours the Ti, Ni, Al and Cr concentrations showed no significant variations while after 32 hours none of the elements exhibited segregation beyond the range of the experimental error.

An attempt was made to assess the segregation profiles in terms of a relaxation time, t, where:

$$t = \frac{d^2}{D} \qquad \text{eqn. 2.1}$$

The system was simplified to a solid solution of the most severely segregated element, W, in Ni at 1573K. It was found, appendix B, that the calculated relaxation time was similar to that determined experimentally. It appears that the homogenisation time of the whole alloy can be approximated to the homogenisation time for a binary solid solution of the most severely segregated element with Ni. It is suggested that further work be undertaken on different alloys with different amounts of segregation to show if this simple method can be used to predict the time necessary to achieve adequate homogenisation of complex superalloys without the need for much time-consuming experimentation.

2.6 Homogenised Microstructure

2.6.1 Growth of the γ' precipitate

For convenience, a homogenisation time of 36 hours at 1570K was used. The specimens were air cooled; the microstructure shown in figure 2.7(b) was produced. To facilitate easier measurement of the

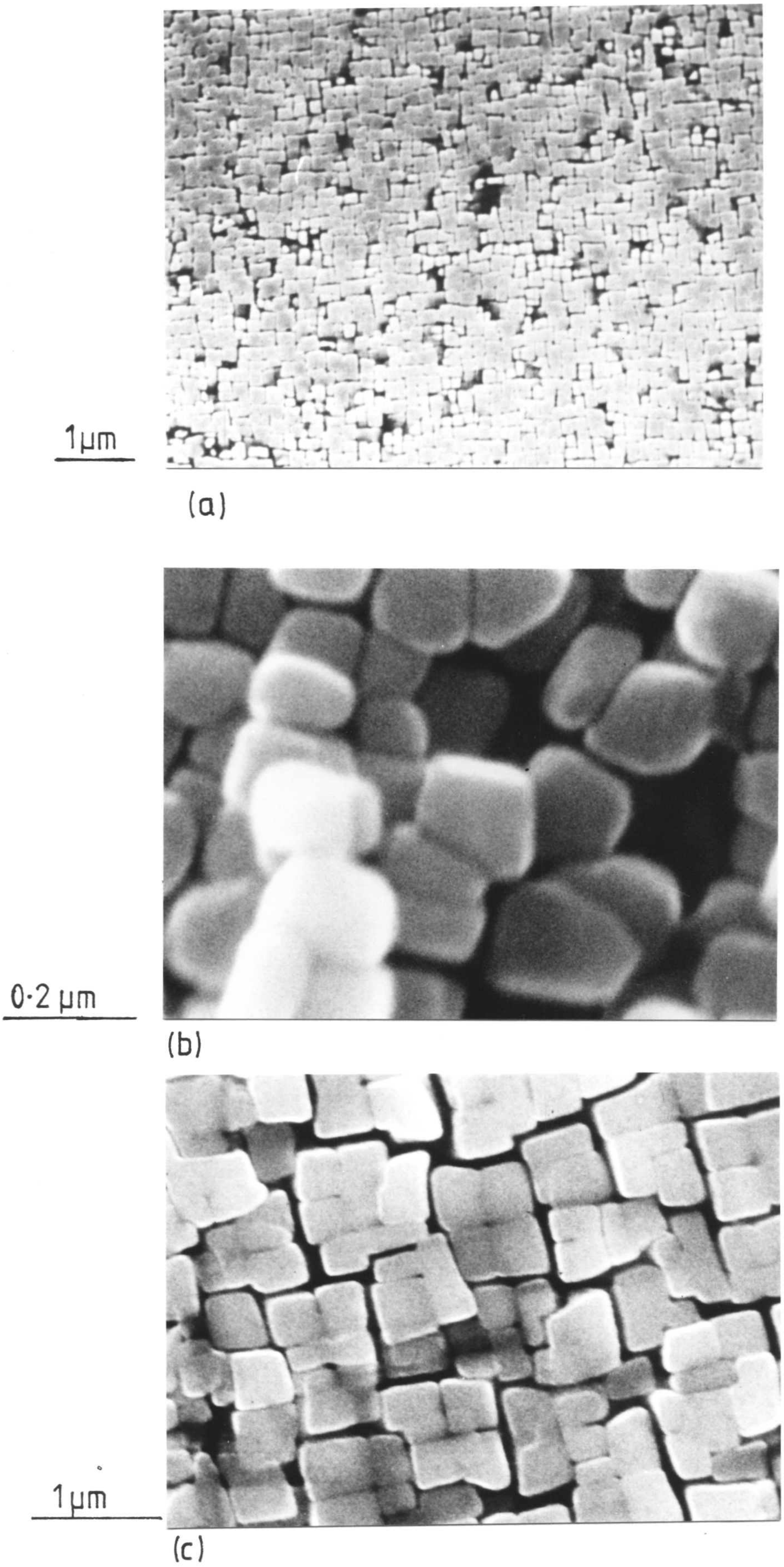

Fig. 2.7. Micrographs showing the microstructures produced after homogenisation for 8 hrs at 1570K (a) and 32 hrs at 1570K (b), and 36 hrs at 1570K followed by 16 hrs at 1390K (c).

superlattice defect energies it was decided to increase the γ' size from about 0.2μm to about 0.5μm. Facilities were available for this to be done either by slow cooling from the homogenisation temperature or by a further heat treatment at a temperature just below the γ' solvus. Both methods were tried. Slow cooling at 30K/min. produced an unsatisfactory microstructure containing an irregular γ' size distribution. By heat treating for 16 hours at 1390K a suitable microstructure consisting of an even distribution of similar sized γ' octdoadigally diced cubes (fig. 2.7c). The growth of gamma prime to form octdoadigally diced cubes proceeds by the development of solid state dendrites, with {001} facets, in <111> directions, figure 2.8, as discussed by Ricks, Porter and Ecob (1983). In most high γ' volume fraction alloys soft impingement prevents the growth process passing stage (e) of figure 2.8. This can be clearly seen in the final heat treated microstructure shown in figure 2.7(c).

2.6.2 Microanalysis of the homogenised structure

Fine scale compositional variations within the homogenised microstructure were studied using a Philips 400T TEM/STEM with a Link 860 analysis unit. Thin foils were manufactured by the route described in 3.3.1. Foil thicknesses were determined using the convergent beam method described by Kelly, Jostsons, Blake and Napier (1975). At least ten γ' areas and six γ areas were analysed in each of the seven alloys. The spot size used was 20nm (after allowing for beam broadening in the foil) and the results were corrected for atomic number and absorption; typical analysis points are shown in figure 2.9.

Analysis of the dendritic carbide showed it contained 42 at.% Ti, 31.5 at.% Ta, 19 at.% W and 8 at.% Ni. There was little compositional or morphological change between the as-cast and heat treated carbides.

The γ and γ' analyses collected are listed in tables 2.1 and 2.2. It is worth noting that for most elements the errors in the γ analysis were

Table 2.1. Gamma Prime Compositions (at.%)

	Alloy							
Element	A	B	C	D	E	F	G	Error
Ni	67.8	72.4	71.3	70.5	70.6	71.0	69.8	±0.7
Al	18.6	13.8	15.9	17.1	16.6	17.0	17.2	±0.8
Ti	3.9	3.8	3.5	3.3	3.2	3.1	2.8	±0.2
Cr	3.9	3.8	3.3	3.5	3.3	3.4	4.0	±0.2
Co	3.1	3.1	2.9	3.0	2.9	2.6	3.0	±0.2
Ta	1.2	1.3	1.2	1.3	1.5	1.2	1.2	±0.1
W	1.4	1.2	1.9	1.4	1.9	1.6	2.0	±0.2

Determined by EDS of 10 sample points per alloy

Table 2.2. Gamma Compositions (at.%)

	Alloy							
Element	A	B	C	D	E	F	G	Error
Ni	63.0	65.2	64.9	66.1	63.9	64.0	64.1	±1.3
Al	9.7	6.1	11.1	9.1	8.5	8.7	8.7	±0.9
Ti	1.7	1.2	1.5	1.5	1.1	0.9	0.9	±0.2
Cr	17.1	17.6	14.7	14.6	18.2	17.0	17.0	±1.5
Co	6.3	7.0	5.9	6.2	6.5	6.6	6.6	±0.4
Ta	-	0.1	0.1	0.3	0.4	0.3	0.3	±0.3
W	2.3	2.4	2.9	2.2	2.4	2.5	2.5	±0.2

Determined by EDS of 6 sample points per alloy

Errors quoted are the standard deviations for each of the alloys.

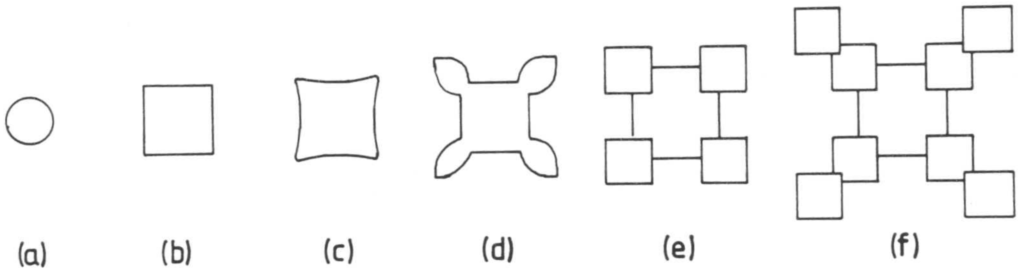

Fig. 2.8. Diagram showing the stages in the growth of a γ' precipitate (after Ricks et al., 1983).

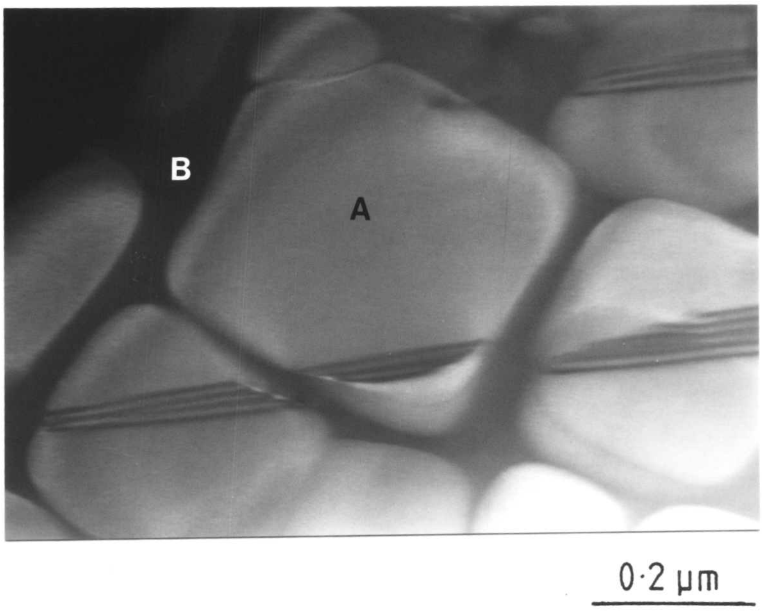

Fig. 2.9. Bright field transmission electron micrograph showing typical γ' (A) and γ (B) analysis points used to obtain the compositions reported in tables 2.1, 2.2 and 2.3.

significantly larger than those in the γ' regions. This was because in these alloys the γ regions were so narrow that the broadened beam almost certainly passed through a small amount of the γ'. The aluminium analyses were not thought to be accurate due to the way in which the Link 860 software performs the background subtraction - appendix C.

Tables 2.1 and 2.2 show that the heat treatment was sufficient to give an acceptably homogeneous product. As shown, the error in the Ti determination was assessed to be ±0.2 at.%. Table 2.3 shows that the interval in Ti content between the alloys was less than the error in their determination. Consequently it was decided to study three significantly different alloys. The alloys chosen were A, D and G; table 1.2 shows that these alloys were identical except for the systematic replacement of some Ni by Ti.

The results in tables 2.1 and 2.2 show that Al, Ti and Ta partitioned to the γ' phase and that Co, Cr and W partitioned to the γ. Table 2.3 shows that as the alloy Ti content was increased, the level in the γ' gradually rose as did the level in the γ.

It must be noted that these microanalysis results were obtained from the Link 860 with no additional corrections. They must therefore be treated as comparisons of one alloy with another and not as absolute accurate analysis values.

2.7 Lattice Parameter and Alloy Misfit

The γ' lattice parameter of alloys A, D and G was obtained by X-ray powder photography in a Debye-Scherer camera using CuK$_\alpha$ radiation. Extracts of γ' were obtained from homogenised alloys electrolytically using a solution of 20% phosphoric acid in water containing 4 gm/l of tartaric acid, to suppress the formation of heavy metal hydroxides, at room temperature. This is the technique used by Rolls-Royce Ltd. TEM examination of a sample of the extract showed no evidence of residual γ on the γ'. Extracts of γ were

Table 2.3. Alloy, γ and γ' Ti Contents (at.%)

Alloy	A	B	C	D	E	F	G
Bulk composition	2.7	2.5	2.4	2.2	2.1	2.1	1.8
γ' composition	3.9	3.8	3.5	3.3	3.2	3.1	2.8
γ composition	1.7	1.2	1.5	1.5	1.1	0.9	0.9

error = ±0.2

Table 2.4. Lattice Parameters of Alloys A, D and G from X-ray Powder Diffraction Photographs (Kenyon, 1983)

Alloy	Overall Ti content (at.%)	γ' Ti content (at.%)	γ Ti content (at.%)	Corrected lattice parameter, a (nm)	
				γ'	γ
A	2.7	3.9	1.7	0.35823	0.35810
D	2.2	3.3	1.5	0.35808	-
G	1.8	2.8	0.9	0.35797	0.35800

error in a = ±0.00005nm

also manufactured by an electrolytic method in 5% hydrofluoric acid, 10% glycerol and 85% water at room temperature. A stainless steel cathode was used; unfortunately this reacted with the electrolyte to produce an unidentified iron compound. The addition of tartaric acid suppressed this reaction sufficiently for γ lattice parameter determinations to be made for alloys A and G. It was not possible to see if any γ' was present in the extract by TEM (Kenyon, 1983).

Powder films were taken using an exposure time of 2 hours and the lattice spacings and unit cell size were calculated by the normal methods (Cullity, 1978).

In table 2.4 it is shown that as the Ti content increases so the γ' lattice parameter increases. This disagrees with Nordheim and Grant (1954) who have reported that the lattice parameter of Ni_3Al changed by only 1% when 60 at.% Ti was added. However, the results of Fell (1961) agree with the observations made in this investigation: no change in misfit was predicted as table 2.3 shows that the γ Ti content rises in unison with the γ' Ti content.

The misfit values calculated using the formula:

$$M = \frac{a_{\gamma'} - a_{\gamma}}{a_{\gamma'}} \qquad \text{eqn. 2.2}$$

were smaller than the errors. It was concluded that there was no measurable γ/γ' misfit. The fact that the γ' particles observed in the alloy were cubic even though low misfit alloys are expected to contain spherical particles supports the suggestion, previously reported, of Havalada (1969a) that precipitate shape is affected by factors other than the γ/γ' misfit. It is thought that soft impingement between the growing γ' particles could explain this observation.

The <u>in situ</u> misfit was measured using the convergent beam HOLZ method of Ecob, Ricks and Porter (1981). As expected, no misfit was detected; any misfit would be taken up by the γ' planes pulling the planes of the narrow γ regions to match the lattice parameters.

Although no γ/γ' misfit could be detected at room temperature, it may be that there is a difference in thermal expansivity between γ and γ' which will result in a misfit at higher temperatures. No data are available for the thermal expansivity of γ and γ' and no measurements of misfit have been undertaken at high temperatures. These experiments could provide some useful information about deformation of superalloys at high temperatures.

2.8 γ' Long Range Order Parameter

The APB energy of a material is closely related to its degree of ordering. As one of the aims of this project is to evaluate the APB energy it would perhaps be useful to relate the energy values to the degree of ordering. Mihalisin (1969) found that the order parameters of γ' extracted from IN-731, 713C and 713LC were high (~0.95) in IN-713C and LC, and that they were largely unchanged by heat treatment.

Calculation of the order parameter involves comparing the relative intensities of a fundamental line and a superlattice line. (100) is usually chosen as the superlattice line and (200) as the fundamental. These are high intensity lines which eliminate any preferential orientation effects. Diffractometer traces and Guinier camera films of the alloys studied showed no superlattice lines with an intensity significantly above the background value, thus making it impossible to calculate the order parameter.

Reference to table 1.2 shows that these alloys contain significant amounts of W and Ta; elements which strongly absorb X-rays. It is possible that the presence of these elements reduces the intensity of the superlattice lines to undetectable levels. The effect has previously been observed by Oblak and Kear (1972) in Mar-M 200.

It has been assumed that the order parameter is greater than 0.8, the lowest value reported by Mihalisin, and at room temperature there was no significant change in ordering through the alloy series. It would be interesting to perform a heating experiment on a γ' extract to see if order parameters can be calculated at higher temperatures.

2.9 Conclusions

(i) The results indicate that Ti decreases the width of the heat treatment window for cast single crystal superalloys due not only to the lowering of the solidus with increasing Ti, but also because the volume fraction of γ/γ' eutectic increases with overall Ti concentration. The effect could be mitigated by means of longer heat treatments which would have the effect of reducing the apparent γ/γ' eutectic solvus.

(ii) The alloys achieve adequate homogeneity after annealing at 1570K for 32 hours (36 hours was used for reasons of convenience) and this homogeneity is both long range and on the level of individual γ' particles.

(iii) Subsequent heat treatment at 1390K for 16 hours grows the γ' from 0.2μm to 0.5μm without any observable loss in coherency or change in composition.

(iv) Increasing the Ti content increases the γ' and γ lattice parameters but not the γ/γ' misfit.

(v) The measured misfit between extracted γ and γ' phases was zero for alloys A and G.

(vi) It was not possible to calculate the long range order parameter of γ' because the intensity of the superlattice lines was not significantly different from the background radiation.

(vii) The error in titanium determination was ±0.2 at.%. This was larger than the intervals between the alloy compositions (table 1.2). Consequently, only alloys A, D and G were studied. These three alloys have identical compositions except for the systematic change in Ti.

(viii) All specimens used for the determination of APB and SSF energies were homogenised for 36 hours at 1570K, treated to grow the γ'

for 16 hours at 1390K and air cooled. This heat treatment produced an acceptably homogeneous product of γ' cubes in a γ matrix. After heat treatment all three alloys had the same volume fraction of γ' ($\sim$0.6) and the same γ' size. No misfit was measured so it was assumed that the misfit strengthening was negligible.

By heat treating in this way, any contributions to alloy strengthening by factors (ii) to (iv) of 1.5.3 will be constant.

CHAPTER 3

EXPERIMENTAL TECHNIQUES: DISLOCATION GENERATION AND OBSERVATION

3.1 Introduction

The aim of this investigation was to measure accurate values for the superlattice stacking fault (SSF) and anti-phase boundary (APB) energies of γ'. These energies are functions of state and as such are independent of the method by which defects are generated. A process of cold deformation and annealing has been used to produce extended superdislocation nodes (super nodes) and superdislocation networks, where the extended nodes contain superlattice stacking faults; these dislocation configurations allow simultaneous determination of stacking fault and APB energies. This chapter describes the deformation and annealing process used to create suitable defects. It then reviews the electron microscopical methods used to analyse these defects and describes the way in which they were applied in this investigation.

3.2 Dislocation and Defect Generation

Prior to deformation, samples of each of the as-cast alloys were heat treated in accordance with the conclusions of chapter 2.

Dislocations were introduced into the material by room temperature compression to between 1 and 2% strain by a stress of 400MPa. Specimens were deformed along the [001] axis. In this orientation the highest Schmidt factor lies in two directions on each of the (111), $(\bar{1}11)$, $(\bar{1}\bar{1}1)$ and $(1\bar{1}1)$ planes. Thus, eight intersecting slip systems are simultaneously active and these produce many intersecting dislocations on different planes (4.4).

After deformation the specimens were annealed for 24 hours at 1173K. At this temperature there was no change in the γ' size or structure but dislocation climb was apparently possible allowing recovery to produce a more equilibrated dislocation structure.

3.3 Electron Microscopy

3.3.1 Thin specimen preparation

Thin foils for electron microscopy were manufactured from the deformed and annealed specimens. Three foil normals were studied: <001>, <110> and <111>. Specimens with the required orientations were obtained using the Laue back reflection technique with unfiltered tungsten radiation. First, the specimens were electro-polished for 15 secs. using Struers Al electrolyte in a Struers Polectrol (voltage: 25V, flow rate: 2.5) before mounting them on a three-circle tilting goniometer. A Laue back reflection X-ray photograph of the polished surface was taken on Polaroid type 57 film. The specimen orientation was plotted onto a stereographic projection using a Greninger chart, as described by Cullity (1977). The specimen was then tilted to approximately the required orientation and a further Polaroid was taken to check the accuracy of the manipulation. If necessary, adjustments in orientation were made. The specimen was then carefully transferred to a fixed holder. Slices of material between 0.3 and 0.4mm thick were cut using a carborundum slitting disc. 3mm diameter blank discs were carefully stamped from the slices. These were ground down to between 0.13 and 0.2mm and profile electro-polished in a Fishione twin jet polisher or a Metalthin twin jet polisher containing a solution of 10% perchloric acid in ethanol at a temperature of between 268K and 273K, using a voltage of 30V and a current of approximately 70mA. The specimens were thoroughly washed in ethanol. The profiled blanks were polished to perforation using the equipment shown in figure 3.1. A solution of 20% perchloric acid in ethanol was used at 275K with a voltage of 10V and a current of 50mA. Polishing was stopped when the foil perforated and the hole was seen to grow rapidly. The specimen was again thoroughly washed in

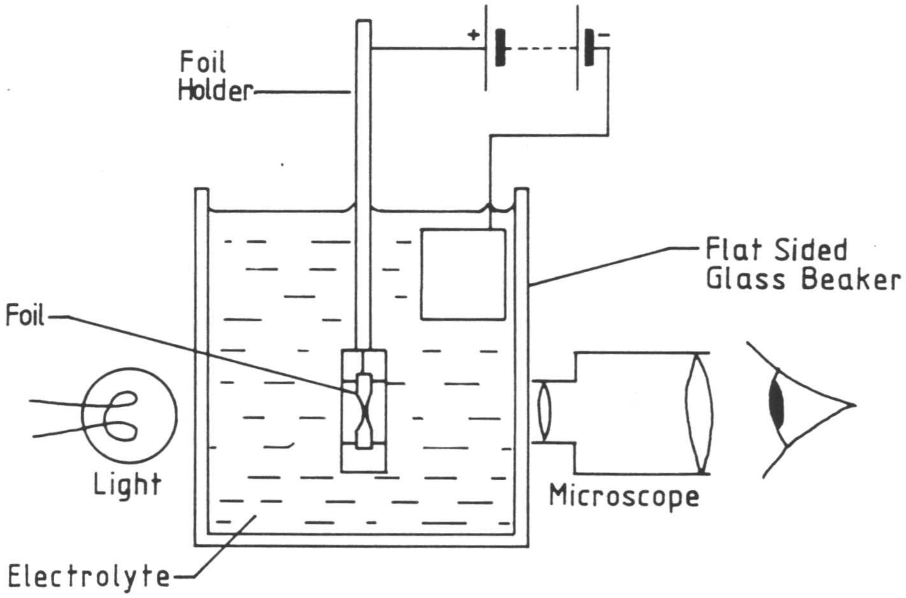

Fig. 3.1. Schematic illustration of the apparatus used for final polishing and perforation of foils.

ethanol. Specimens were stored in specimen boxes in a vacuum desiccator. Foils stored in this way lasted for up to three months.

3.3.2 Examination of thin specimens

All the transmission electron microscopy (TEM) reported in this thesis has been carried out on either a Philips 400T operating at 120kV ($\lambda = 3.35 \times 10^{-3}$nm) or a JEOL 200CX operating at 200kV ($\lambda = 2.51 \times 10^{-3}$nm). In addition to the conventional bright field technique, centred weak beam dark field imaging has also been extensively used. A detailed discussion of dynamical electron diffraction theory has not been undertaken.

3.3.3 Dislocation images in the electron microscope

Bright field dislocation images occur because the defect introduces a phase factor relative to the perfect lattice at the distorted planes around the core. This results in a broad dark line which represents the position of the dislocation but does not coincide with the core position. If the dislocation is viewed using a reflection from undistorted planes no image will result (3.3.5). Information which can be most easily interpreted is gained from the TEM image if diffraction is limited to one set of planes. This is done by tilting the foil so only one reciprocal lattice point is excited. Images formed in this condition are bright field two-beam conditions (fig. 3.2a) and the diffraction vector from (000) to (hkℓ), $\underline{g}$, describes the image. Bright field image contrast is improved if a slight positive deviation, $\underline{s}$, from the Bragg condition is applied (Hirsch, Howie, Nicholson, Pashley and Whelan, 1977 and fig. 3.2b). The sign and size of $\underline{s}$ can be measured as described in 3.3.4.

Under bright field conditions, with $\underline{s}$ close to zero, many planes around the dislocation are strongly diffracting; this gives rise to a low resolution dislocation image. If the diffracted beam is tilted so that it passes down the optic axis of the microscope (fig. 3.2c), the image is formed only by diffracted electrons. This is a centred dark field image;

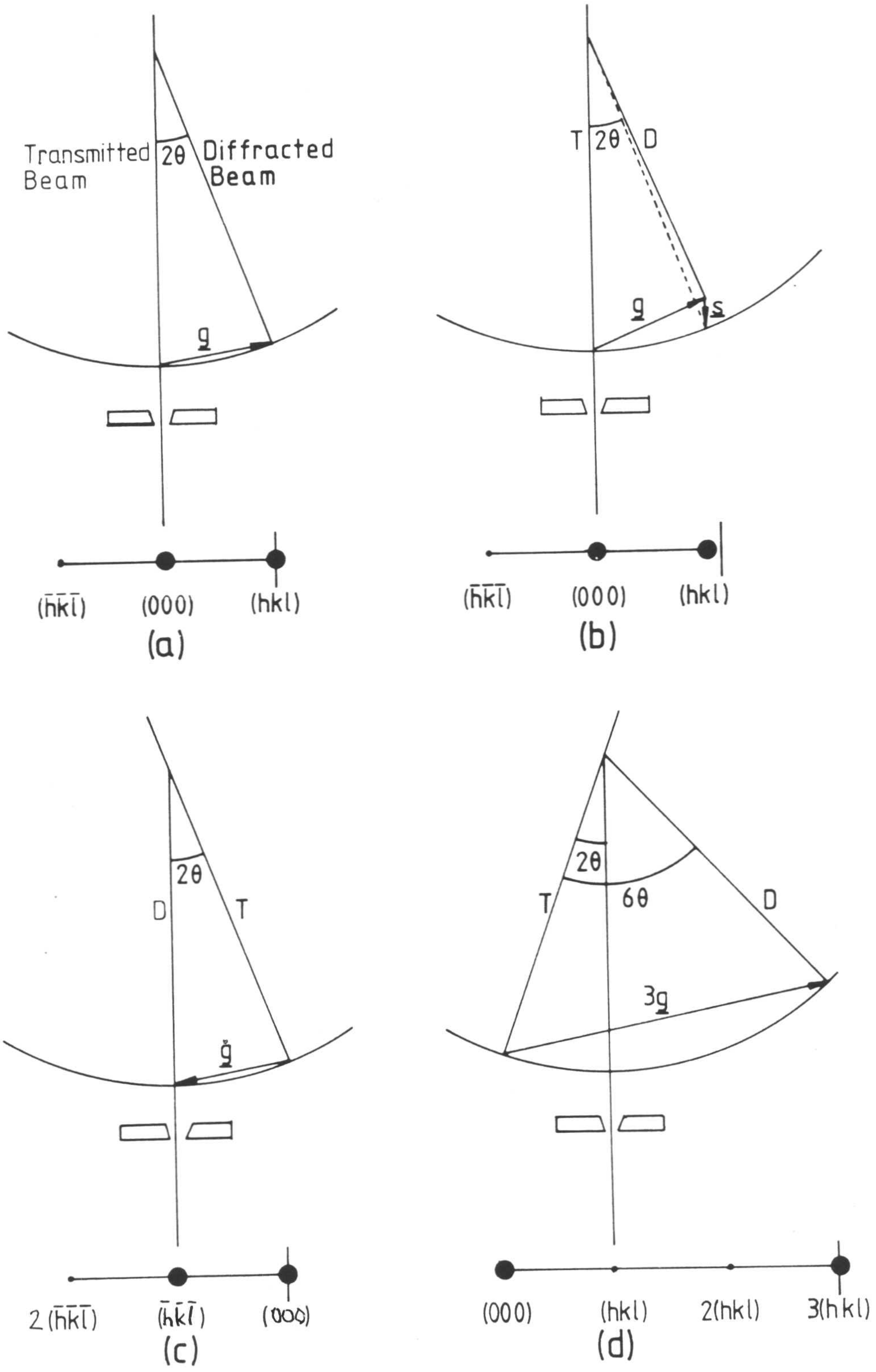

Fig. 3.2. Ray diagrams and Ewald sphere constructions showing conventional two-beam bright field in the Bragg condition (a), conventional two-beam bright field with a positive deviation from the Bragg condition (b), two-beam centred dark field (c), and ($\underline{g}$,3$\underline{g}$) weak beam dark field (d).

maximum intensity is gained when $\underline{s} = 0$.

An increase in resolution and contrast can be gained by forming centred dark field images from weak beams (fig. 3.2d), rather than the strong beams used for bright field and dark field. This is the weak beam technique (Cockayne, Ray and Whelan, 1969) and it is useful because the image is formed from the strongly distorted planes near the dislocation core which are in an orientation which diffracts strongly. In weak beam, dislocations appear as very narrow bright lines against a low intensity background. Cockayne et al. (1969) have shown that as $\underline{s}$ is increased, the width of the dislocation image is decreased and gets closer to the true position of the dislocation core.

Weak beam images are most easily produced following the method described by Howie and Sworn (1970). Their method, known as the $3\underline{g}$ weak beam technique, requires the bright diffracted spot of a normal two-beam condition to be tilted to the optic axis of the microscope to produce the configuration shown in figure 3.3. This method is preferred to that of Cockayne et al. (1969) because it provides more accurate positioning of defects and also allows switching between bright field and weak beam images; a useful aid to focusing the often very faint weak beam images. If a weak beam image from a higher order reflection is required, the specimen can be tilted so that the $n\underline{g}$ Kikuchi line intersects the $n\underline{g}$ diffraction spot (fig. 3.4a) or the next diffraction spot can be tilted to the optic axis of the microscope (fig. 3.4b). Throughout this thesis weak beam diffraction conditions will be reported as $W_{(n\underline{g},\ n\underline{g})}$. The first $n\underline{g}$ refers to the imaging spot, while the second $n\underline{g}$ refers to the strongly excited diffraction spot. Care must be taken in weak beam conditions because when $\underline{s}_{3\underline{g}} = 0$, in certain cases double images are formed from single dislocations. These can be misinterpreted as a single dislocation dissociated into two partials. However, Stobbs and Sworn (1971) showed that when $\underline{s}$ is made slightly positive of the $3\underline{g}$ reciprocal lattice point single

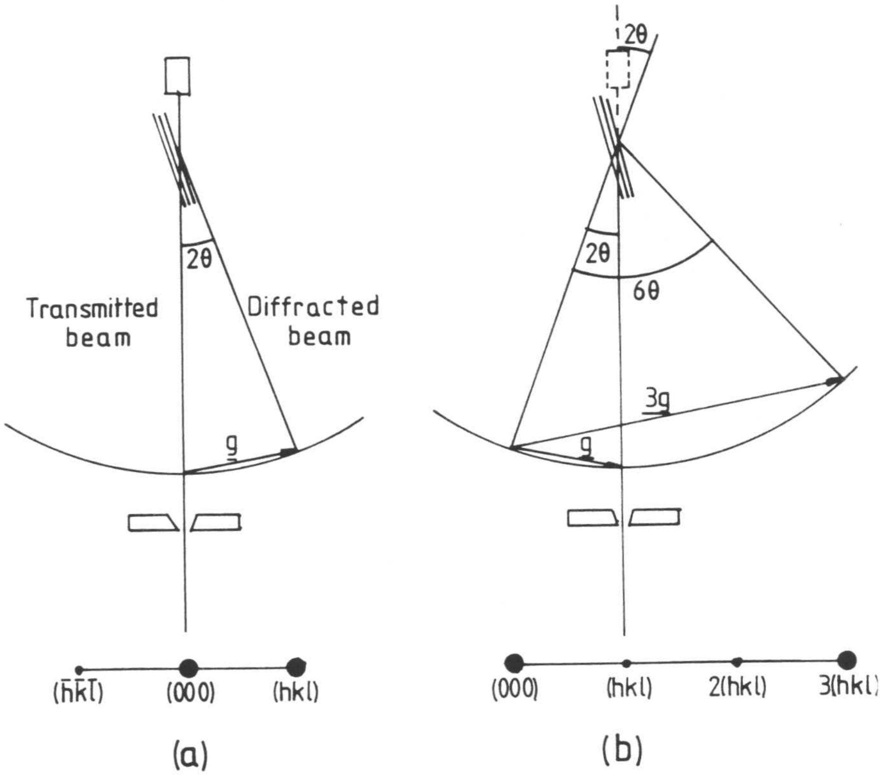

Fig. 3.3. Ray diagrams showing conventional two-beam bright field (a) and two-beam $W_{(\underline{g},3\underline{g})}$ weak beam dark field. If the gun is tilted to bring $(\overline{hk}\ell)$ in (a) to the centre as in (c), the diffraction condition is changed to produce the $W_{(\underline{g},3\underline{g})}$ weak beam dark field condition.

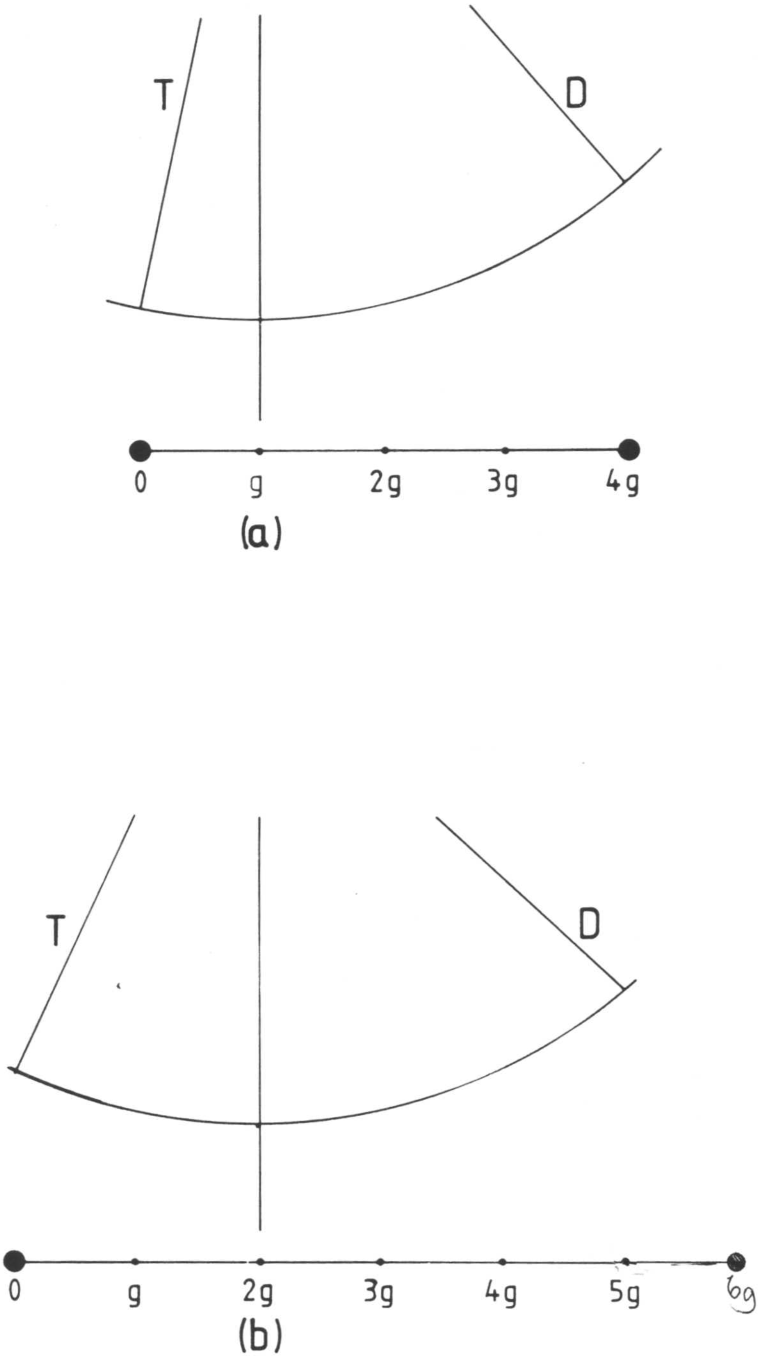

Fig. 3.4. Two possible diffraction conditions which can be used to obtain high values of $|\underline{s}|$: the $W_{(\underline{g},4\underline{g})}$ weak beam dark field condition (a), and the $W_{(2\underline{g},5\underline{g})}$ weak beam dark field condition (b).

dislocations always produce single images. To avoid this difficulty all weak beam micrographs presented were recorded with $\underline{s}$ slightly positive of the $3\underline{g}$ reciprocal lattice point. Care was always taken to ensure that no unwanted beams were excited during the tilting operation.

There are other dangers inherent in the quantitative interpretation of weak beam micrographs, particularly in thin areas and near specimen surfaces. These have been discussed by Stobbs and Sworn (1971) and Stobbs (1973). These papers suggest that reliable dislocation spacings may be obtained from centrally placed defects in foils greater than 70nm thick.

Cockayne et al. (1969) show from theory and by example that the intensity, and less strongly the position, of the peaks in sufficiently weak beam images from partial dislocations depends upon various factors; most critically on the depth of the dislocation in the foil. Cockayne (1973) shows by computation that the change in image with depth is a dynamical effect.

Cockayne also reported that the presence of a stacking fault or APB between paired dislocations may reduce the contrast of one of the pair. Experimentally these variations may lead to the disappearance of one of the dislocation images. If such a disappearance causes difficulties, a second image with a slight change in $\underline{s}$ can be used to overcome the difficulty. Reduction in the intensity of one image has frequently been observed during this investigation (eg. fig. 4.24b), probably due to a combination of the presence of a fault and a difference in dislocation depth.

3.3.4 Application of the weak beam technique to γ'

Cockayne (1973) has defined true weak beam conditions as those in which $|\underline{s}| > 2.0\times10^{-3}\text{nm}^{-1}$ (for $\underline{g}.\underline{b} \leq 2$) and $|\underline{\omega}| = |\underline{s}\xi_{\underline{g}}| \gtrsim 5$ with no other reflection excited. Under these conditions a dislocation image will be within 2nm of its core, it will have a half peak height width of ∿1.5nm and its position will vary by <±0.5nm with depth in the foil.

To check that these conditions are satisfied the deviation parameter, $\underline{s}$, can be calculated from:

$$|\underline{s}| = \frac{(n-1)\,|\underline{g}|^2\lambda}{2} \qquad \text{eqn. 3.1}$$

where n is the excited reflection which need not be integral, $|\underline{g}|$ is the modulus of the diffraction vector and λ is the wavelength of the electrons. This formula can be geometrically derived from figure 3.2(a) and can be applied equally well to any diffracting condition.

The γ' precipitate in the alloys studied has a fairly large lattice parameter, $\underline{a} = 0.358$nm (2.7), consequently $\underline{g}$ is fairly small. Using extinction distance data calculated, for an alloy similar to those studied here, by Oblak and Kear (1972) (table 3.1), values for $\underline{s}$ and $\underline{\omega}$ have been calculated. It was found that at 120 kV true weak beam conditions were obtained for $\underline{g} = \{111\}$ and $\{200\}$ when $W_{(\underline{g},5\underline{g})}$ conditions were satisfied for $\underline{g} = \{220\}$ and $\{311\}$ $W_{(\underline{g},3\underline{g})}$ was found to be adequate. Thus good weak beam images were obtainable from all four of the commonly used $\underline{g}$ vectors. For 200 kV the $W_{(\underline{g},4\underline{g})}$ condition was sufficient for $\underline{g} = \{220\}$ and $\{311\}$, but $\underline{g} = \{111\}$ and $\{200\}$ required a prohibitively large reflection to be excited for true weak beam conditions to be obtained.

It is worth remembering that although $\underline{s} = 2.0\times10^{-3}\text{nm}^{-1}$ is the lower limit for accurate quantitative weak beam microscopy near weak beam conditions using large deviation parameters less than $2.0\times10^{-3}\text{nm}^{-1}$ can be very useful in improving the contrast and resolution at complex dislocation interactions. Both true and near weak beam conditions have been extensively employed to aid the identification of dislocation types and the interpretation of complicated dislocation interactions.

The weak beam dark field technique is an invaluable aid to the kind of quantitative microscopy required for an investigation of this type. It enables more accurate determination of dislocation spacings and positions than bright field imaging and it therefore allows more accurate values of

Table 3.1. Extinction Distances (in nm) for Selected Reflections in Mar-M 200 (table 1.1) after Oblak and Kear (1972)

Fundamental		Superlattice		
hkℓ	Extinction distance	hkℓ	Extinction distance	Effective extinction distance
111	34	100	1547	700
200	39	110	30614	-
220	57	300	1748	5880
311	70			

Table 3.2. Summary of g.b Values for Partial Dislocations

$\underline{g}\cdot\underline{b}$	ω $(\underset{\sim}{s}\cdot\xi_{\underline{g}})$	Comment	Reference
0	ALL	INVISIBLE	Howie & Whelan (1961) Silcock & Tunstall (1964)
± 1	$\omega \lesssim 1$	VISIBLE	
$\pm\frac{1}{3}$	$1 < \omega < 1$	INVISIBLE N.B SF in contrast	Howie & Whelan (1962) Clarebrough & Morton (1969)
$\pm\frac{2}{3}$	$\omega < 0.7$	VISIBLE	
$*-\frac{2}{3}$	$\omega \gtrsim 0.7$	VISIBLE	Silcock & Tunstall (1964)
$*+\frac{2}{3}$	$\omega \gtrsim 0.7$	INVISIBLE	
$*-\frac{4}{3}$	$\omega \gtrsim 0.7$	INVISIBLE	Oblak & Kear (1972)
$*+\frac{4}{3}$	$\omega \gtrsim 0.7$	VISIBLE	

* Table constructed with the fault to RIGHT of dislocation line; if the fault is to the LEFT the signs are reversed.

stacking fault energies and APB energies to be calculated (chapter 5). The technique has been applied to many alloy systems to determine stacking fault energies: for example in Cu-Al (Cockayne et al., 1969), in Si (Ray and Cockayne, 1970), in Ag (Cockayne, Jenkins and Ray, 1971), in Cu (Stobbs and Sworn, 1971) and in austenitic stainless steel (Bampton, Jones and Loretto, 1978). APB energies in ordered structures have been determined in Fe-3% Al by Ray, Crawford and Cockayne (1970), in $L1_2$ structures, Zr_3Al (Howe, Rainville and Schulson, 1974) and Ni_3Ga (Suzuki, Ichihara and Takeuchi, 1979). The technique has also been employed to observe complex dislocation interactions, for example, Ray and Cockayne (1971) observed nodes in silicon.

3.3.5 Burgers vector analysis of $a/_2$<110> dislocations

This section discusses the use of the $\underline{g}\cdot\underline{b} = 0$ and $\underline{g}\cdot\underline{b}\times\underline{u} = 0$ invisibility criteria for the identification of $a/_2$<110> dislocations. The theoretical description of the contrast arising from crystal defects such as dislocations and stacking faults has been formulated by Howie and Whelan (1961) and is contained in the Howie-Whelan equations. These equations may be represented in many ways but the most useful in this case is the one shown below.

In a two-beam dynamical diffraction condition the amplitudes of the transmitted (ϕ_o) and diffracted (ϕ_g) waves may be represented as:

$$\frac{d\phi_o}{dz} = \frac{i\pi\phi_o}{\xi_o} + \frac{i\pi\phi_g}{\xi_g}\exp(2\pi i\underline{s}z+2\pi i\underline{g}.\underline{R}) \qquad \text{eqn. 3.2a}$$

and

$$\frac{d\phi_g}{dz} = \frac{i\pi\phi_o}{\xi_g}\exp(-2\pi i\underline{s}z-2\pi i\underline{g}.\underline{R}) + \frac{i\pi\phi_g}{\xi_o} \qquad \text{eqn. 3.2b}$$

where $\underline{s}$ is the deviation vector, ξ_g is the extinction distance, $\underline{g}$ is the diffraction vector, $\underline{R}$ is the defect displacement vector, i is $\sqrt{-1}$, and z is the distance of the defect from the top surface of the foil, as shown in figure 3.5. Effectively, these equations mean that distortion of the lattice creates a phase factor $\exp(-i\alpha)$ where $\alpha=2\pi\underline{g}\cdot\underline{R}$. This phase factor is superimposed on the normal crystal scattering. So, if an atom is displaced by $\underline{R}$, then the phase of the scattered wave is changed by $\exp(-2\pi i\underline{g}\cdot\underline{R})$. This phase factor represents the scattering from the diffracted to the transmitted beam as $\exp(2\pi i\underline{g}\cdot\underline{R})$ while the reverse is $\exp(-2\pi i\underline{g}\cdot\underline{R})$. Thus, in a bright field image, as stated in 3.3.3, the strain field will diffract electrons away and appear darker.

Hirsh et al. (1977) have shown that for an edge dislocation in an isotropic medium:

$$\underline{R} = \frac{1}{2\pi}\left[\underline{b}\Phi+\underline{b}\quad\frac{\sin 2\Phi}{4(1-\nu)}+(\underline{b}\times\underline{u})\left(\frac{(1-2\nu)}{2(1-\nu)}\ln r+\frac{\cos 2\Phi}{4(1-\nu)}\right)\right] \qquad \text{eqn. 3.3}$$

where $\underline{b}$ is the dislocation Burgers vector,

, $\underline{u}$ is a unit vector in the positive direction of the dislocation line, ν is Poissons ratio, r is a radial co-ordinate measured from the dislocation and Φ is an angular co-ordinate in the plane normal to the line measured from the slip plane (fig. 3.5). The definition of $\underline{b}$ is consistent with the definition of Bilby, Bullough and Smith (1955) more commonly known as the FS/RH perfect crystal convention (fig. 3.6).

Now, if the crystal is orientated such that the beam 'sees' no distortion (i.e. the dislocation cannot be seen by an incoming beam) the phase factor, α, must be zero, so $\underline{g}\cdot\underline{R}=0$. If eqn. 3.3 is multiplied through by $\underline{g}$ and equated to zero, it is seen that the condition for the invisibility of a general dislocation is when $\underline{g}\cdot\underline{b}$, $\underline{g}\cdot\underline{b}_e$ and $\underline{g}\cdot\underline{b}\times\underline{u}$ are all zero.

This is the basis for the determination of $a/_2$<110> dislocation

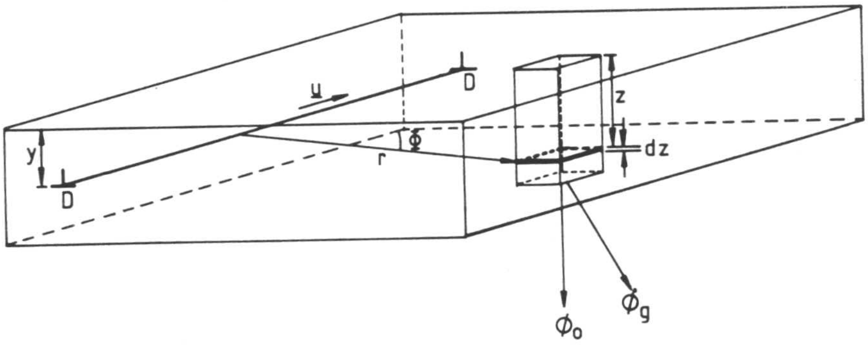

Fig. 3.5. The column approximation for a thin foil containing a dislocation DD. This approximation is used to produce equations 3.2 and 3.3. See text for details.

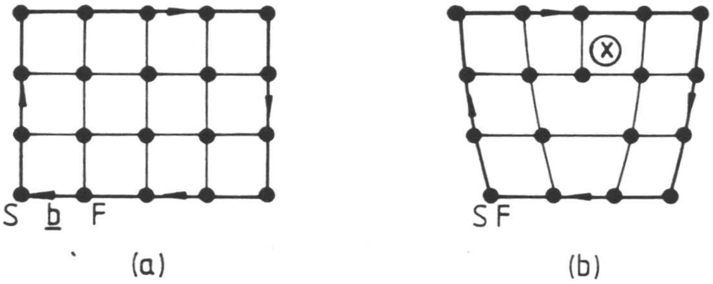

(a)

(b)

Fig. 3.6. A Burgers circuit around a dislocation (b) does not close in the perfect lattice without the introduction of a vector equal to the Burgers vector (a). The criterion used for Burgers vector determination is the FS/RH criterion.

Burgers vectors in isotropic materials because $\underline{g}\cdot\underline{b}$ is either zero, when the reflection used is for undistorted plane , or an integer, when the reflection used comes from distorted planes. When $\underline{g}\cdot\underline{b}=0$ the dislocation is invisible and it is visible when $\underline{g}\cdot\underline{b}$ is an integer. This method is equally applicable to weak beam as well as bright field conditions.

By recording a series of bright field or weak beam micrographs in various two beam conditions the identity and type of any $a/_2\langle 110\rangle$ dislocation can be obtained. In this investigation the commonly used diffraction vectors were {111}, {200}, {220} and {311}. In all cases $\underline{s}$ was positive.

Many dislocation analyses have been undertaken using the technique described above and these are presented in subsequent chapters.

3.3.6 Burgers vector analysis of $a/_6\langle 211\rangle$ and $a/_3\langle 211\rangle$ dislocations

The determination of the Burgers vectors of $a/_6\langle 211\rangle$ and $a/_3\langle 211\rangle$ dislocations in γ' is rather more complex than that for $a/_2\langle 110\rangle$ dislocations discussed above because the $\underline{g}\cdot\underline{b}$ values are not necessarily integral. Some general rules for identification have been set out using image simulation techniques. Unfortunately, these have some associated anomalies which cannot be explained adequately and the rules must, therefore, be applied with discretion. Each of the possible $\underline{g}\cdot\underline{b}$ values is discussed individually below.

As above, when $\underline{g}\cdot\underline{b}=0$ dislocations are invisible and when $\underline{g}\cdot\underline{b}$ is an integer they are visible for all values of $\underline{s}$ and $\underline{\omega}$ (Howie and Whelan, 1961 and Silcock and Tunstall, 1964).

When $\underline{g}\cdot\underline{b}=\pm\frac{1}{3}$ it is generally accepted that when $\underline{\omega}\lesssim 1$ all $a/_3\langle 211\rangle$ and $a/_6\langle 211\rangle$ dislocations are invisible; this also appears to hold for values of $\underline{\omega}$ above one (Howie and Whelan, 1962, Clareb~~o~~rough and Morton, 1969a,b and Clareb~~o~~rough, 1971). However, Clareb~~o~~rough and Morton (1969a,b) have reported that strong contrast can arise from Frank partial dislocations when particular beam directions are employed and it is clearly possible that other anomalies could exist.

When $\underline{g}\cdot\underline{b}=\pm\frac{2}{3}$ the situation is more complex as the position of the stacking fault associated with the partial dislocation is important, except for $\underline{\omega}\lesssim 0.7$ where the dislocation will be visible for $\pm\frac{2}{3}$. According to Silcock and Tunstall (1964) when $\underline{\omega}\gtrsim 0.7$ and the fault lies to the right of the dislocation, when $\underline{g}\cdot\underline{b}=-\frac{2}{3}$ a dislocation is visible and when $\underline{g}\cdot\underline{b}=+\frac{2}{3}$ a dislocation is invisible. Again this rule is not correct in all cases.

The final condition to be considered is $\underline{g}\cdot\underline{b}=\pm\frac{4}{3}$. Only a small amount of work has been performed at this condition. Using a combination of computation and practical observation Oblak and Kear (1972) have found that for $\underset{\sim}{\omega}\gtrsim 0.7$ with the fault lying to the right of the dislocation line when $\underline{g}\cdot\underline{b}=-\frac{4}{3}$ the dislocation was invisible and when $\underline{g}\cdot\underline{b}=+\frac{4}{3}$ the dislocation was visible.

If the dislocation sense, $\underline{u}$, is reversed then the $\pm\frac{2}{3}$ and $\pm\frac{4}{3}$ conditions will also be reversed. Table 3.2 summarises the invisibility criteria for $a/_3\langle 211\rangle$ and $a/_6\langle 211\rangle$ dislocations which have been applied throughout this investigation.

As in the case of $a/_2\langle 110\rangle$ dislocations a series of bright field and weak beam micrographs at various two beam conditions can unambiguously identify the Burgers vector and type of any $a/_3\langle 211\rangle$ or $a/_6\langle 211\rangle$ dislocations. Commonly used diffraction vectors were {111}, {200}, {220} and {311} with $\underline{s}$ positive. Since the reference system described above is based on the image seen on the microscope viewing screen all photo micrographs reproduced in this dissertation have been printed in that orientation.

3.3.7 The effect of crystal anisotropy on dislocation images

The equation for $\underline{R}$ in an anisotropic medium is considerably more complex than equation 3.3. A detailed derivation can be found in the papers of Eshelby, Read and Shockley (1953) and Stroh (1958). Head, Humble, Clareb~~o~~rough, Morton and Forwood (1973) have shown that in certain cases, which correspond to elastic isotropy, the invisibility criteria hold but that in many anisotropic crystals dislocation invisibility when $\underline{g}\cdot\underline{b}=0$ only occurs due to the weak contrast in this condition. Many papers have been written stating that for high diffraction vectors, e.g. {311}, {301}, {420} some dislocations will be invisible when $\underline{g}\cdot\underline{b}\neq0$, e.g. France and Loretto (1968) and Loretto and France (1969a,b). Oblak and Rand (1972) have shown that in Ni_3Al $\underline{g}\cdot\underline{b}=2$ and $\underline{g}\cdot\underline{b}=4$ give dislocation invisibility in certain conditions.

Despite the results of these papers and the fact that the anisotropy factor of the γ' in the alloys studied is 2.7 (see 6.2.1), the application of the effective invisibility criteria has always given self-consistent results. Other investigations of superalloy microstructures such as those reviewed by Kear (1974) have also given self-consistent results by applying the same criteria. All the dislocation analyses presented here have been carried out without the aid of image contrast computation.

3.3.8 Dislocation image position with respect to the line sense

The position of a dislocation image with respect to the actual dislocation line is dependant upon the value of $\underline{g}$ and $\underline{s}$. It will always lie to a given side of the true dislocation line for a given $\underline{s}$ and on different sides of the dislocation line for $+\underline{g}$ and $-\underline{g}$ (fig.3.7 and Hirsch et al., 1977).

If two bright field micrographs are taken, one at $+\underline{g}$ and one at $-\underline{g}$, then the dislocation line position can be defined and, provided $\underline{g}$ and $\underline{s}$ are also known, then, following the FS/RH system, the sense of the dislocation Burgers vector can be determined unambiguously.

The switch in dislocation image position when $\underline{g}$ is reversed can also be used to study dislocation pairs. In the gamma prime phase of superalloys two types of dislocation pairs are observed: the dipole (two dislocations of opposite sign on different planes) and the superdislocation

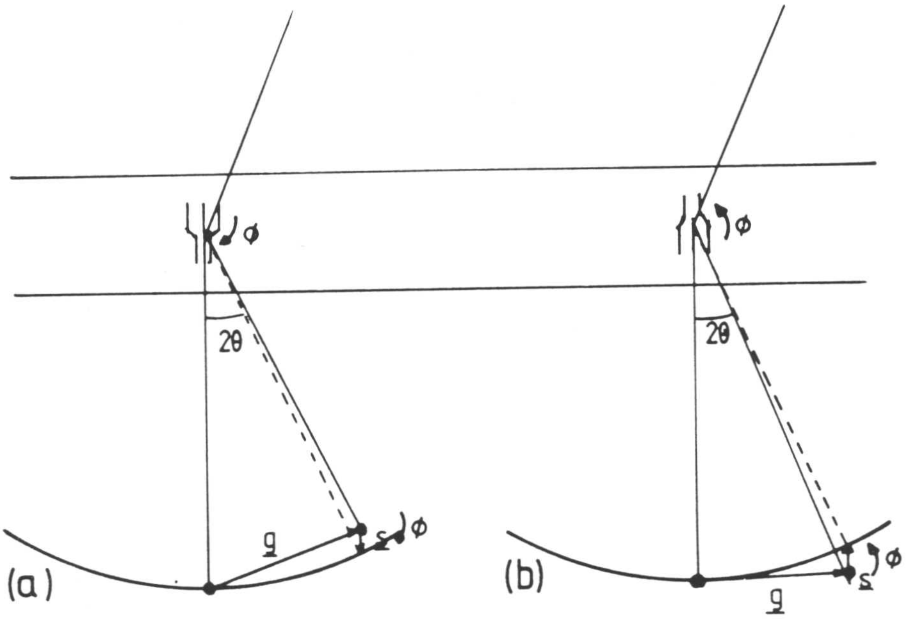

Fig. 3.7. Illustration showing that a dislocation locally tilts the reflecting planes to produce a positive deviation from the Bragg condition (a). An identical inverted dislocation in the same diffracting conditions tilts the reflecting planes to produce a negative deviation from the Bragg condition (b). The images must therefore be to one side of the dislocation line.

(two dislocations of the same sign on the same plane). These dislocation pairs are discussed in more detail in chapters 4 and 5. As shown in figure 3.8, if the two dislocations are of the same type and sense then, when $\underline{g}$ is reversed, both the images will move in the same direction and there will be no change in image spacing (fig. 3.8a). However, if the dislocations are of opposite sign, then the image spacing will change when $\underline{g}$ is reversed (fig. 3.8b). Simply, then, if the image spacing changes on reversing $\underline{g}$ then the dislocation pair is usually a dipole. If it does not change the dislocation pair is a superdislocation. The technique was first described and used by Bell, Roser and Thomas (1964) to distinguish between superdislocations and dipoles in austenitic stainless steels, α-brasses and Cu-Sn solid solutions. There is one discrepancy which must be considered when looking at a superdislocation which is dissociated into four partial dislocations as shown in figure 3.9. If this is the case an apparent change in image spacing will be observed if $\underline{b}_3$ is in contrast for $+\underline{g}$ and out of contrast for $-\underline{g}$ and $\underline{b}_2$ is out of contrast for $+\underline{g}$ and in contrast for $-\underline{g}$. The apparent spacing change will only occur when $\underline{g}.\underline{b}=\pm\frac{2}{3}$ and $\pm\frac{4}{3}$. If $\underline{g}.\underline{b}$ for the partials is integral, then the image characteristics for any $\pm\underline{g}$ pair will be as for undissociated superdislocations.

The $\pm\underline{g}$ pair provides a method of distinguishing between dipoles, superdislocations and dissociated superdislocations.

3.3.8 Contrast from stacking faults

The Howie-Whelan equations stated in eqn. 3.2 can be applied to provide a description of the contrast from stacking faults. If a stacking fault is present in a lattice and inclined to the surface of the foil, then the introduction of the phase factor $\alpha=2\pi\underline{g}.\underline{R}$ creates interference between the transmitted and diffracted waves. α can have a range of values from 0 to 2π depending on $\underline{R}$. The specific case of $\alpha=\pi$ is discussed as a special case in 3.3.9.

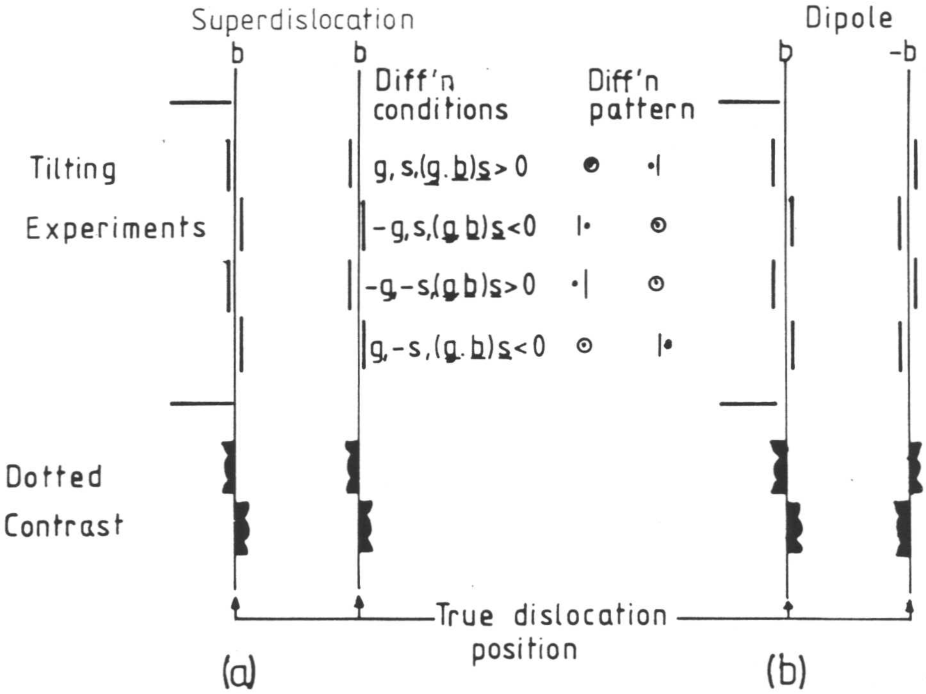

Fig. 3.8. Schematic diagram illustrating the technique for distinguishing between superdislocations and dipoles. When both dislocations are the same there will be no change in spacing when $\underline{g}$ is reversed (a). If the dislocations are opposite the image spacing changes on reversing $\underline{g}$ (b) (after Bell et al., 1964).

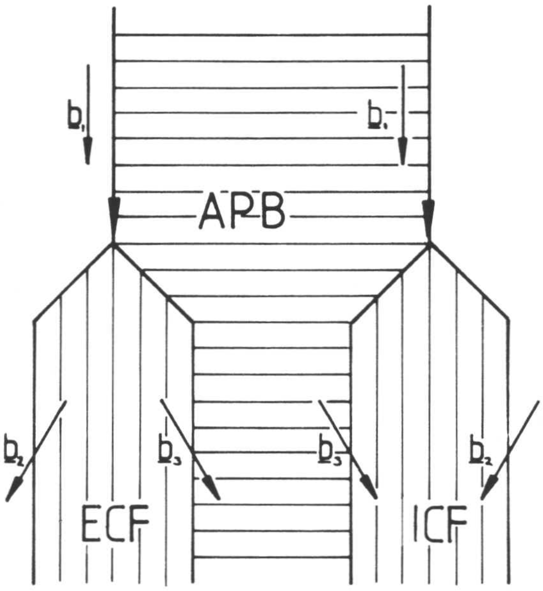

Fig. 3.9. Possible dissociation of a superdislocation to form an extrinsic and an intrinsic fault. $\underline{b}_1 = a/_2[\bar{1}01]$, $\underline{b}_2 = a/_6[\bar{2}11]$ and $\underline{b}_3 = a/_6[\bar{1}\bar{1}2]$.

By way of example consider a stacking fault on a {111} plane of an FCC material. As shown in 4.2 stacking faults in $L1_2$ structures are different from those in FCC structures but the principle behind their identification in the TEM is the same. In FCC materials stacking faults can be formed either by the splitting of an $a/_2\langle 110\rangle$ dislocation under a shear stress to form a fault bounded by two $a/_6\langle 211\rangle$ partial dislocations or by the growth or aggregation of point defects, the fault being bounded by an $a/_3\langle 111\rangle$ edge loop. Two types of fault exist: the intrinsic stacking fault which is equivalent to the removal of a (111) plane giving an ABCABABC stacking sequence, or the extrinsic stacking fault which is equivalent to the inclusion of an extra (111) plane giving an ABCABACABC stacking sequence. The fault vector, $\underline{R}$, is $\pm\frac{1}{3}[111]$ and $\alpha=0$, $\pm\frac{2}{3}\pi$, $\pm\frac{4}{3}\pi$, etc. Whelan and Hirsch (1957a,b) studied the contrast arising from these faults and they have shown that when $\underline{g}\cdot\underline{R}$ is integral the fault is invisible. When $\underline{g}\cdot\underline{R}$ is non-integral the bright field image will consist of a series of dark and bright fringes running parallel to the intersection of the fault with foil surface (fig. 3.10). In bright field both the outer fringes are either dark or light and the image is symmetric. In dark field the outer fringes are not the same and the image is asymmetric. The intrinsic/extrinsic nature of faults can be determined from this contrast variation. The simplest method has been described by Gevers, Art and Amelinckx (1963) which uses the asymmetric dark field image. If the origin of $\underline{g}$ is placed at the fault centre when $\underline{g}$ points away from the light outer fringe the fault is extrinsic and if it points towards the light outer fringe it is intrinsic for Class A reflections ({200}, {222} and {440}) and the reverse is true for Class B reflections ({400}, {111} and {220}).

An analysis of the fringe contrast from stacking faults cannot distinguish between those created by shear and those created by point defect aggregation because a lattice translation vector can be added to the

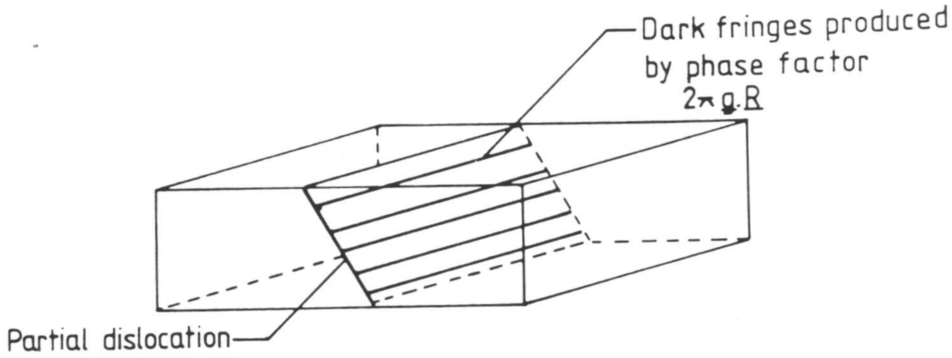

Fig. 3.10. Schematic diagram of a stacking fault lying on a plane which intersects the foil surface showing the dark fringes produced by the phase factor.

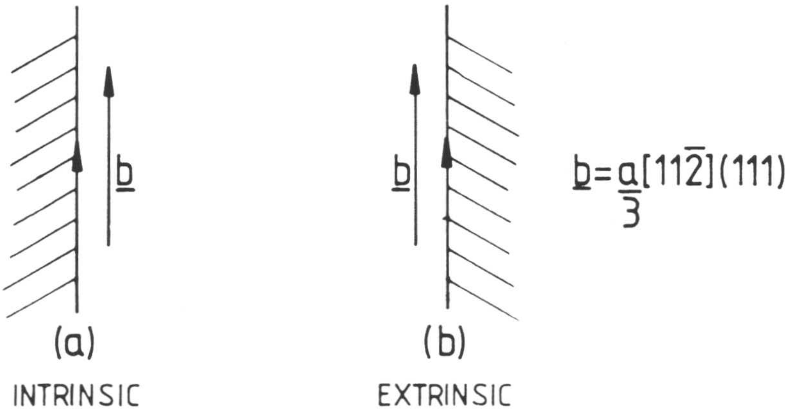

Fig. 3.11. Illustration showing the technique used to identify superlattice stacking faults from the bounding partial dislocation for superlattice intrinsic stacking faults (a), and superlattice extrinsic stacking faults (b).

shear displacement, $a/_6\langle 211\rangle$, to produce an $a/_3\langle 111\rangle$ fault. If it is necessary to distinguish between the fault types the Burgers vectors of the bounding dislocations must be determined.

Stacking faults lying parallel to the foil surface (e.g. those on (111) in a [111] foil) do not exhibit fringe contrast. However, the phase change, $\alpha=2\pi \underline{g}.\underline{R}$, still occurs and contrast will result from the fault except when $\underline{g}.\underline{R}$ takes an integral value. The rules for fault nature determination as outlined above cannot be applied to faults totally enclosed within the foil. However, if the Burgers vector of the bounding partial dislocation and its line sense are determined as described in 3.3.5 and 3.3.6 then the fault nature may be determined as follows.
If the stacking fault lies to the left of a bounding $a/_3\langle 211\rangle$ screw partial dislocation it is an intrinsic stacking fault, but if the stacking fault lies to the right of the same bounding partial it is an extrinsic stacking fault (fig. 3.11). Further confirmation of the nature of flat faults can be gained by use of the anomalous contrast from weak beam images of extrinsic stacking faults. This effect was first noted in silicon by Cullis and Booker (1972); they reported that extrinsic stacking faults showed a marked change in contrast when imaged using $+\underline{g}$ and $-\underline{g}$ beams but that intrinsic faults showed no such anomaly. Later, Föll, Carter and Wilkens (1980) showed that the contrast anomaly was much weaker for $\underline{g}=(111)$ than other reflections and that there was a slight but weak anomaly from intrinsic stacking faults. The origins of the contrast anomaly have since been studied by Self, Shaw and Stobbs (1982) and Cockayne, Pirouz, Liu, Anstis and Karnthaler (1984) who used a Bloch wave approach. In this investigation, where possible, the anomaly has been qualitatively applied to support the results gained by the determination of the Burgers vector bounding the faults. Only (200) and (220) reflections have been used and in many cases any contrast change was indistinguishable from changes in dislocation contrast as the faults, particularly the intrinsic faults, were very small.

3.3.9 Contrast from APBs

The contrast from APBs is similar to that described in 3.3.8 but for fundamental reflections in ordered materials the phase factor, $\alpha=2\pi\underline{g}\cdot\underline{R}$, can only take the values 0, 2π, 4π, etc. because $\underline{R}$ is a lattice vector of the disordered lattice. This means that the APB is always invisible in fundamental reflections. For superlattice reflections α can take the values 0, π, 2π, etc. so fringe contrast will occur from inclined faults when $\alpha=(2n-1)\pi$. The contrast is due to the change in phase across the APB because of the change in the ordering sequence (4.2.2). When $\underline{\omega}=0$ the dark field and bright field images are symmetric about the centre of the foil. When $\underline{\omega}>0$ the bright field image is still symmetric, but the dark field image is not. It has proved impossible to image APBs using the γ' superlattice reflections. This is probably due to the large extinction distance of γ'. No values have been calculated for the γ' of the alloys studied in this investigation but Oblak and Kear (1972) quote extinction distances for γ' superlattice reflections in Mar-M 200 (table 3.1).

3.3.10 Stereo pairs

Many of the dislocation configurations created by deformation and annealing had complex forms. To aid glide plane determination (6.2.2) and analysis many stereo pairs were taken using tilts of between $12-14^{\circ}$. A two beam condition was set up and the image recorded. The foil was then tilted along the Kikutchi lines associated with the chosen reflection until the necessary tilt had been applied and an equivalent image recorded with the same diffraction conditions. After printing and marking $\underline{g}$ onto the micrographs they were viewed in a stereoviewer with $\underline{g}$ along the tilt axis. No quantitative measurements were performed on these images: they were only used to give a qualitative representation of the dislocation configurations.

3.3.11 Tilting experiments

To determine the habit plane of a screw superdislocation a tilting experiment can be performed. If a g vector parallel to the dislocation line is chosen the dislocation can be tilted clockwise or anticlockwise around this g and if the tilt is measured it is possible to evaluate the superdislocation habit plane from its change in spacing on tilting. An experiment of this type was performed once in this investigation.

CHAPTER 4

PLANAR DEFECTS AND HEXAGONAL DISLOCATION NETWORKS

4.1 Introduction

Dislocation configurations of many diverse types have been predicted and observed in $L1_2$ structures. Many papers have been published about these interactions, for instance, Flinn (1960) on all $L1_2$ structures, Kear (1974), Staton-Bevan and Rawlings (1975(a) and (b)) and Nicholls and Rawlings (1977) on γ' in Ni-base alloys, Kear and Wilsdorf (1962) on Cu_3Au, Takeuchi, Kuramoto, Yamamoto and Taaka (1973) and Suzuki, Ichihara and Takeuchi (1979) on Ni_3Ga and Howe et al. (1974) on Zr_3Al. According to Yamaguchi, Vitek and Pope (1981), almost forty different $L1_2$ alloys have been studied in some way. Most of these studies have been brought together in the most comprehensive review of the deformation and mechanical properties of $L1_2$ related alloys by Pope and Ezz (1984).

These investigations have shown that the deformation of $L1_2$ structures can be temperature and strain rate sensitive, can occur on one or more planes of the same or different types, and that dislocation interaction can occur between groups of identical or different dislocations. Because of the immense complexity of the possible deformation mechanisms, this chapter and chapter 5 are limited to the interactions observed in the γ' of alloys A-G. Where necessary, reference has been made to the work of others but no attempt has been made to review all the available literature. The results presented here are those which were considered to be relevant to the evaluation of the anti-phase boundary (APB) and superlattice stacking fault energies (SSF) and those which may help in the explanation of the alloy deformation mechanisms.

Three main types of planar defects can be formed in the $L1_2$ structure. They are the APB, the complex fault (CF) and the two SSFs. This chapter describes the planar defects which can occur and discusses how these are related to the bounding dislocations when the defects are created by shear. It goes on to report the dislocation configurations in annealed, and annealed and deformed TEM foils. The major part of the chapter, 4.5, is devoted to the formation and observation of superlattice nodes (supernodes) and hexagonal dislocation networks. The creation of these networks is shown to be important to the evaluation of the fundamental defect energies.

4.2 Planar Defects in the $L1_2$ Structure

4.2.1 The $L1_2$ structure

The ordered $L1_2$ structure has the chemical formula A_3B. Gamma prime has the $L1_2$ structure and for convenience will be referred to as Ni_3Al or $Ni_3(Al,Ti)$, although in most commercial superalloys it contains significant amounts of alloying additions (1.5). It has already been reported that the γ' of alloys A-G has atomic species other than the Ni and Al within its structure (2.6.2).

Disordered Ni_3Al has the FCC structure where the shortest lattice repeat distance is $a/_2\langle 110\rangle$. On ordering the structure becomes primitive cubic; the shortest lattice repeat being $a\langle 110\rangle$. This lattice can be thought of as four interpenetrating simple cubic lattices, figure 4.1 (Fisher and Marcinkowski, 1961). The lattice has four lattice sites as shown: 1 at $(0,0,0)$; 2 at $(0,\frac{1}{2},\frac{1}{2})$; 3 at $(\frac{1}{2},0,\frac{1}{2})$ and 4 at $(\frac{1}{2},\frac{1}{2},0)$. Perfectly ordered Ni_3Al is usually said to have site 1 occupied by Al while 2, 3 and 4 are all occupied by Ni. In fact, any one of the sites may be occupied by Al as long as the others are occupied by Ni.

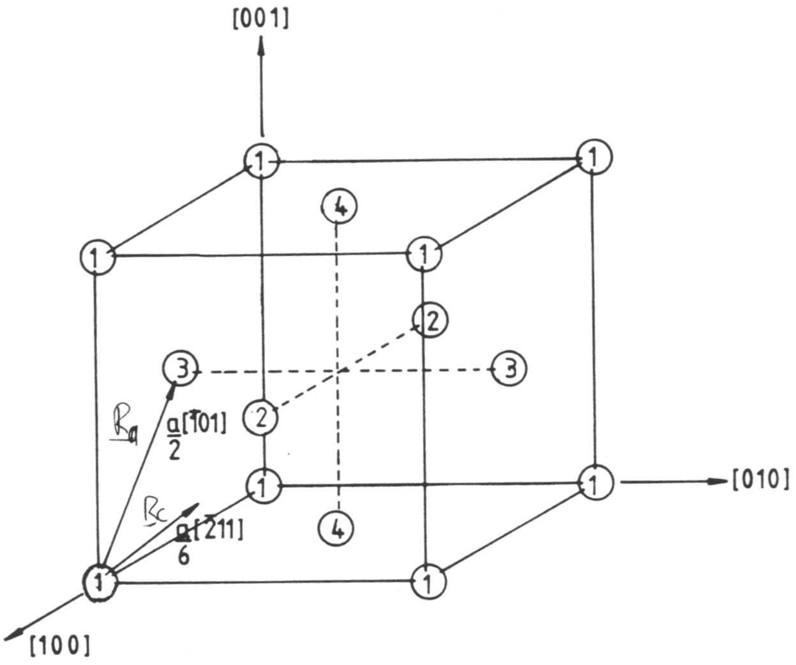

Fig. 4.1. Diagram of the $L1_2$ structure showing the four lattice sites (1, 2, 3 and 4) and the APB and CF displacements $\underline{R}_a$ and $\underline{R}_c$ respectively.

4.2.2 Antiphase boundaries in $L1_2$ structures

In $L1_2$ APBs can lie on any plane. In many cases the APB energy is not increased significantly by displacements from the glide plane (Hirth and Lothe, 1982). In fact, in $L1_2$ the APB energy may well be considerably decreased by such a displacement (Flinn, 1960). The most important APBs for the purposes of this discussion lie on {111} and {001}. Only these will be discussed in detail, although those displaced from these planes will be mentioned in 4.5.2.

To create an APB an Al atom must be displaced from a corner site (1) to a face centred site (2, 3 or 4), see figure 4.1. A (111) section is shown in figure 4.2. In figures 4.1 and 4.2 the vector $\underline{R}_a$ ($=a/_2[\bar{1}01]$) is the displacement necessary to create an APB on the (111) plane. The vectors $a/_2[\bar{1}10]$ and $a/_2[01\bar{1}]$ are exactly equivalent to $a/_2[\bar{1}01]$, therefore there are three displacement vectors associated with APBs on each of the {111}planes. When an APB is created on {111} a certain number of incorrect nearest neighbours are produced (fig. 4.3b). These nearest neighbour violations will contribute to the fault energy.

As shown in figure 4.4, the $\underline{R}_a$ displacement can also be made to create an APB on the (001) plane. In this case there are only two equivalent displacement vectors on each {001} plane. When an APB is created on {001} there is no change in the first order nearest neighbours distribution, but there is in the second order nearest neighbours (fig. 4.3c).

Flinn (1960) derived expressions for the APB energy on both the {111} and {001} planes by calculating the increase in energy when 'wrong' first order nearest neighbour bonds were created by an $\underline{R}_a$ displacement. He ignored the second order nearest neighbour interactions and consequently found the {001} APB energy to be zero. This is clearly not true as second order interactions do contribute to the overall APB energy; a better expression considering second order interactions is that presented by Yamaguchi et al. (1981). Despite the difference in com-

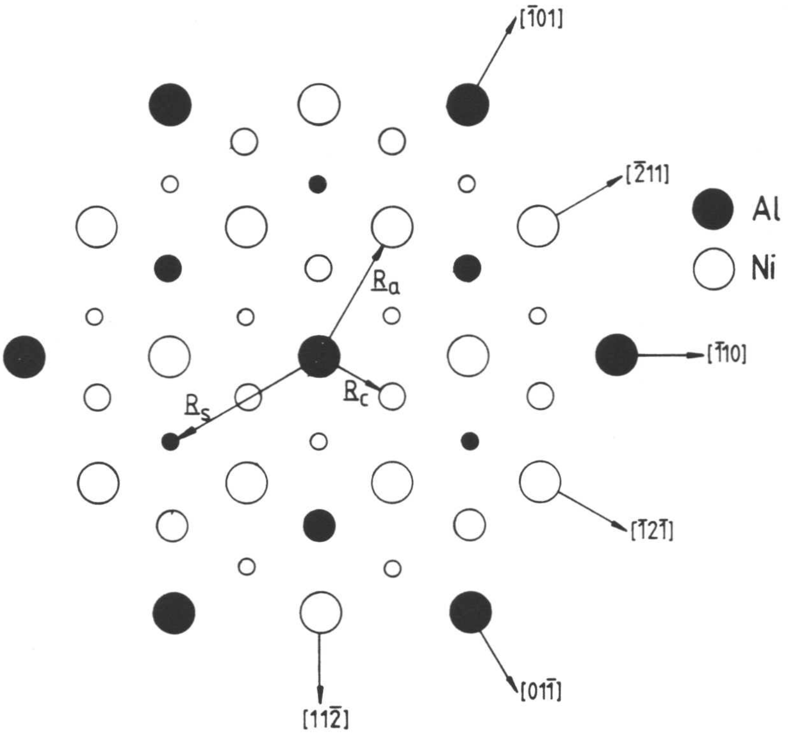

Fig. 4.2. Plan view of (111) planes in the $L1_2$ lattice. The full circles represent atomic species which occupy Al sites and open circles represent atomic species which occupy Ni sites. Large, medium and small circles represent a, b and c layers respectively. The diagram shows examples of the displacement vectors required to produce an APB ($\underline{R}_a = a/_2[\bar{1}01]$), a CF ($\underline{R}_c = a/_6[\bar{1}2\bar{1}]$) and an SSF ($\underline{R}_s = a/_3[2\bar{1}\bar{1}]$) on the (111) plane.

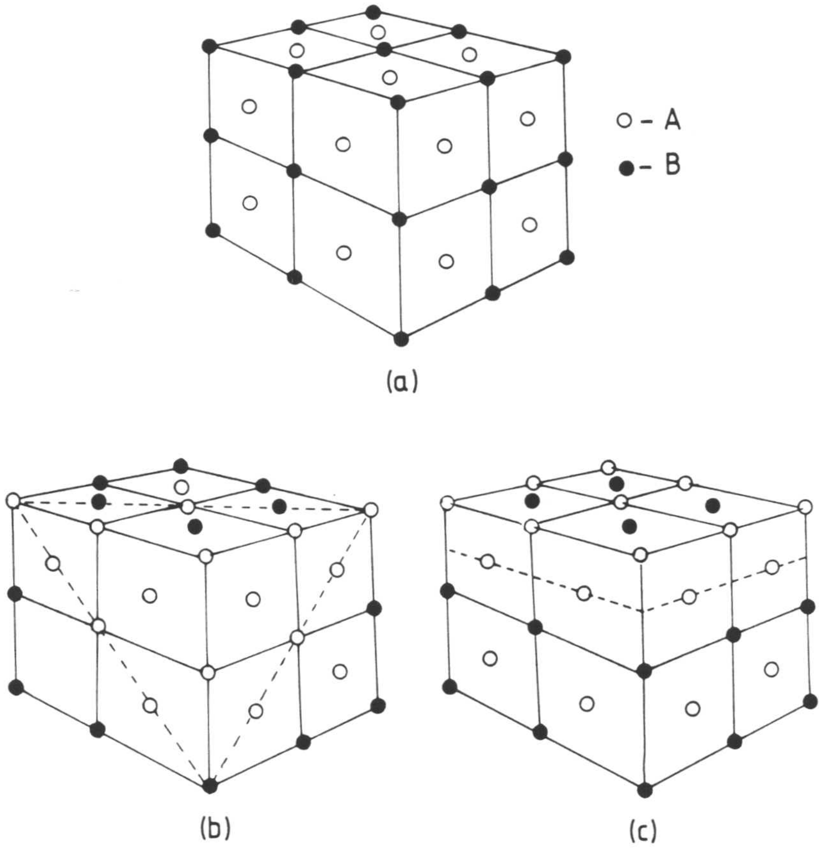

(a)

(b)

(c)

Fig. 4.3. The $L1_2$ structure (a), with a displacement of $a/_2\langle 110\rangle$ on the $\{111\}$ plane (b), and with a displacement of $a/_2\langle 110\rangle$ on the $\{001\}$ plane (c).

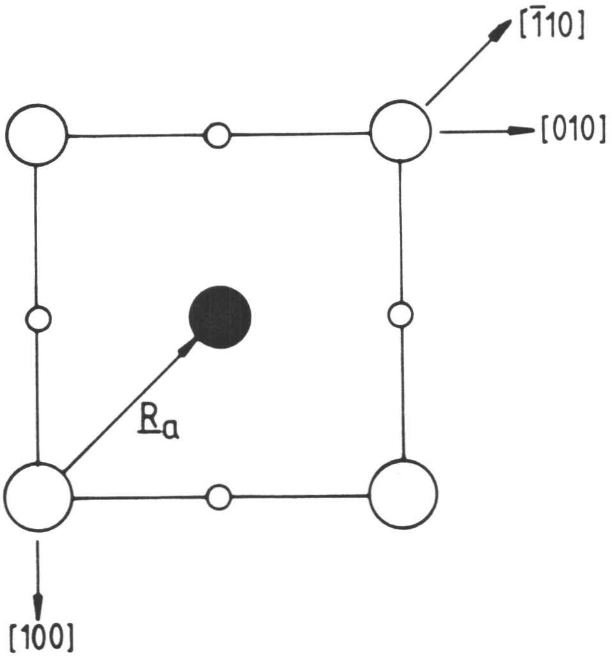

Fig. 4.4. Plan view of (001) planes in the $L1_2$ lattice showing an example of the displacement vector required to produce an APB ($\underline{R}_a = a/_2[\bar{1}10]$) on the (001) plane. The symbols have the same meanings as figure 4.2.

putation, both authors report that the {001} APB has a considerably lower energy than the {111} APB and consequently should be more stable. Yamaguchi et al. studied the stability of APBs, on {111} and {001}, superlattice intrinsic stacking faults (SISFs) and complex faults (CFs), using a central force potential to calculate the γ-surface energy.

In this way they have shown that an APB will always have the lowest fault energy on a {001} plane and will therefore always be the most stable defect. The energy of an APB on a {111} plane increases as the degree of ordering increases; thus they showed that in highly ordered structures the APB energy may be too high for a stable APB to form.

4.2.3 Complex faults in $L1_2$ structures

In the FCC structure an $a/_6$<211> displacement vector on {111} produces an intrinsic or an extrinsic stacking fault. However, when this displacement is applied to $L1_2$ (figs. 4.1 and 4.2), a {111} APB is produced in addition to a stacking fault. This combination is known as a complex fault (Marcinkowski, 1963). The vector shown in figure 4.1 is $a/_6[\bar{2}11]$ and in figure 4.2 is $a/_6[\bar{1}2\bar{1}]$. There are twelve equivalent $a/_6$<211> displacements which will produce complex faults. In common with the FCC lattice, CFs can be either intrinsic or extrinsic. No CF can exist on {001} because it is not possible for necessary displacements to be made on these planes.

It is expected that at room temperature the energy of a CF will be considerably larger than that of an APB. Yamaguchi et al. (1981) state that γ-surface calculations show that, in some instances, CFs may be stable in weakly ordered materials when they have energies lower than the APB energy.

4.2.4 Superlattice stacking faults in $L1_2$ structures

As the shortest lattice repeat in $L1_2$ is twice that in FCC it is logical to assume that the displacement required to produce a fault equivalent to an FCC stacking fault should be doubled. This is found to be true and a displacement of $a/_3[2\bar{1}\bar{1}]$ (fig. 4.2) produces an SSF. In common with the CF there are twelve equivalent $a/_3\langle 211 \rangle$s which will produce SSFs. The same fault can also be created by an $a/_3\langle 111 \rangle$ climb displacement. The concept of the SSF was first suggested by Carnahan, Cullen, Demel, McIlwain, Marcinkowski, Munford, Pahlman, Prevender and Warner (1967) who showed that the fault could have intrinsic or extrinsic character and when created the first and second nearest neighbours are unchanged.

It is worth noting that if the stacking sequence of ordered Ni_3Al is assumed to be ABCABCABC, then the stacking sequence of a superlattice intrinsic stacking fault (SISF) is ABCABABABC, which is equivalent to four layers of the DO_{19} structure or DO_{24} structure. The stacking sequence of a superlattice extrinsic stacking fault (SESF) is ABCABACABACABC which is equivalent to seven layers of the DO_{24} structure (Kear et al., 1968 and Kear et al., 1970).

Yamaguchi et al. (1981) found SISFs to be stable irrespective of ordering energy. They did not study the SESF but the results are expected to be the same. It is thought that under certain conditions the SSF energy and APB energy will be similar, and that they will compete for existence. This competition is likely to have a significant effect on the mechanical behaviour of the alloys. The effects of this type of interaction are discussed in detail in chapters 6 and 7.

In their papers, Yamaguchi and co-workers (Yamaguchi et al., 1981 and Yamaguchi, Paidar, Pope and Vitek, 1982) state that their computer modelling techniques predict that the displacement vectors of the faults described may deviate slightly from the exact values. No attempt was made to measure the exact displacement vectors. It was felt that any deviation would be so small that it could be assumed to be negligible.

4.3 Shear Dislocations in the $L1_2$ Structure

4.3.1 Nomenclature

In FCC structures $a/_2$<110> dislocations are known as perfect dislocations because the passage of one leaves perfect crystal behind and has no effect on the crystal stacking. $a/_6$<211> dislocations are known as partial dislocations because their passage changes the crystal stacking sequence.

In $L1_2$ an a<110> dislocation is a perfect dislocation. An $a/_2$<110> dislocation has no effect on the crystal stacking sequence but does change the chemical bonding. $a/_3$<211> and $a/_6$<211> dislocations do change the crystal stacking and are partial dislocations. In this thesis a total Burgers vector of a<110> will be referred to as a superdislocation, usually consisting of a pair of $a/_2$<110> dislocations which will simply be referred to as $a/_2$<110> dislocations, while $a/_3$<211> and $a/_6$<211> will be referred to as partial dislocations.

4.3.2 Antiphase boundary dislocations

Koehler and Seitz (1947) were the first to suggest that the shear deformation of ordered material may take place by a pair of perfect dislocations from disordered material. Bakish and Robertson (1956) suggested that for (111) deformation an $a[\bar{1}10]$ superdislocation would split to form two equivalent $a/_2[\bar{1}10]$ dislocations. The first dislocation through the material destroys the order to create an APB and the second identical dislocation travelling in the same direction on the same crystallographic plane restores it (fig. 4.5a). The region between the two dislocations contains APB and its width will be controlled by a balance between the APB energy pulling the dislocations together and the repulsion between the dislocations pushing them apart. By measuring the dislocation spacing it is possible to compute the APB energy (6.2.1).

Pairs of dislocations forming {111} superdislocations were first

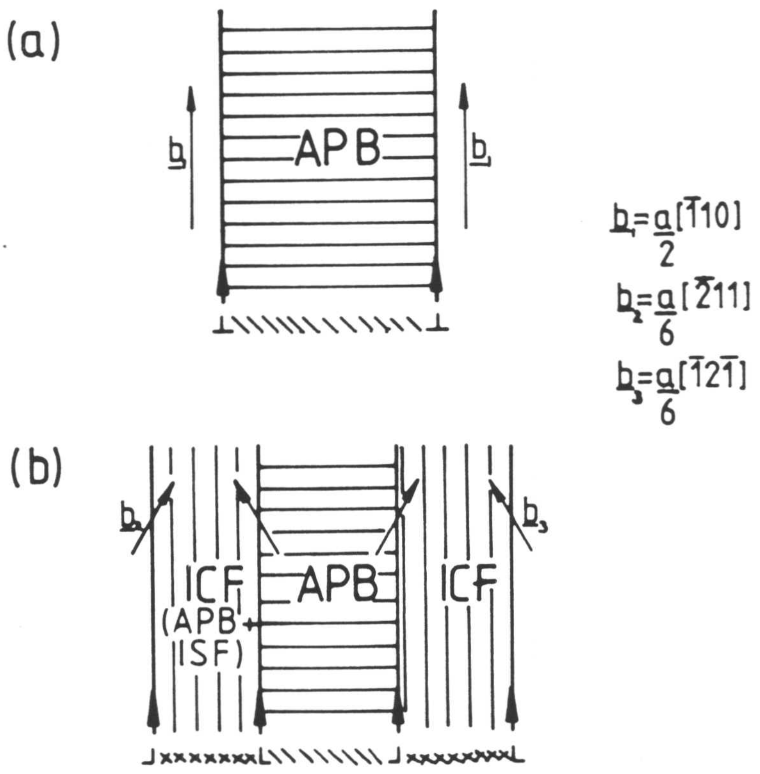

Fig. 4.5(a) and (b). Illustration of a superdislocation split into two $a/_{2}[\bar{1}10]$ dislocations bounding an APB (a). Each of the $a/_{2}[\bar{1}10]$ dislocations can dissociate into two $a/_{6}\langle 211\rangle$ Shockley partials bounding CF on (111) (b).

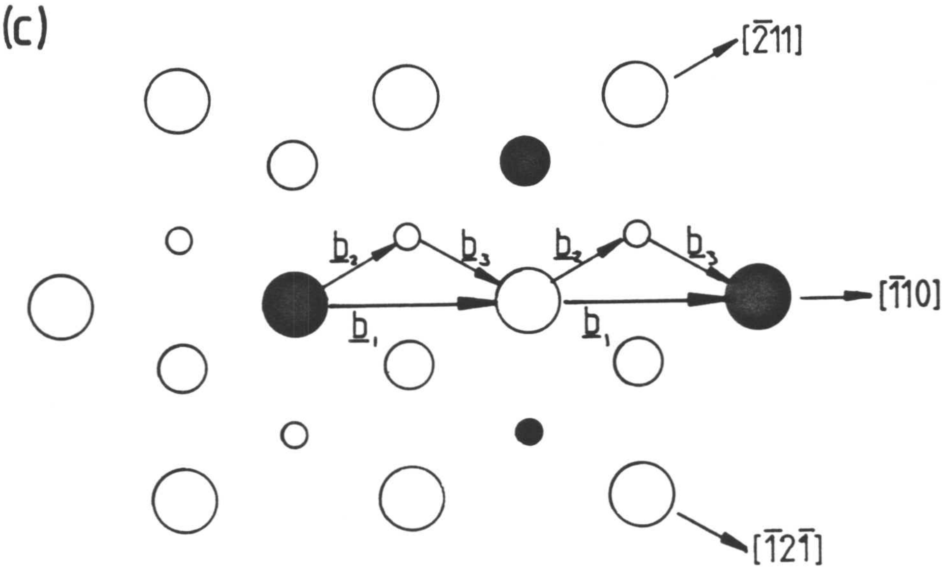

Fig. 4.5(c). Plan view of (111) showing a typical superdislocation displacement by two $a/_{2}[\bar{1}10]$ dislocations ($\underline{b}_1$) and the equivalent dissociated dislocations ($\underline{b}_2$ and $\underline{b}_3$).

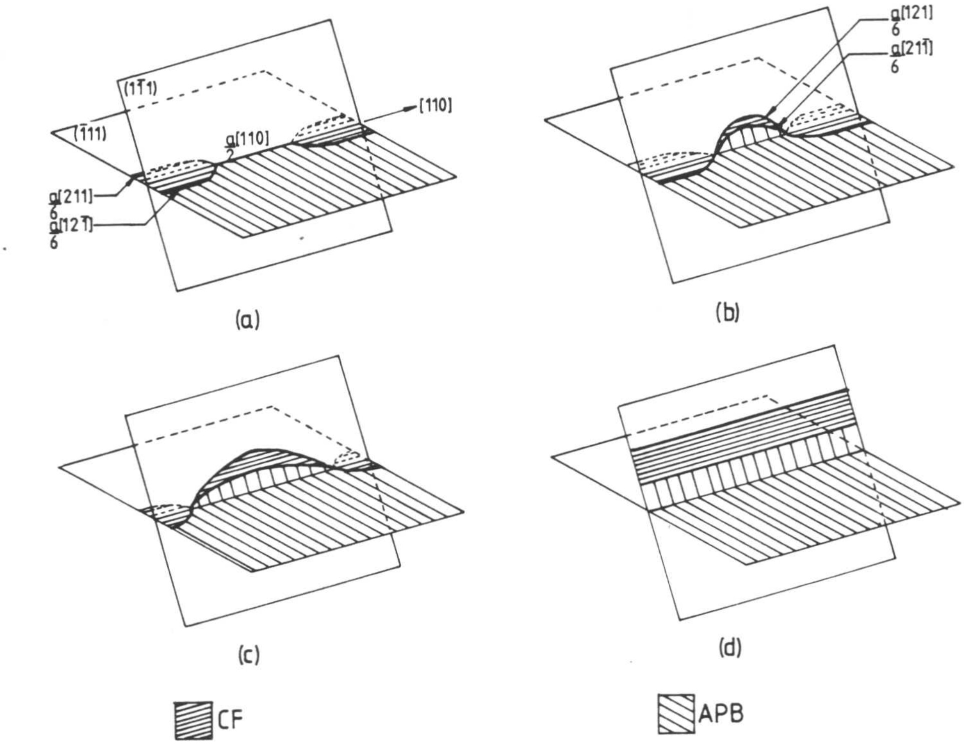

Fig. 4.6. Stages of cross-slip from ($\bar{1}11$) to ($1\bar{1}1$) for a dissociated $a/_2[110]$ dislocation bounding an APB showing constriction of the dislocation on ($\bar{1}11$) (a), cross-slip and dissociation on ($1\bar{1}1$) (b), and glide on ($1\bar{1}1$) (c). As glide continues the APB will be dragged onto ($1\bar{1}1$) (d).

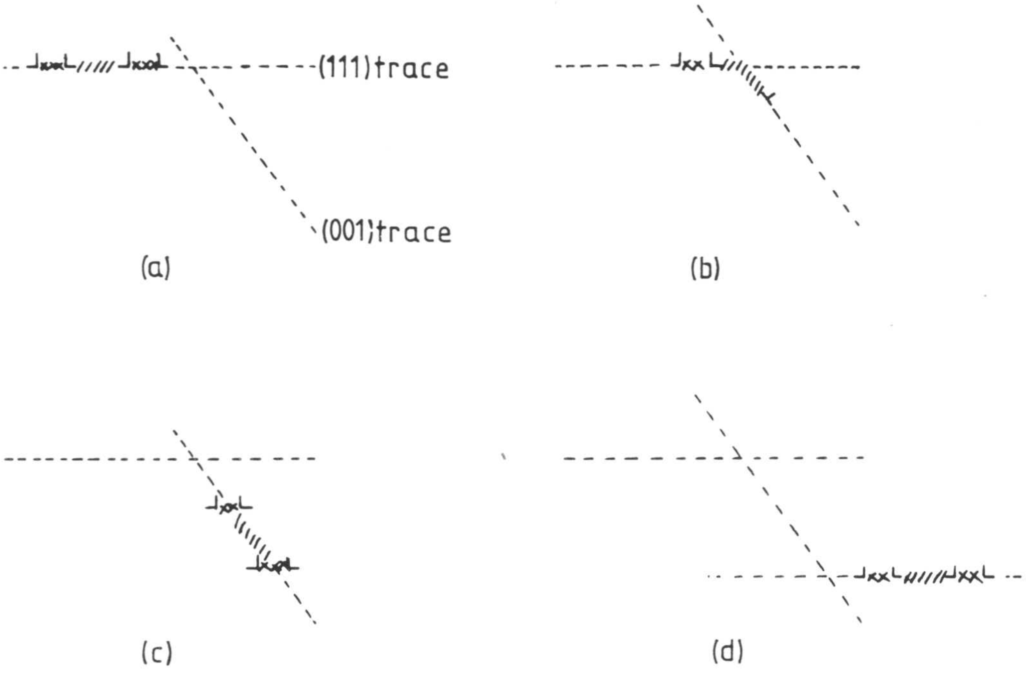

Fig. 4.7. Stages of cross-slip from {111} to {001} to form a Kear-Wilsdorf lock showing a superdislocation gliding on (111) (a), the leading dislocation is constricted on (111) and cross-slips onto (001) (b). Dissociation of the dislocations occurs on (111), there by locking the superdislocation (c). In certain cases cross-slip back onto (111) may occur (d).

observed in the TEM by Marcinkowski, Brown and Fisher (1961). They suggested that if the CF energy was small the $a/_2$<110> dislocations may each dissociate into two $a/_6$<211> partial dislocations forming a CF on either side of the APB (fig. 4.5b). Figure 4.5(c) shows the displacement in terms of Burgers vectors on a (111) section. The dissociation hinders cross-slip between {111} planes and from high APB energy {111} planes, where the superdislocations are glissile, to the low APB energy {001} planes, where the superdislocations are less mobile. This is because the $a/_6$<211> partials are unique to one plane and must be constricted to $a/_2$<110> before cross-slip can occur - as shown for {111} cross-slip in figure 4.6 and for {111} to {001} cross-slip in figure 4.7. Once on {001} the superdislocation is relatively immobile because the non-close-packed plane will have a high Pierls stress and because any dissociation of the dislocation will occur on {111} (fig. 4.7c). If enough energy and stress are available to constrict the dislocation, glide on {001} may occur (Yamaguchi et al., 1982, and Paidar, Pope and Vitek, 1984). Otherwise the dislocations can only move by climb, or cross-slip back onto {111} (figure 4.7d).

At high temperatures the probability of cross-slip onto {001} is increased. The resulting difficulty of motion once cross-slip has taken place forms the basis of the Kear-Wilsdorf (1962) strengthening mechanism. Slip by $a/_2$<110> dislocation pairs on {001} has been seen to occur at high temperatures when the dislocations are constricted - see, for instance, Copley and Kear (1967), Takeuchi and Kuramoto (1973), and Staton-Bevan and Rawlings (1975a).

However complex the dislocation dissociation bounding an APB, the total Burgers vector between the APB and perfect crystal will always be $a/_2$<110>. Figure 4.5(c) shows the displacements necessary to form an APB on (111).

4.3.3 Superlattice stacking fault dislocations

In addition to splitting into two $a/_2<110>$ dislocations an $a<110>$ superdislocation can be split into two $a/_3<211>$ partial dislocations (fig. 4.8a). The fault shown has intrinsic character. The leading $a/_3<211>$ $\{111\}$ partial dislocation gliding through the γ' will create an SSF. The trailing $a/_3<211>$ will destroy the SSF and restore perfect order. As with the APB, measurement of the partial dislocation spacing should allow calculation of the SSF energy. However, all the reported observations of SSF ribbons (Kear, 1974; Howe et al., 1974; and Suzuki et al., 1979) have either shown faults which passed through more than one γ' particle or were metastable due to interaction with the foil surface. Spacing measurements made from SSFs in these conditions cannot be used to calculate fault energies.

Under certain conditions, it has been shown by Kear et al. (1968) and by Kear et al. (1970) that the $a/_3<211>$ partials can dissociate into six $a/_6<211>$ partials.

$$a[\bar{1}10] = a/_3[\bar{1}2\bar{1}] + a/_3[\bar{2}11] \qquad \text{eqn. 4.1a}$$

$$a[\bar{1}10] = a/_6[11\bar{2}]+a/_6[\bar{1}2\bar{1}]+a/_6[\bar{2}11] + a/_6[\bar{1}2\bar{1}]+a/_6[\bar{2}11]+a/_6[\bar{1}\bar{1}2] \qquad \text{eqn. 4.1b}$$

The dissociation is shown for a SISF in figures 4.8(b). It can be seen that the first $a/_6<211>$ partial of the leading dislocation creates an extrinsic CF, the second creates an APB and the third creates the SISF. The trailing dislocations reverse the process. It is expected that the widths of the defects are an inverse function of their energies. In most practical situations when the APB and CF energies are high relative to the SSF energy, the bounding dislocation will exhibit the TEM contrast expected from an $a/_3<211>$ partial dislocation because the separation of the $a/_6<211>$ partials will be of the same order as the dislocation image width.

However complex the dislocation structure, the total Burgers

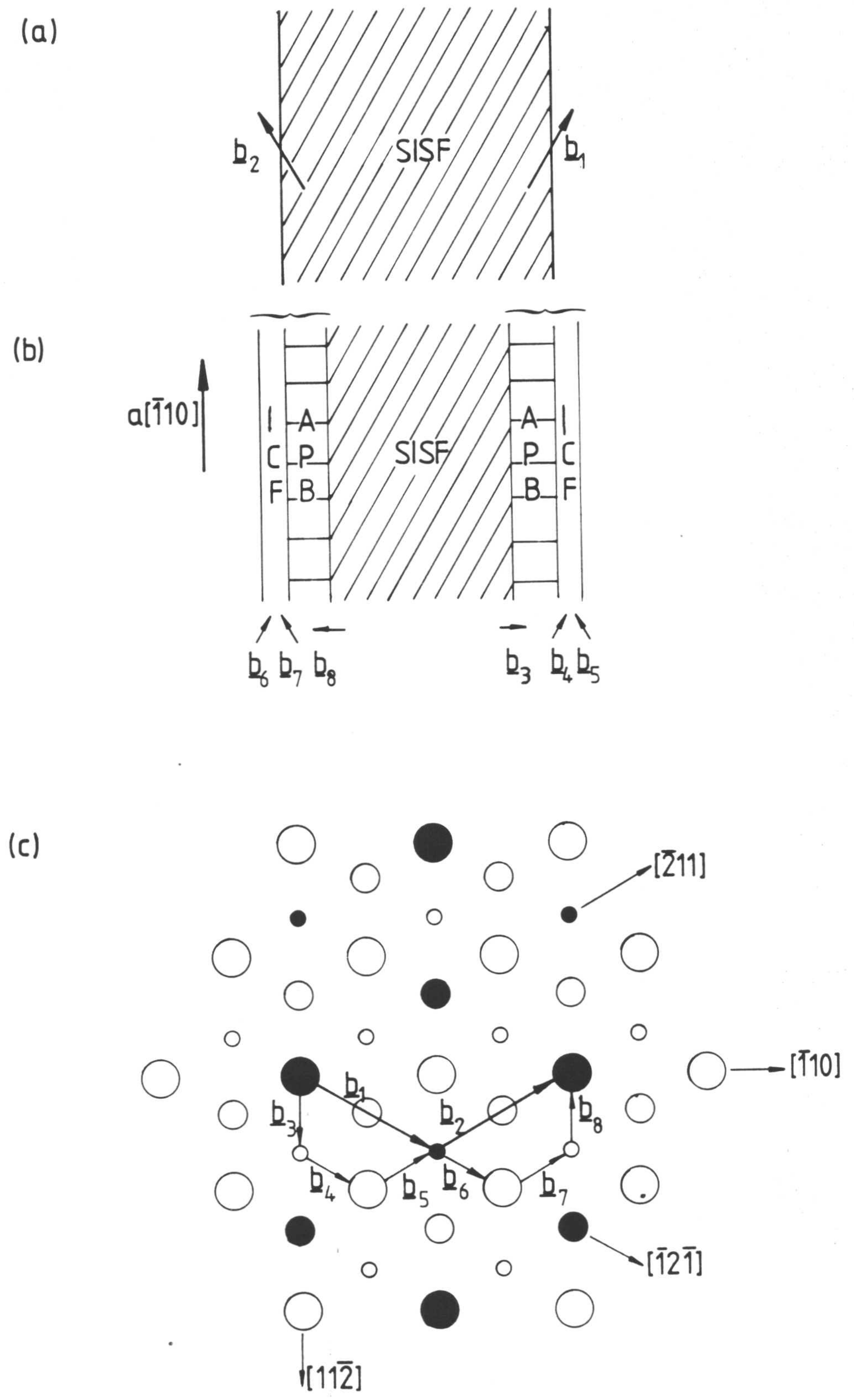

Fig. 4.8. Dissociation of an a[$\bar{1}$10] superdislocation on (111) into $a/_3$<211> partial dislocations ($\underline{b}_1$ and $\underline{b}_2$) bounding an SISF (a). The $a/_3$<211> partial dislocations may each dissociate into three $a/_6$<211> Shockley partial dislocations ($\underline{b}_3$ to $\underline{b}_8$) producing the faults shown (b). A plan view on (111) showing the superdislocation displacement by two $a/_3$<211> partial dislocations ($\underline{b}_1$ and $\underline{b}_2$) producing an SISF and the equivalent $a/_6$<211> partial dislocations ($\underline{b}_3$ to $\underline{b}_8$) is also shown (c). The symbols have the same meanings as figure 4.2. The Burgers vectors are $\underline{b}_1=a/_3[\bar{1}2\bar{1}]$, $\underline{b}_2=a/_3[\bar{2}11]$, $\underline{b}_3=a/_6[11\bar{2}]$, $\underline{b}_4=a/_6[\bar{1}2\bar{1}]$, $\underline{b}_5=a/_6[\bar{2}11]$, $\underline{b}_6=a/_6[\bar{1}2\bar{1}]$, $\underline{b}_7=a/_6[\bar{2}11]$ and $\underline{b}_8=a/_6[\bar{1}\bar{1}2]$.

vector between the APB and the perfect crystal will be $a/_3$<211>, the Burgers vector between APB and SSF will always be $a/_6$<211>, and the Burgers vector between CF and SSF can be $a/_2$<110> or $a/_6$<211>.

The dislocation configuration required to create an SESF has been constructed in the same way as the SISF and is shown in figure 4.9. In this configuration, if an SESF is to form, the cores of the bounding dislocations must stretch over more than one atomic plane if the lattice displacement is to be accommodated.

4.3.4 Complex fault dislocations

It is thought that because of the high energy of the CF they do not occur unless associated with APBs or SSFs (4.3.2 and 4.3.3). No observations of independent CFs have been reported. When observed in association with other defects, the Burgers vector between the CF and perfect crystal will be $a/_6$<211>. A Burgers vector of $a/_2$<110> has also been observed between two CFs (see 4.5.3).

4.4 Dislocation Structures in $L1_2$ Prior to Annealing

4.4.1 Dislocation structure in undeformed crystals

After homogenisation and growth, very few dislocations were observed in the γ' when foils were examined in the TEM. A typical microstructure is shown in figure 4.10. In many areas no dislocations were observed under any imaging condition.

The dislocations which were present tended to form boundaries of the type shown in figure 4.11. These boundaries were very uncommon. Because the microstructure contained very few dislocations, there are correspondingly few nucleation sites for carbide precipitation. It was found that strings of small FCC MC carbides form along these dislocation tangles with a cube/cube orientation relationship with the matrix (figure 4.12); the carbide lattice parameter is approximately three times greater

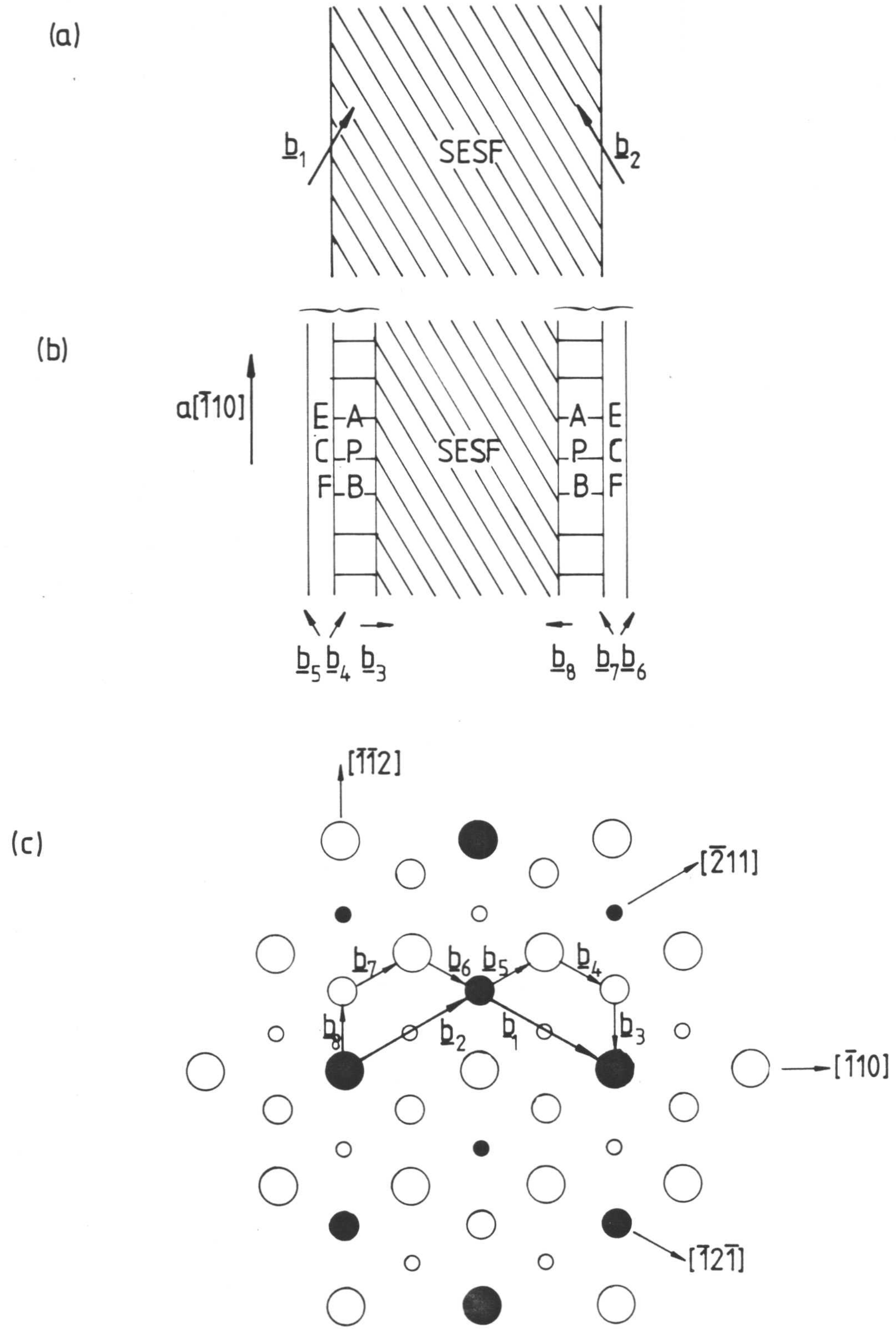

Fig. 4.9. Dissociation of an a[$\bar{1}$10] superdislocation on (111) into a/$_3$<211> partial dislocations ($\underline{b}_1$ and $\underline{b}_2$) bounding an SESF (a). The a/$_3$<211> partial dislocations may each dissociate into three a/$_3$<211> Shockley partial dislocations ($\underline{b}_3$ to $\underline{b}_8$) producing the faults shown in (b). A plan view on (111) showing the superdislocation displacement by two a/$_3$<211> partial dislocations ($\underline{b}_1$ and $\underline{b}_2$) producing an SESF and the equivalent a/$_6$<211> partial dislocations (b_3 to B_8) is also shown (c). The symbols have the same meanings as figure 4.2 and the Burgers vectors are the same as figure 4.8.

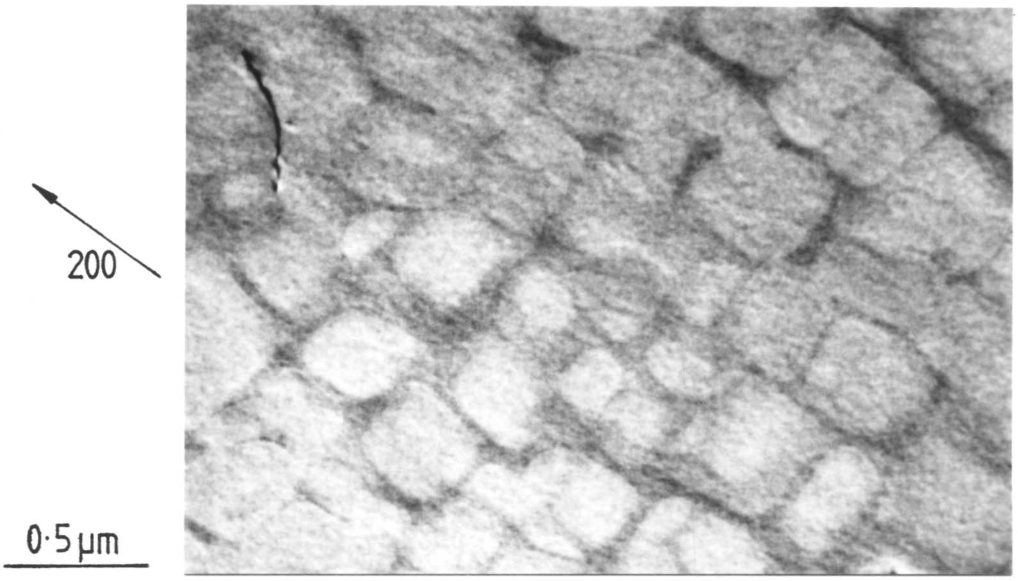

Fig. 4.10. Bright field TEM micrograph showing γ/γ' microstructure after homogenisation for 36 hrs at 1570K followed by 16 hrs at 1390K (foil normal: ~[001]).

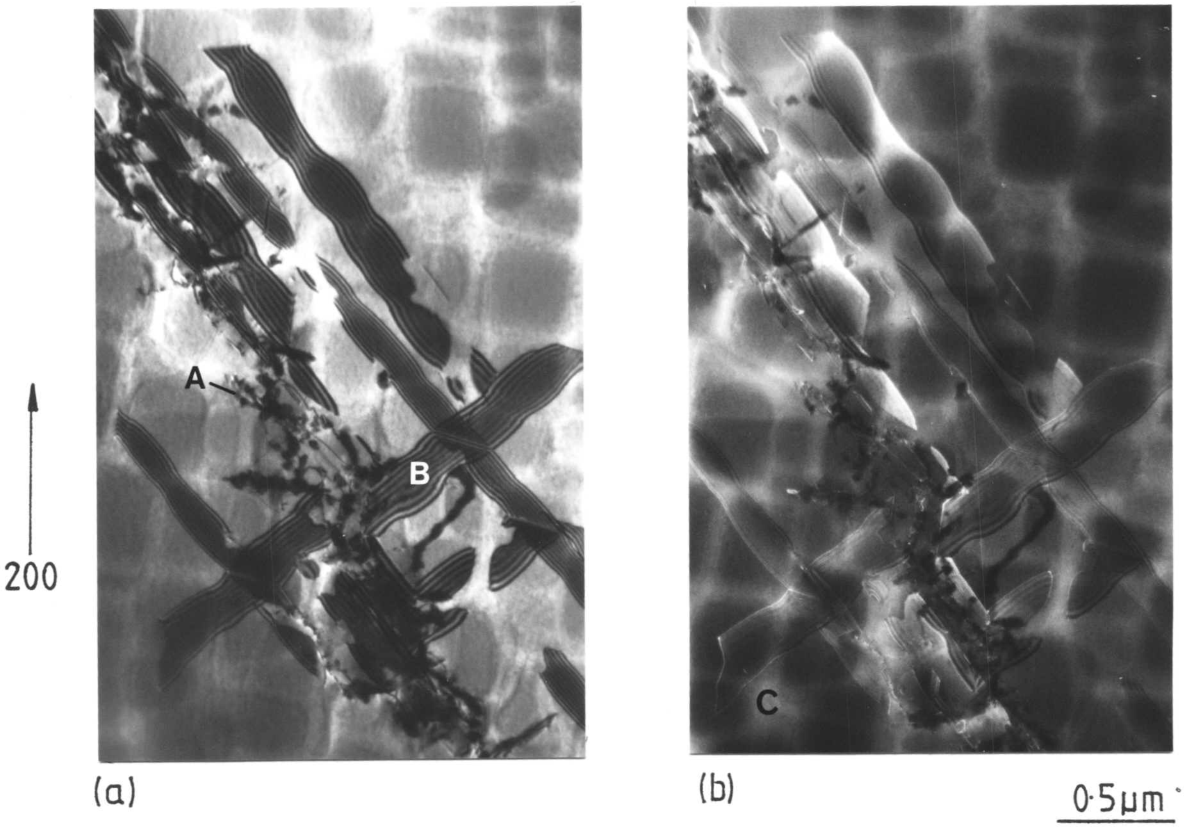

Fig. 4.11. Bright field (a) and weak beam (b) TEM micrograph of dislocation tangles showing globular MC precipitation (A) and planar Ni_3Ti (B) bounded by an a/3<111> dislocation (C). (foil normal: ~[001]).

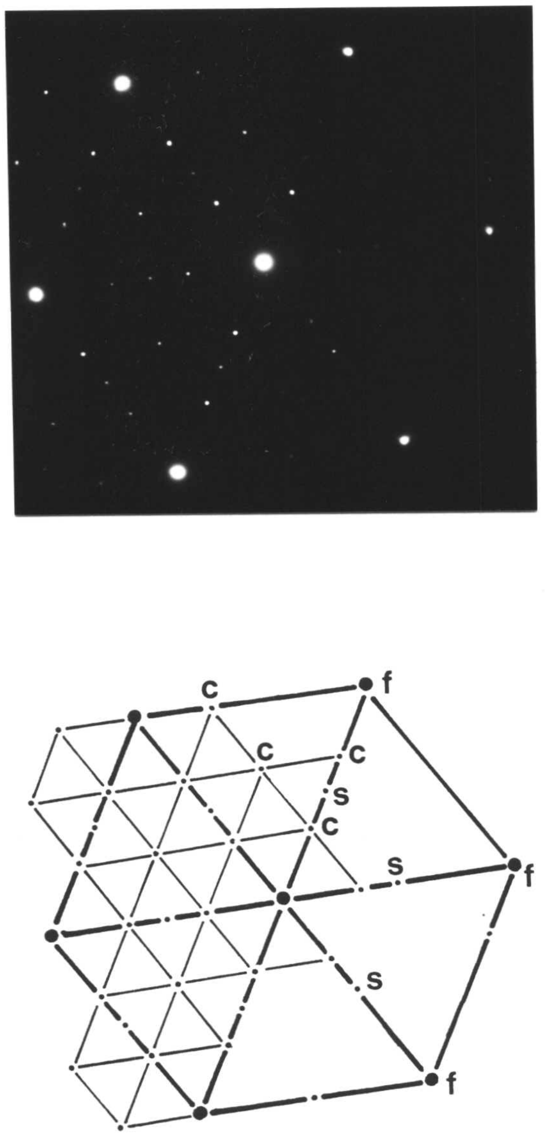

Fig. 4.12. Diffraction pattern taken from carbides, on a boundary similar to that shown in figure 4.11, showing fundamental (f), superlattice (s) and carbide (c) reciprocal lattice points. (foil normal: ~[111]).

than the γ matrix. MC carbides are rich in Ta, Ti and W (see 2.6.2).

The large planar defects visible in figure 4.11 were observed to be linked to boundaries containing carbides. These defects, which exhibit stacking fault contrast, were bounded by $a/_3\langle 111\rangle$ Frank partial dislocations (Rae, 1984) demonstrating that they could not have been formed by shear. The defects could either be stacking faults, formed by agglomeration of point defects or interstitials, or thin planar precipitates. They were observed to pass through γ and γ' without any change at the interphase boundaries. It is the opinion of Rae and the author that these large planar defects are planar precipitates of Ni_3Ti, similar to those observed in Udimet 700 by Kear et al. (1970), which are growing out into the bulk material from the precipitate loaded boundaries. Further work to confirm this opinion is being undertaken by Rae.

4.4.2 Dislocation structure in deformed crystals

Room temperature deformation considerably increased the dislocation density (fig. 4.13). The majority of the dislocations generated were in the γ matrix between the γ' particles. This is at least in part due to the difficulty encountered by $a/_2\langle 110\rangle$ dislocations trying to enter the γ' at low temperatures. To enter the γ' dislocations must 'pair-up' to form superdislocations of two $a/_2\langle 110\rangle$ dislocations of the same type on the same plane. At 293K it is highly unlikely that sufficient cross-slip can occur in the γ to produce superdislocations. The few superdislocations observed in the γ' must have formed by the 'pairing-up' of like dislocations which were lying adjacent on the same plane.

Cold deformation produced inhomogeneous deformation in the form of slip bands on $\{111\}$ as shown in figure 4.14. This figures shows that most of the deformation took place by dislocations looping around the γ'. Some superdislocations, however, were forced through the γ'. At the intersection of the slip bands, superdislocations on different planes were

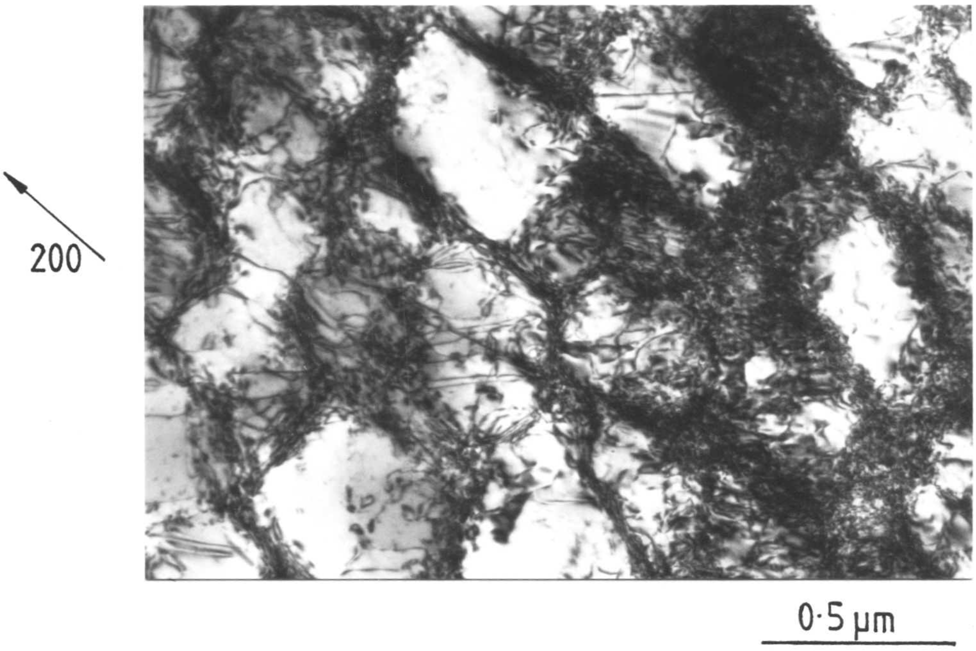

Fig. 4.13. Bright field TEM micrograph showing dislocations generated by cold deformation. Most of the dislocations lie in the γ matrix although some are visible in the γ'. (foil normal: ~[001]).

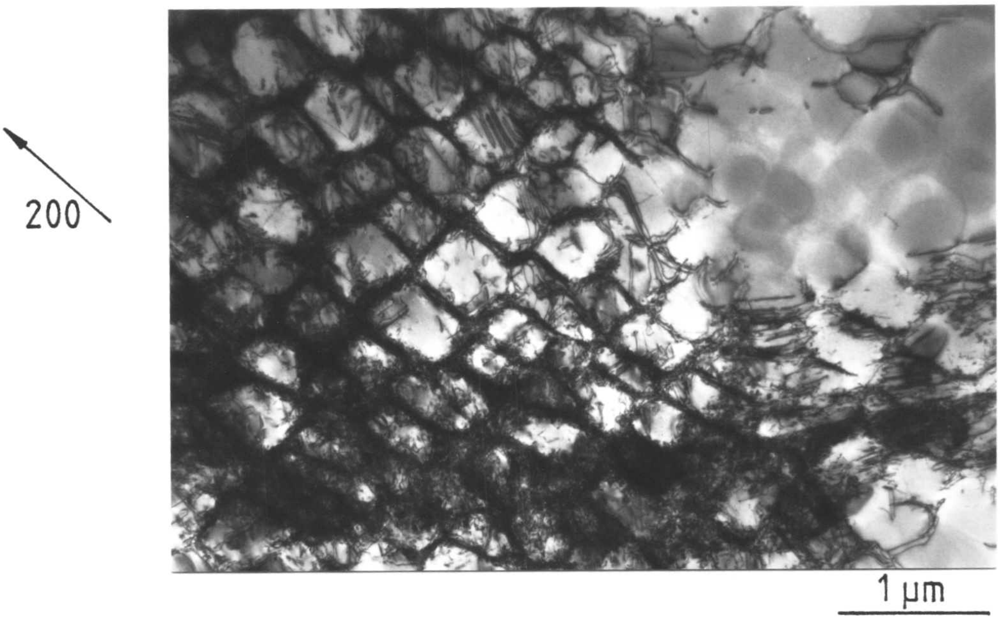

Fig. 4.14. Bright field TEM micrograph showing intersecting slip bands. (foil normal: ~[001]).

seen to interact. In the annealed condition these superdislocations adopted the supernode configurations described later in this chapter.

Little work was carried out to characterise the dislocation interactions in the low temperature deformed structures. But they were carefully examined as it was vital to make certain that the dislocation structures observed in the annealed structures were not residual interactions left from the cold deformed microscructures.

4.5 Hexagonal Dislocation Networks in Deformed and Annealed Crystals

4.5.1 Theoretical arrangement

As discussed more fully in 5.2.1, during annealing $a/_2\langle 110\rangle$ dislocations in the γ matrix climb to form pairs of $a/_2\langle 110\rangle$ dislocations on the same plane. These superdislocations glide into the γ' and can interact with other superdislocations. This section describes the formation of the interaction which is most important in the evaluation of APB and SSF energies. As part of the annealing process, the superdislocations gliding through the γ' will aim to adopt the lowest energy configuration possible. In disordered materials the configuration adopted is often a hexagonal network on a $\{111\}$ plane (Whelan, 1959).

Whelan stated that when two dislocations of different Burgers vector AB and A'B' (figure 4.15a) intersect on the same or different planes, there will be an elastic interaction between the segments of dislocation line at the point of intersection (Read, 1953 and Amelinckx, 1956). The interaction will depend upon the Burgers vectors of the dislocations involved but, in general, if there is an attraction, the dislocations may combine to form a third dislocation A"B" (figure 4.15b). The interaction will possibly occur when the angle between the dislocation Burgers vectors is 120° and if the attraction reduces the total strain energy of the system.

In the rest of this chapter Whelan's ideas for interaction between single dislocations in FCC are extended to account for similar interactions

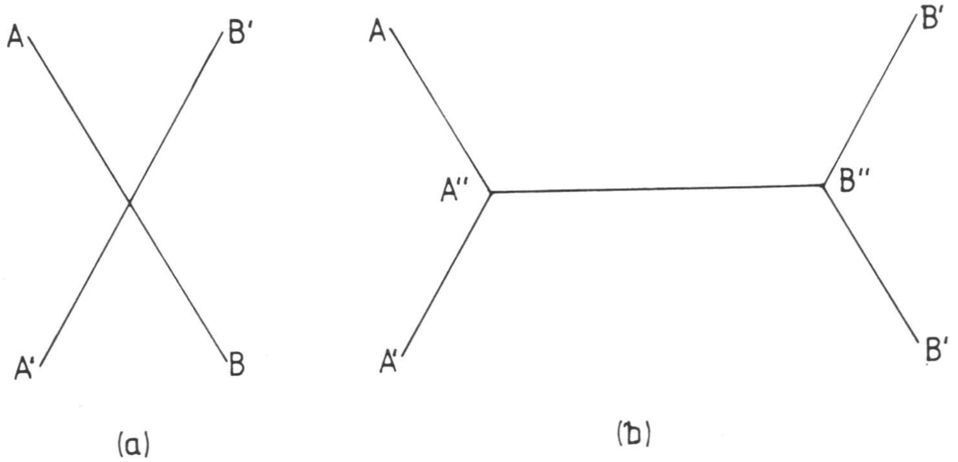

Fig. 4.15. Schematic diagram showing the interaction of two dislocations AB and A'B' to produce a third A"B".

in $L1_2$. For simplicity it will be assumed that the dislocations have pure screw sharacter. In describing the interactions, Thompson's notation (Thompson, 1951 and fig. 4.16) will be used in addition to the normal notation. This will help the reader to appreciate which planes the various dislocations inhabit, particularly when the more complex case is considered.

Two cases are considered. First, when both superdislocations lie in (111),δ. The dislocation reaction will be:

$$a[01\bar{1}] + a[\bar{1}01] = a[\bar{1}10] \qquad \text{eqn 4.2a}$$

$$2AC + 2CB = 2AB$$

Secondly, when $a[01\bar{1}]$ lies in $(1\bar{1}\bar{1})$,β and $a[\bar{1}01]$ lies in $(\bar{1}1\bar{1})$,α. This reaction produces $a[\bar{1}10]$ which lies in either (111),δ or $(11\bar{1})$,γ

Both interactions will produce the configuration shown in figure 4.17 if it is assumed that each superdislocation is split into two $a/_2$<110> dislocations.

4.5.2 Observations of the dislocation interaction

The dislocation interactions at the nodal points are complex and cannot be described adequately without dissociating the $a/_2$<110> dislocations into their component $a/_6$<211> partials. These reactions are described in 4.5.3 and 4.5.4. However, using the TEM techniques described in this thesis, no dissociation of the $a/_2$<110> dislocations was observed in the regions away from the nodal points.

Interactions similar to that shown in figure 4.18 were frequently observed in the γ' of the deformed and annealed foils. Table 4.1 shows some of the $\underline{g}.\underline{b}$ values for the $a/_2$<110> dislocations shown in figure 4.18. The dislocations were identified as $a/_2[0\bar{1}1]$ and $a/_2[\bar{1}10]$ which have interacted to produce $a/_2[10\bar{1}]$, although some residual contrast is visible from $a/_2[\bar{1}10]$ in figure 4.18(b). They have adopted a roughly screw orientation

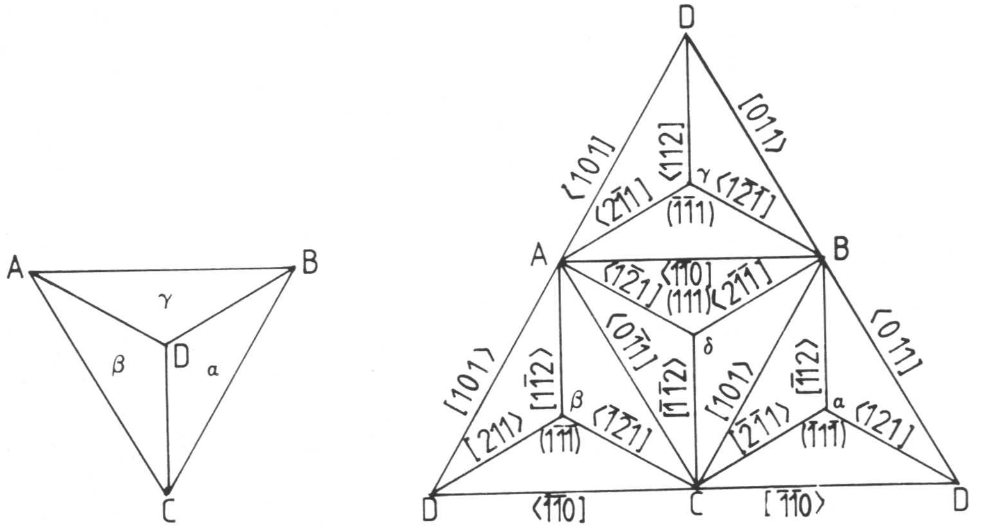

(a)

(b)

Fig. 4.16. A Thompson tetrahedron from above (a) and in planar projection (b). In (b) the arrow heads indicate the sense of the vectors.

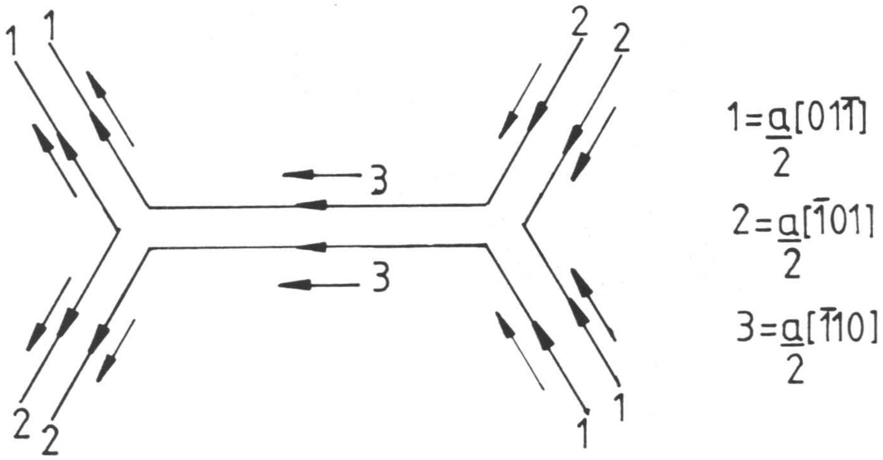

Fig.4.17. Schematic diagram showing the interaction between a superdislocation of two $a/_2[01\bar{1}]$ dislocations and a superdislocation of two $a/_2[\bar{1}01]$ dislocations to produce $a/_2[1\bar{1}0]$.

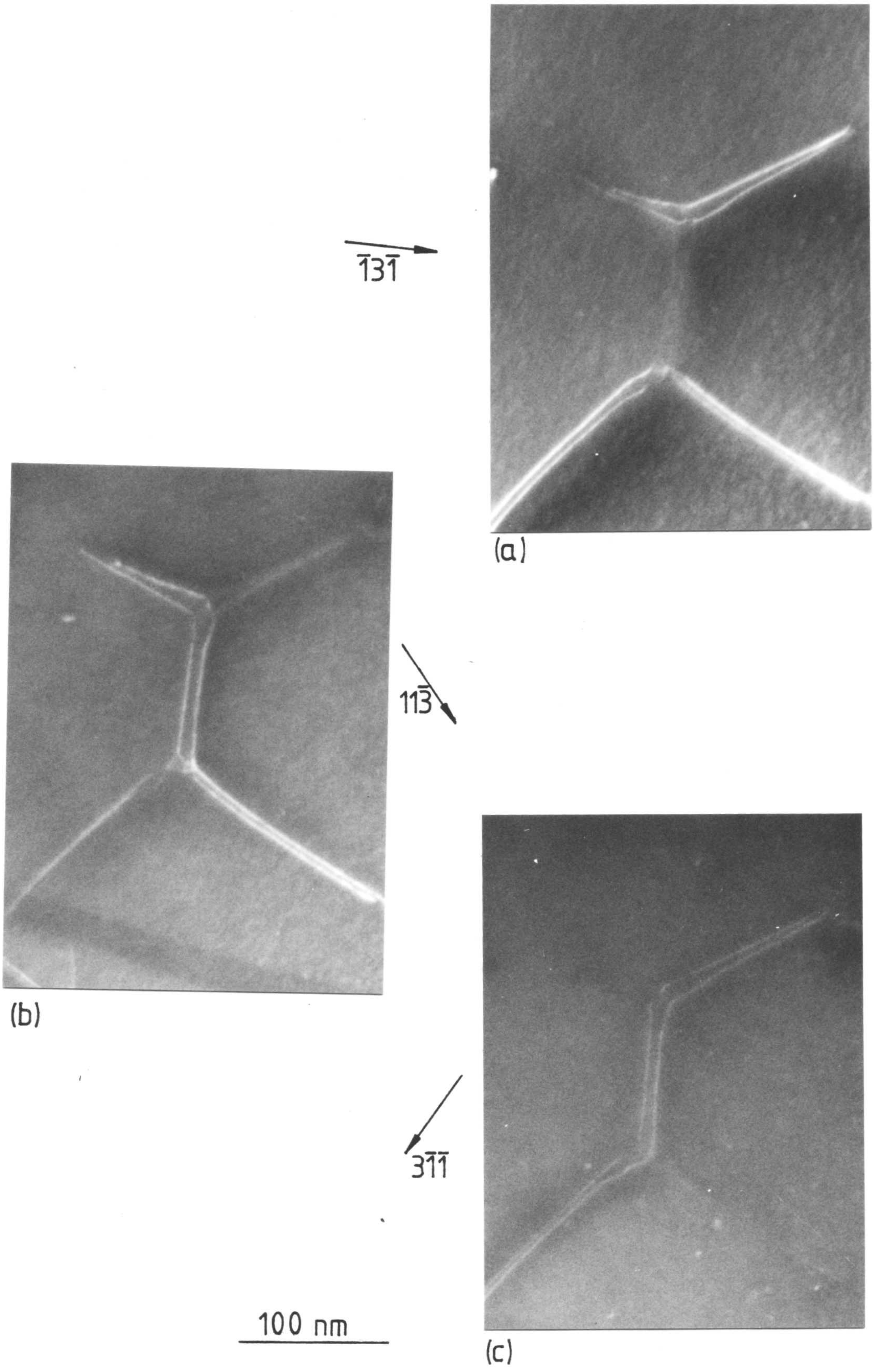

Fig. 4.18. Weak beam dark field TEM micrographs taken in conditions between $W_{(\underline{g},2\underline{g})}$ and $W_{(\underline{g},4\underline{g})}$ showing a typical superdislocation interaction in the γ'. The dislocations were identified using table 4.1 and are shown in (d). Some residual contrast is visible from $a/_2[\bar{1}10]$ in (b). (foil normal: ~[111]).

(Figure continued overleaf)

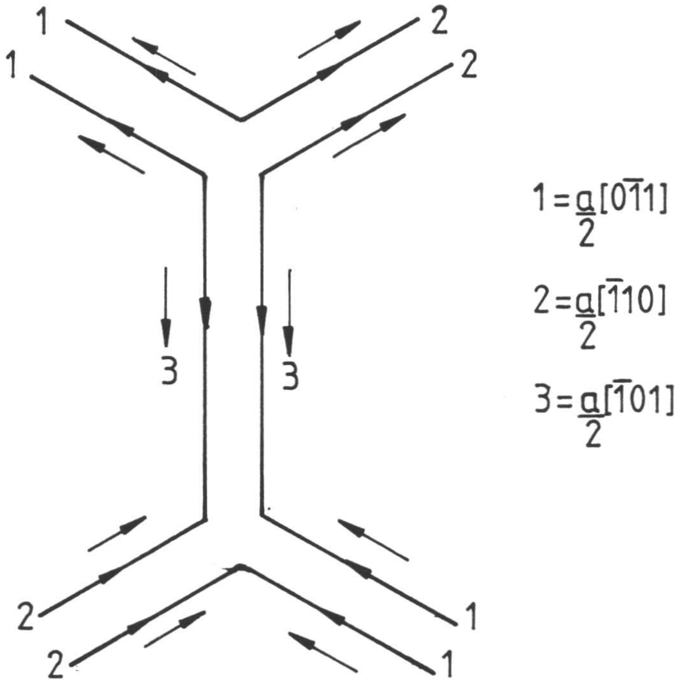

(d)

Fig. 4.18. For caption see previous page.

Table 4.1. $\underline{g}\cdot\underline{b}$ values for the $a/_2\langle 110\rangle$ dislocations shown in figure 4.18

Micrograph	Diffraction vector ($\underline{g}$)	Burgers vector ($\underline{b}$)		
		$\pm a/_2[01\bar{1}]$	$\pm a/_2[1\bar{1}0]$	$\pm a/_2[10\bar{1}]$
(a)	$\bar{1}3\bar{1}$	±2	∓2	[0]
(b)	$11\bar{3}$	±2	[0]	±2
(c)	$3\bar{1}\bar{1}$	[0]	±2	±2

Table 4.2. $\underline{g}\cdot\underline{b}$ values for the $a/_2\langle 110\rangle$ dislocations shown in figure 4.22

Micrograph	Diffraction vector ($\underline{g}$)	Burgers vector ($\underline{b}$)		
		$\pm a/_2[10\bar{1}]$	$\pm a/_2[1\bar{1}0]$	$\pm a/_2[01\bar{1}]$
(a)	$1\bar{1}1$	[0]	±1	∓1
(b)	$11\bar{1}$	±1	[0]	±1
(c)	$\bar{1}11$	∓1	∓1	[0]
(d)	$2\bar{2}0$	±1	±2	∓1
(e)	$20\bar{2}$	±2	±1	±1

[ ] - invisible

but close to the nodal regions the superdislocations have been distorted and no longer lie in their original glide planes. This non-planarity is related to the dislocation structure at the nodal points (see 4.5.3).

Planar hexagonal networks were also observed, such as the one shown in figure 4.25. This network lies on (111) in a [001] foil. The network is therefore tilted through the foil. The dislocation structure is discussed in more detail later (4.5.3).

In many cases the networks adopted a hexagonal equilibrium configuration of screw superdislocations at 120°. Many APB energies have been determined by measuring the equilibrium spacing (6.3.3).

4.5.3 Dislocation interactions at the nodal points

In order to interpret the nodal reactions effectivly it has proved necessary to split each of the $a/_2\langle110\rangle$ dislocations forming the superdislocation into two component $a/_6\langle211\rangle$ partial dislocations. As in 4.5.2, the $a/_2\langle110\rangle$ dislocations considered are all pure screw and the Burgers vector of these dislocations will always be taken in the same direction as the dislocation line sense.

First, the interaction between an $a/_2[01\bar{1}]$ pair and an $a/_2[\bar{1}01]$ pair at 120° on (111) will be considered. Each of the $a/_2\langle110\rangle$ dislocations will be dissociated as follows:

$$a/_2[01\bar{1}] = a/_6[11\bar{2}] + a/_6[\bar{1}2\bar{1}] \qquad \text{eqn. 4.3a}$$

$$AC = \delta C + A\delta \qquad \text{eqn. 4.3b}$$

and

$$a/_2[\bar{1}01] = a/_6[\bar{2}11] + a/_6[\bar{1}\bar{1}2] \qquad \text{eqn. 4.4a}$$

$$CB = \delta B + C\delta \qquad \text{eqn. 4.4b}$$

If these dislocations were to interact on (111) the initial configuration would be that shown in 4.19(a). The $a/_6\langle211\rangle$ partial dislocations crossing at points A, B, C and D would be the same and these will

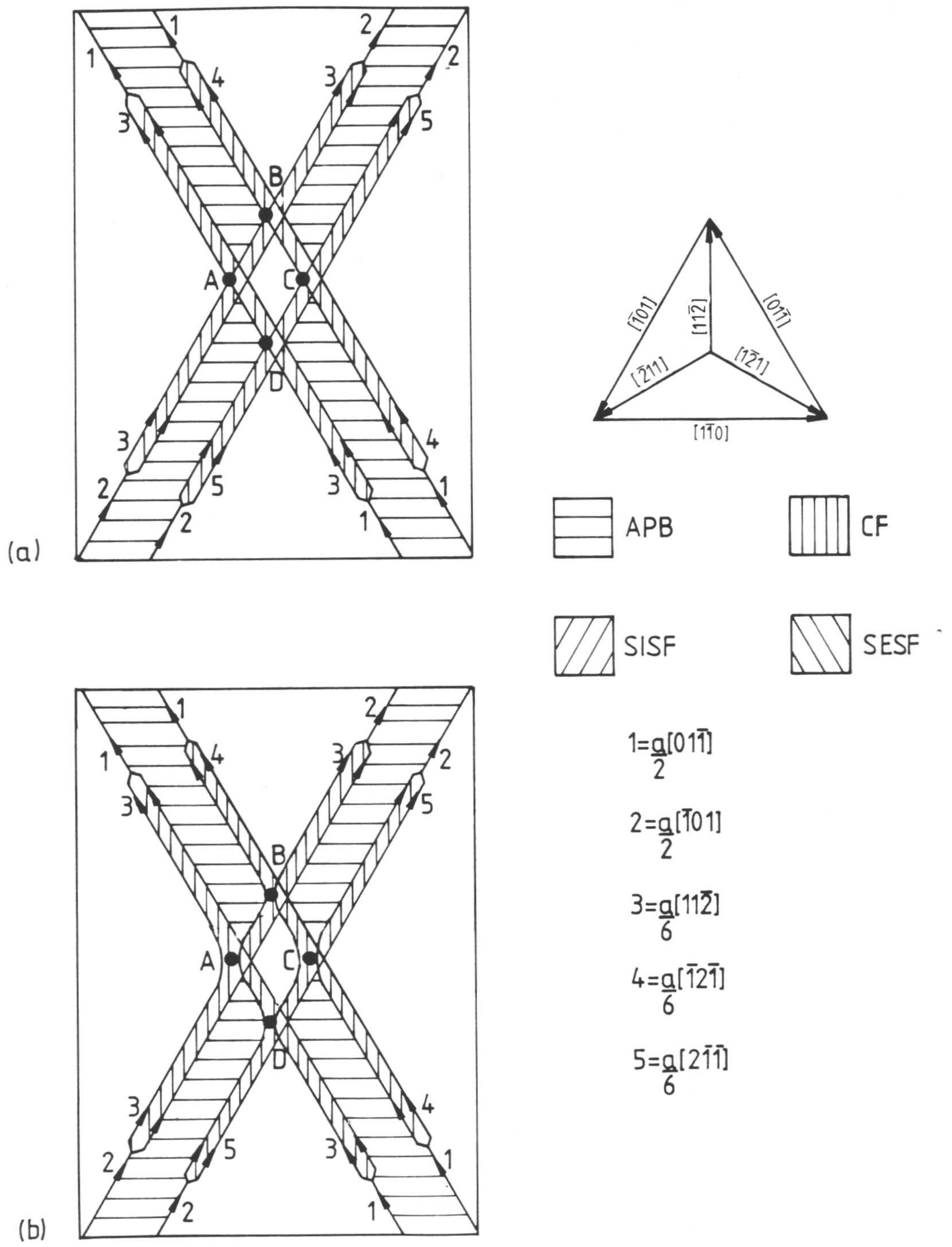

Fig. 4.19. Schematic illustration of the proposed interaction between two superdislocations on (111) showing the initial position (a), the configuration after parting at A, B, C, D (b), the configuration after limited glide (c), and the final configuration (d). See text for details. Each $a/_2\langle 110\rangle$ dislocation has been split into two $a/_6\langle 211\rangle$ Shockley partial dislocations. The Burgers vectors are shown in the triangle to the right of figure (a).

(Figure continued overleaf)

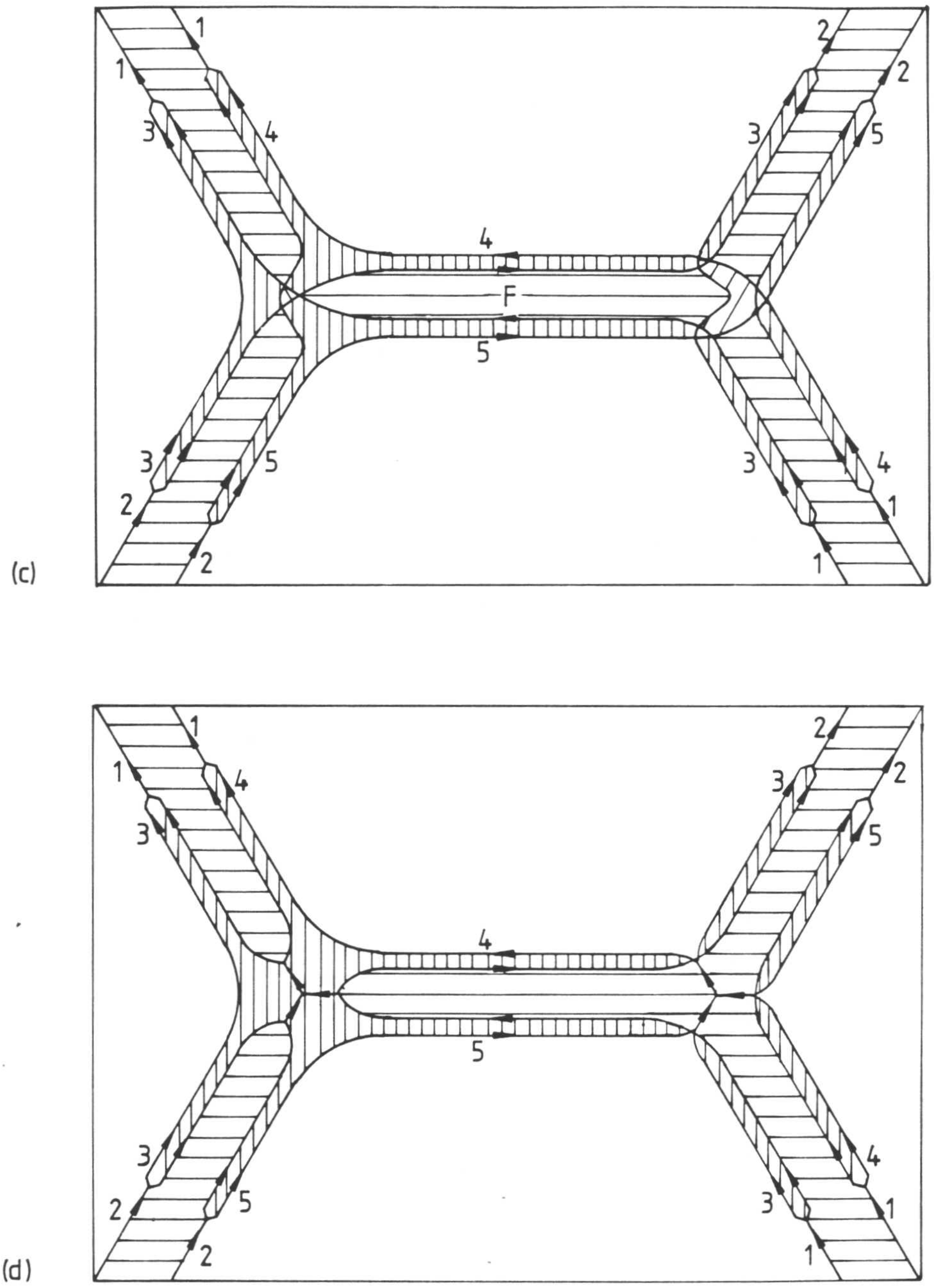

Fig. 4.19. For caption see previous page.

interact (when they are coplanar) to produce the configuration shown in figure 4.19(b). When the two interacting superdislocations glide away, lengths of partial dislocation will be drawn out between them to form two three-fold nodes (fig. 4.19c). If it is assumed that the CF energy is higher than the APB energy, the network will try to lower its energy by expanding the new APB region marked F. Partials 4 and 5 will be strongly attracted to form $a/_2[1\bar{1}0]$, thus reducing the total CF area. Partials at the nodal points are also likely to be attracted to one another, also to lower their energy by adopting the screw orientation. The dislocations at the nodal points will balance their energies so that when resolved they equal zero. This balance may produce three equal sized metastable regions of CF at some nodes. The predicted equilibrium configuration is shown in figure 4.19(d).

When two superdislocations, on different glide planes, with Burgers vectors which intersect at 120° interact, the dislocation interaction will be considerably more complex. Dislocation cross-slip must occur if a network is to form. $a/_2\langle 110\rangle$ dislocations can cross-slip between $\{111\}$ planes but if there is any dissociation into $a/_6\langle 211\rangle$ partial dislocations, this must be constricted before cross-slip can occur as $a/_6\langle 211\rangle$ dislocations only have one glide plane (fig. 4.7).

Consider the same two superdislocations as previously but in this case the $a/_2[01\bar{1}]$ pair lies in $(\bar{1}11)$, β and the $a/_2[\bar{1}01]$ pair lies in $(1\bar{1}1)$, α; the $a/_2[1\bar{1}0]$ dislocation pair produced can lie on (111), δ or $(\bar{1}\bar{1}1)$, γ. It will be assumed to lie on (111), δ.

The dislocation dissociations are:

$$a/_2[01\bar{1}] = a/_6[12\bar{1}] + a/_6[\bar{1}1\bar{2}] \qquad \text{eqn. 4.5a}$$

$$AC = \beta C + A\beta \qquad \text{eqn. 4.5b}$$

$$a/_2[\bar{1}01] = a/_6[\bar{1}12] + a/_6[\bar{2}\bar{1}1] \qquad \text{eqn. 4.6a}$$

$$CB = \alpha B + C\alpha \qquad \text{eqn. 4.6b}$$

and

$$a/_2[1\bar{1}0] \quad = \quad a/_6[1\bar{2}1] \quad + \quad a/_6[2\bar{1}\bar{1}] \qquad \text{eqn. 4.7a}$$

$$BA \qquad \delta A \qquad B\delta \qquad \text{eqn. 4.7b}$$

The expected interaction is shown in figure 4.20. It will be assumed that the interaction and the dislocations produced by the interaction will lie on (111),δ. However, it is possible that the nodal interaction may lie on a different plane from the new APB which will be produced. No energy calculations have been performed to evaluate which plane would be energetically most favourable. It is thought that this will be related to the stress direction which was not controlled carefully enough for an accurate determination to be made.

Figure 4.20(a) shows the first stage of the interaction. The leading AC and CB dislocations intersect. The two partials βC and $C\alpha$ combine and cross-slip onto δ forming a very short $\beta\alpha$ stair-rod dislocation at the point of intersection while $A\beta$ and αB combine and cross-slip onto δ to form BA. The applied stress and the line tensions of $\beta C/C\alpha$ and $A\beta/\alpha B$ will pull BA out along δ until the trailing CA and CB dislocations interact. Further cross-slip will produce the dislocation configuration shown in figure 4.20(b). The reduction of total strain energy will force this configuration to extend on δ. A plan view of the equilibrium structure, which is similar to figure 4.19(d), is shown in figure 4.20(d). In this configuration the interacting superdislocations are twisted away from their original glide planes to meet (111),δ. If enough energy is available the APBs and their bounding dislocations will cross-slip to form a planar network on (111),δ. The equilibrium structure for a fully cross-slipped network will be the same as that shown in figure 4.21.

Two types of nodes are evident at the junctions (figs. 4.19, 4.20 and 4.21). In this configuration both are constricted. In certain conditions they may expand to form the extended nodes discussed in 4.5.5.

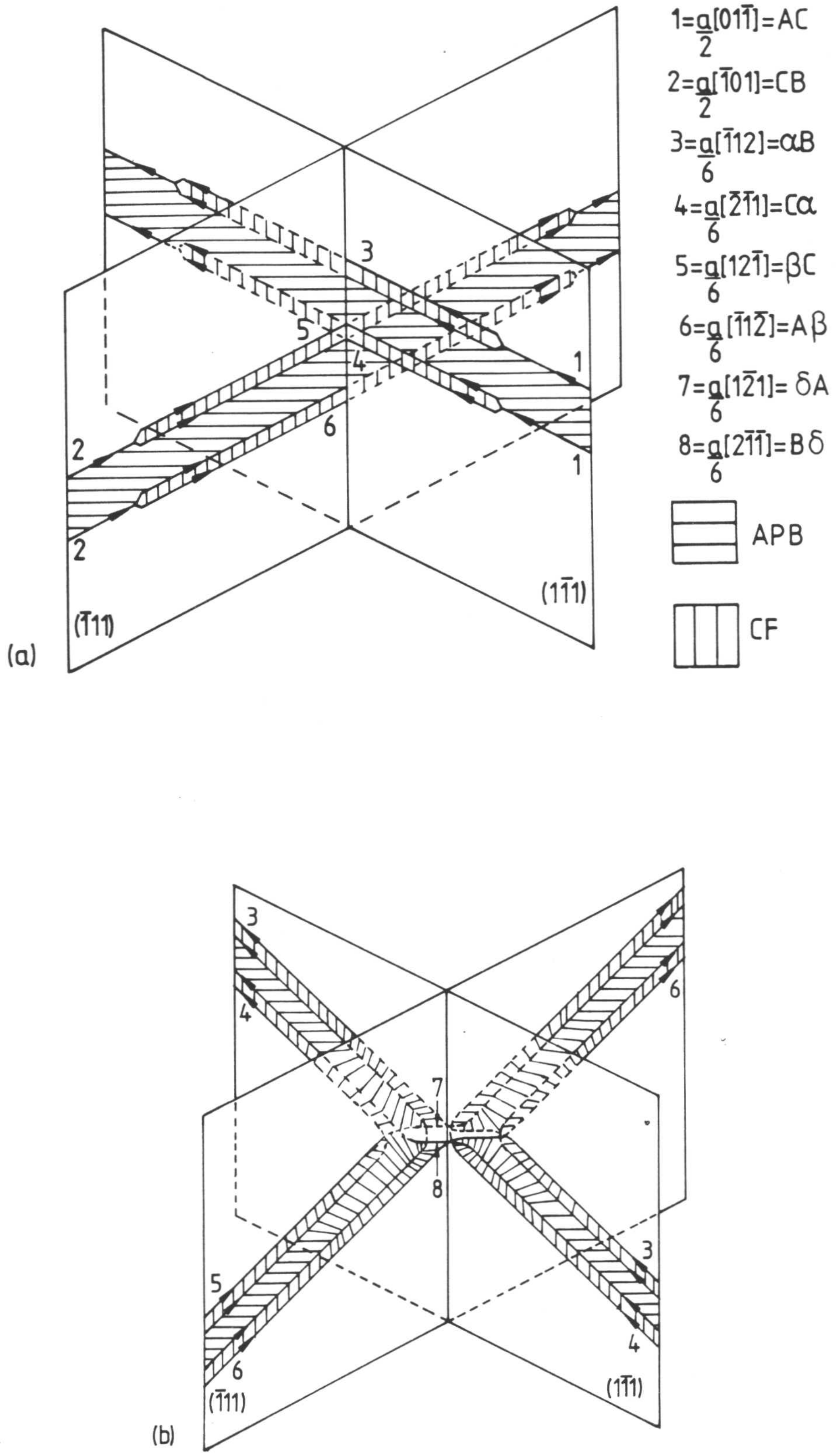

Fig. 4.20. Schematic illustration of the proposed interaction between two superdislocations on different {111} planes showing the initial position (a), a projection of the interaction at an intermediate point showing that the superdislocations are twisted from their glide planes (b), a plan of stage (b), (c), and a plan of the final configuration (d). See text for details.

(Figure continued overleaf)

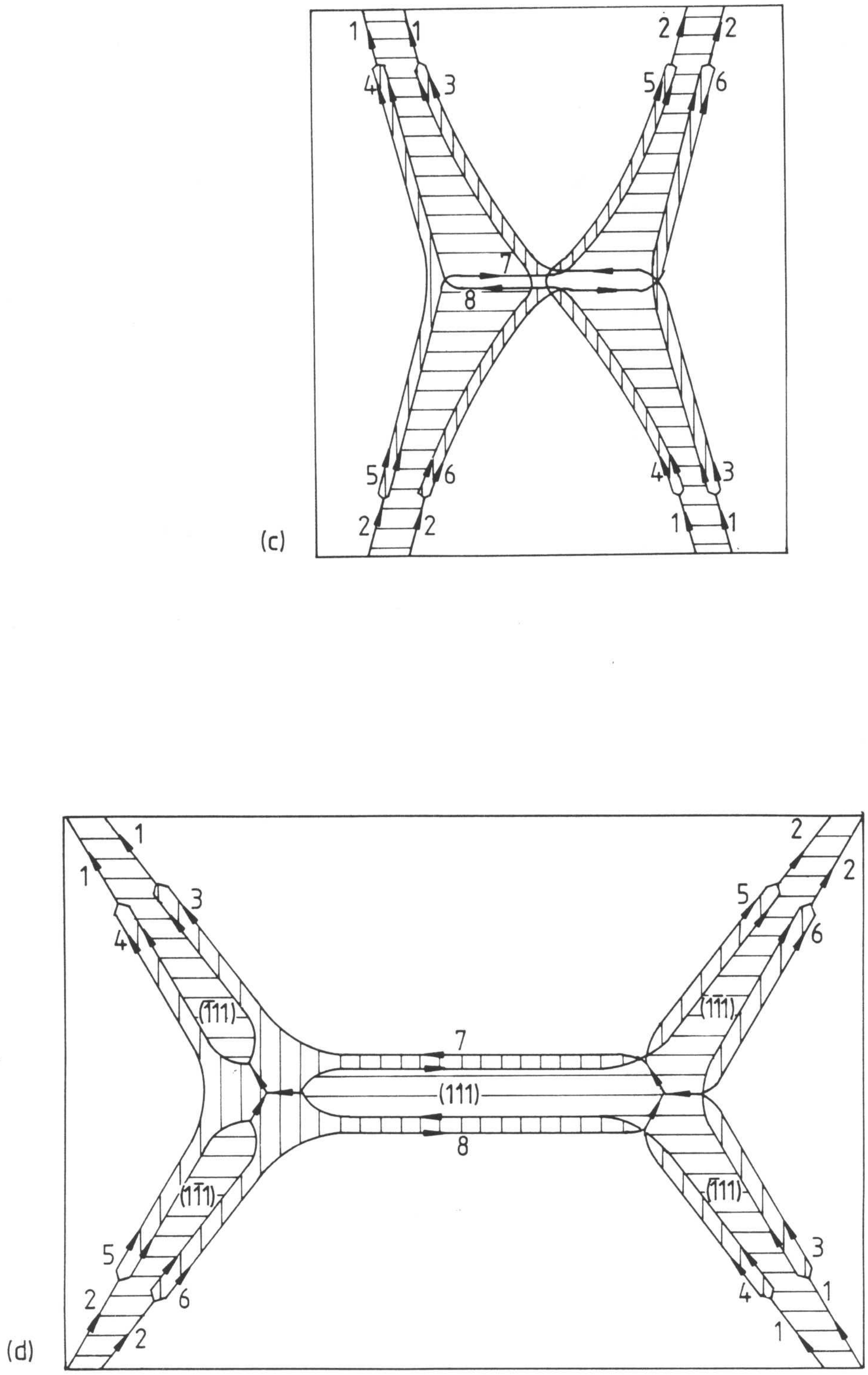

Fig. 4.20. For caption see previous page.

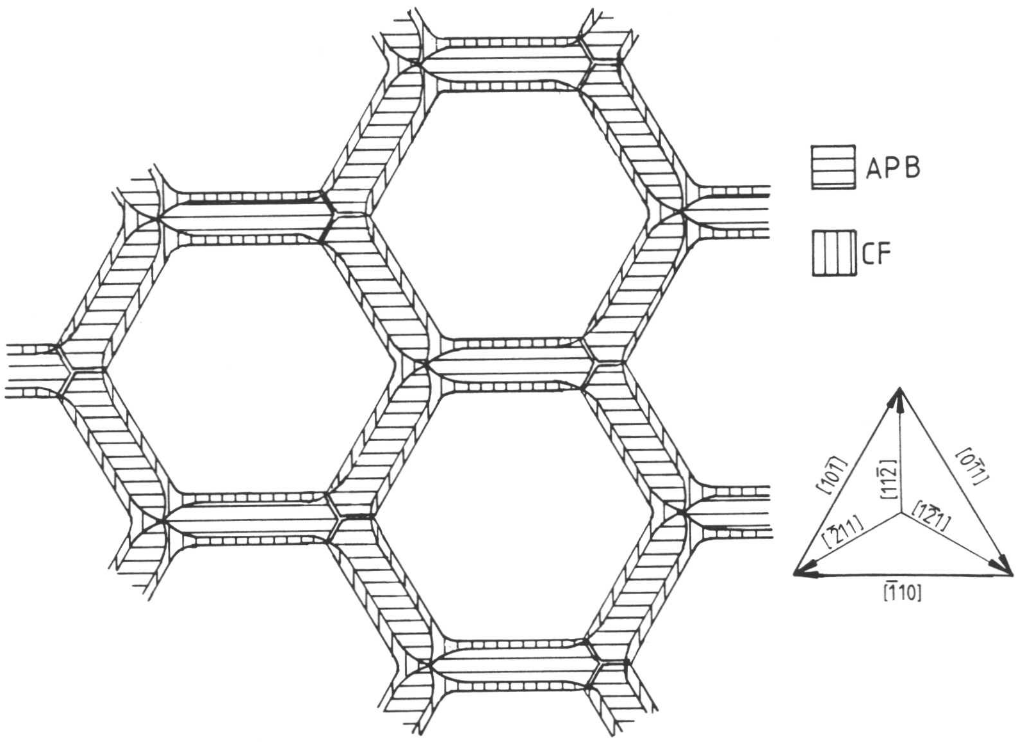

Fig. 4.21. The equilibrium configuration of a superdislocation network in a $L1_2$ structure (predicted by Amelinckx, 1979).

If these interactions to form networks are to occur in practice, a considerable amount of energy will be required. It is likely that the necessary interactions will only occur by the relief of strain energy held in highly deformed structures when they are annealed at a temperature which provides sufficient energy to promote cross-slip by the constriction of dissociated dislocations. This will initially produce a network which resides on two, three, or even four {111} planes. Figure 4.20(d) shows $a/_2[01\bar{1}](\bar{1}11)$ and $a/_2[\bar{1}01](1\bar{1}1)$ interacting to produce $a/_2[1\bar{1}0]$ on (111). The nodal reaction has been assumed to be on (111).

4.5.4 Observations of nodal reactions

Many interactions similar to those described above were observed in deformed and annealed microstructures of alloys A, D and G. Figure 4.22 is part of a $\underline{g}\cdot\underline{b}$ series of TEM micrographs recorded from an interaction equivalent to that shown in figure 4.20(b). Table 4.2 lists the $\underline{g}\cdot\underline{b}$ values for the $a/_2\langle 110\rangle$ dislocations in this configuration. It was found that figure 4.22 showed an interaction between an $a[10\bar{1}]$ superdislocation gliding on $(1\bar{1}1)$ and an $a[1\bar{1}0]$ superdislocation gliding on $(11\bar{1})$. The interaction produced two segments of $a/_2[01\bar{1}]$ which could lie in either (111) or $(1\bar{1}1)$ depending upon the glide plane of the partial dislocations forming the $a/_2[01\bar{1}]$ dislocation. The central dislocation configuration was too fine to be resolved using bright field TEM but if each of the constituent $a/_2\langle 110\rangle$ dislocations is assumed to be dissociated onto (111) the dislocation would be that shown in figure 4.22(f). No dissociation of any of the $a/_2\langle 110\rangle$ dislocations was observed. As predicted in 4.4.3, the APBs were twisted from their initial glide planes by the interaction on (111).

If the interactions were subsequently to follow the scheme proposed in 4.4.3, a structure similar to that shown in 4.20(d) would be formed. Figure 4.23 shows that the reaction did occur. This figure

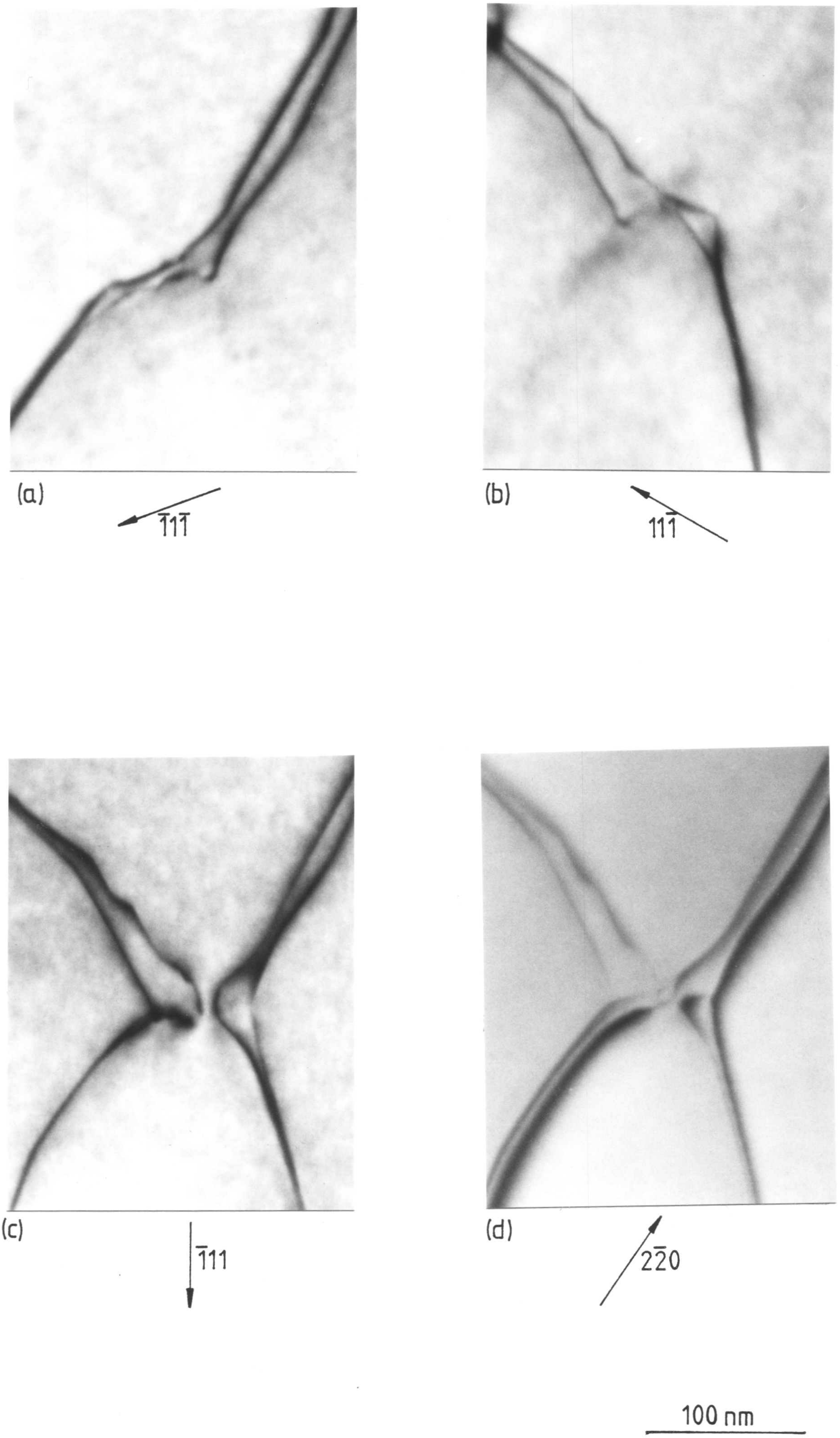

Fig. 4.22. For figure caption, see overleaf.

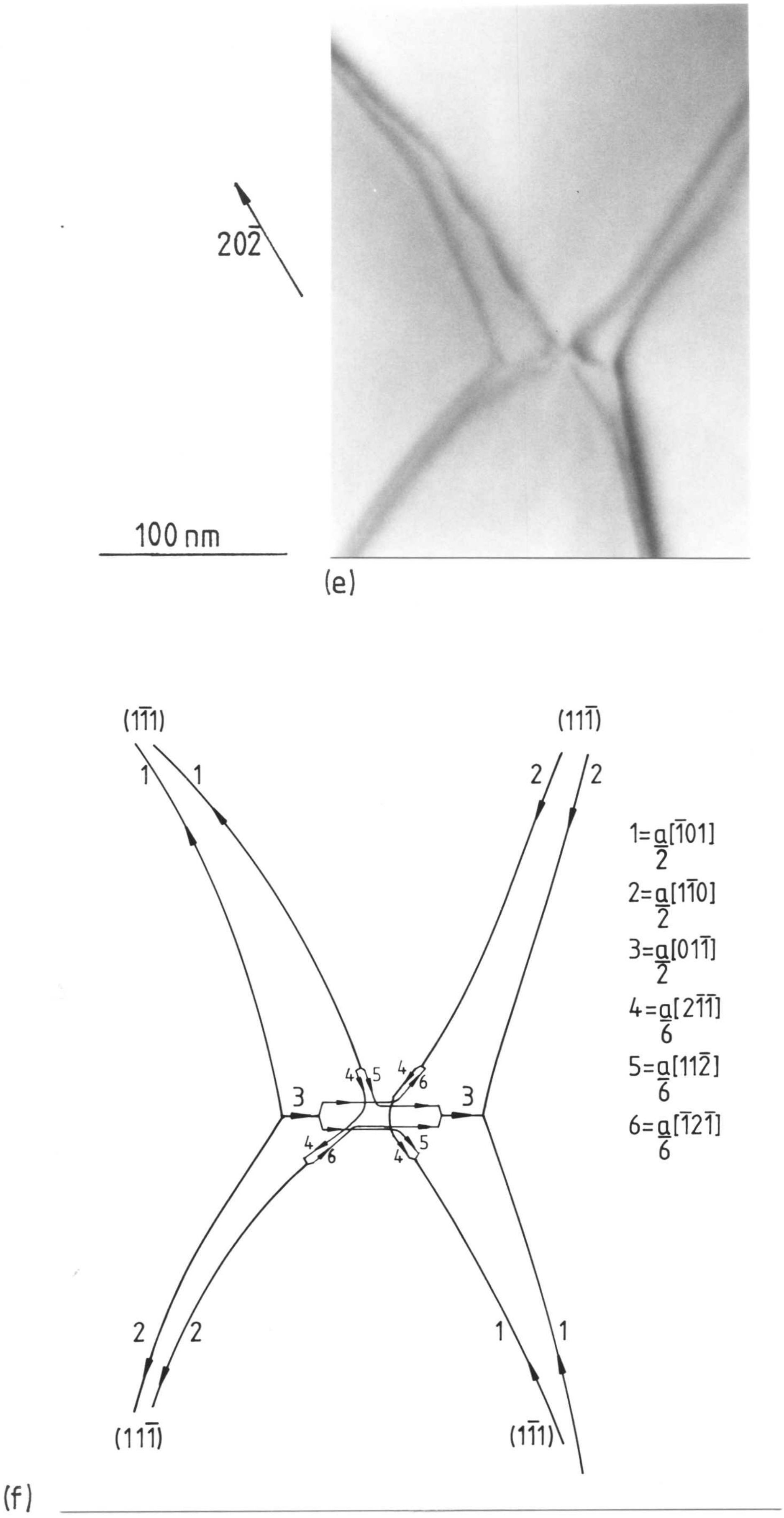

Fig. 4.22. Part of a bright field g.b analysis showing an early stage (fig. 4.20b and c) of the interaction between two a<110> superdislocations on two {111} planes. In the schematic diagram of the interaction (f), it has been assumed that the dislocation dissociation is on (111). The g.b values of the $a/_2$<110> dislocations are given in table 4.2. (foil normal: ~[111]).

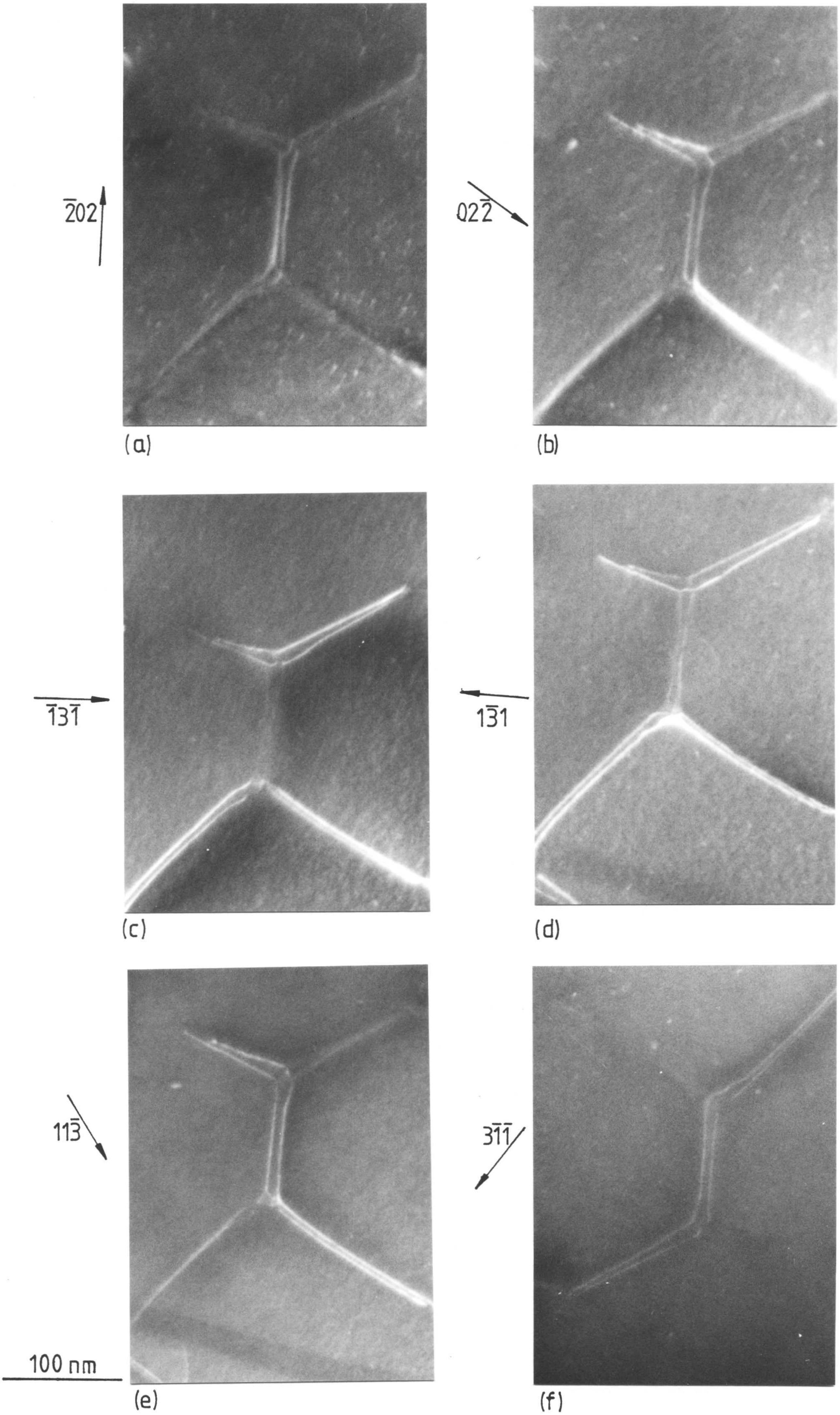

Fig. 4.23. For figure caption, see next page but one.

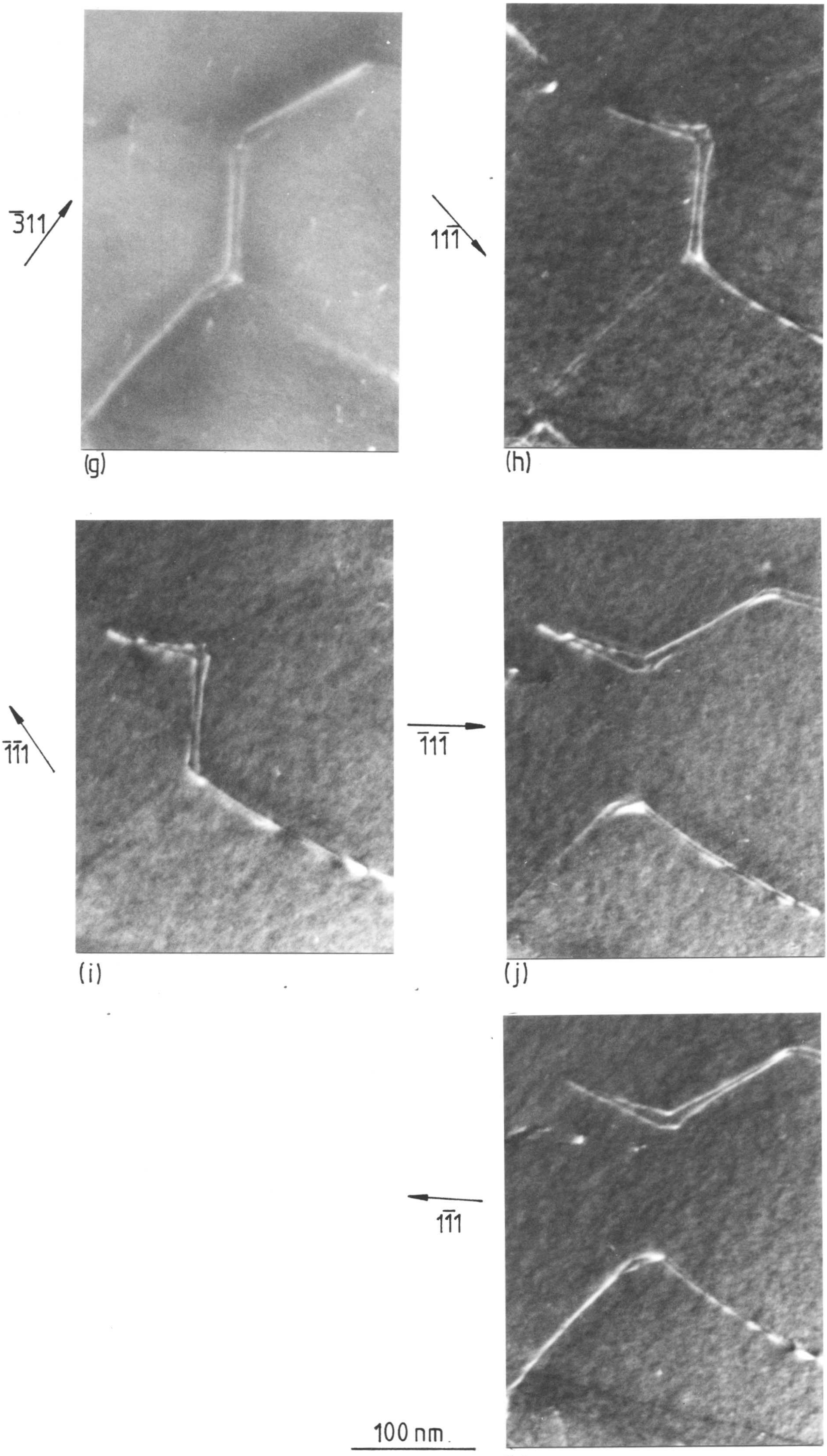

Fig. 4.23. For figure caption, see overleaf.

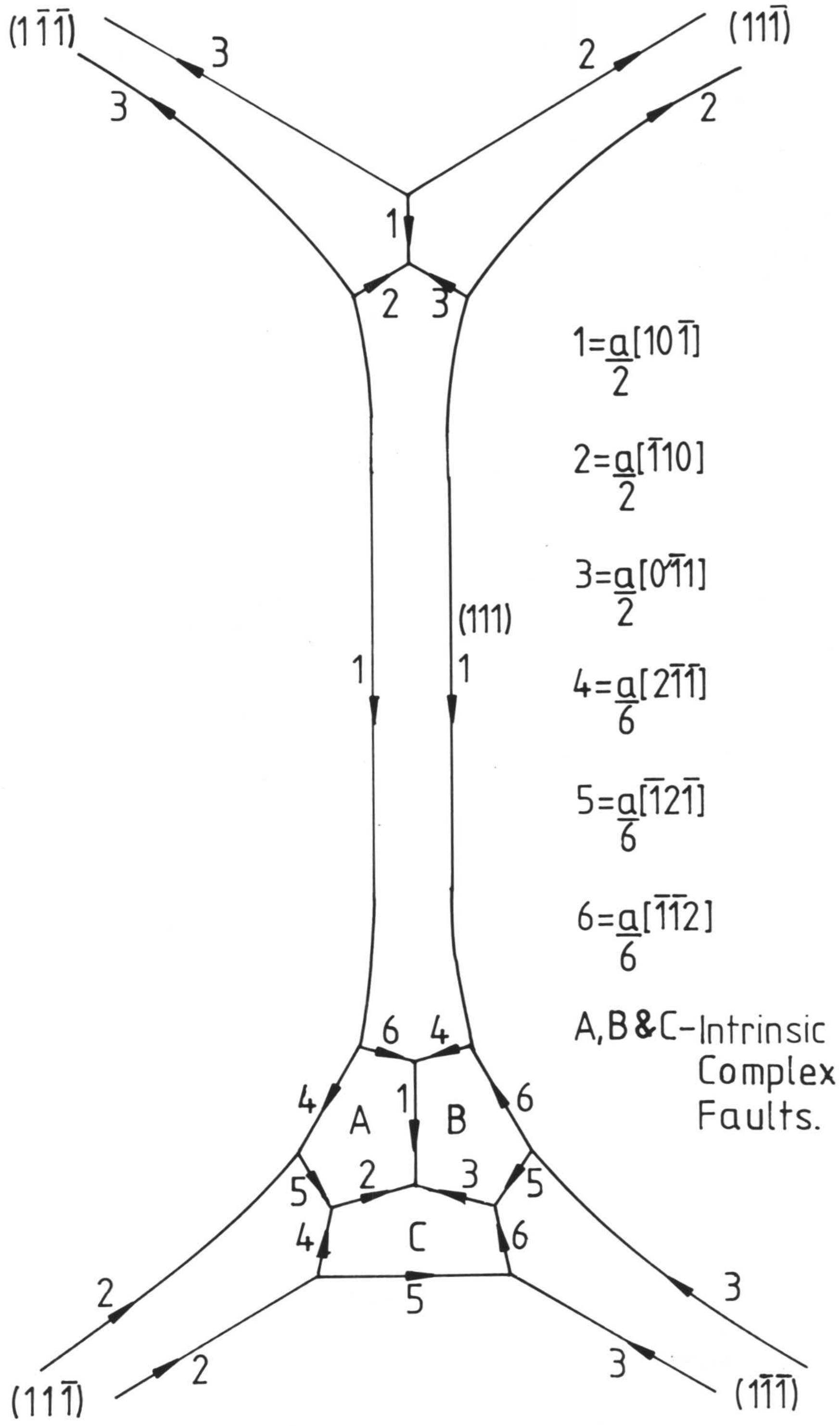

Fig. 4.23. Weak beam dark field TEM micrographs taken in conditions between $W_{(\underline{g},2\underline{g})}$ and $W_{(\underline{g},4\underline{g})}$ showing dislocation configuration, shown in figure 4.20(d), formed after interaction between two a<110> superdislocations on different {111} planes. The $\underline{g}.\underline{b}$ values for the dislocations in the configuration are given in table 4.3. A schematic representation of the configuration is shown in (ℓ) assuming that the nodal regions both lie on (111) (foil normal: ~[111]).

shows a full weak beam $\underline{g}\cdot\underline{b}$ analysis of the interaction; the $\underline{g}\cdot\underline{b}$ values for the identified dislocations are tabulated in Table 4.3 In this case the interaction occurred between an $a[\bar{1}10]$ superdislocation on $(11\bar{1})$ and an $a[0\bar{1}1]$ on $(1\bar{1}\bar{1})$. The superdislocation produced by the interaction was $a[10\bar{1}]$ on (111). The partial dislocation structure at the nodal points, which is shown in figure 4.23(l) was essentially the same as that described in 4.4.3 and shown in figure 4.19(d). The dislocation analysis can be confirmed by referring to table 4.3. It was not possible to determine the identity of all of the dislocations due to the fine structure of the interactions and the possible effect of the complex faults A, B and C on the images of the dislocations between them. However, the $a/_2\langle 110\rangle$ dislocations forming the superdislocations and the top node were identified unambiguously as were the $a/_6\langle 211\rangle$ partial dislocations between the complex faults and the unfaulted crystal. The identities of the remaining dislocations were deduced from the known dislocations and the image contrast was compared with that predicted in table 4.3. In this way it was possible to identify all the dislocations of the network shown in figure 4.23.

From the dislocation analysis it was concluded that faults A, B and C were intrinsic complex faults. These faults have the highest energy of any of the planar defects possible in $L1_2$ and should consequently be unstable with respect to the SSFs and APB. It is thought that the CFs are metastable because the desire of the dislocations to minimise their own energy by adopting a screw orientation and to balance the forces at the three-way supernode is greater than the driving force to anihilate the CFs. Consequently, the configuration shown in figure 4.23 could lower its energy further if the complex faults were anihilated and replaced by a lower energy fault. Many of the nodes observed appeared to form extended nodes with no internal structure and these are discussed below.

Table 4.3. $\underline{g}$ $\underline{b}$ values for the dislocations shown in figure 4.23

Micrograph	Diffraction vector (g)	Burgers vector ($\underline{b}$)					
		$a/_2[10\bar{1}]$ (1)	$a/_2[\bar{1}10]$ (2)	$a/_2[0\bar{1}1]$ (3)	$a/_6[2\bar{1}\bar{1}]$ (4)	$a/_6[\bar{1}\bar{1}2]$ (5)	$a/_6[\bar{1}2\bar{1}]$ (6)
(a)	$\bar{2}02$	-2	+1	+1	-1	$-\frac{2}{3}^*$	[0]
(b)	$02\bar{2}$	+1	+1	-2	[0]	+1	[$+\frac{1}{3}$]
(c)	$\bar{1}3\bar{1}$	[0]	+2	-2	$-\frac{2}{3}^*$	$+\frac{2}{3}^*$	$+\frac{4}{3}^*$
(d)	$1\bar{3}1$	[0]	-2	+2	$+\frac{2}{3}^*$	$-\frac{2}{3}^*$	$-\frac{4}{3}^*$
(e)	$11\bar{3}$	+2	[0]	-2	$+\frac{2}{3}^*$	$+\frac{4}{3}^*$	$+\frac{2}{3}^*$
(f)	$3\bar{1}\bar{1}$	+2	-2	[0]	$+\frac{4}{3}^*$	[$-\frac{1}{3}$]	$-\frac{2}{3}^*$
(g)	$\bar{3}11$	-2	+2	[0]	$-\frac{4}{3}^*$	[$+\frac{1}{3}$]	$+\frac{2}{3}^*$
(h)	$11\bar{1}$	+1	[0]	-1	[$+\frac{1}{3}$]	$+\frac{2}{3}^*$	[$+\frac{1}{3}$]
(i)	$\bar{1}\bar{1}1$	-1	[0]	+1	[$-\frac{1}{3}$]	$-\frac{2}{3}^*$	[$-\frac{1}{3}$]
(j)	$1\bar{1}1$	[0]	-1	+1	[$+\frac{1}{3}$]	[$-\frac{1}{3}$]	$-\frac{2}{3}^*$
(k)	$\bar{1}1\bar{1}$	[0]	+1	-1	[$-\frac{1}{3}$]	[$+\frac{1}{3}$]	$+\frac{2}{3}^*$

[ ] - Invisible * - See below

* $\underline{g}.\underline{b}$	Fault to right of dislocation	Fault to left of dislocation
$+\frac{2}{3}$	I	V
$-\frac{2}{3}$	V	I
$+\frac{4}{3}$	V	I
$-\frac{4}{3}$	I	V

4.5.5 Extended nodes in superdislocation networks

The occurrence of extended intrinsic and extrinsic nodes in disordered materials has frequently been reported; see, for instance, Aerts, Delavignette, Siems and Amelinckx (1962) in Si, Loretto (1964) in Au-Sn and Gallagher (1966) in Ag-In. In contrast, the occurrence of extended intrinsic and extrinsic nodes in $L1_2$ has only been reported twice other than in this investigation. The first observations were made by Howe et al. (1974) in deformed and annealed Zr_3Al; their results are compared to those gained from this investigation in 4.6. More recently, Baker, Viens and Schulson (1984) commented on their existence.

Extended nodes were frequently observed in alloys A, D and G. Figures 4.24 and 4.25 are two examples which will be discussed. Figure 4.24 shows a single node, while figure 4.25 shows a planar network on (111) containing a number of extended nodes.

A weak beam $\underline{g} \cdot \underline{b}$ study was undertaken on one defect; selected micrographs are shown in figure 4.24. The three superdislocations entering the node were identified as pairs of $a/_2\langle 110\rangle$ dislocations. These were all pure screw and were on (111) at the centre of the node. As previously discussed, they were displaced from their original glide plane to form the node. The contrast from the central fault was consistent with a stacking fault displacement of $\pm a/_3[111]$; the fault was visible in all diffraction conditions other than $\underline{g}=(2\bar{2}0)$. No fault fringes were observed because the fault is almost parallel to the foil surface. The fault must be bounded by six partial dislocations. Segments 1, 3 and 5 (fig. 4.24) were not characterised as any contrast resulting from them became confused with that from the fault. Segments 2, 4 and 6 were identified. They could be $\pm a/_3[111]$, $a/_6\langle 211\rangle$ or $a/_3\langle 211\rangle$. The Frank partial was quickly eliminated as it would be invisible in all conditions except $\underline{g}=(200)$. This was clearly not the case as the dislocations under consideration were clearly seen in other conditions. If the dislocations

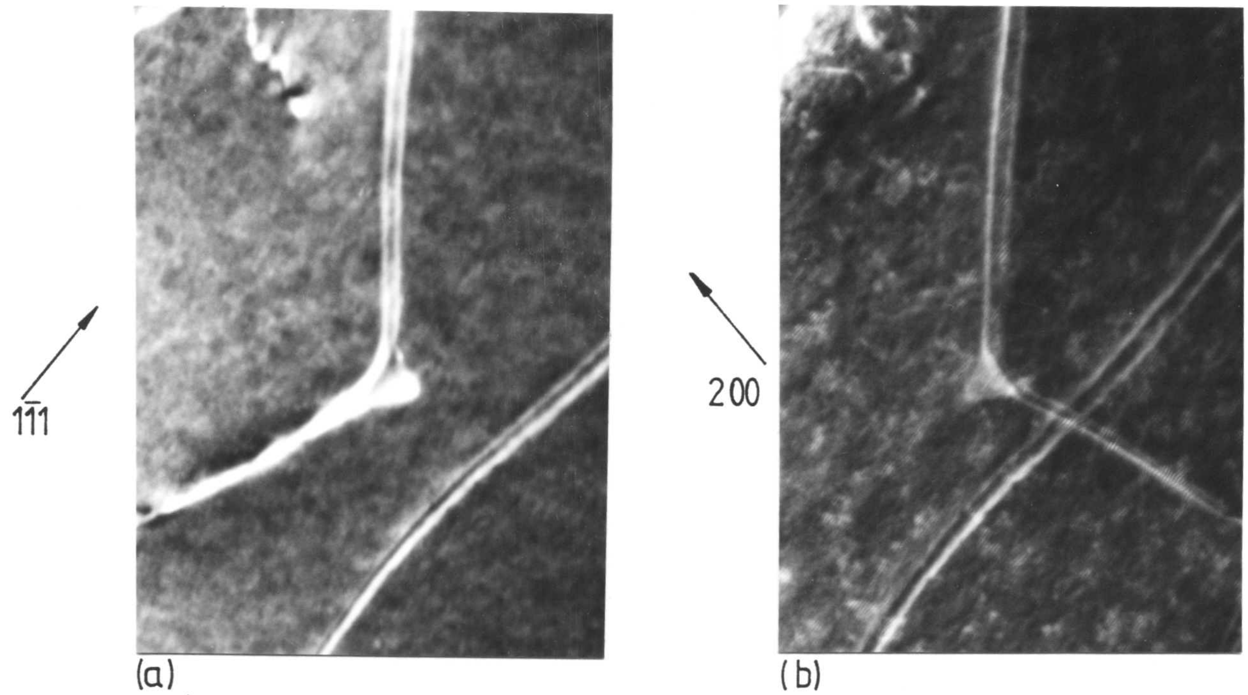

Fig. 4.24. Examples of weak beam dark field TEM micrographs taken in $W_{(\underline{g},2.5\underline{g})}$ conditions showing the dislocations and fault contrast at an extended node. The dislocation configuration identified by $\underline{g}.\underline{b}$ analysis is shown in (d). (foil normal: ~[111]).

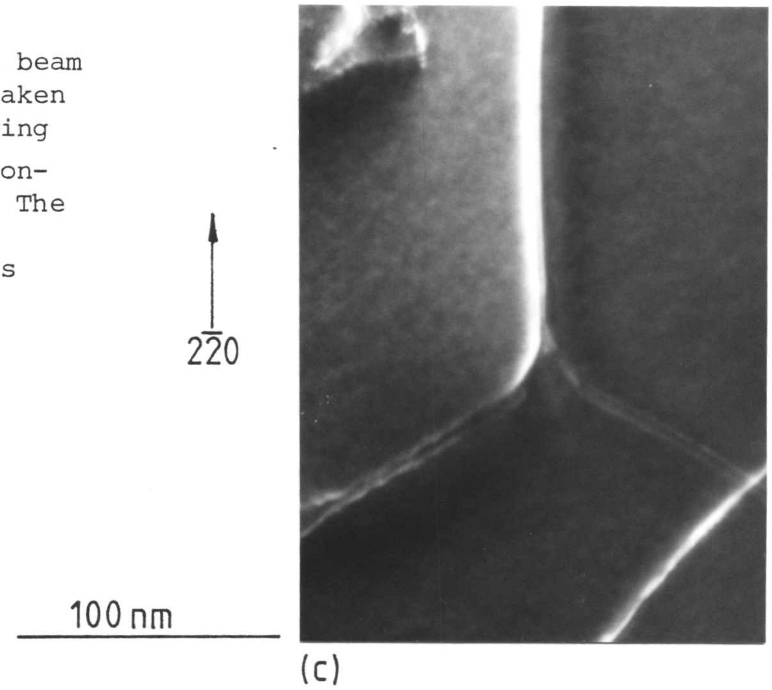

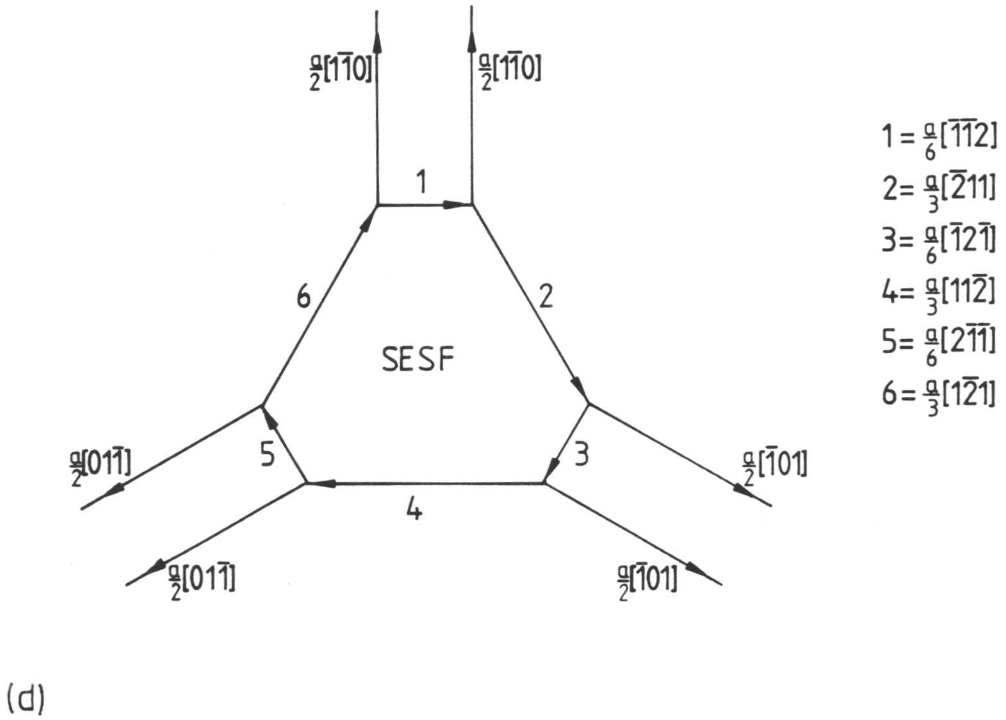

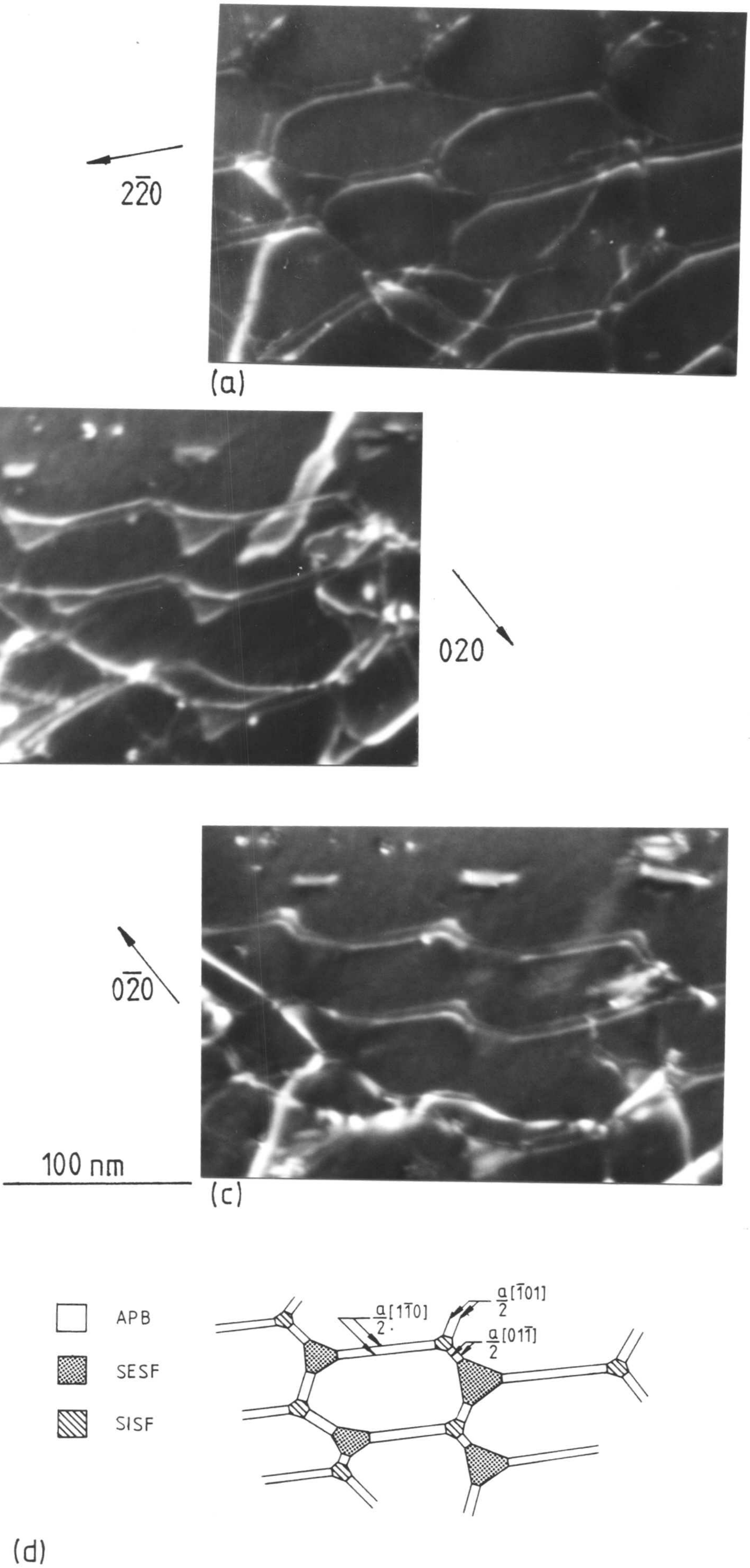

Fig. 4.25. Part of a weak beam dark field TEM $\underline{g}.\underline{b}$ analysis, using $W_{(\underline{g},2.5\underline{g})}$, showing a planar superdislocation network on (111) with extended nodes at the nodal points. The dislocations identified are shown in (d). The SESFs are larger than the SISFs. Note the change in contrast from the SESFs in $(020)_{3\underline{g}\pm\underline{g}}$ conditions (b and c) may be due to anomalous contrast from SESFs (see 3.3.8 for details). (foil normal: ~[001]).

were $a/_6\langle 211\rangle$, as in the configuration shown in figure 4.23, the defect would be a CF; if the dislocations were $a/_3\langle 211\rangle$ the defect would be a SSF.

The analysed dislocation configuration is shown in figure 4.24(d). Segments 1, 3 and 5 were deduced from the known dislocations to be $a/_6\langle 211\rangle$ partial dislocations. The dislocation line sense was determined using a $\pm\underline{g}$ pair and dislocation 2 was used to determine the fault type. In this case the fault was found to be a superlattice extrinsic stacking fault.

Figure 4.25 shows a network consisting of two different sizes of superdislocation nodes. Dislocation analysis similar to that described above was carried out on the network. It showed that the larger nodes were SESF while the smaller nodes were SISF (fig. 4.25d). This analysis was supported by the contrast change observed in weak beam conditions at the larger nodes on reversing $\underline{g}$. This observation was only used to confirm the dislocation analysis as the contrast from the smaller nodes cannot easily be observed (3.3.8). The network consisted of alternating intrinsic and extrinsic nodes joined by screw superdislocations (fig. 4.25d).

Extended nodes form from the metastable structure previously proposed and observed (figs. 4.19d and 4.20) in the following way. It can be seen that the central points of the nodes in 4.19(c) contain a small area of extrinsic or intrinsic SSF. Once the activation energy for SSF growth has been overcome, it is proposed that this region will extend on (111) forcing the $a/_6\langle 211\rangle$ partial dislocations apart until it eventually adopts the structure shown in figure 4.26(a). The three $a/_6\langle 211\rangle$ partial dislocations bounding the faults would be so close together that their spacing is of the order of the image width and in the TEM they will behave as a $a/_3\langle 211\rangle$ partial dislocation. The resultant structure would adopt the low energy screw configuration (fig. 4.26b). The driving force for this reaction will be, at least in part, due to the reduction in the area

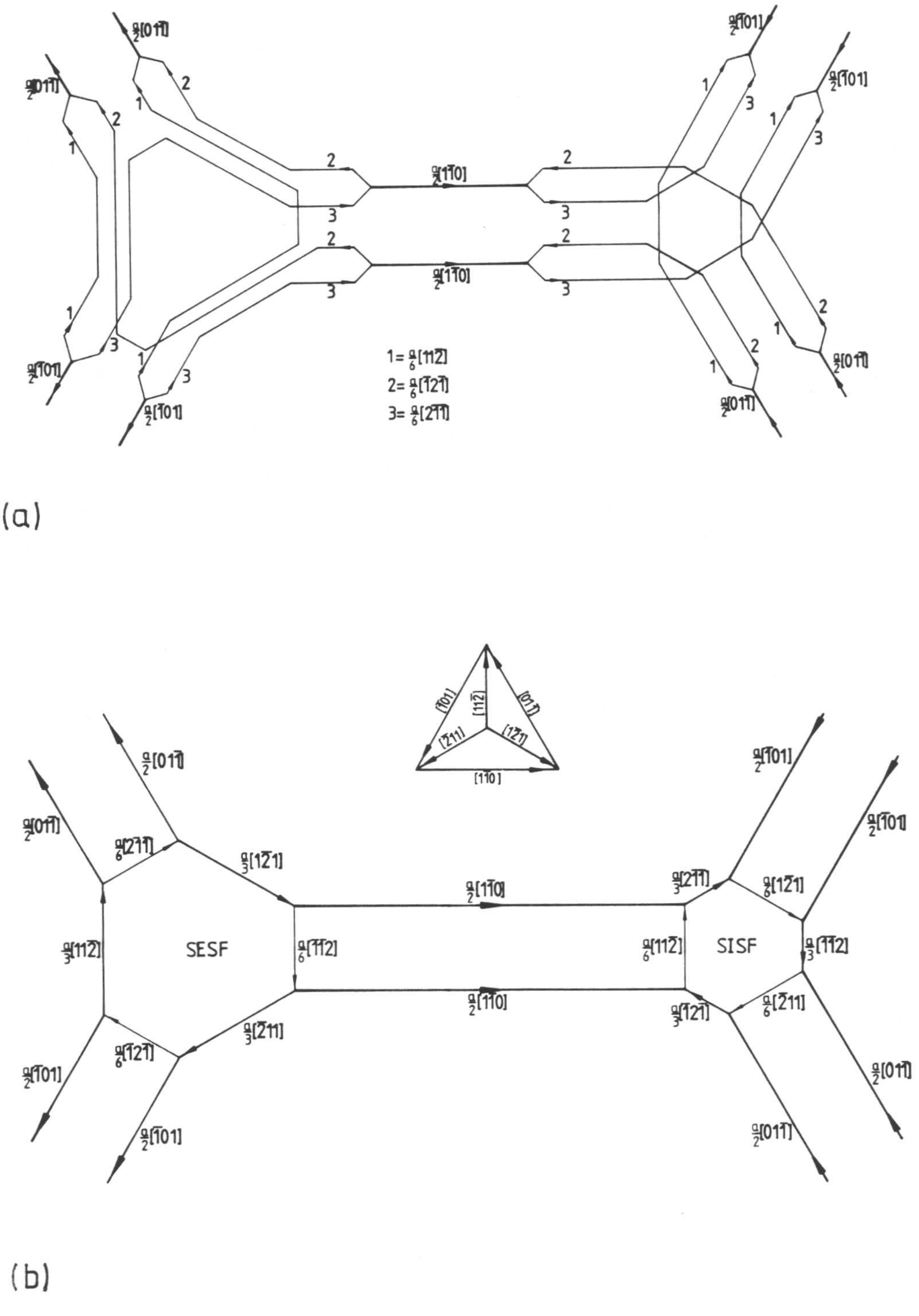

Fig. 4.26. Schematic illustration of the dislocation structure at an extended intrinsic node and an extended extrinsic node on (111). The structure is shown in terms of $a/_6$<211> partial dislocations (a) and with the $a/_6$<211> partials summed to produce the configuration observed in the TEM (b).

of high energy CF, but it is also likely to be accelerated by the presence of alloying elements, in this investigation Ti, which will segregate to the SSFs, particularly the SESF. This effect is discussed in detail in 6.3.4.

4.6 Conclusions and Comparison of the Networks with those Observed by Other Workers

By following a similar approach to that adopted for interactions between $a/_2\langle110\rangle$ dislocations in austenitic stainless steels (Whelan, 1959), the hexagonal dislocation supernodes and networks described theoretically and observed experimentally in the γ' of single crystal superalloys have been explained. They were formed by interactions between two $a\langle110\rangle$ superdislocations, consisting of two $a/_2\langle110\rangle$ dislocations on the same or different $\{111\}$ planes bounding an APB and enclosing an angle of 120° between their Burgess vectors, to produce a third $a\langle110\rangle$ superdislocation. Each of the $a/_2\langle110\rangle$ dislocations was assumed to have the capacity to dissociate into two $a/_6\langle211\rangle$ partial dislocations on the $\{111\}$ habit plane. This scheme of dislocation interactions was shown to produce networks of superdislocations with supernodes at the junction points. With the nodal reactions in the metastable state (fig. 4.19d), the networks were found to be equivalent to those predicted by Amelinckx (1979) (fig. 4.21). In this state the nodal points support large CFs so that the dislocations can adopt a lower energy pure screw orientation and balance the forces between the dislocations at the supernodes. In his paper of 1979 Amelinckx states that up to that time no observations of hexagonal networks in $L1_2$ have been reported. This investigation rectifies this situation.

In the configuration shown in figure 4.23 an activation barrier exists which suppresses the nucleation and growth of a more stable SSF at the nodal points. It has been shown that once the activation barrier is exceeded, SSFs consume the nodal area to create the stable lowest energy nodal structure of alternating intrinsic and extrinsic SSFs linked by superdislocations. By measuring the superdislocation spacing and the size of the supernodes, it was possible to evaluate the APB energy and the SSF energies from one network. This process is described in 6.3. No other suitable method for the evaluation of SSF energy has been developed before this investigation. It was observed that the nodal SESFs were considerably larger than the nodal SISFs. It is thought that this may be a function of the concentration of certain alloying elements, as discussed in 6.3.4.

Howe et al. (1974) published a paper which reported the observation of hexagonal networks in the $L1_2$ compound, Zr_3Al. Amelinckx (1979) was clearly not aware of this paper when he wrote his article as no reference was made to it. In the paper, Howe et al. appear to misinterpret the evidence in their micrographs. They correctly state that the $L1_2$ lattice repeat is a<110> and that this can be dissociated to form two $a/_2$<110> dislocations bounding an APB (4.3.2) or to form two $a/_3$<211> dislocations bounding an SSF (4.3.3). But they incorrectly assume that only one of these dissociation mechanisms can occur at any time so that any dislocations which dissociate can do so by only one method. They assume that dissociation of a<110> into two $a/_3$<211> partial dislocations occurs and interaction between these pairs produces the network shown in figure 4.27. This allows no segments of $a/_2$<110> dislocation pairs between the alternating SESFs and SISFs. It is clear from figure 10 (Howe et al., 1974) that the extended faults are linked by long straight dislocation pairs which exhibit contrast which is consistent with superdislocations but inconsistent with screw $a/_3$<211> pairs. It is suggested that the dislocation networks observed in Zr_3Al are analogous to those observed, and described in the γ' precipitate of cold deformed and annealed single crystal superalloys (4.5.5). It is worth noting that Howe et al. observed the SISFs and SESFs to be equally extended. This is in

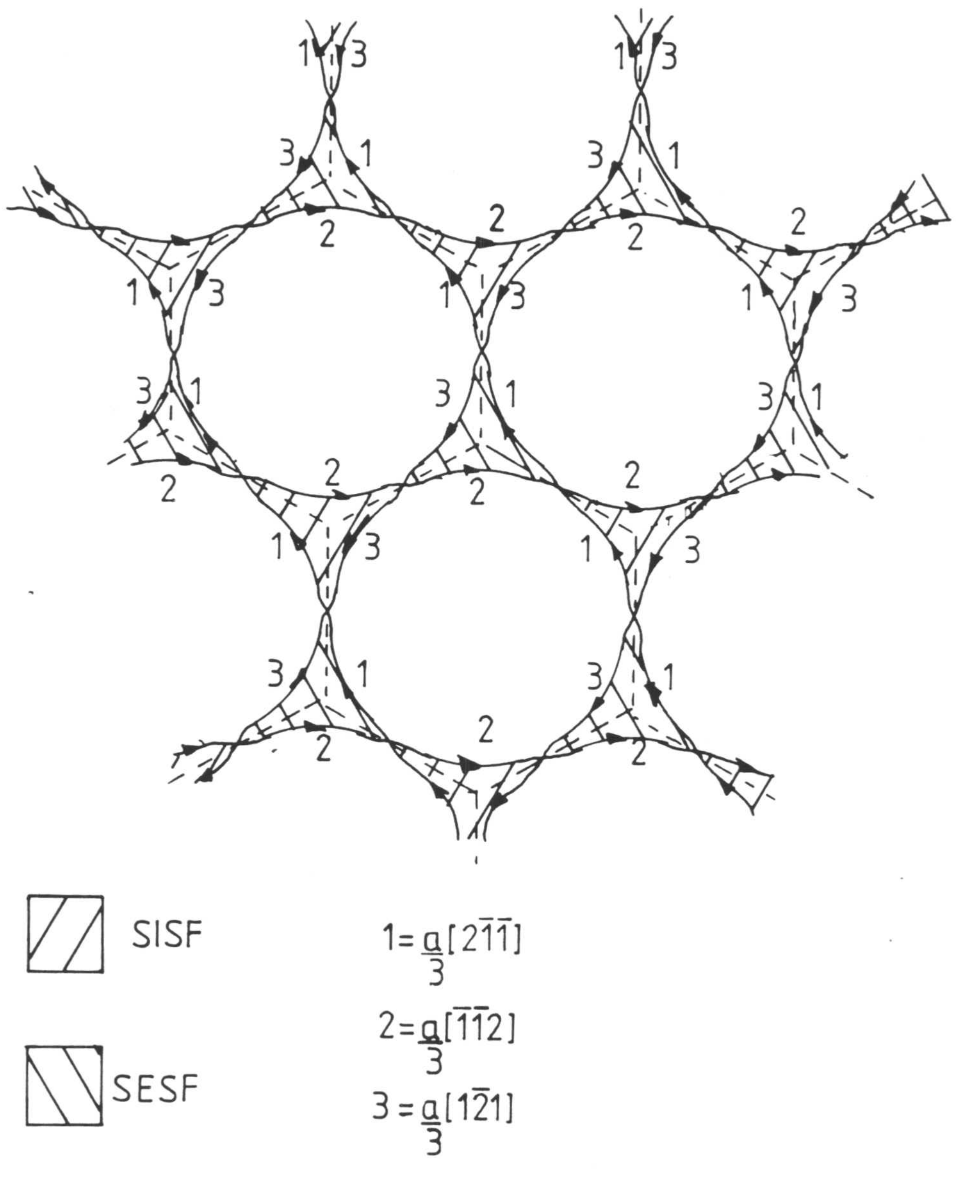

Fig. 4.27. Schematic illustration of the super dislocation network proposed by Howe et al. (1972). Note that there are no $a/_2\langle 110\rangle$ dislocation pairs between the nodal points.

marked contrast to this investigation where SESFs were considerably larger than SISFs- see 6.3.4 for discussion.

Although the interaction to form supernodes was by far the most significant to be observed, many other dislocation interactions were observed and some of these, which were relevant to the investigation as a whole, are discussed in the following chapter.

CHAPTER 5

FURTHER DISLOCATION INTERACTIONS

5.1 Introduction

Some of the other dislocation interactions observed in deformed and annealed γ' of alloys A, D and G are discussed in this chapter. It includes observations of isolated superdislocations, superdislocation dipoles and large planar faults. Mechanisms for the formation of superdislocation dipoles and planar faults are suggested. Consideration is also given to the formation of square and rectangular dislocation networks by dislocations with Burgers vectors which enclose an angle of 90°.

5.2 Observations of Isolated Dislocations

5.2.1 Superdislocations in the annealed microscructure

At the annealing temperature of 1173K enough energy is available to promote climb of the unpaired $a/_2\langle 110\rangle$ dislocations in the γ matrix. This process considerably increases the probability of two dislocations of the same type gliding on the same $\{111\}$ plane. These dislocations can 'pair-up' to form superdislocations which then lower the dislocation density in the γ by gliding into the γ'. Once inside these superdislocations can interact with others entering the γ' and those already present after deformation. In many cases these gliding $\{111\}$ superdislocations reduced strain energy by forming hexagonal or square dislocation networks as discussed in 4.5 and 5.3 respectively. Some superdislocations, however, remained isolated. Although the majority of these were pure screw $a/_2\langle 110\rangle$ dislocation pairs on $\{111\}$ planes some (fig. 5.1) were seen to be curved; probably due to pinning of the superdislocations at the γ/γ' interface. The screw orientation was most usually adopted to reduce the dislocation energy.

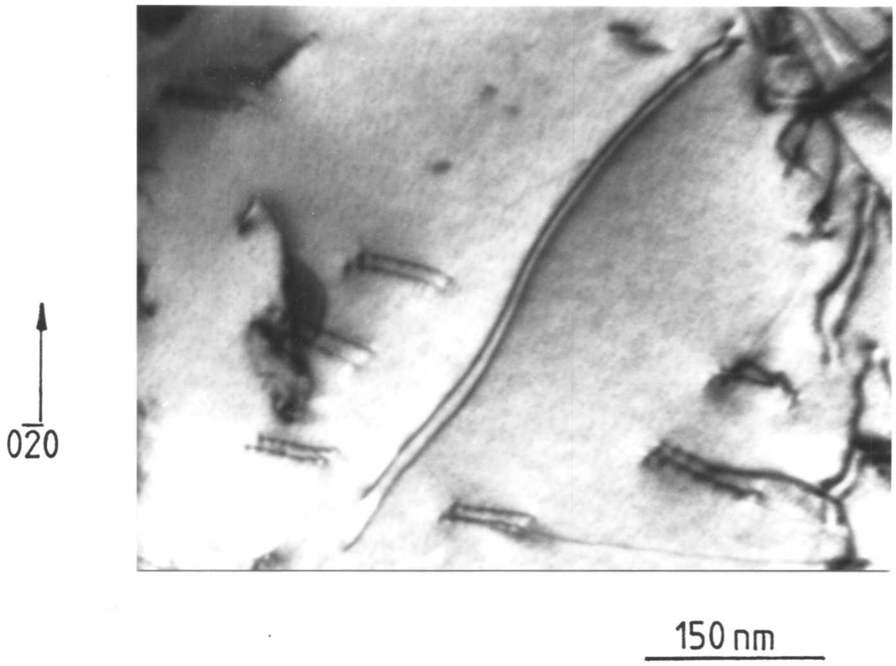

Fig. 5.1. Bright field TEM micrograph showing curved superdislocation in γ'. (foil normal: ~[011]).

It has been suggested (e.g. by Suzuki et al., 1979) that the straightness of the superdislocations is an indication that cross-slip onto {001} has occurred to form Kear-Wilsdorf locks (Kear and Wilsdorf, 1962). This was by no means always the case, although some superdislocations on {001} planes were observed (fig. 5.2). A tilting experiment in the TEM (3.3.11) showed most of the superdislocations to be resident on {111} planes. It was also noted that dislocations in the hexagonal networks invariably adopted a straight screw orientation on {111} planes to minimise the network energy. The cross-slip necessary to produce these networks took place between {111} planes, rather than from {111} planes to {001} planes (fig. 4.25). It is concluded that no generalisation which states that straight screw superdislocations are locked onto {001} planes by the Kear-Wilsdorf mechanism can be made because such dislocations have been observed on {111} planes.

As stated, slip most commonly occurred on {111} planes in γ'. However, cross-slip from {111} planes to {001} planes has been cited many times to explain the unusual work-hardening characteristics of γ' strengthened alloys (for a review see Pope and Ezz, 1984). Cross-slip onto {001} was seen to occur during the deformation and annealing of alloys A, D and G. Figure 5.2 shows the dislocations at A have {111} slip traces while those at B could have {100} slip traces. Observations of {001} slip traces were unusual and it was concluded that most of the superdislocations were on {111} planes. It appeared that cross-slip usually occurred between different {111} planes rather than from {111} onto {001} planes. Very few superdislocations were observed on {001} planes, so it was assumed that Kear-Wilsdorf locking (Kear and Wilsdorf, 1962) was insignificant in specimens annealed at 1173K.

5.2.2 Dipoles in annealed microstructures

Analysis of dislocation pairs which exhibited a change in spacing

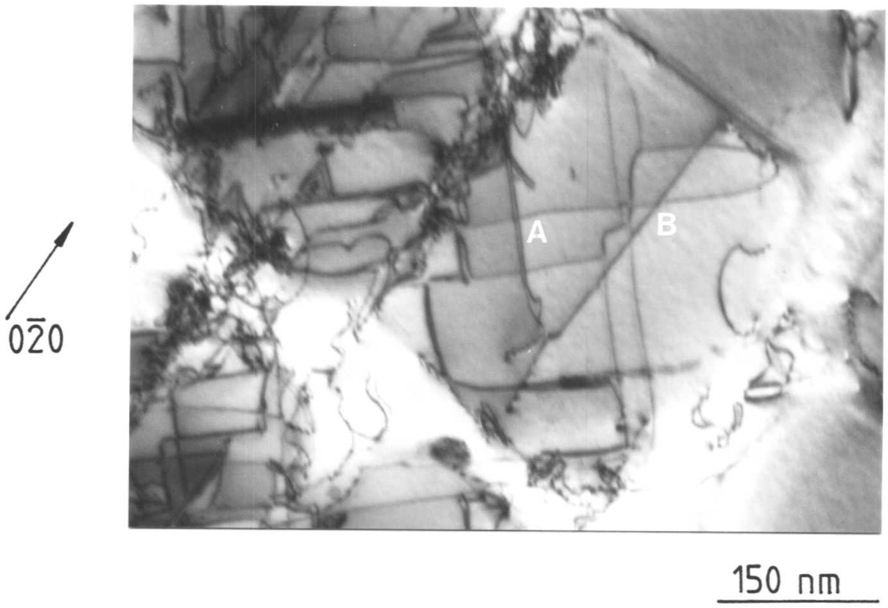

Fig. 5.2. Bright field TEM micrograph showing superdislocations lying on $\{111\}$ (A) and possibly $\{001\}$ (B) planes in γ'. (foil normal: ~[001]).

when g was reversed were all found to have the image characteristics of dipoles rather than the dissociated APBs suggested in 3.3.8. This was expected as the dissociation shown in figure 3.9 is extremely unlikely to occur as it would require opposite dissociations for each $a/_2$<110> dislocation.

TEM micrographs of dipoles are shown in figure 5.3. It is thought that each of the lines forming the image is a superdislocation. Dipoles are of no direct relevance to the calculation of defect energies but they must be distinguished from superdislocations to prevent misinterpretation of the dislocation images. It is interesting to consider how the dipoles may have been formed. Two methods are to be considered: the first based on the mechanism of Johnston and Gilman (1960) and the second based on the mechanism of Tetelman (1962). Both were proposed to explain dipole formation in disordered structures. These proposals have been developed to explain dipole formation in $L1_2$ structures.

Johnston and Gilman suggested that an undissociated screw dislocation (AB fig. 5.4a), travelling in its own glide plane, may become jogged either by interaction with another dislocation (Cottrell, 1953) or by cross-slip. If the jog formed is more than one atomic spacing high, the jogged section CD (figure 5.4b) will be sessile on the glide plane. Movement of AB will then drag out a pure edge dipole (fig. 5.4c) behind the gliding screw. Under certain circumstances cross-slip may subsequently occur to produce an edge dislocation loop in the unfaulted crystal (fig. 5.4d). If the dislocation is a screw superdislocation, the same type of process would occur as shown in figure 5.5. The defect produced would be a pure edge superdislocation dipole (fig. 5.5c) which may part to form a superdipole loop. As shown in figure 5.5(e), the region between the $a/_2$<110> dislocation loops would be an APB. This mechanism of loop formation was observed in this investigation. Figure 5.6 shows a TEM micrograph of a pure screw superdislocation which is trailing a line

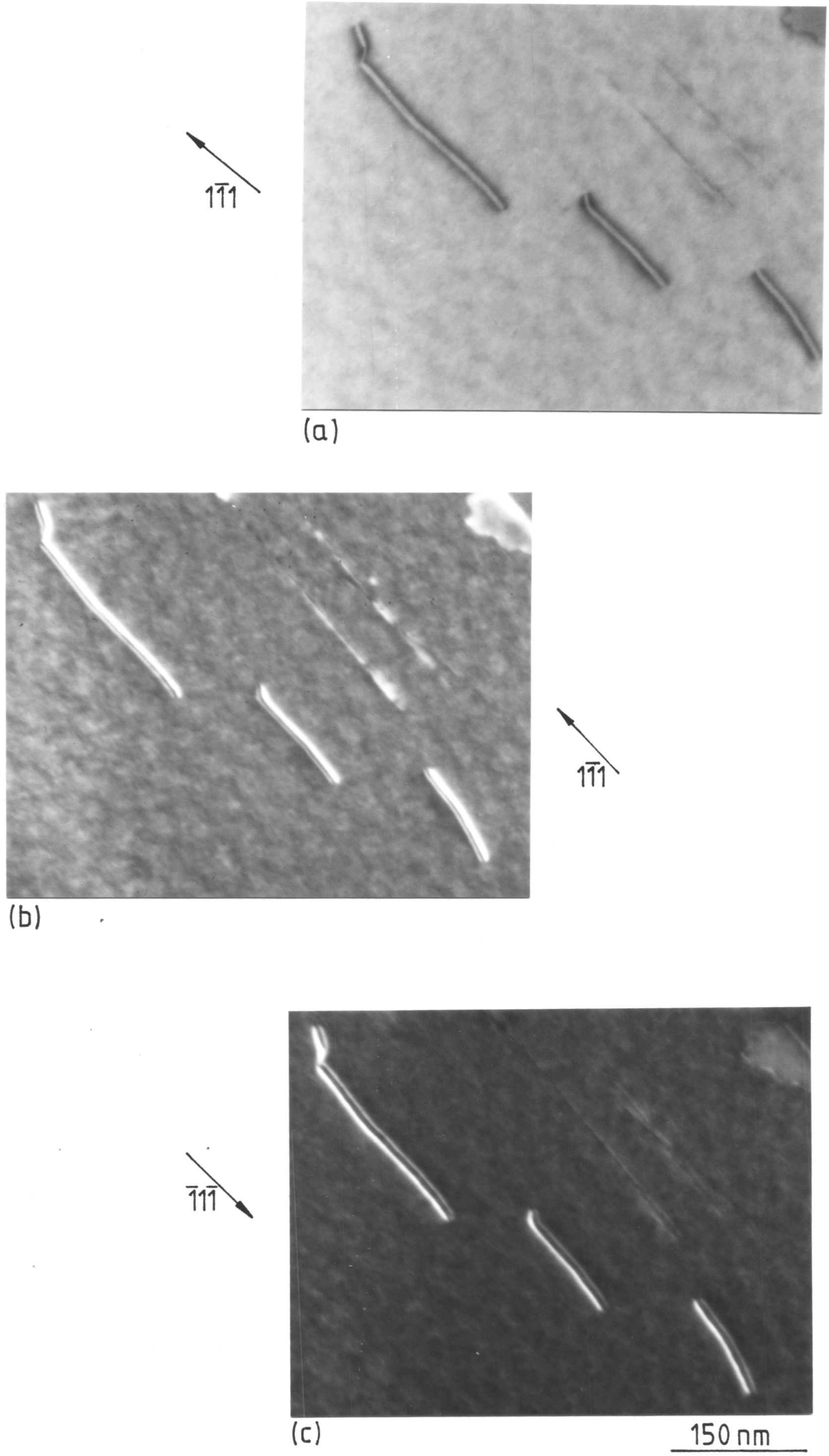

Fig. 5.3. TEM micrographs in bright field (a) and $W_{(g,3g)}$ weak beam dark field (b and c) showing possible superdislocation dipoles. The weak beam micrographs show the change in spacing on reversing $\underline{g}$. Note there is a large difference in image intensity between the dislocations bounding the APB. See text for details. (foil normal: ~[111]).

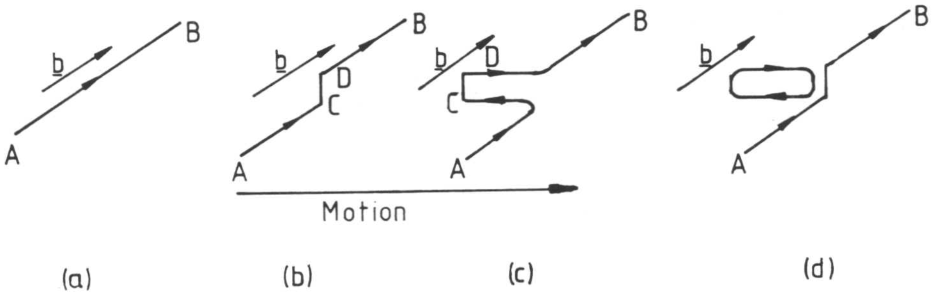

Fig. 5.4. Formation of an edge dipole from a jog on a screw dislocation (b). The jogged segment CD is dragged out to form a dipole (c) which may be pinched off to form a dislocation loop (d).

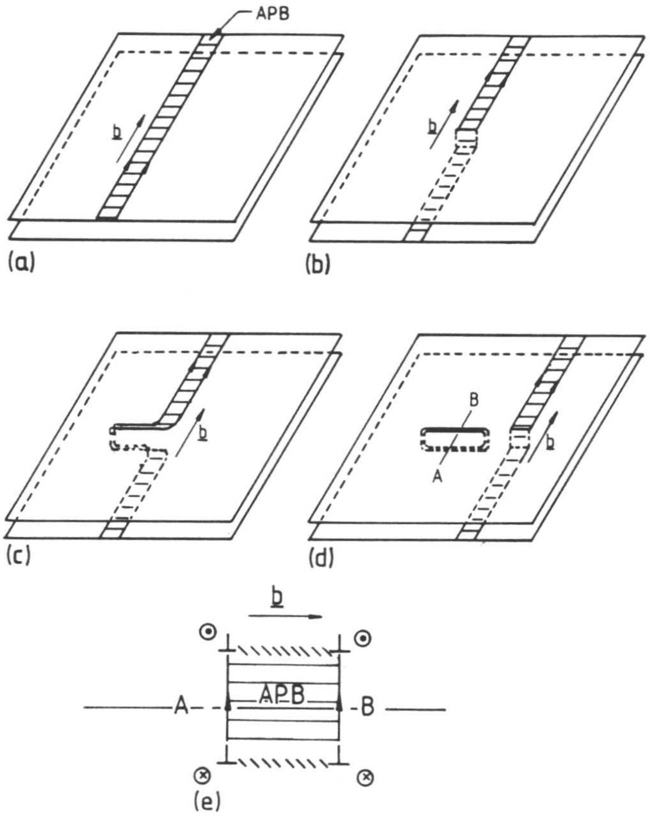

Fig. 5.5. Formation of an edge superdipole by the formation of a double jog in a superdislocation (b). An edge superdipole of APB is dragged out behind the superdislocation (c), which can pinch off to form an APB loop (d). A section through the APB loop along AB is shown in (e).

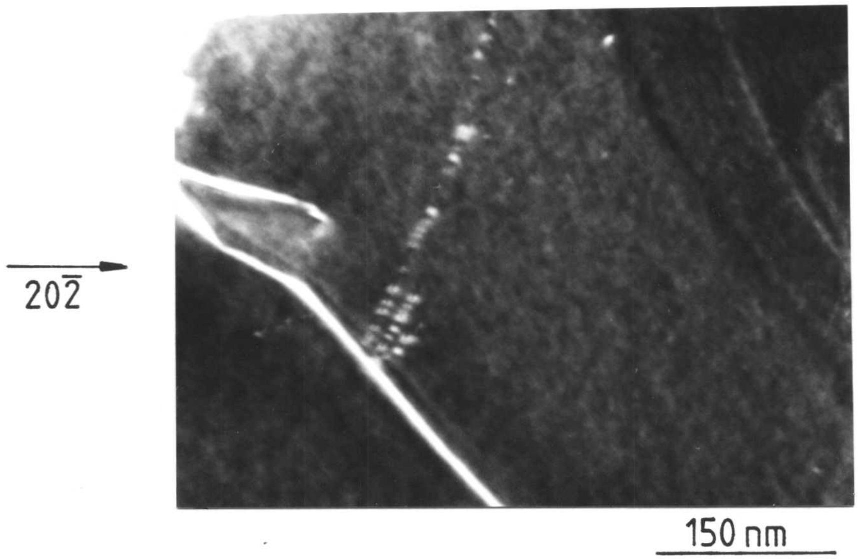

Fig. 5.6. $W_{(\underline{g},3\underline{g})}$ weak beam dark field TEM micrograph of an APB trailing a line of small dislocation loops. (foil normal: ~[111]).

of small dislocation loops behind it. However, the Johnston and Gilman mechanism predicts that the trails behind a moving screw dislocation will always be pure edge. While these were often observed, many dipoles (including that shown in figure 5.3) were of mixed character. A model for the formation of these dipoles has been proposed by Tetelman (1962).

Tetelman assumed that during shear deformation two mixed dislocations of equal and opposite Burgers vector may intersect while gliding on parallel {111} planes, as shown in figure 5.7(a). These two dislocations may lower their total energy by reorientation in the same glide plane (fig. 5.7b). If cross-slip occurs at the cross-over point, the sum of the dislocations will be zero and a dipole will form as shown in figure 5.7(c). If the opposite end also cross-slips, as shown in figure 5.7(d), a dipole is created. This model provides an explanation for the occurrence of mixed dislocation dipoles. The model can also be extended to ordered materials as shown in figure 5.8. The initial interaction for this reaction is similar to the mechanism proposed for the creation of hexagonal networks (fig. 4.15). Limited cross-slip must occur at the cross-over points before the superdipole can form. As in the previous case the region between the two $a/_2$<110> dislocation loops would contain APB.

Superdipoles of pure and mixed character can be generated by these two mechanisms. In each case they will consist of a loop of APB between $a/_2$<110> dislocations. Superdipoles are low energy configurations and it is expected that they will be sessile.

The interaction of two superdislocations to form a jog which could form a superdipole (fig. 5.5) will only occur if one of the superdislocations is stationary at the moment of intersection. If, for any reason, both superdislocations are moving the jogged superdislocation will form an APB tube when it glides away from the intersection. The result is shown in figure 5.9. This process was proposed by Vidoz and Brown (1962)

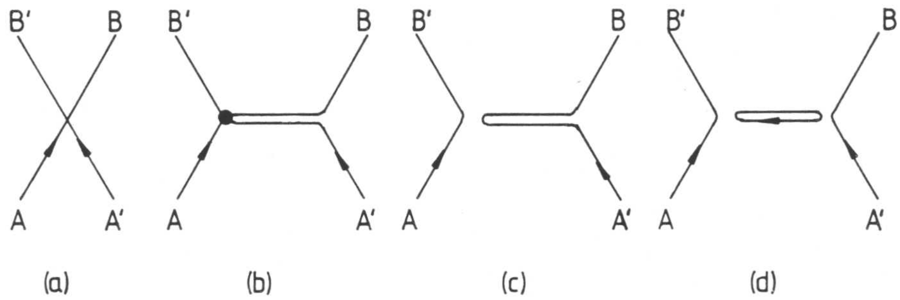

Fig. 5.7. Formation of a dipole by the interaction of two similar dislocations AB and A'B' (a). The dislocations lower their energy by reorienting to form a region with equal and opposite parallel Burgers vectors (b). This region may pinch off at ● to form a dipole (c), which may then pinch off to form loop (d). (After Tetelman, 1962.)

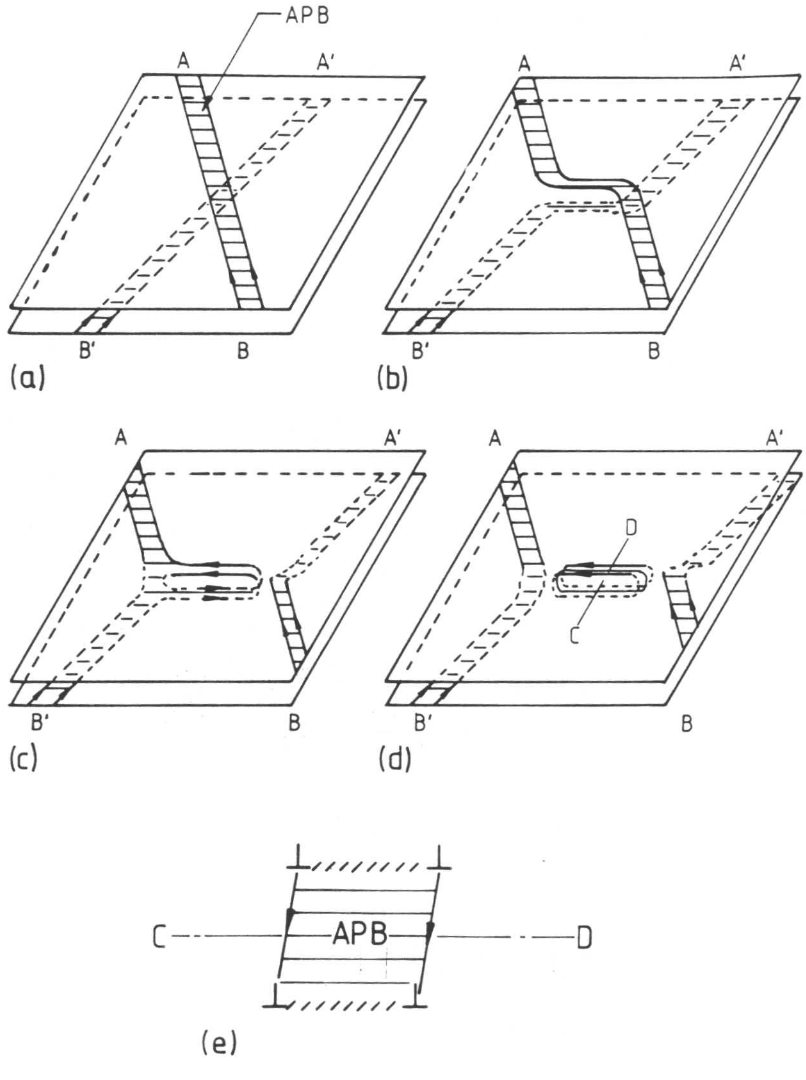

Fig. 5.8. Formation of a superdipole loop from an interaction between two superdislocations (a), showing reorientation to lower the configuration energy (b), cross-slip to form a superdipole (c) and further cross-slip to produce a superdipole loop (d). The loop is shown in section along CD (e).

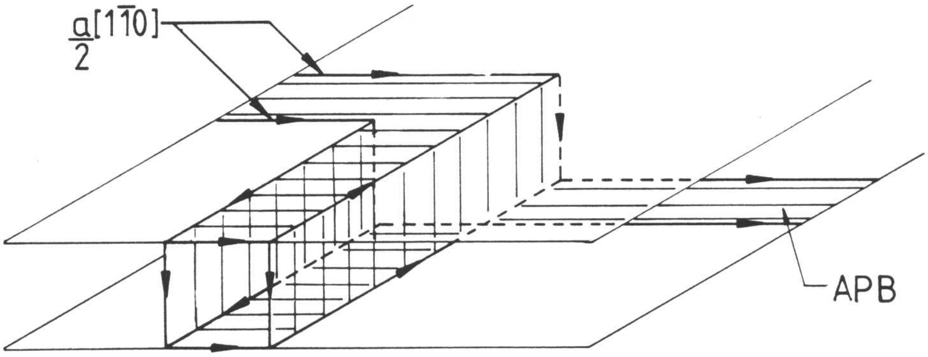

Fig. 5.9. Illustration showing an APB tube which will form if both superdislocations are gliding at the time of interaction.

and has been cited as a strengthening mechanism in $L1_2$ structures (Kear, 1966). At present, there is little evidence for the existence of APB tubes. Chou, Hirsch, McLean and Hondros (1982) claim to have observed APB tubes in Ni_3Al. The tubes gave strong contrast in superlattice weak beam imaging conditions but no contrast was observed in fundamental weak beam imaging conditions. The defects observed in this investigation showed strong dislocation contrast in fundamental weak beam and superlattice weak beam imaging conditions. They were assumed to be superdipoles rather than APB tubes.

The superdipoles observed exhibited unusual dislocation contrast in weak beam micrographs as shown in figure 5.3(b) and (c). These micrographs show that the dislocations at the edges of the defects exhibited a large difference in intensity. The difference was judged to be much greater than that from a superdislocation in the same imaging conditions. It is proposed that figure 5.3 shows a superdipole observed along one of its edges, thus, only two dislocation images were seen, and the change in image intensity was caused by the extra layer of APB and the occurrence of one dislocation directly above another (fig. 5.5e and 5.8e).

Dislocation loops and dipoles have previously been reported in $L1_2$ structures by Kear (1966), Staton-Bevan and Rawlings (1975a) and Baldan (1983). Baldan has drawn similar conclusions to those drawn from this investigation.

In summary, it has been shown that the established techniques for the generation of dipoles in disordered crystals can be adapted to explain the occurrence of dipoles in $L1_2$ ordered crystals. It is proposed that both the Johnston and Gilman and Tetelman models operate to produce sessile superdipoles of all characters. Unusually, screw dipoles were observed. In disordered materials these would anihilate by cross-slip but in γ' they were stabilised, probably by the APB regions. The loops and dipoles will hinder the movement of other superdislocations and may generate more jogs and produce more dipoles when intersected by gliding dislocations. This process was suggested by Thornton, Davies and Johnston (1970) to explain the work hardening of superalloys by what they termed 'debris hardening'.

5.2.3 Large planar defects

Large planar defects of the type shown in figure 5.10 were observed in foils cut on (111). $\underline{g}\cdot\underline{b}$ analyses coupled with line vector determination and fault contrast studies have shown that defects exhibit the contrast expected from extrinsic superlattice stacking faults lying parallel to the plane of the foil. The faults were bounded by a loop of $a/_3\langle 211\rangle$ dislocation (fig. 5.10), showing that they were formed by a shear process and not by the agglomeration of vacancies or interstitial atoms. The latter processes would produce an $a/_3\langle 111\rangle$ bounding dislocation.

Superlattice stacking faults of this type have been frequently observed in $L1_2$ for example by Enami and Nenno (1968), Giamei, Oblak, Kear and Rand (1970), Oblak and Kear (1971), Takeuchi et al. (1973), Howe et al. (1974), Pak, Saburi and Nenno (1976) and Suzuki et al. (1979). All these workers report that the majority of the defects observed were intrinsic. The dislocation line vector was determined for all the SSFs analysed in this investigation and it was shown that the majority of faults were extrinsic. A possible reason for this discrepancy is given below.

This type of planar defect can be formed by the following mechanism proposed by Suzuki et al. (1979). The mechanism is inaugurated by the immobilisation of one, usually the trailing one, of the $a/_2\langle 110\rangle$ dislocations forming the superdislocation. Takeuchi and Kuramoto (1973) suggested that this could occur by the cross-slip of a short segment of dislocation onto an {001} plane. Alternatively the trailing dislocation may become jogged while the other does not. Whatever the reaction, a part of the trailing

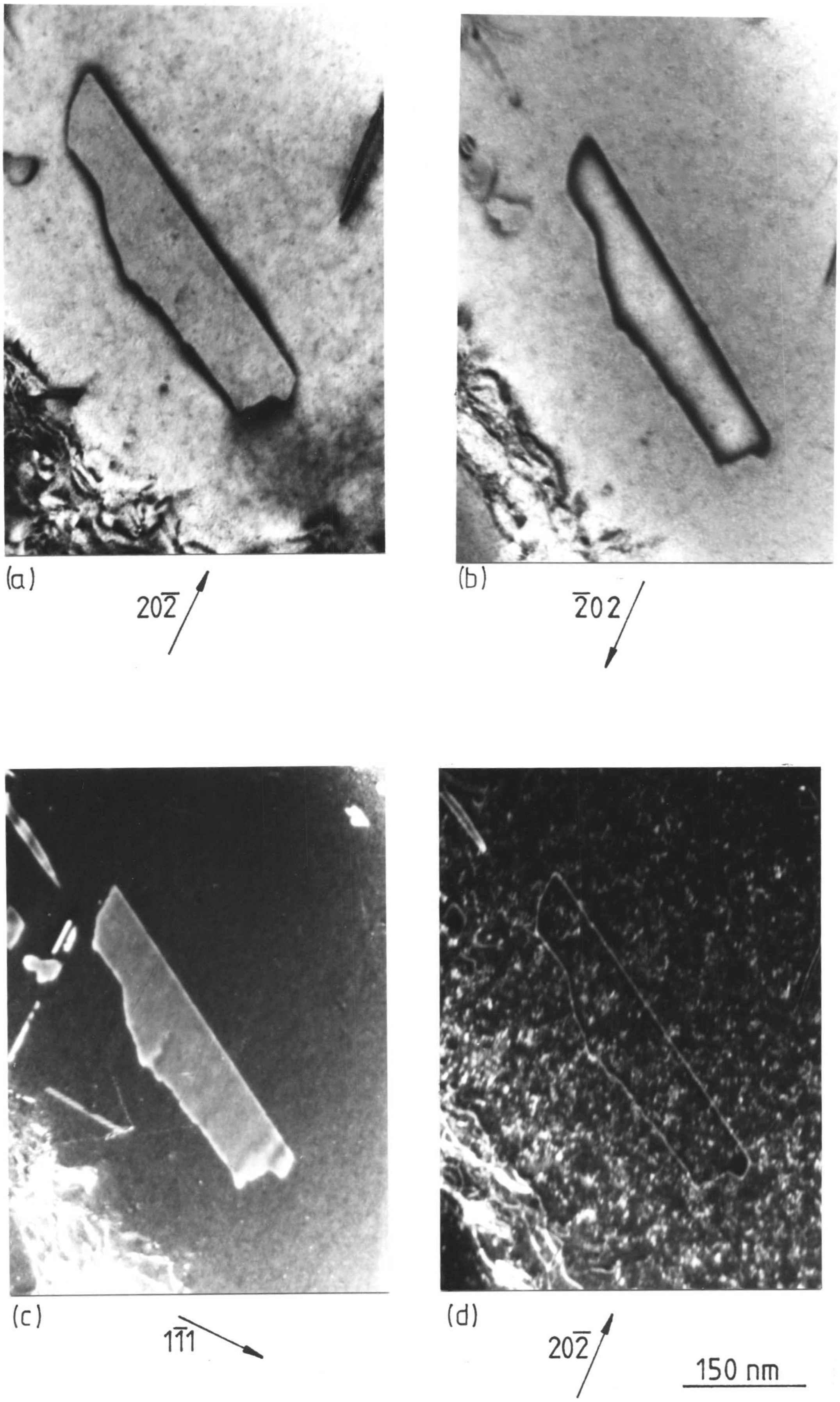

Fig. 5.10. Bright field TEM ±g pair (a and b) and two $W_{(\underline{g},3\underline{g})}$ weak beam dark field TEM micrographs showing a large SESF. (a) and (b) show that the SESF is bounded by a dislocation loop; in this case an $a/_3[11\bar{2}]$ shear dislocation which is shown in (d). Contrast from the fault lying parallel to the foil surface is shown in (c). (foil normal: ~[111]).

dislocation becomes pinned, the leading dislocation glides on extending the APB (fig. 5.11a). Suzuki et al. suggest that the extension of the APB was aided by the line tension of the superdislocation attempting to straighten itself; otherwise the force required to separate the superdislocation would be too large for the reaction to occur. After a certain extension it becomes energetically favourable for the APB to transform to an intrinsic or extrinsic SSF by nucleating an $a/_6\langle 211\rangle$ dislocation loop or by the splitting of the bounding $a/_2\langle 110\rangle$ dislocation into an $a/_3\langle 211\rangle$ partial and an $a/_6\langle 211\rangle$

e.g. $$a/_2[10\bar{1}] = a/_3[11\bar{2}]+a/_6[1\bar{2}1] \qquad \text{eqn. 5.1}$$

The superdislocation must continue to glide forward dragging out an SSF bounded by by an $a/_3\langle 211\rangle$ partial dislocation which is apparently locked in position by the Kear-Wilsdorf mechanism (fig. 5.11b) (Pak et al., 1976). To form the defect shown in figure 5.10 the fault would need to be pinched off at some point (fig. 5.11c).

Many SESF defects of this type were observed in deformed and annealed foils of alloy A, while very few were seen in alloys D and G. It is proposed that formation of a very thin layer of Ni_3Ti occurs at this type of defect thus promoting the formation of defects with extrinsic characteristics rather than those with intrinsic characteristics observed by other workers. This is possible because SESFs are equivalent to seven layers of the hexagonal Ni_3Ti structure (4.2.4). Titanium may diffuse to the faults and stabilise them by forming a very thin layer of Ni_3Ti. (Heterogeneous precipitation of Ni_3Ti on stacking faults has previously been reported in the Ni-base alloy Nimonic 901 by Oblak, Owczarski and Kear (1971).) The formation of Ni_3Ti on the fault plane would effectively pin the $a/_3\langle 211\rangle$ dislocation. It could also aid fault growth by assisting the passage of the leading dislocation. If this mechanism does operate it could be significant that the lower titanium alloy contains fewer defects. The likelihood of this pinning mechanism occurring and its effect on the SSF

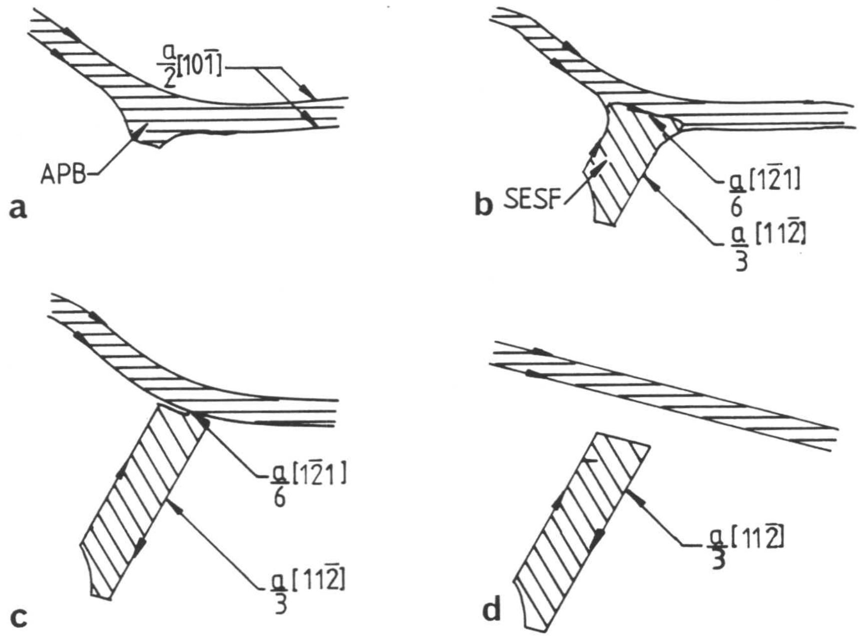

Fig. 5.11. Schematic illustration showing the proposed mechanism for the formation of a large SESF from a moving superlattice dislocation. See text for details. (After Suzuki et al., 1979).

energies are discussed in 6.3; its effect on the deformation mechanism is discussed in chapter 7.

Because these defects were locked in a metastable condition it was impossible to use them to evaluate the SSF energies. It is expected that defects of this type will slow the passage of superdislocations through the γ' and thereby assist the strengthening of the material.

5.3 Rectangular Networks formed by Dislocations with Burgers Vectors which Intersect at 90°

5.3.1 Theoretical arrangement

Rectangular or square networks will occur in $L1_2$ when two different screw superdislocations with perpendicular Burgers vectors intersect on the same or different {111} planes. The networks formed will appear rectangular on both {001} and {111} planes as shown in figure 5.12. No interaction can occur between perpendicular dislocations to form SSFs but it is possible for the APB fault vectors to cancel out to produce an area of unfaulted crystal.

5.3.2 Square networks on {111}

Square and rectangular networks have been frequently observed in the γ' of alloys A-G by TEM. Stereo pairs have produced qualitative evidence for the existence of two different rectangular networks. One which has a stepped configuration is discussed below; the other, which is coplanar, is discussed in 5.3.2.

Analysis of the dislocations constituting the square network shown in figure 5.13 shows that the network was formed by an interaction between $a[1\bar{1}0]$ screw superdislocations on $\{11\bar{1}\}$ and $a[110]$ screw superdislocations on $\{1\bar{1}1\}$. No dissociation of the $a/_2\langle110\rangle$ dislocations constituting the superdislocations was observed and was therefore assumed to be negligible.

The interaction occurred by the passage of one $a/_2\langle110\rangle$ dislocation

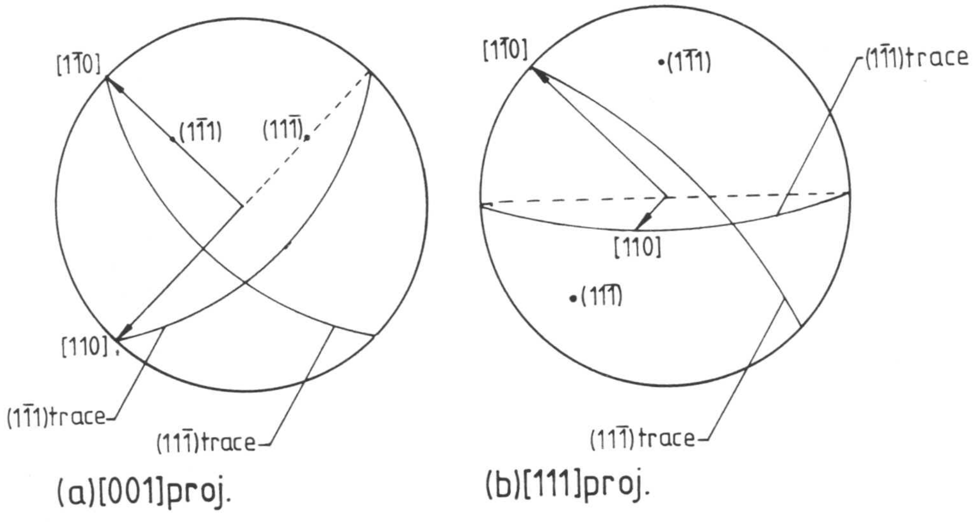

Fig. 5.12. Stereographic projections on [001] (a) and [111] (b) showing that screw dislocations with Burgers vectors at 90° produce networks which appear square or rectangular in both [001] and [111] TEM foils.

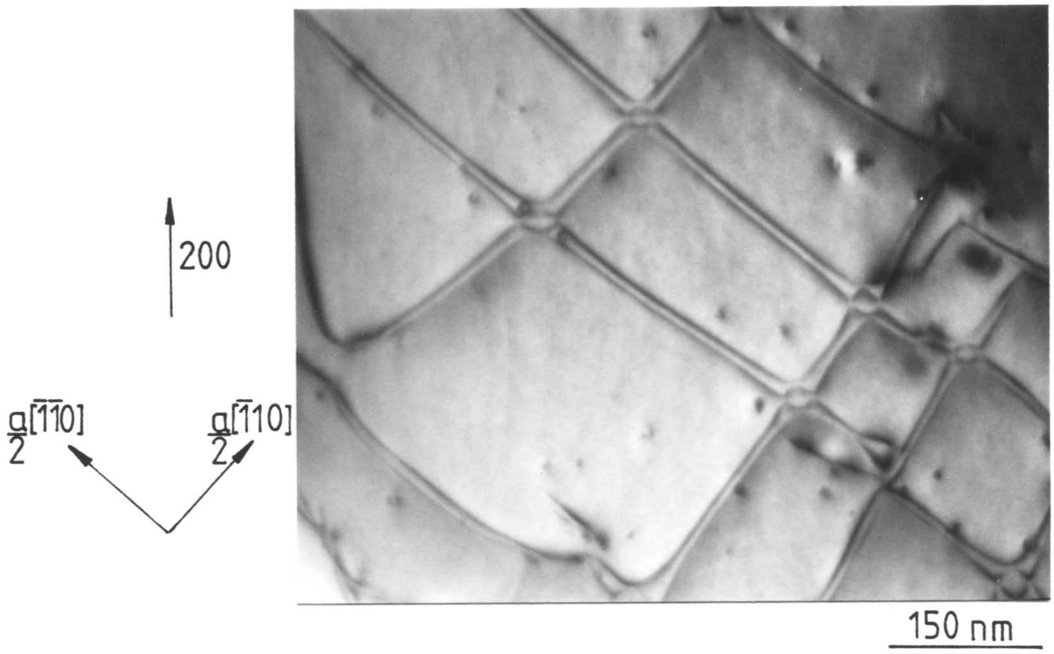

Fig. 5.13. Bright field TEM micrograph of a rectangular network of pairs of $a/_2[\bar{1}\bar{1}0]$ and $a/_2[\bar{1}10]$ dislocations on different {111} planes. (foil normal: ~[001]).

which created an APB; the next dislocation to pass will be perpendicular to the first and will destroy the APB, producing an unfaulted region. The unfaulted region (marked A on figure 5.14) must be a non-planar saddle point with the APBs on either side twisted slightly from their glide planes as shown in figure 5.14(b). Region A is perfectly stacked and as such is more stable than the APB so the region A will extend as much as possible to reduce the network energy. This explanation would produce the structures observed in deformed and annealed specimens (fig. 5.13).

It is probable that the interaction described above could only take place at high temperature when the dislocations are very mobile. Because the unfaulted region is formed the configuration will become sessile once formed, particularly when the temperature is lowered, thus explaining the large number of experimental observations of this unusual network. The stepped square networks observed had a large mesh size which allowed the superdislocations to adopt their equilibrium spacing on the {111} glide plane, there not being enough of a driving force to make cross-slip onto the lower energy {001} planes favourable. APB energies for pure screw dislocations were determined from portions of superdislocations well away from the points of intersection, thereby avoiding any change in dislocation spacing caused by the unfaulted region (6.2).

5.3.3 Square networks on {001}

Co-planar square dislocation networks were observed on (001) planes in foils with [001] normals (fig. 5.15). These networks were meshes of a[110] and a[$1\bar{1}0$] screw superdislocations on [001].

As described in 5.3.2 an unfaulted region is created as shown on an [001] section through $L1_2$ in figure 5.16. The unfaulted region on [001] expanded until equal amounts of APB and unfaulted region constituted the network (fig. 5.14a). Because of the considerably lower APB energy on {001} planes the $a/_2$<110> dislocations are not so tightly constrained as those on {111} planes; consequently the unfaulted regions grow considerably larger

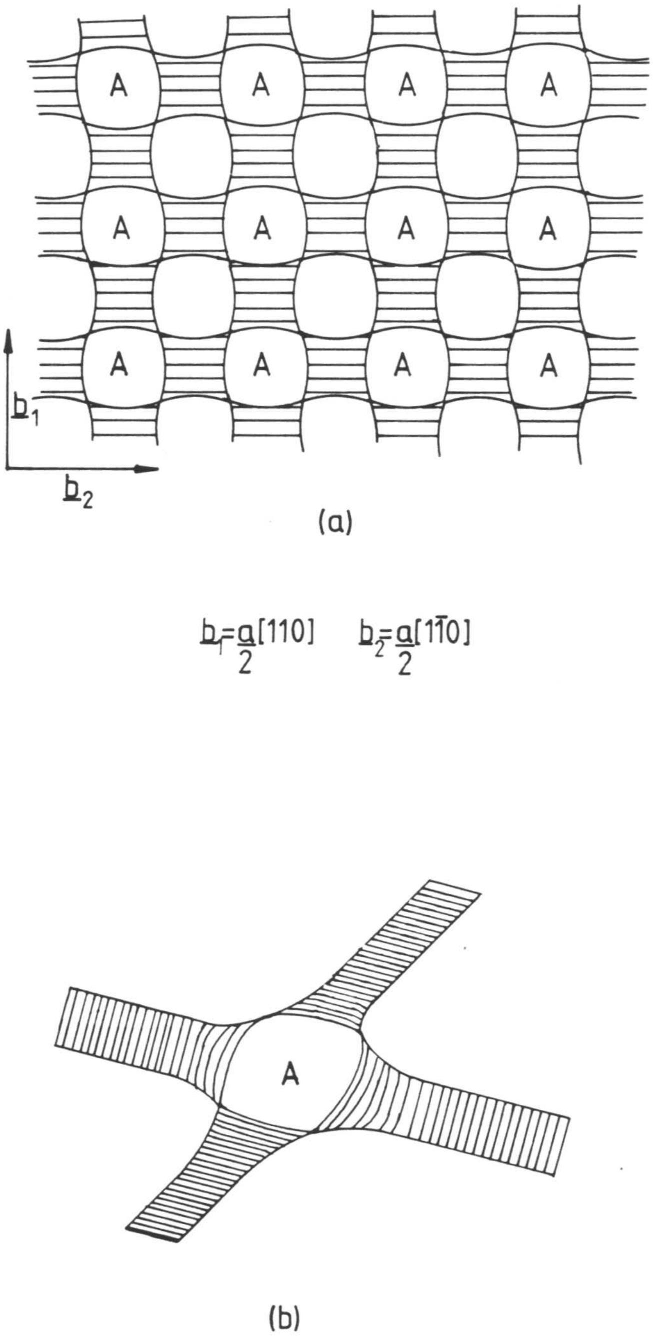

Fig. 5.14. Schematic diagrams showing plan view of a square network (a). If the network lies on two {111} planes the unfaulted region (A) is an unfaulted non-planar saddle point (b). See text for details.

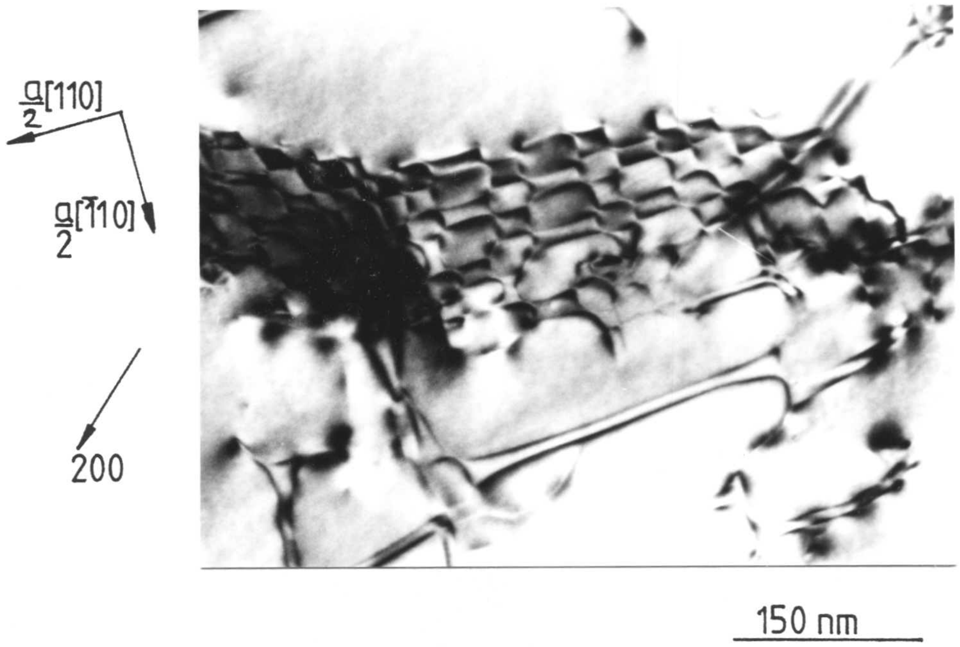

Fig. 5.15. Bright field TEM micrograph showing a square network of screw dislocations on (001). (foil normal: ~[111]) .

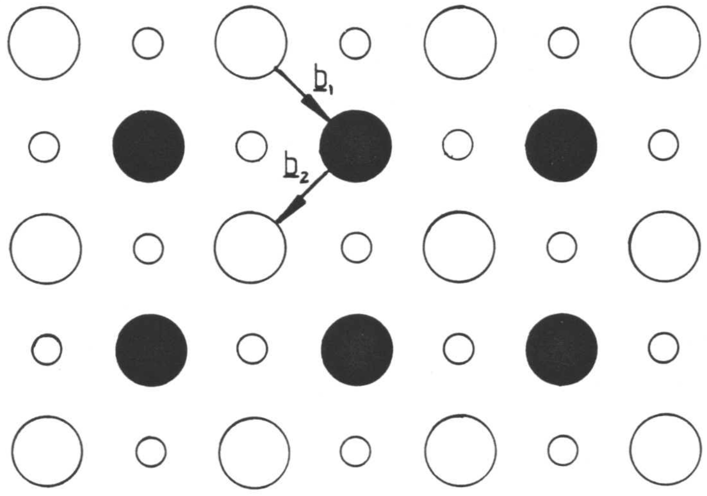

Fig. 5.16. Plan view of (001) planes in L1$_2$ shwoing that the passage of a single $a/_2[\bar{1}10]$ dislocation will create an APB, but that the passage of $a/_2[110]$ will restore perfect stacking to form the unfaulted region shown in figure 5.14.

$b_1 = a/_2[\bar{1}10]$, $b_2 = a/_2[110]$.

than those on {111} planes. This network is very similar to that proposed by Czernickow, Gudas, Marcinkowski and Weng Feng Tseng (1971). Once the configuration has achieved its lowest energy configuration with approximately equal areas of APB and unfaulted crystal it will be effectively sessile.

Networks on {001} may be formed either by glide of screw superdislocations on {001} or by cross-slip from {111}. The first mechanism seems highly unlikely due to the difficulty of slip on the non-close packed {001} planes (as stated in 4.3.2). It seems more likely that the networks are created by cross-slip of the {111} networks. {111} networks obviously have a high energy due to the non-planar APBs and saddle points. At the annealing temperature the $a/_2$<110> dislocations will be constricted so they will provide little barrier for cross-slip to {001}. Cross-slip from {111} to {001} in $L1_2$ alloys was first suggested by Kear (1966).

If the activation for cross-slip is overcome, networks on {001} can form as shown schematically in figure 5.17. Limited glide will occur on {001} to equilibrate the structure to that shown in figure 5.15. It is proposed that the cross-slip of {111} networks onto an {001} plane will occur more readily for fine mesh networks than for coarse mesh networks. The superdislocations in the fine mesh networks on {111} planes are distorted and cannot adopt an equilibrium configuration on the initial glide plane. This distortion may provide some of the driving force for cross-slip onto {001} planes.

The mesh size of {001} networks was too small for the APB regions to adopt an equilibrium spacing between the unfaulted regions: consequently accurate dislocation spacings could not be measured, thus precluding the evaluation of the {001} APB energies.

5.4 Discussion and Conclusions

The dislocation interactions discussed in this chapter are less significant to the calculation of defect energies than the supernodes

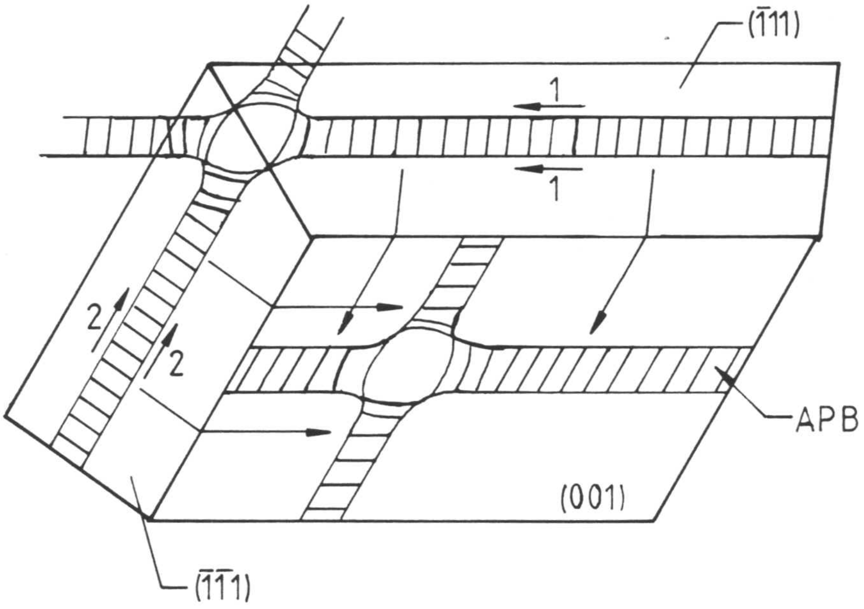

$$1=\frac{a}{2}[110] \qquad 2=\frac{a}{2}[1\bar{1}0]$$

Fig. 5.17. Schematic illustration showing cross-slip from a square network on {111} planes to form a square network on [001].

reported previously. However, many APB energy measurements were made from isolated superdislocations and rectangular superdislocation networks, and the identification of dipoles meant that no incorrect dislocation spacings were measured, thus avoiding spurious APB energy results.

Some authors have suggested that the interactions reported here are of considerable significance to the strengthening of superalloys. Thornton et al. (1970) proposed that the glide of jogged superdislocations produced dislocation debris, such as loops, which they applied to explain the unusual work hardening characteristics of superalloy materials (Copley and Kear, 1967). There has subsequently been considerable controversy in the literature as to whether debris hardening is a significant strengthening mechanism. Staton-Bevan and Rawlings (1975a and b) found that their flow stress results correlated more closely with the mechanism proposed by Davies and Stoloff (1965) which is based solely on the traditional model for dislocation particle interaction where second phase particles pin the dislocations. More recently, Takeuchi and Kuramoto (1973) have introduced a third element into the work hardening model by proposing that cross-slip of short segments of one or both of the $a/_2\langle 110\rangle$ dislocations of a superdislocation onto {001} during deformation has a major strengthening role.

In complex superalloys with large volume fractions of γ' it is unrealistic to adopt the premise that only one dislocation interaction or strengthening mechanism is effective. In this investigation it was noted that dislocations generated in the γ have great difficulty entering the γ' without dislocation climb occurring, showing that a significant strengthening effect is being produced by the Davies and Stoloff (1965) model. It was also noted that once inside the γ' dislocation interactions occurred to form networks which will further act to provide strength by reducing dislocation motion. Dislocation 'debris' in the form of loops and dipoles was also produced showing that the model of Thornton et al. (1970) was also operative. Large flat stacking fault defects were also observed. It is likely that these occur as a consequence of the slip of small segments of dislocation onto {001} as proposed by Takeuchi and Kuramoto (1973). It is almost certain that all three of these mechanisms will play some role in the strengthening of alloys A to G.

In addition to these established strengthening mechanisms it is proposed that a further mechanism may be having some effect. The large flat extrinsic stacking faults reported in 5.2.3 have the $DO_{24}(Ni_3Ti)$ structure: it is thought that during creep deformation enough time would be available for the diffusion of Ti to the fault and the formation of a very thin planar precipitate of Ni_3Ti. This precipitate will strengthen the alloy by pinning or obstructing the passage of superdislocations. It was noted that the higher Ti containing alloy (A) contained more planar faults than either of the other alloys, indicating that if Ti is stabilising the SSFs, the effect is stronger at higher Ti contents. This effect is discussed more fully with reference to diffusion data, stress rupture data from alloys A, D and G, and SSF and APB energy measurements from hexagonal networks in chapters 6 and 7.

CHAPTER 6

MEASUREMENT OF ANTI-PHASE BOUNDARY ENERGY AND SUPERLATTICE STACKING FAULT ENERGY

6.1 Introduction

This chapter presents the experimental techniques employed and the values obtained for the anti-phase boundary (APB) energies and superlattice stacking fault (SSF) energies of alloys A, D and G. The APB energies were determined from dislocation spacing measurements made on pure screw superdislocations. This is described in 6.2.1. The results are presented and discussed in 6.2.3.

The SSF energies were considerably more difficult to measure than the APB energies. Although it is known that the shear of gamma prime can occur by pairs of $a/_3\langle 211\rangle$ dislocations bounding ribbons of SSF (Kear et al, 1968), no evidence for this was found during this investigation. Consequently the SSF energies could not be determined by the same method as the APB energies. Instead hexagonal dislocation networks containing extended nodal points were produced by cold deformation and annealing (chapter 4.5). These extended supernodes (fig. 6.1b) were superficially similar to extended nodes in FCC materials (fig. 6.1a), but there were significant differences in the types of dislocations and faults present. Consequently the well established techniques of stacking fault energy measurements (for details see the reviews by Christian and Swann, 1965, Ruff, 1970, and Amelinckx, 1979) were found to be inapplicable to the evaluation of SSF energy from supernodes.

A new technique has been developed by Rae and Hillier (1984) in which the SSF energy can be evaluated from a supernode by calculating the

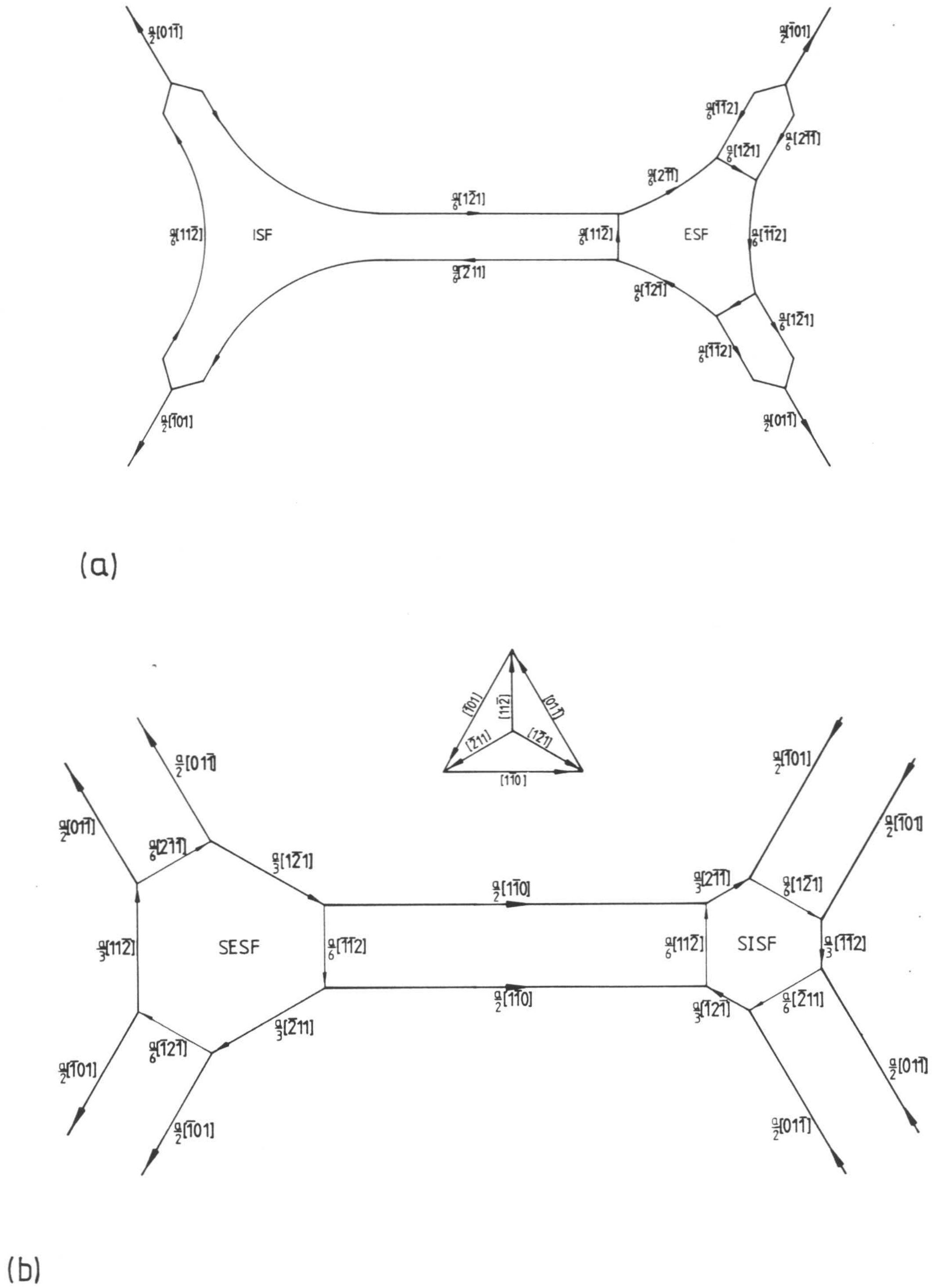

Fig. 6.1. Illustration showing an intrinsic and an extrinsic node in FCC (a) and in $L1_2$ (b).

force exerted on one dislocation by the stress fields of the other dislocations when the superdislocation spacing is known; this is described in 6.3.1. The method has been used to evaluate SSF energies in alloys A, D and G. These results are discussed in 6.3.4.

The significance of the results with respect to the creep behaviour of superalloys is discussed in chapter 7.

6.2 Anti-Phase Boundary Energy Measurement

6.2.1 Theory

The energy of an APB can be evaluated from the equilibrium spacing between the two bounding $a/_2\langle 110\rangle$ dislocations, since the repulsive force between the dislocations is balanced by the APB energy drawing them together.

According to Eshelby, Read and Shockley (1953) the non-vanishing stress components, σ_{ij}, on a straight dislocation in an anisotropic medium are:

$$\sigma_{\theta z} = \frac{c_{44} b}{2\pi\beta r} \qquad \text{eqn. 6.1(a)}$$

and

$$\sigma_{rz} = \frac{c_{44}}{2\pi\beta}\,\frac{b}{r}\,\frac{(1-\beta^2)\cos\theta\sin\theta}{(\cos^2\theta+\beta^2\sin\theta)} \qquad \text{eqn. 6.1(b)}$$

where

$$\beta^2 = 2c_{44}/(c_{11}-c_{12}) \qquad \text{eqn. 6.1(c)}$$

c_{ij} are the elastic constants, b is the magnitude of the dislocation Burgers vector, r is the distance from the dislocation and θ is the angle between the dislocation line vector, u, and the Burgers vector.

For a pure screw dislocation θ is zero; therefore $\sigma_{rz} = 0$, so the only stress component is:

$$\sigma_{\theta z} = \frac{b}{2\pi r}\left[\frac{c_{44}(c_{11}-c_{12})}{2}\right]^{\frac{1}{2}} \qquad \text{eqn. 6.2}$$

Consider the interaction between two parallel co-planar screw dislocations bounding an APB. A dislocation lying at the origin of a co-ordinate system along the z direction, as shown in figure 6.2, exerts a tangential shear stress, which is given by eqn. 6.2, on the APB plane if end effects are ignored. The force per unit length on a parallel screw dislocation at P(r,θ) is normal to $\sigma_{\theta z}$ and O, and is therefore along OP. It has the magnitude:

$$F = \frac{b^2}{2\pi r}\left[\frac{c_{44}(c_{11}-c_{12})}{2}\right]^{\frac{1}{2}} \qquad \text{eqn. 6.3}$$

where F is the force per unit length on the dislocation.

The energy of the APB, γ_A, between the dislocations can thus be determined by examining the work done on moving the dislocation δx

Equation 6.3 was used extensively to evaluate APB energies from superdislocation spacings measured from TEM micrographs.

Values for the elastic constants, c_{ij}, were supplied by Rolls-Royce Ltd. They were calculated from measured sound velocities in alloy A. As there are only small differences between alloy compositions and lattice parameters, these values have also been taken to be typical of alloys D and G. Unfortunately, no specific values of c_{ij} in γ' are available, but, as the alloys contain in excess of 0.6 volume fraction of γ', the bulk alloy values were considered acceptable for use in the calculation of APB energies. The c_{ij} values used were determined at 300K and could be in error by up to 10%. They were:

$c_{11} = 2.5\times10^{11}$ Pa
$c_{12} = 1.633\times10^{11}$ Pa
$c_{44} = 1.154\times10^{11}$ Pa

The anisotropy factor, $A = \dfrac{2c_{44}}{c_{11}-c_{12}} = 2.66$ eqn. 6.4

The only other available values for the elastic constants of γ' were published

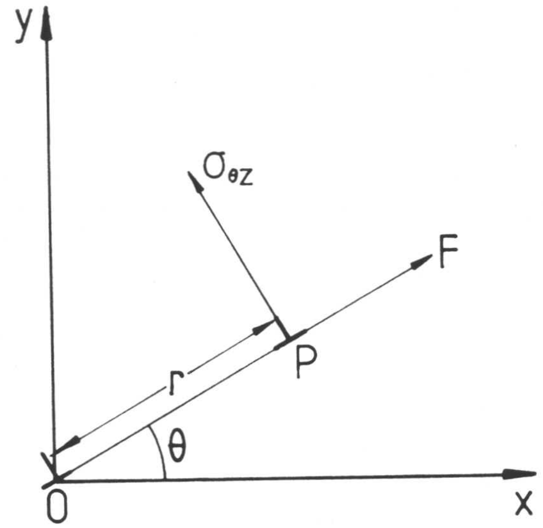

Fig. 6.2. Illustration showing the configuration used to determine the force between two $a/_2\langle 110\rangle$ dislocations (at O and P) bounding an APB as described in the text.

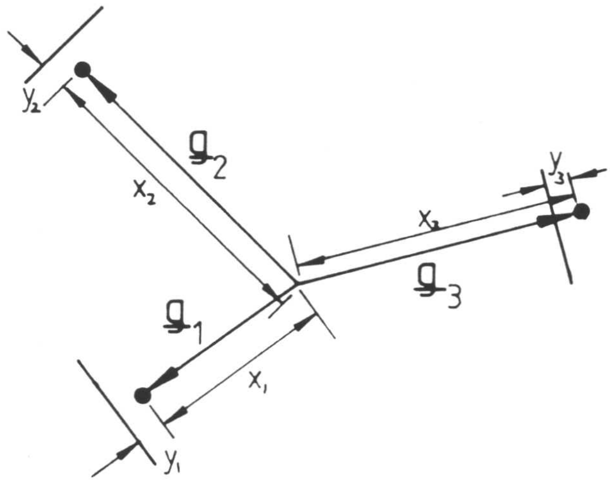

Fig. 6.3. Illustration showing the method used to evaluate the electron beam direction, $\underline{B}$, from a diffraction pattern with three identifiable reflections.

The beam direction

$$\underline{B} = \alpha_1|\underline{g}_1|^2(\underline{g}_2\mathrm{x}\underline{g}_3)+\alpha_2|\underline{g}_2|^2(\underline{g}_1\mathrm{x}\underline{g}_3)+\alpha_3|\underline{g}_3|^2(\underline{g}_1\mathrm{x}\underline{g}_2)$$

where $\alpha_i = \dfrac{(x_i+2y_i)}{x_i}$

by Ono and Stern (1969). For pure Ni_3Al containing less than 0.1% impurities, they found c_{11} and c_{12} to be about 20% lower and c_{44} to be the same as the values used in this investigation. This difference probably arises because they were studying an alloy with a smaller lattice parameter and lower density from the γ' in alloys A, D and G. Ono and Stern showed that the elastic constants do not vary significantly with temperature between 83K and 600K. As a result of this observation it was decided that it was reasonable to use the elastic constants measured at 300K to evaluate the APB energy at higher temperatures in the absence of any more detailed data.

6.2.2 APB energy measurement

To evaluate the APB energy it was necessary to measure the true dislocation spacing, r, and to identify the bounding dislocations. The Burgers vectors were obtained by using the TEM techniques described previously (3.3.5): for dislocations separating APB from unfaulted crystal they are $a/_2\langle 110\rangle$. The magnitude of b calculated using the average lattice parameter of alloys A, D and G (table 2.4) is 0.253nm.

In most cases the anti-phase boundary plane was at an angle to the electron beam direction, $\underline{B}$. Consequently, the measured superdislocation spacing, m, was only an apparent value. To evaluate the true spacing, r, the electron beam direction, $\underline{B}$, and the plane normal of the superdislocation, $\underline{N}$, are required in addition to the dislocation line vector, $\underline{u}$. $\underline{B}$ was evaluated following the technique described by Ryder and Pitsch (1968) which is shown in figure 6.3. $\underline{N}$ was found by the trace analysis of dislocation pairs and stereo imaging. In some cases tilting experiments were also employed.

Simple geometry was then used to find r. Figure 6.4 shows that:

$$r = \frac{m}{\sin\theta} \qquad \text{eqn. 6.5(a)}$$

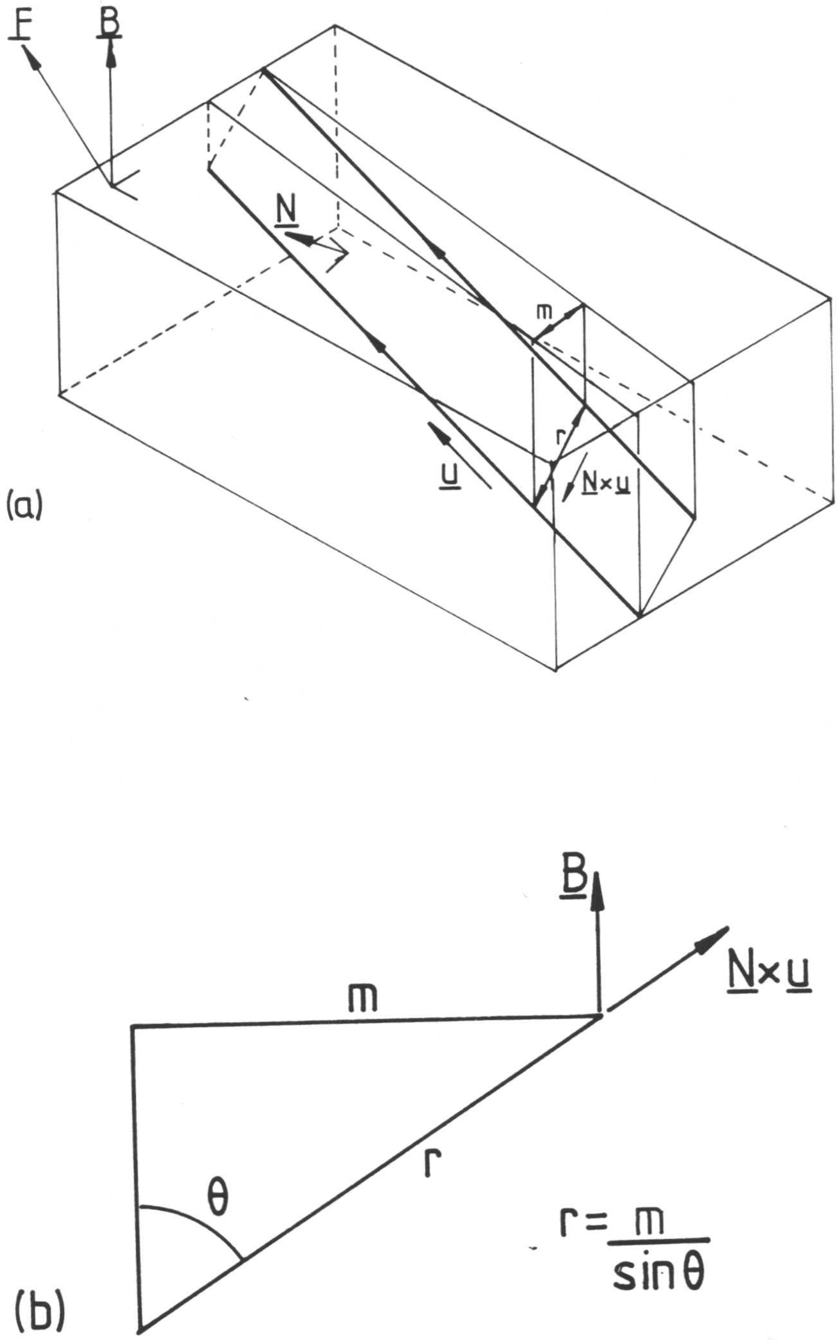

Fig. 6.4. Illustration showing the method used to evaluate the true spacing, r, of a superdislocation from the apparent dislocation spacing, m. B is the electron beam direction, N is the APB normal, u is the dislocation line sense and θ is the angle between B and Nxu. A schematic representation of the APB in the foil is shown in (a) and the geometrical configuration is shown in (b).

where

$$\sin\theta = \underline{B}\times(\underline{N}\times\underline{u}) \qquad \text{eqn. 6.5(b)}$$

and $\underline{B}$, $\underline{N}$ and $\underline{u}$ are unit vectors. This value of r was substituted in eqn. 6.3 to evaluate the APB energy.

6.2.3 Results and discussion

The APB energy results are shown in figure 6.5. The individual true dislocation spacings and APB energy values from each of the analysed networks are presented in appendix E. The results are summarised in table 6.1 which shows that the average APB energy for alloys A, D and G is $83\pm20\,\mathrm{mJm}^{-2}$.

There appears to be no significant variation in the APB energy of γ' with titanium content in single crystal superalloys containing between 1.8 and 2.7 at.% titanium. There is, however, a large range of APB energies for each alloy. No obvious reason was found for this range which amounted to a difference of about 6nm in dislocation pair spacing between the lowest and the highest values. This is considerably greater than the maximum error in spacing measurement. One explanation is that it may be related to the behaviour of the dislocations during cooling of the specimens after annealing. The specimens were air cooled from 1173K and it is suggested that some glide of the dislocations bounding the APBs may have occurred in an attempt to maintain the equilibrium spacing at lower temperatures. It is thought that cooling was too rapid for the respacing to have a major effect on the APB energies; if there was any effect it would act to produce a slightly higher APB energy than that at 1173K because a smaller dislocation spacing was expected at room temperature. The possibility of the contraction of superdislocations means that it is impossible to relate the measured energies to a particular temperature but it is assumed that the values are typical of 1173K as any movement of the dislocations will have been limited by the more stable parts of the networks.

Table 6.1. Summary of the Anti-phase Boundary Energies

	Alloy		
	G	D	A
γ' Ti content (at.%)	2.8	3.3	3.9
Mean APB energy (mJm^{-2})	87	78	83
Overall mean APB energy (mJm^{-2})		83	
Standard deviation (mJm^{-2})	20	17	15
Range of results (mJm^{-2})	56-108	55-114	57-114

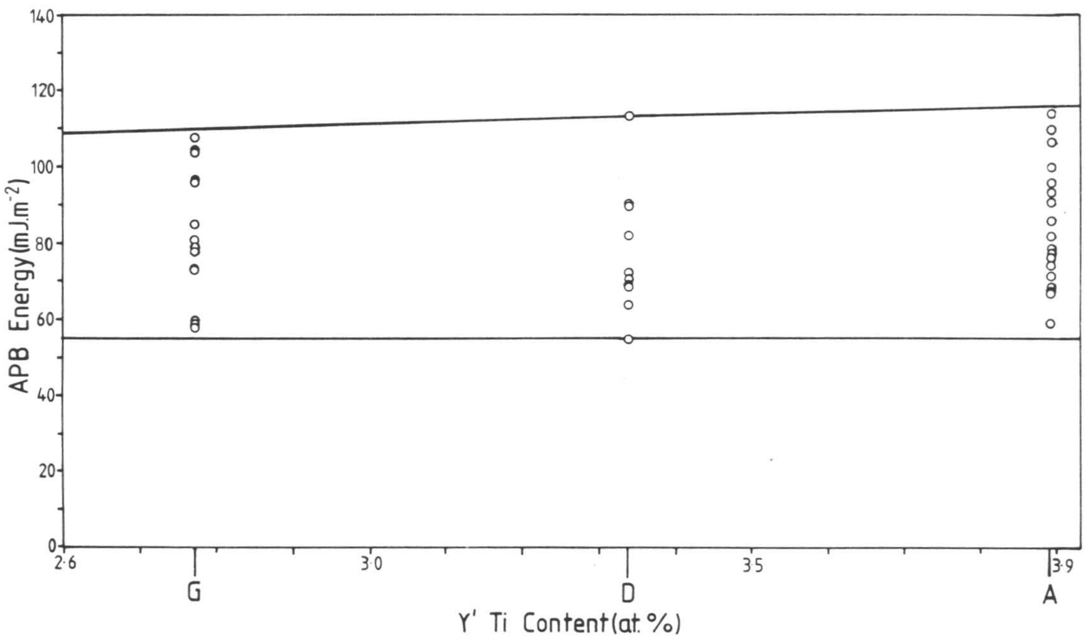

Fig. 6.5. The variation in APB energy with γ' titanium content for alloys A, D and G.

6.2.4 Comparison with the results of other workers

In the past seventeen years many references have been made to the effect the APB energy may have on deformation in $L1_2$ structures, for example, Copley and Kear (1967), Kear, Leverant and Oblak (1969), Kear et al. (1970), Leverant, Gell and Hopkins (1970 and 1971), Leverant and Kear (1970), Raynor and Silcock (1970), Thornton et al. (1970), Brown and Ham (1971), Leverant, Kear and Oblak (1973), Takeuchi and Kuramoto (1973), Kear (1974), Staton-Bevan and Rawlings (1975a and b), Noguchi, Oya and Suzuki (1981), and Pope and Ezz (1984). Since so much work has been reported, it is surprising that there are so few quantitative APB energy data available.

Some values have been measured, the most popular value quoted in recent papers (e.g. Pope and Ezz, 1984) being that measured in the field ion microscope (FIM) by Taunt and Ralph (1974). These authors measured a superdislocation spacing of 3nm (considerably smaller than the present data) which corresponds to a higher APB energy of between 250 and 350 mJm^{-2}. This value is close to the values of 300 mJm^{-2} and 254 mJm^{-2} calculated theoretically for perfectly ordered pure Ni_3Al by Taunt (1973) and Copley and Kear (1967) respectively. Taunt and Ralph performed their experiments on a highly ordered pure Ni_3Al at about 77K, and they consequently gained the expected good agreement with the theoretical value.

It is unrealistic to suggest that this value is typical of the APB energy of a highly alloyed commercial superalloy in the region of 1000K. Alloying of the γ' means that atoms other than Ni and Al will occupy adjacent sites in the $L1_2$ lattice. Consequently the interatomic forces will be different from those in Ni_3Al as will the change in those forces when an APB is created. Also, as temperature is increased, entropy increases, order decreases and so does APB energy. This is shown in the calculated value of 164 mJm^{-2} quoted by Copley and Kear (1967) for Ni_3Al with a long range order parameter of 0.803 (they calculated the APB energy of fully ordered Ni_3Al to be $254mJm^{-2}$). As a consequence of these two factors the APB energy of most superalloys is expected to be lower than that of perfectly ordered Ni_3Al.

Experimental values measured indirectly by various means have been reported by Brown and Ham (1971). These values are mainly from small γ' volume fraction, low alloy superalloys with gamma prime particle sizes less than 0.1μm. Energies calculated using equations 2.63 and 2.64 from Brown and Ham (1971) were mostly between 150 and $200mJm^{-2}$. The most important of these are due to Raynor and Silcock (1970) who reported that for a mixture of superalloys and stainless steels the APB energy of gamma prime increased with titanium additions concluding that the Ti/Al ratio affected the APB energy. This conclusion was drawn although other alloying elements in the compositions, particularly Ni and Fe, were changed by a considerably greater margin than the titanium. Raynor and Silcock's observations are contrary to the findings of this investigation; probably because they were comparing radically different alloys rather than a systematic set where one element (Ni) was replaced by another (Ti), as in this investigation. Another factor contributing to the differences might be that Raynor and Silcock's alloys contain more Ti than Al, whereas alloys A, D and G contain more Al than Ti. It seems that the compositional differences in Raynor and Silcock's alloys have a considerable effect on their APB energies, although it is not certain that these differences are due to changes in Ti. It is concluded that the alloys studied by Raynor and Silcock are too widely different from alloys A, D and G for their APB energies to be usefully compared. This is supported by the results of Miller and Ansell (1977) who evaluated the APB energies for Ni-Cr-Al-Mo alloys and Ni-Cr-Al-Ti-Mo alloys where the titanium content was larger than the Al content. Using the techniques described by Brown and Ham (1971) they found that the APB energy of the alloys with titanium was $200mJm^{-2}$ and for alloys without titanium the lower value of

$133mJm^{-2}$ was obtained.

Data from Ni-Al-Cr alloys (Hornbogen and Mukerjee, 1964 and Hornbogen, 1965) were reprocessed by Brown and Ham (1971) and gave APB energies of about $90mJm^{-2}$. These results are similar to the present data but the agreement may be fortuitous as the alloys studied are so different from one another. It does, however, appear that the presence of chromium alone considerably lowers the APB energy of Ni_3Al.

The first APB energy value quoted for a commercial superalloy was a value of $150mJm^{-2}$ (Leverant and Kear, 1970). It was not stated how this value was obtained but it is close to the theoretical value quoted by Copley and Kear (1967). In a later paper, Leverant et al. (1973) stated that after creep deformation at 1023K the superdislocation spacing was too small to be measured from bright field electron micrographs, but that after creep deformation at 1133K the spacing could be measured and was found to be 9nm. They concluded that this single observation showed an effective drop in the local APB energy on {111} planes between 1023 and 1133K. In this investigation superdislocations were frequently observed after annealing at 1173K. Their spacings, measured using weak beam imaging, were found to be similar to the value quoted by Leverant et al. (1973) after deformation at 1133K.

From the results presented above it is clear that no systematic study of the way in which APB energy varies with alloy composition has been undertaken previously. APB energies have been measured in significantly different alloys using a wide range of techniques and it is impossible to compare results. Other than the result reported by Leverant and Kear (1970), no other values for the APB energy of Ni-base superalloys strengthened by large volume fractions of gamma prime have been reported before this investigation.

The APB measurement technique employed here involves the measurement of dislocation spacings. This method was first used by Marcinkowski, Brown and Fisher (1961) on pure Cu_3Au. They also calculated the variation in spacing which could be expected with change in order and showed that a change of up to 8nm was possible for a given APB energy between the fully ordered state and the point at which ordering becomes negligible. It could be that the range of spacings measured in this investigation was due to a local change in the order. However, this is highly improbable because long homogenisation and annealing times used here were deliberately employed to produce uniformly ordered materials.

In summary, it has been shown that the APB energy of three single crystal superalloys does not seem to vary with titanium content. A range of values was found which is probably due to limited glide of superdislocations during cooling from the annealing temperature rather than regions of different order. The average APB energy was $83mJm^{-2}$ (fig. 6.5); it has been assumed that this value is typical of 1173K.

The author is not aware of any data which directly relate APB energy to temperature. An experiment could be undertaken using a heating stage in the TEM which could be of great value to the prediction of superalloy deformation mechanisms. It would also establish whether there is a major change in APB energy between 1023K and 1133K as proposed by Leverant et al. (1973).

The evaluation of APB energies from measured dislocation spacings is the most direct and accurate method available, and it is suggested that this technique should be used to study the effect of other alloying elements on the APB energies of superalloys.

6.3 Superlattice Stacking Fault Energy Measurement

6.3.1 Theory

A method (Rae and Hillier, 1984) has been developed which enables superlattice stacking fault (SSF) energies to be deduced from the supernode configurations described previously. The SSF energy per unit area is related to the net force acting at point O on dislocation 6 of the configuration shown in figure 6.6. To do this, the stress field due to each screw dislocation segment forming the supernode is calculated using a different set of co-ordinate axes and these stresses are then resolved along the Z direction of the co-ordinate system attached to dislocation 6 to evaluate the total force on that dislocation. A detailed description of this process is given in appendix D.

All the stresses except that resulting from dislocation 3 act to expand the node by pulling it outwards. When the stresses due to these dislocations are taken to be positive, the stress due to dislocation 3 is negative. The total force per unit length which can be equated to the SSF energy acting on the supernode, γ_{SSF}, is:

$$F = [\sigma_1+\sigma_2-\sigma_3+\sqrt{3}\sigma_4+\sqrt{3}\sigma_5].b_6 = \gamma_{SSF} \qquad \text{eqn. 6.6}$$

The expressions from appendix D are homogeneous in r, the dislocation spacing, and R, the internal dimension of the node. They can consequently be written in terms of R and the ratio r/R which will be termed ρ. The expression can be separated into a dimensionless geometrical function of ρ multiplied by 1/R. The geometrical function depends only upon the shape of the node. If the total stress is multiplied by the Burgers vector of dislocation 6 ($b_6=\frac{\sqrt{2}a}{3}$) the force per unit length at the centre of the dislocation acting on the extended node is:

$$F = \frac{\mu a}{4\pi R}\frac{\sqrt{2}a}{3}G(\rho) \qquad \text{eqn. 6.7}$$

This can be equated to the SSF energy so that:

$$\gamma_{SSF} = \frac{\mu a^2 G(\rho)}{2\sqrt{6}\pi R} \qquad \text{eqn. 6.8}$$

where μ is the isotropic shear modulus and is equivalent to $[C_{44}(C_{11}-C_{12})/2]^{\frac{1}{2}}$

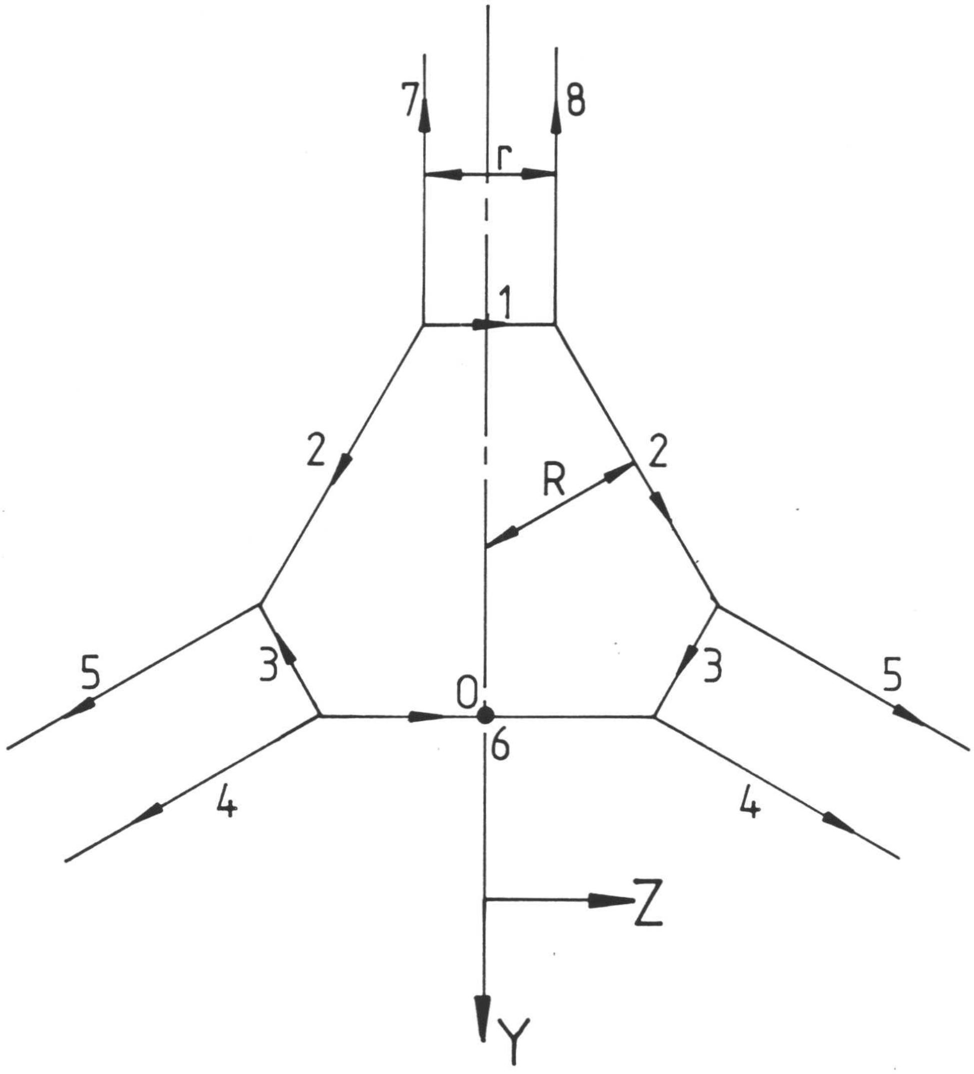

Fig. 6.6. Supernode dislocation configuration used to evaluate SSF energy. Only five dislocation stresses are required because the supernode is symmetrical. Dislocations 7 and 8 have no component in the Z direction and can therefore be ignored. See appendix D for details.

for pure screw dislocations, a is the gamma prime lattice parameter, R is the internal dimension of the node, and $G(\rho)$ is the geometrical function.

If $G(\rho)$ is plotted as a function of ρ (fig. 6.7) it is found that when ρ is zero $G=3.82$ and lies within 8% of that value until $\rho=1.3$. Between $\rho=1.3$ and $\sqrt{3}$ the SSF energy rapidly increases to infinity since the strain field of dislocation 6 is decreasing as its length decreases, and the strain fields of the infinitely long dislocations 4 and 5 become dominant. When $\rho\leq1.3$ the SSF energy is relatively insensitive to ρ and therefore the superdislocation spacing, r. In this region the SSF energy can be approximated to equation 6.9:

$$\gamma_{SSF} = \frac{K}{R} \qquad \text{eqn. 6.9}$$

in this case $K=0.654\text{Jm}^{-2}$.

As the length of the $a/_3\langle211\rangle$ dislocations becomes shorter the centre of the node becomes more like a triangle and the SSF energy rises very rapidly. In this configuration (fig. 6.8a) the Rae-Hillier model predicts that an energy of many Joules would be necessary to maintain the shape. It is proposed that when $r>\sqrt{3}R$ the configuration shown in figure 6.8(b) may form. In this investigation the unextended nodes adopted the configuration shown in figure 4.19(d). The configuration shown in figure 6.8(b) will not be discussed further.

6.3.2 SSF energy measurement

In 6.3.1 it was shown that the SSF energy is a function of ρ. Rae and Hillier (1984) have computed the superlattice stacking fault energy, γ_{SSF}, from the true superdislocation spacing, r, and the internal dimension of the node, R. Values of r and R were measured from weak beam dark field electron micrographs of foils with approximately <111> normals. In all cases it was assumed that the nodes were planar and that the dislocations adopted the equilibrium spacing on that plane. This was seen to be true even when the superdislocations at the nodes were twisted between the

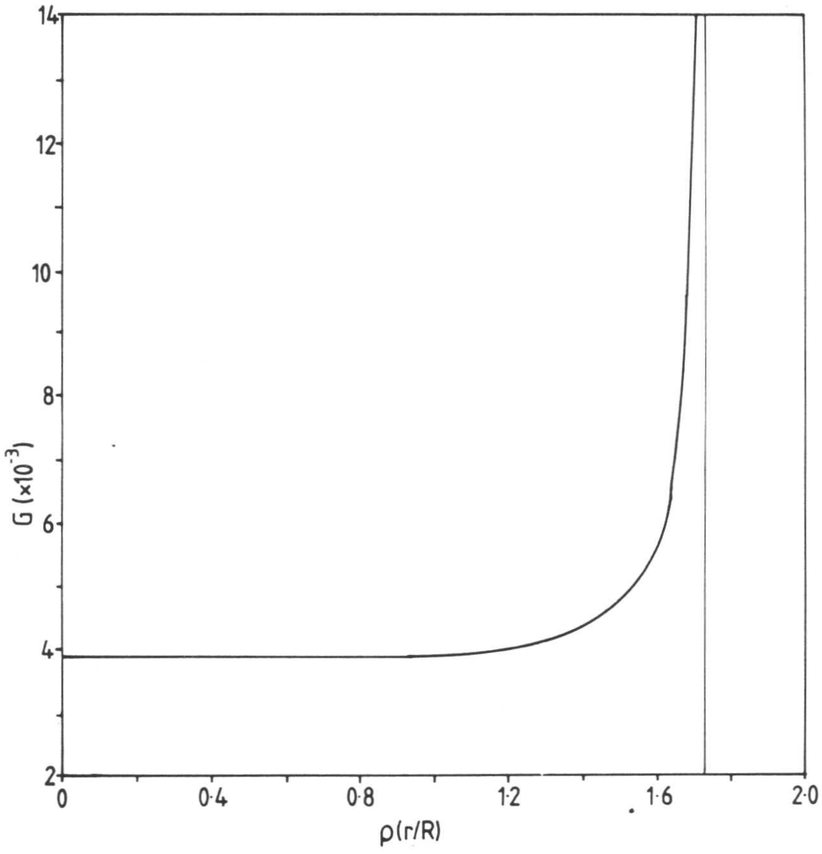

Fig. 6.7. Dependence of the geometrical function, $G(\rho)$, on ρ.

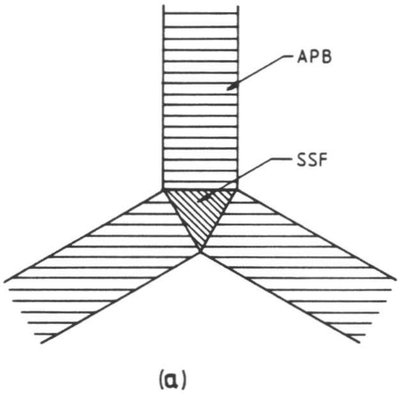

Fig. 6.8. Illustration of the supernode configuration with an infinite SSF energy (a) and the configuration which may replace it at high SSF energies (b).

SSF plane and the APB plane. The values measured were corrected for foil tilt before the fault energies presented in 6.3.3 were computed.

6.3.3 Results

The superlattice stacking fault energies are shown graphically in figure 6.9. The dislocation spacings at the node, r, the internal dimension, R, the ratio r/R, ρ, and the energies, γ_{SSF}, are listed in full in appendix F. The results are summarised in table 6.2 and the total number of node observations are shown in table 6.3.

The trends can be seen most clearly in figure 6.9. The SESF energy is always lower than the SISF energy, as expected from the relative node size. Both energies decrease as the titanium content of the alloy is increased. The SESF decreases more sharply than the SISF. The standard deviation and range of the SSF energies is considerably smaller than those for the corresponding APB energies. It is thought that this is because the SSFs are stabilised by a diffusion process at the annealing temperature and unlike the APBs are unable to contract during cooling from the annealing temperature. It is thought that the SSF energy values are typical of 1173K, the annealing temperature.

The SISF energies measured from alloys A and D could be significantly in error because the values of ρ are greater than 1.3 for these alloys. (See appendix F.) Rae and Hillier (1984) have shown that under these conditions the SSF energy is very sensitive to small changes in superdislocation spacing; the value can change by 60mJm^{-2} for a 1nm change in r. As a consequence of this, any error in the measurement of r and R could have a significant effect on the SISF energy values. Also, most of the supernodes containing SISFs in alloy G were not extended and the SISF energy could not be measured from them.

In summary, as shown in figure 6.9, at 1173K the SESF energy is considerably lower than SISF energy. The SESF energy decreases at a

Table 6.2. Summary of Superlattice Stacking Fault Energies

	Alloy		
	G	D	A
γ' Ti content (at.%)	2.8	3.3	3.9
Mean extrinsic SSF energy (mJm^{-2})	94	74	46
Standard deviation (mJm^{-2})	10	5	5
Mean intrinsic SSF energy (mJm^{-2})	137	131	117
Standard deviation (mJm^{-2})	-	7	1

Table 6.3. Number of Node Observations

Alloy	Node Type				Total Observations
	Extended Extrinsic	Not extended Extrinsic	Extended Intrinsic	Not extended Intrinsic	
A	8	1	7	1	17
D	9	0	6	3	18
G	5	2	1	6	14

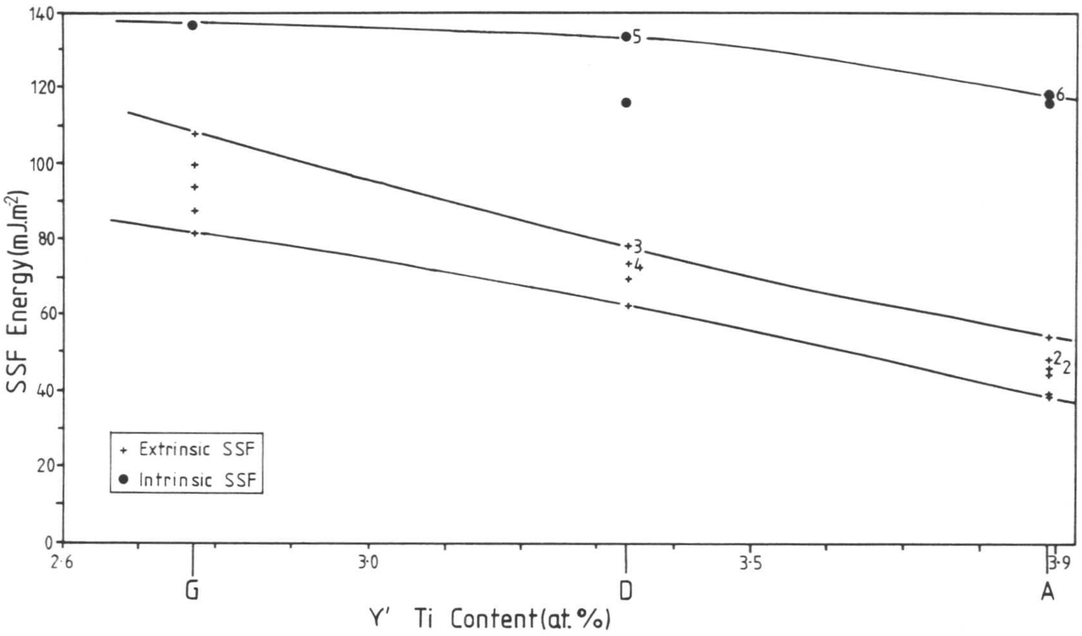

Fig. 6.9. The variation in the SSF energies with γ' titanium content for alloys A, D and G. Numbers next to points indicate the number of measurements represented at that point.

higher rate than SISF energy. The SESF energy drops by approximately 50% with a 1.1 at.% change in the γ' titanium content while the SISF energy falls by only 14% for the same change. The values exhibit a smaller scatter than the APB energies because it is thought that they are stabilised at the annealing temperature.

6.3.4 Discussion

The author is aware of only three values of SSF energy in $L1_2$ structures which have been published prior to this investigation. The first by Leverant and Kear (1970) is a value for the SISF energy in the gamma prime measured from a creep specimen of Mar-M 200. The value quoted is 8-17mJm^{-2}. Leverant and Kear do not state how they arrived at this figure. It is thought that they measured the spacing between the dislocations bounding a SISF forming part of a superdislocation shearing the gamma prime. The value is very small, perhaps because no account was taken of the influence of surrounding dislocations and faults. The dislocation and fault arrangement at these defects has been shown to be complex (Kear et al. 1969 and Rae, 1984), and any calculation of fault energies from them is expected to be extremely complicated. As this value was measured from a crept specimen where the faults may not be in equilibrium, and no information has been given by the authors to explain how they evaluated the quoted value, it was treated with suspicion.

The other values were measured from other $L1_2$ structures. Sastry and Ramaswami (1976) have measured the APB energy and an unspecified SSF energy thought to be the SISF energy at room temperature in Cu_3Au. From dislocation spacings they concluded that the SISF energy was considerably lower than the APB energy. Howe et al. (1974) measured what they claim to be the SISF energy of Zr_3Al using a dislocation spacing method similar to that used to measure the APB energy in this investigation. They found the energy to be between 70 and 90mJm^{-2} and confirmed their results by measuring the SISF energy of nodes using the method described by Brown and Thölen (1964). It seems, however, (see 4.6) that Howe et al. incorrectly identified the dislocation pairs they observed and their interpretation of the network dislocation structure is doubtful. It has been shown that due to the difference in structure between dislocation networks in ordered and disordered materials it is incorrect to apply the method of Brown and Thölen to superdislocation networks in $L1_2$ structures. It is suggested that the energy values quoted by Howe et al. are not SSF energies. An important observation made by Howe et al. which will be considered later was that the SISFs and SESFs were extended by about the same amount.

Although so few SSF energy values have been measured, Kear et al. (1968) pointed out that the stacking sequence at an SISF was equivalent to four layers of the DO_{24} (Ni_3Ti) structure or four layers of the DO_{19} structure while the stacking sequence at an SESF was equivalent to seven layers of the DO_{24} structure. They also pointed out that these SSFs could be stabilised by segregation of DO_{24} forming elements such as titanium. This stabilisation process has also been proposed by Leverant and Kear (1970) and Kear et al. (1970).

By using a novel approach, values for the SSF energies of the gamma prime in three superalloys with different titanium contents have been evaluated and show that the SSF energy drops with increasing titanium content. These observations strongly suggest that the predictions of Kear et al. (1968) are correct and that titanium does segregate to the nodes and stabilise the nodes by forming a titanium rich region or perhaps precipitating very thin planar Ni_3Ti. Such precipitation has previously been observed on stacking fault in the titanium rich superalloy Nimonic 901 by Oblak et al. (1971) and in Udimet 700 by Kear et al. (1970).

In this investigation the extrinsic SSFs were seen to be more extended than the intrinsic SSFs; this is expected as the SESF has a greater thickness of DO_{24} than the SISF implying that it is likely to be stabilised by a greater degree. Also similar extended nodes observed in Zr_3Al by Howe et al. (1974) which contained no DO_{24} stabilising elements were seen to be equally extended - another observation supporting titanium segregation to the SSFs.

The stabilisation of SSFs by the precipitation of Ni_3Ti is a diffusion controlled process. It is expected that the apparent SSF energy of the stabilised faults will decrease with time until an equilibrium related to the overall titanium content of the alloy is reached. This is borne out in the SSF energy values measured. It can be seen from figure 6.9 that the alloy containing the smallest amount of Ti has the highest SSF energies.

The titanium which stabilises the fault can migrate from either the gamma matrix or the gamma prime itself, and it can arrive at the fault either by bulk diffusion through the γ' or by diffusion through γ and/or γ' to dislocation cores followed by rapid diffusion along the dislocation cores.

Very few data are available for Ti diffusion in γ'. The best available value is that reported by Larikov, Geichenko and Fal'chenko (1981) in $Ni_3(Al_{0.6}Ti_{0.4})$. They report that at 1223K the activation energy for the bulk diffusion of Ti in $Ni_3(Al_{0.6}Ti_{0.4})$ was $145 kJmole^{-1}$ and the pre-exponential factor, D_o, was $1.9 \times 10^{-10} m^2 s^{-1}$. The simple diffusion equation $X=\sqrt{Dt}$ was applied for a γ' particle size of 0.5µm and this showed that bulk diffusion of Ti to a fault in the centre of a γ' particle would occur in about 16 minutes at the annealing temperature of 1173K. The γ' precipitates in alloys A, D and G are compositionally more complex than the alloy studied by Larikov et al. They contain elements such as tantalum and tungsten which are expected to lower diffusion rates. Consequently, titanium diffusion will be slower so fault stabilisation will take considerably longer in these alloys.

However, this simple approach does show that it is quite plausible for titanium to diffuse to, and stabilise, the SSFs.

Many more diffusion data are required before a quantitative assessment of titanium diffusion and fault stabilisation in single crystal superalloys can be made.

In summary, there is strong evidence to suggest that Ti stabilises SSFs by forming thin planar regions of Ni_3Ti on the fault planes. Consequently, the SESF energy is lower than the SISF because the SESF is equivalent to a larger portion of the Ni_3Ti lattice than the SISF. There is also evidence to suggest that the stabilisation is greater in alloy A than in alloy G because A contains more Ti. Tables 2.1 and 2.2 show that the γ matrix of alloy A contains twice as much Ti as the γ of alloy G while there was about 40% difference in the γ' Ti contents. It is suggested that stabilisation of SSFs by the precipitation of Ni_3Ti on the favourable sites at the nodal points occurred by bulk diffusion of Ti through γ and γ' to faults and to dislocations which then provide rapid transport to faults. The rate controlling step will be the bulk diffusion of Ti in γ and γ' either to the faults or to the dislocation cores.

The SSF energies shown in figure 6.9 and table 6.2 are the values at the annealing temperature of 1173K. It would be interesting to examine extended nodes at other temperatures to study the effect of temperature on SSF energies. Another useful experiment would be to follow diffusion of Ti and other alloying elements by a radioactive tracer to evaluate the diffusion coefficient and prove that fault stabilisation is occurring.

The stabilisation of SSFs and the difference in the energies between APB and SSF could be important to the mechanical properties of superalloy materials. This aspect of alloy behaviour is discussed in the next chapter.

6.4 Conclusions

(i) It is found that the APB energy calculated from measured dislocation spacings is not sensitive to alloy titanium content for γ' titanium between about 2.7 and 3.9at.%.

(ii) The mean APB energy is 83±20mJm^{-2}.

(iii) The first analysis of supernodes has allowed the evaluation of SSF energies from supernode geometry. This technique, proposed by Rae and Hillier, can be used to study the SSF energies of other superalloy materials.

(iv) It is found that SISF and SESF energies decrease as alloy Ti content increases as shown in figure 6.9.

(v) The SESF energies were found to be 94±15, 74±10 and 46±12mJm^{-2} for alloys G, D and A respectively, and the equivalent SISF energies were 137, 131±10 and 117±5mJm^{-2} respectively.

(vi) It is suggested that diffusion of Ti to the nodal points by diffusion through the γ,γ' and along dislocation cores stabilises the SSFs by forming thin planar regions of Ni_3Ti.

(vii) The SESF energy is considerably lower than the SISF energy because the SESF is equivalent to a greater number of planes of Ni_3Ti stacking.

CHAPTER 7

THE EFFECT OF TITANIUM ON DEFORMATION MECHANISMS IN SINGLE CRYSTAL SUPERALLOYS

7.1 Introduction

The important variables influencing the strength of Ni-base superalloys are (see 1.5.3):

(i) Solid solution strengthening of the γ

(ii) The γ' volume fraction

(iii) The γ' particle size

(iv) Misfit strengthening

(v) The superlattice stacking fault and antiphase boundary energies.

The inaccurate determination of these parameters and the failure to consider their interdependence create uncertainties in the various deformation models proposed. This chapter reviews the established deformation model and proposes a modification to that model as a result of the energy data reported previously. The modified model is then used to explain the stress-rupture results reported in chapter 1.

It is well documented that different heat treatments can affect alloy properties by producing differences in precipitate size and distribution (e.g. Decker, 1969). It is also reported that changes in alloy composition can affect precipitate volume fraction (Decker, 1969) and γ/γ' misfit (e.g. Grouse and Ansell, 1981). For the purposes of this investigation it was necessary to keep factors (i) to (iv) constant so that the only variable parameters were the APB and SSF energies. Any changes can then be attributed to variations in the alloy Ti content (as proposed by Roome, 1982).

Factors (i) to (iii) were kept constant by choosing a small compositional range, near to the value of interest and using a long homogenisation treatment so that changes due to compositional variations were negligible. The mean precipitate size of each alloy was the same because each specimen underwent an identical heat treatment cycle. Factor (iv) was also seen to be constant as there was no observable γ/γ' misfit in any of the alloys (see 2.9). Hence, the only variable quantities were the SSF and APB energies. Any observed change in stress rupture life between the alloys must have been due to the change in fault energies brought about by the change in titanium content.

7.2 Deformation Modes in Ni-Base Superalloys

Pope and Ezz (1984) have recently produced a comprehensive review of the established deformation mechanisms and the mechanical properties of high volume fraction γ' superalloys. The present work therefore focuses on deformation mechanisms involving dislocation glide through the γ' and the effect changes in titanium may have upon these mechanisms are discussed. It is emphasised that much of the material's strength is derived from the ability of the γ/γ' interface to resist the passage of dislocations into the γ'. This is borne out by the observation that single-phase polycrystalline γ' alloys creep much more rapidly than two-phase γ/γ' alloys (Pope and Ezz, 1984).

7.2.1 Information from the deformation-mechanism map

As far as the author is aware only one creep deformation-mechanism map has been produced for a large grain size high volume fraction γ' superalloy. A reproduction of this map, for Mar-M 200 (Frost and Ashby, 1982), is shown in figure 7.1. The test conditions used to generate figure 1.17 are shown on the map and it can be seen that these three conditions lie either in the power-law creep or plasticity regions. Power-law creep is a region where deformation is usually dominated by dislocation glide and

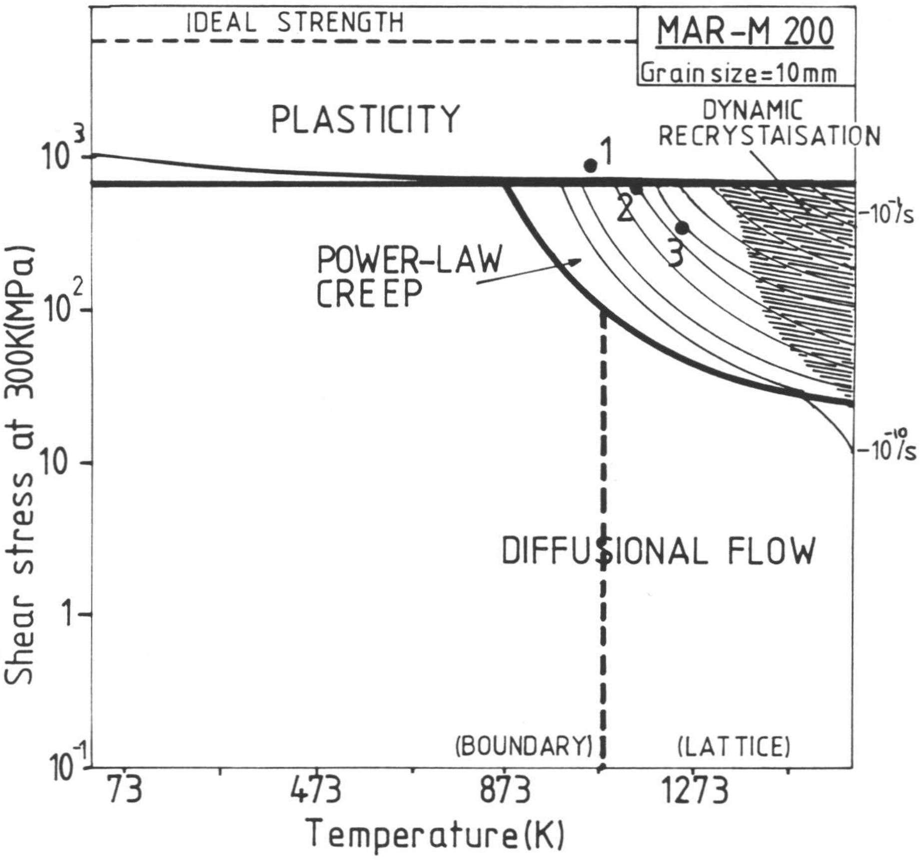

Fig. 7.1. Deformation mechanism map for Mar-M 200 (table 1.1) with a grain size of 10mm from Frost and Ashby (1982). The test conditions used in this investigation are marked on the map: 710MPa at 1023K (1), 430MPa at 1123K (2) and 225MPa at 1223K.

climb while plasticity is dominated by glide alone. The deformation map is, however, not for a single crystal and admitted, by its authors, to be approximate, therefore, the information drawn from it is not definitive but it seems that deformation will be controlled by dislocation glide and climb.

7.2.2 Deformation by dislocations looping around the γ'

The majority of mechanisms proposed to explain the strengthening of Ni-base superalloys appear to have been based on the assumption that deformation will only occur by the glide of dislocations through the γ' because the particles are so close together that the dislocations would have to follow such a tortuous route that looping and climb would not occur. Only one deformation mechanism proposed to explain the strengthening of high volume fraction γ' alloys considers looping or climb to be an important mechanism. This is due to Carry and Strudel (1975, 1977, 1978) and Carry, Houis and Strudel (1981) who state that deformation occurs by the glide of $a/_2\langle 110\rangle$ dislocations on $\{110\}$ planes in the γ to form networks in the γ/γ' interfaces. At high temperatures it is proposed that these dislocations climb over the γ' particles rather than gliding through them.

No analysis of the slip planes of $a/_2\langle 110\rangle$ dislocations in the γ was undertaken in this investigation but it is thought rather unlikely that slip would occur on the non-close packed $\{110\}$ planes suggested by Carry and Strudel. The movement of dislocations within gamma and the structure at the γ/γ' interfaces have been largely ignored by researchers studying superalloy deformation in high volume fraction γ' superalloys. It is suggested earlier (4.4.2) that the regions of γ between the precipitates are so small that at low temperatures it is unlikely that many superdislocations can be formed easily. Unpaired dislocations will have little chance of entering the γ' so for deformation to occur they must loop around the particles. This is known to occur in lower volume fraction γ' alloys, see for instance Davies and Stoloff (1965).

Many fewer dislocations were observed in the γ' than the γ and this suggests that up to about 1000K a significant number of dislocations by-pass the γ' precipitates. It appears that dislocation looping and climb may be a significant strengthening mechanism during power-law creep and the dislocation behaviour in γ would be worth investigating.

7.2.3 Deformation by dislocations gliding through the γ'

Glide of dislocations through γ' frequently occurs and it is thought that much of the improvement in superalloy properties in recent years has been due to the steady increase in resistance to γ' glide produced by careful alloying.

(i) Shearing by superdislocations

The most common γ' shearing mode is the passage of superdislocation, consisting of pairs of $a/_2\langle 110\rangle$ dislocations on $\{111\}$ planes bounding an APB (fig. 7.2 and Kear and Oblak, 1974). Superdislocation shear is the dominant γ' shearing mode up to about 1000K in creep and up to about 1100K in tensile deformation. In creep, between 1000K and 1200K the dominant shearing mode is partial dislocation shear.

At temperatures above ~1200K shear by superdislocations becomes dominant again (Leverant et al., 1973). Leverant et al. proposed that this change was due to a precipitous drop in the APB energy caused by rapid diffusion at the dislocation core leading to local lowering of the order. This proposal seems a highly unlikely explanation for the change in deformation mode observed at high temperatures.

(ii) Shearing by partial dislocations

In the temperature range between 1000K and 1200K shear of γ' occurs by the passage of partial dislocations (Kear et al., 1969 and Leverant and Kear, 1970). This has been shown to occur either by the passage of $a/_3\langle 211\rangle$ partial dislocations producing single SSF ribbons (fig. 7.3a), which are

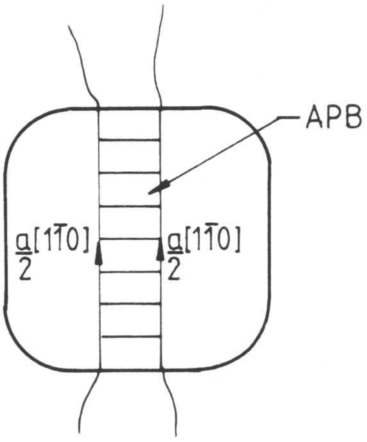

Fig. 7.2. γ' shearing by a superdislocation of two a/$_6$[110] dislocations.

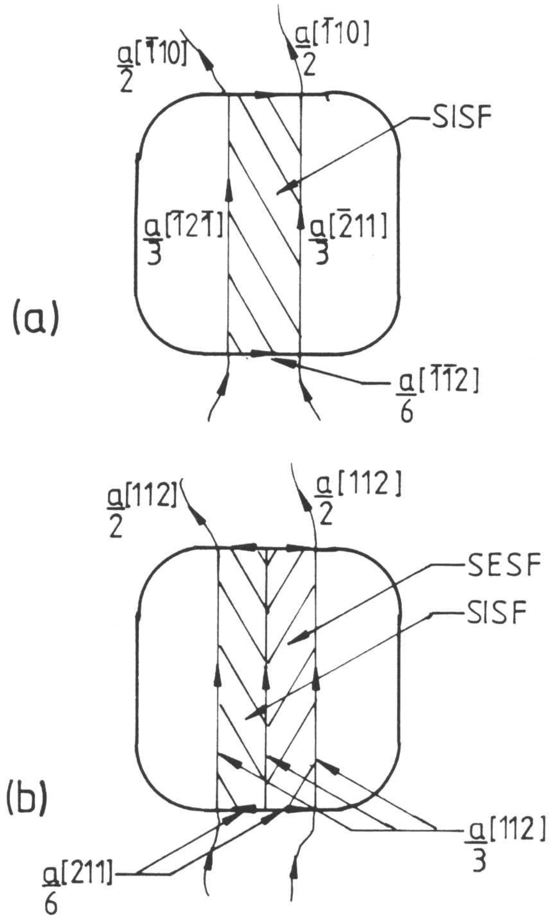

Fig. 7.3. γ' shearing by a pair of a/$_3$<211> partial dislocations bounding a SSF (a), and a triplet of a/$_3$<211> partial dislocations forming a SISF/SESF pair. In both instances an a/$_6$<211> partial dislocation is required in the γ/γ' interface

produced by a superdislocation of two identical $a/_2$<110> dislocations in the γ, or by SISF/SESF fault pairs (fig. 7.3b), which are produced by groups of dislocations in the γ with a complete Burgers vector of a<211>. Although the SISF/SESF pair deformation mechanism appears rather unlikely they have been observed by Kear et al. (1969), Roome (1982) and Rae (1984); also Leverant and Kear (1970) showed that the rotations of the tensile axes of creep specimens were consistent with the <112> {111} slip mode.

As shown in figure 7.3, both these mechanisms require the production of various partial dislocations at the γ/γ' interface. Leverant and Kear (1970) suggest that the dislocation dissociations required to form SISF/SESF pairs will not occur at lower temperatures because they require thermal activation to nucleate an additional dipolar dislocation at the dislocation core. A more likely mechanism is that due to Rae (1984) who proposes that the 'dipole displacement' is unnecessary because two different $a/_2$<110> dislocations may combine at intermediate temperatures to produce $a/_2$<211> dislocations which can subsequently dissociate to produce the $a/_3$<211> dislocations required to form SISF/SESF pairs.

(iii) Other mechanisms

Many mechanisms which enhance the strengthening effect of the main shear modes by the creation of dislocation jogs and loops have been reported. Some of these are described in 5.2.2 and 5.2.3 and discussed with the debris hardening mechanism proposed by Thornton et al. (1970) and the cross-slip mechanism of Takeuchi and Kuramoto (1973) in 5.4. These mechanisms also help to increase the alloy properties by enhancing resistance to γ' shear.

7.2.4 Established model for γ' shear during creep

Kear et al. (1968) first suggested that at any given temperature the most prolific shearing mode will be that which has the lowest fault energy. On this basis it was suggested that the change in shear mode observed between 1000K and 1200K occurred because the SSF energy falls below the APB energy; both energies were assumed to decrease with increasing temperature. It was also observed that the required dislocation dissociations into $a/_3\langle 211\rangle$ partial dislocations were more likely at higher temperatures (Leverant and Kear, 1970, and Rae, 1984).

At temperatures above 1200K it was predicted that the APB energy decreased rapidly due to local disordering at the dislocations (Leverant et al., 1973) and deformation was again seen to occur by superdislocation glide. These ideas are summarised schematically in figure 7.4(a).

7.3 Modified Model for γ' Shear During Creep

In 5.4 and 6.3 evidence was presented to indicate that the diffusion of Ti to SSFs stabilised the faults by forming very thin planar Ni_3Ti on the fault plane. This stabilisation process could have a significant effect on γ' shearing and it was with this in mind that the modified deformation mechanism presented below was produced.

The refined model is based on an extension of Kear's hypothesis that the most prolific slip mode will be the one with the lowest fault energy. It is noted that in addition to the fault energy the dislocation Burgers vector, the applied stress and the dislocation friction stress will also contribute to the overall deformation mechanism. The fault energy, however, is considered to be the most important factor because under the conditions used in this investigation the applied stress is constant and the magnitudes of the dislocation Burgers vectors of $a/_2\langle 110\rangle$ and $a/_3\langle 211\rangle$ dislocations differ by only 12%.

Between room temperature and about 1000K γ' shearing occurs by the glide of pairs of $a/_2\langle 110\rangle$ dislocation on $\{111\}$ planes. At low temperatures little γ' shear occurs because only a few superdislocations can form (4.4.2): the majority of the deformation occurs by dislocation looping. As the temperature is increased the APB energy steadily decreases due to an increase in entropy producing a small reduction in the long range order parameter. This would be manifested by a small increase in the super-

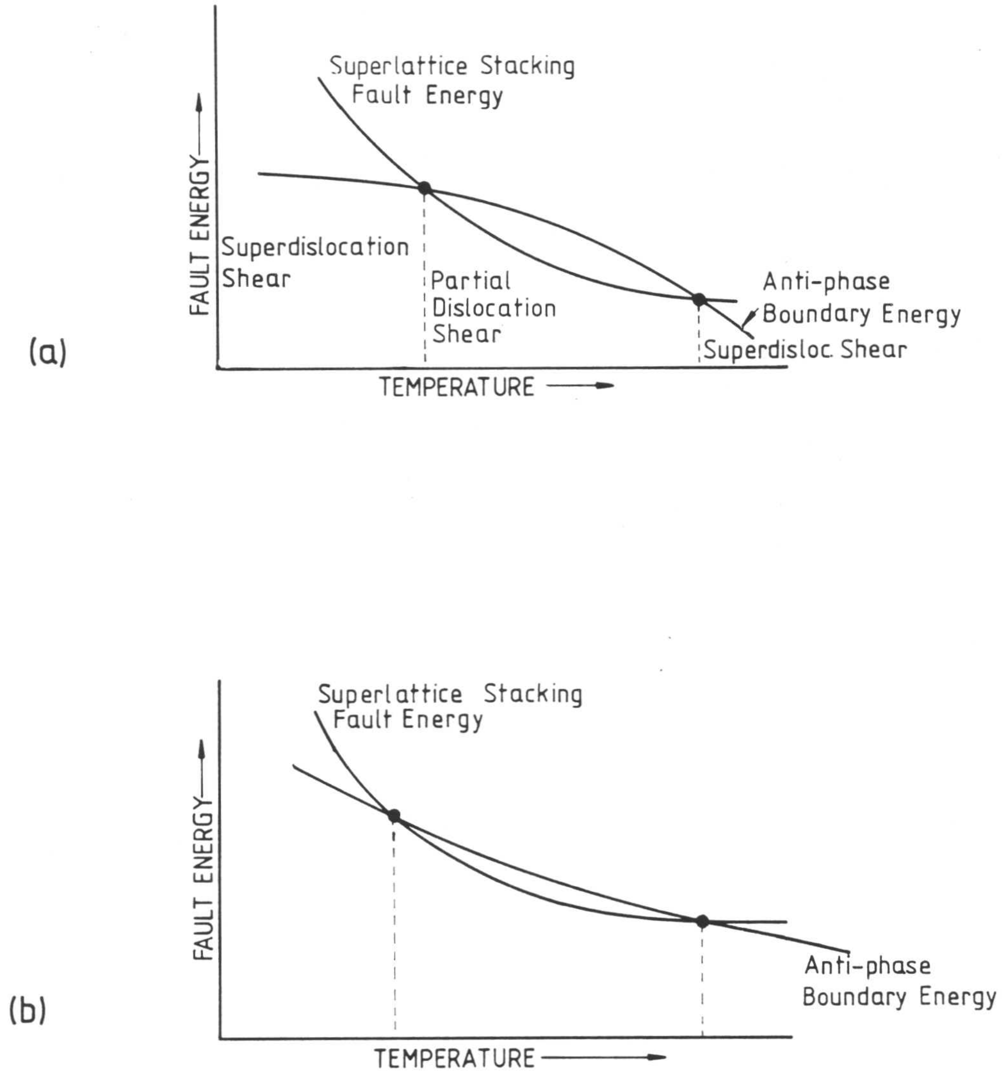

Fig. 7.4. Schematic plot of the APB and SSF energies vs. temperature for the model proposed by Leverant and Kear (1970) (a), and that proposed in this investigation (b).

dislocation spacing.

It is proposed that at a temperature just below 1000K the Ti diffusion rate is sufficiently fast to stabilise SISFs and SESFs and there is enough thermal energy available for unpaired $a/_2<110>$ dislocations to combine in the γ to form $a/_2<211>$ dislocations which subsequently dissociate into $a/_3<211>$ partial dislocations. When the energy of this dislocation combination falls below that of an APB bounded by two $a/_2<110>$ dislocations partial dislocation shear will occur. In addition this mechanism reduces the number of $a/_2<110>$ dislocations able to form superdislocation pairs, thus reducing the frequency of superdislocation shear.

It is suggested that free titanium, either in the γ or the γ', diffuses towards the newly formed SSF through the precipitate, the matrix and along the dislocation cores. The SSF is stabilised by the agglomeration of titanium on the fault plane or by the formation of a thin planar precipitate of Ni_3Ti. This process will lower the energy of the SSF and allow it to extend further into the γ'. The stabilisation of superlattice stacking faults in this way can be likened to Suzuki locking seen in non-ordered materials (Suzuki, 1952; as discussed by Nabarro, 1967). The SSF will expand until the equilibrium spacing equivalent to the stabilised fault energy is reached. At this point the fault may stretch across more than one γ' particle. The stabilisation process will have no effect on the dislocation configuration during deformation. It will only act to delay the passage of those dislocations through the gamma prime.

Once segregation has occurred the dislocation configuration will only be able to continue its motion through the γ' particle by diffusion of Ti with the fault or by the dissolution of the stabilising atmospheres at high temperatures where the increase in entropy means that the system energy cannot be lowered by segregation to the SSFs. Consequently, as temperature increases, the retarding of gliding partial dislocations by Ti segregation will become increasingly unlikely, perhaps leading to an apparent increase in SSF energy. Consequently the mechanism will only be effective over the temperature range when the diffusion rate of the pinning species is fast enough to allow Ti to migrate with the dislocations, to the temperature when the thermal energy is so great that the pinning species cannot lower its energy by migrating to the fault.

A simple calculation has been made using an estimated dislocation density, an approximate creep rate and the diffusion data of Larikov et al. (1981) for $Ni_3(Al_{0.6}Ti_{0.4})$ (appendix G). This shows that diffusion would occur rapidly enough to allow Ti to move with the dislocations and stabilise an SSF at temperatures above 630K. However, the γ' precipitate in alloys A, D and G is more highly alloyed than $Ni_3(Al_{0.6}Ti_{0.4})$. It contains W which was seen to lower the diffusivity of Ti in Ni at 1170K (Pridantsev, 1967) and Ta which is expected to have a similar effect. Consequently it is suggested that the diffusivity of Ti may be reduced in complex superalloys and that fault stabilisation will not occur at temperatures as low as 630K. Little is known of the diffusion constants of Ti in modern superalloys, and much further work is required to evaluate accurate diffusion coefficients and dislocation velocities in these materials before accurate values for the temperature at which Ti stabilises moving faults can be determined. It does, however, appear that fault stabilisation is possible. It must be remembered that γ' shearing by partial dislocations will not occur during creep deformation regardless of whether SSF stabilisation is possible until the total energy for the process is lower than the total energy for superdislocation shear.

At higher temperatures dislocation pinning does not occur. It was observed that superdislocation shear becomes dominant again. This is probably not due to any precipitous drop in the APB energy but rather to a combination of the decrease in SSF stabilisation and the increased climb of dislocations in the γ matrix. Unpaired $a/_2$<110> dislocations will climb until two like dislocations inhabit the same {111} plane. It will then be favourable for the newly formed superdislocations to glide through the γ'. This mechanism involving the decrease in SSF stabilisation and the increase in dislocation climb appears to be more likely than the local disordering mechanism suggested by Leverant et al. (1973) which was reported earlier. Figure 7.4(b) is a schematic diagram showing how the variations in fault energy with Ti content differ from those assumed before (fig. 7.4a).

No TEM investigation was undertaken to verify this modified deformation because it was felt that this would be of little value, as the proposed change is a reinterpretation of previous results.

7.4 The Effect of Titanium on Stress-Rupture Life

Stress-rupture tests designed by the author were kindly undertaken by Rolls-Royce Ltd., Derby to assess the effect of Ti variation on the stress-rupture life of alloys A, D and G. These results were referred to in chapter 1 (fig. 1.13). They are the only results which have been performed on a set of alloys with systematic variations in Ti which had undergone identical heat treatment cycles. After homogenisation for 36 hrs at 1573K followed by a slow argon gas fan quench to room temperature and a subsequent 16 hr ageing treatment at 1143K, the specimens were machined to a standard Rolls-Royce test piece. This heat treatment was used to produce a microstructure which was as close as possible to that used for fault energy measurement (2.4). Before testing, the specimen orientations were measured using the Laue back reflection X-ray technique. All the specimens except three had their initial tensile stress axis within 8° of [001], the others were between 8° and 14° of [001]. There were no obvious differences in deformation behaviour. Consequently, specimen orientation effects were ignored.

The specimens were tested at 710MPa/1023K, 430MPa/1123K and 225MPa/1223K. The results are listed in appendix A and plotted in figure 1.13. It is clear that small increases in the Ti content considerably improve the stress-rupture life at 1023K and 1123K. At 1223K the improvement in properties still occurs but is less substantial.

The γ' shearing mode at 1023K and 1123K is expected to be a combination of superdislocation and partial dislocation shear. The effects of this are discussed in 7.5. At 1223K it is expected that γ' shearing would be occurring mainly by $a/_2\langle 110\rangle \{111\}$ superdislocation glide with only a small contribution from partial dislocation glide; however, some of the deformation would be occurring by the climb of $a/_2\langle 110\rangle$ dislocations in the γ matrix allowing dislocations to by-pass the γ' particles.

7.5 The Effect of SSF and APB Energies on Stress-Rupture Life

The fault energy measurements reported in chapter 6 were representative of a temperature at or a little below 1173K. They should therefore show the best correspondence with the tests conducted at 1123K. The following discussion relates the measured energies at 1173K with the stress-rupture properties at 1123K.

It is clear from figure 1.17 that there is a major increase in stress-rupture life between alloy D and alloy A. This is in agreement with the observations of Roome (1982) who noted a drastic improvement in properties with a difference of 0.8at.% Ti from 1.84at.% to 2.62at.% Ti in overall alloy Ti content.

It is proposed that the improvement in stress-rupture life is brought about by a change in deformation mechanism due to the change in total fault energy induced by Ti. If it is assumed that the unstabilised SSF energies are equal for all three alloys, the APB energy would be considerably lower than the SSF energies, and deformation would occur only by superdislocation shear because it has the lowest total configuration energy. However, it appears that Ti does stabilise SSFs to some degree. The higher the Ti content the greater the fault stabilisation and consequently the lower the SSF energy. When the curves of energy versus Ti content shown in figures 6.5 and 6.10 are superimposed (fig. 7.5), it is seen that the APB energy and SESF energy are of the same order in alloys D and G. (The SISF energy was considerably higher than both the SESF and APB energies, therefore deformation by SISFs alone was thought to be unlikely.) Assuming that the dislocation configuration with the lowest total energy will provide the most prolific deformation mode, both superdislocation and partial dislocation shear would be occurring at 1173K in these two alloys. Although SESFs will form and will be stabilised by Ti, they will only slightly reduce the creep rate because γ' shearing by superdislocations would still occur because an insufficient number of $a/_2$<110> dislocations will be combining to produce the dislocations required for shear by partial dislocations. In support of this only a small increase in stress-rupture life is observed between alloys G and D because the strengthening effect of SSF pinning was annulled by the continuation of superdislocation shear.

Figure 7.5 shows that at 1170K in alloy A the SESF energy is lower than the APB energy, therefore it is easier to form SESFs than APBs and the partial dislocation configuration will have the lowest energy. Consequently deformation by superdislocations is much less likely. As a result of·this nearly all deformation will be by partial dislocation shear. The glide of partial dislocations bounding SESFs and SESF/SISF pairs will be retarded by fault stabilisation due to Ti. This will increase the shear resistance of the γ' and as observed for alloy A the stress-rupture life should be increased.

These observations support the hypothesis (Roome, 1982 and fig. 1.14b) that for a given test condition - Roome used 760MPa at 1033K and this investigation used 410MPa at 1123K - partial dislocation shear occurs at lower temperatures with increasing Ti content and that the early onset of partial dislocation shear increases stress-rupture life. Using the

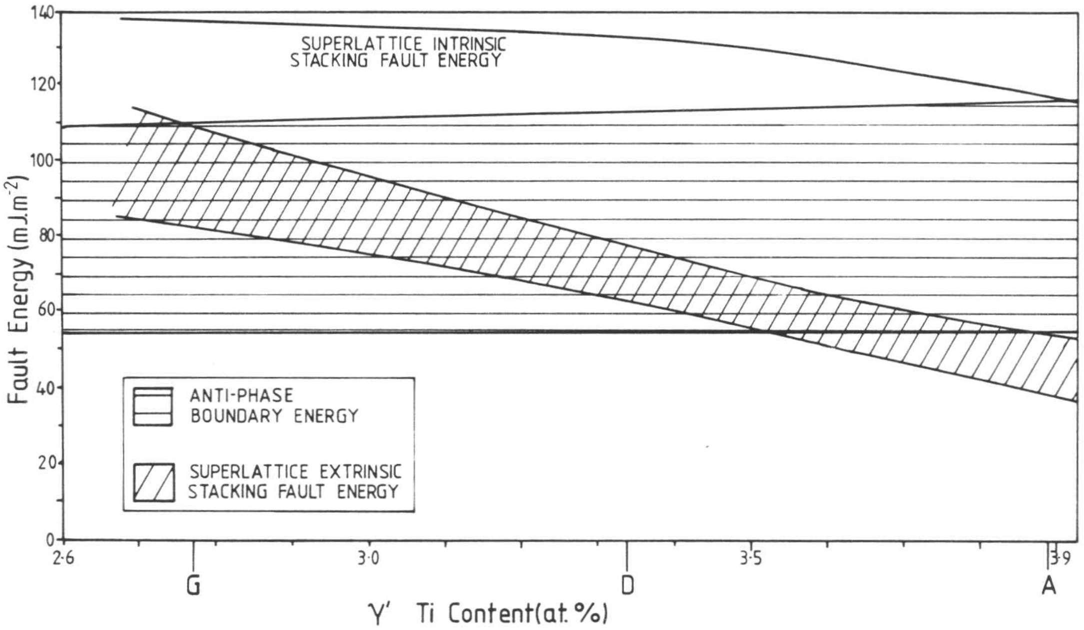

Fig. 7.5. The variation of the APB energy and the SSF energies versus γ' titanium content for alloys A, D and G.

results of this investigation this effect has now been explained by the observed drop in SESF energy lowering the partial dislocation configuration energy to a value below the superdislocation configuration energy with increasing Ti. This is brought about by the segregation of Ti stabilising faults; perhaps by forming thin planar regions on the SSFs which have the Ni_3Ti structure. A schematic representation of the relationship between deformation mechanism, temperature and titanium content proposed as a result of this investigation is shown in figure 7.6. For alloys based on A, D and G the change from mixed shear to partial dislocation shear occurred when the γ' Ti content was approximately 3.7at.% (which is equivalent to an overall Ti content of about 2.6at.%). The best intermediate temperature stress-rupture resistance in this series of alloys will be obtained with alloys which contain greater than 2.6at.% Ti.

The properties are unlikely to continue to improve if considerably larger amounts of Ti are added as these may have a deleterious effect on other properties such as alloy phase stability.

7.6 The Effect of Changes in Strain Rate and Creep Activation Energy Predicted from the Modified Deformation Model

(i) Strain rate

At a given test temperature the fault pinning mechanism may be related to the strain rate. At low strain rates (i.e. in creep), dislocations will be moving fairly slowly through the γ' so sufficient time will be available for Ti to diffuse to and stabilise the moving dislocations. At high strain rates (i.e. in tensile tests) Ti diffusion cannot keep up with the dislocations (assuming the dislocation velocity is increasing with strain rate), and effective pinning will not occur.

At high temperatures Ti diffusion will be more rapid and fault stabilisation can occur more easily. Hence fault stabilisation will be effective to high strain rates. At very high temperatures, however, fault

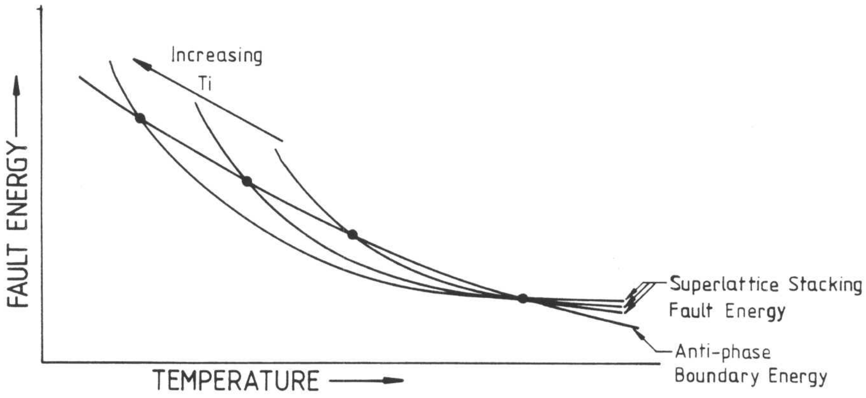

Fig. 7.6. A schematic illustration of the predicted variation in fault energy with titanium content proposed as a result of this investigation.

stabilisation will be ineffective at all strain rates because it will not be thermodynamically favourable for segregation to faults to occur. At low temperatures fault stabilisation will be inoperative because there will not be enough Ti diffusion to form atmospheres on the faults.

(ii) Activation energy

Tien, Kear and Leverant (1972) report that the activation energy for primary creep in single crystal superalloys at 1033K is about 220kJmol^{-1}. They also report that this value increases to about 650kJmol^{-1} when the specimen enters secondary creep, with no obvious change in deformation mechanism. They explain the low value in primary creep by suggesting that it is controlled by vacancy diffusion. They then suggest that the onset of secondary creep coincides with the exhaustion of vacancy diffusion leading to a rise in the activation energy to that characteristic of interstitial diffusion. It is suggested that this mechanism is highly unlikely; interstitial diffusion is only significant for large atoms very close to the melting point.

It may be possible to explain the large increase in activation energy using the model proposed here. It is suggested that at intermediate temperatures in primary creep glide deformation of the γ' is occurring by partial dislocation shear of dislocation combinations present in the structure. The activation energy for this process will be approximately equivalent to the diffusion of Ti in the γ' because the rate controlling step will be Ti diffusion which is required to allow the stabilised stacking faults to move. Secondary creep may begin when the initial dislocation configurations are exhausted. The activation energy will increase to that for dislocation climb in the γ because the rate controlling step will now be dislocation climb to form new dislocation combinations which can glide into the γ'. The application of this mechanism may explain the large increase in activation energy observed by Tien et al. (1973) while maintaining the same deformation mechanism.

Much further work is necessary in order to show that the strain rate sensitivity and activation energies follow the patterns proposed here.

7.7 Summary

Previously it has been shown that Ti stabilises the SSFs by stabilising the region of Ni_3Ti stacking on the fault plane. In this chapter a modification to the established deformation mechanism is suggested where the SSFs formed during partial dislocation shear are stabilised by the diffusion of Ti to the faults. It is also shown that this mechanism may be related to strain rate and creep activation energies, and suggested that experiments should be performed to confirm this.

Chapter 6 shows that the SSF energy decreases with increasing titanium content and this observation has been related to the stress-rupture properties of alloys A, D and G. It is shown here that the modified mechanism can be used to explain the increase in stress-rupture life between alloys D and A when stressed at 430MPa and 1123K. In the cases of alloys D and G the SESF and APB energies are similar and shear of the γ' will occur by a mixture of superdislocation and partial dislocation shear; locking of the SSFs is ineffective because superdislocations are still readily formed. In alloy A the SESF energy is lower than the APB energy and it is predicted that γ' shear occurs by SESF ribbons and SESF/SISF pairs, where the SSFs are strongly pinned. This produces a considerable increase in stress-rupture life because superdislocations cannot form and γ' shear is considerably decreased.

A similar but less pronounced trend is observed at 710MPa and 1023K but it is impossible to draw any conclusion about the effect of the fault energies on this curve as no values have been measured near this temperature. It is suggested that the increase in properties is also due to some change in the proportions of superdislocation shear and partial dislocation shear with increasing temperature.

The tests at 225MPa and 1223K show a gradual increase in life with increasing titanium content. Again, it is impossible to draw any conclusions about the deformation mechanism but it is thought that the APB energy is lower than that at 1123K and the fault pinning mechanism is less effective than at 1123K because the temperature may be high enough for the formation of Ni_3Ti to be energetically unfavourable.

It was not possible to verify the predictions made in this chapter because no TEM was performed on interrupted stress-rupture test specimens and energy results were only measured at one temperature. It would be interesting to examine crept microstructures, measure the activation energies and study the diffusion rates of alloying elements in superalloys as this would add to the knowledge of alloy deformation behaviour. It would also be interesting to measure the energies of APBs and SSFs at a range of temperatures and compare these values with observations of crept microstructures. In this way it would be possible to build up a picture of alloy deformation in creep.

It is clear from the work reported in this thesis that titanium has a major strengthening effect in Ni-base single crystal superalloys. Further research ought to be carried out in a similar way to examine the strengthening role played by other alloying elements such as tantalum and niobium.

CHAPTER 8

CONCLUSIONS AND SUGGESTIONS FOR FURTHER WORK

The major conclusions from this work are summarised below with some suggestions for further research.

8.1 Conclusions

8.1.1 Homogenisation

The single crystal alloys studied achieve adequate homogeneity after annealing for 32 hrs at 1570K. This homogeneity is both long range and on the level of individual γ' particles.

After homogenisation the misfit between extracted γ and γ' is found to be negligible. It is concluded that variation of the Ti content between 1.8at.% and 2.7at.% has no effect on the misfit, presumably because the Ti content of both the γ and the γ' increases by a similar amount through the alloy series.

The γ/γ' misfit and the γ' composition are not perceptibly changed when the γ' particles are coarsened to about 0.5μm by treating for 16 hrs at 1390K.

The heat treatment of 36 hrs at 1570K followed by 16 hrs at 1390K produces specimens with the same γ' volume fraction, γ' particle size and γ/γ' misfit. There is presumably also a negligible difference in the solid solution strengthening of the matrix.

8.1.2 Dislocation interactions

An extension of the mechanism proposed to describe the formation of three-fold nodes in FCC metals (Whelan, 1959) has been used to describe the formation of three-fold supernodes and hexagonal dislocation networks in $L1_2$ ordered structures. Weak beam dark field TEM shows that the proposed mechanism adequately explains the experimental observations.

It is found that two different a<110> superdislocations gliding on the same or different {111} planes can combine to form a third a<110> dislocation and produce two three-fold supernodes and the dislocation intersections. Many interactions produce arrays of screw superdislocations in hexagonal networks. Two different supernodes are produced, one consisting of $a/_6$<211> partial dislocations and complex faults, and the other consisting of $a/_2$<110> dislocations and APBs. In most cases the nodes extend to form alternate regions of intrinsic and extrinsic superlattice stacking fault at the nodal points. The dislocations between the faulted and unfaulted crystal are shown to be $a/_3$<211> partial dislocations, while the boundaries between APBs and SSFs are shown to be $a/_6$<211> partial dislocations. The extended superlattice extrinsic stacking faults (SESF) have larger areas than the extended superlattice intrinsic stacking faults (SISF).

Superdipoles have also been observed in deformed and annealed specimens and two mechanisms are proposed for their formation. These mechanisms are extensions of those proposed for dipole formation in disordered FCC materials. Superdipoles are shown to consist of a loop of APB bounded by like $a/_2$<110> dislocations.

Square dislocation networks lying either on two intersecting {111} planes or on one {001} plane are reported. These seem to form by the intersection of $a/_2$<110> dislocation pairs with Burgers vectors which intersect at 90° gliding on {111} planes. An area of unfaulted crystal is created at the point of intersection. This region is stable and locks the network. At high temperatures the {111} network may cross-slip onto a {001} plane where the APB energy is lower, thus forming a lower energy network.

Large planar defects are observed. TEM analysis shows these to be equivalent to SESFs bounded by $a/_3$<211> partial dislocations. A mechanism for their formation is proposed. It is noted that the SESF is equivalent to seven layers of the Ni_3Ti structure. It is proposed that titanium diffuses to the faults and stabilises them by forming planar regions of Ni_3Ti. Alloy A, which has the highest Ti content, contains the largest number of planar faults.

8.1.3 The effect of titanium on fault energy

No significant variation is found in the APB energy of γ' with titanium content in single crystal superalloys containing between 1.8 and 2.7at.% titanium. There is, however, a large range of values for each alloy. The mean APB energy using anisotropic elasticity is $83\pm20mJm^{-2}$ for screw superdislocations at about 1170K. The large range of values may be due to a small contraction of the APB during cooling from 1170K. If this does occur it will raise the APB energy above the value at 1170K.

A new method has been presented for the determination of SSF energy from the extended three-fold supernodes of the superdislocation networks. The method enables the determination of SSF energies as a function of node shape and size.

It is found that the SSF energies decrease with increasing titanium content. The mean SESF energies at 1170K are 94±15, 74±10 and $46\pm12mJm^{-2}$ for alloys G, D and A respectively while the equivalent SISF energies are 137, 131±10 and $117\pm5mJm^{-2}$ respectively. The SESF energy is considerably lower than the SISF energy in all cases.

It is proposed that the differences in SSF energy are due to fault stabilisation by the segregation of Ti to the faults. Calculations indicate that bulk diffusion of Ti to the centre of a particle of $Ni_3(Al_{0.6}Ti_{0.4})$ takes about 16 minutes at 1173K. Owing to the complex composition bulk diffusion is likely to be slower in the γ' of the alloys studied, but it is thought that equilibrium is achieved in less than 16 hrs. The SSFs may be stabilised by the formation of Ni_3Ti on the fault plane although no evidence for this has been obtained. The Ti stabilised SESF energy is lower than the Ti stabilised SISF energy because the SESF is equivalent to a thicker region of the Ni_3Ti than the SISF.

8.1.4 The effect of titanium on superalloy deformation

It is proposed that the wide SSFs and SSF pairs observed by other workers in the partial dislocation shear régime can be explained in terms of fault stabilisation by Ti. No change to the dislocation configurations is suggested but it is thought that Ti diffuses to the faults and stabilises them. In the appropriate temperature range stabilised faults are effectively pinned by the Ti: the mechanism can be likened to Suzuki locking. Glide of the partial dislocations cannot continue unless the stabilising Ti diffuses with the fault or the fault can break away from the stabilising atmosphere. Using data for $Ni_3(Al_{0.6}Ti_{0.4})$ and a secondary creep rate of alloy A, it is shown that Ti diffusion can keep up with partial dislocation glide at temperatures above 630K. This temperature is expected to be higher for the γ' of alloys A, D and G because they contain elements such as Ta and W which should considerably reduce Ti diffusion.

Tests show that the stress-rupture life improves with increasing Ti in all conditions. This improvement is most obvious at 1123K and 410MPa. The SESF energies in alloys D and G lie within the band of APB energies but that SESF energy is lower than the APB energy in alloy A. The stress-rupture life of alloy A is considerably longer than that of alloy G. It is suggested that alloys D and G deform by a combination of superdislocation shear and partial dislocation shear. SESF stabilisation by Ti will occur but slip can still readily occur by the passage of superdislocations. In alloy A, however, the dislocation interactions necessary to produce SESFs will occur more readily than those to produce APBs. γ' shear will occur mainly by partial dislocation glide but this will be retarded by the stabilisation of SESFs by Ti. This effect may produce the large difference in properties between alloys A and G.

It is predicted that at a given test temperature stress-rupture life is improved if enough Ti is added to produce stabilised SSF configurations with lower energies than the APB configurations. Adding Ti lowers the temperature of the change from superdislocation shear to partial dislocation shear. When more than 2.6at.% Ti is added the SESF energy is lower than the APB energy and it is thought that deformation by partial dislocation shear predominates at 1170K. This can then lead to an increase in stress-rupture life over a similar alloy with a Ti content less than 2.6at.%.

It has been shown that contrary to the predictions of other workers Ti lowers the SSF energies relative to the APB energy, the latter being unaffected by Ti content within the limits of experimental error.

8.2 Suggestions for Further Work

8.2.1 Homogenisation

Detailed theoretical modelling of the homogenisation process is desirable since the heat treatment window and defect energies depend critically on compositional variations. It is anticipated that the problem may be very difficult since the model must treat complex multicomponent diffusion and very few superalloy diffusion data are available. However, it may be possible to simplify the system by approximating it to a binary or a ternary system.

The misfit between extracted γ and γ' at room temperature was found to be negligible but it may depend on temperature. It would be interesting to measure the thermal expansivity of the two phases, using a dilatometer, either as extracts or by manufacturing alloys with γ and γ' compositions. In this way it may be possible to determine if misfit strengthening is related to temperature.

8.2.2 Deformation mechanisms

It has been observed that the SSF energies decrease with increasing Ti content. It is proposed that this is due to Ti migrating to, and stabilising, the SSFs. However, the operation of this process could not be properly confirmed because very few data are available for the diffusion coefficients and activation energies for elemental self-diffusion in the γ' of complex alloys. It is vital to the development of the ideas proposed in this thesis that this lack of data is rectified. The most useful values would be those for Ti diffusion; these could perhaps be found by the use of radioactive tracer techniques to follow Ti diffusion at various temperatures in an alloy with the γ' composition.

The creation and analysis of superdislocation networks and the formulation of a method to evaluate the SSF energies from extended supernodes has established a technique for the evaluation of APB and SSF energies in ordered materials. This investigation has been limited to small variations in one alloy component at one temperature. It is now up to other workers to study the effect of temperature on fault energies either by heat treating networks for long periods at different temperatures and then examining them at room temperature in the TEM, or by studying the behaviour of the networks using a heating stage in the TEM to watch changes in the supernodes in situ.

Further work should also be considered to study the effect of other alloying elements (for example, Nb and Ta) which are thought to affect superalloy strength by changing the fundamental defect energies.

Many interesting and unusual dislocation configurations have been observed in deformed and annealed superalloy microstructures but many have not been analysed. A considerable amount of work could be undertaken to study these other interactions. It would also be interesting to carefully control the deformation of samples to find how stress and strain rate affect the dislocation interactions produced, particularly the hexagonal networks.

Contributions to alloy strengthening by dislocations by-passing the γ' particles have been largely ignored by workers studying superalloy deformation. Most recent improvements in superalloy strengthening mechanisms act to reduce dislocation glide through the γ' by lowering the SSF energy and cause partial dislocation glide. This process increases the dislocation density in the γ matrix. At intermediate and high temperatures it is likely that many un-paired dislocations climb around the γ' particles because the γ cannot glide through. It is suggested that it would be useful to study dislocation behaviour in the γ region of high γ' volume fraction superalloys and relate this behaviour to alloy strengthening, particularly at high temperatures.

The literature contains a considerable amount of data for flow stresses measured from high strain rate tensile tests but very little data for low strain rate creep and stress-rupture tests. This seems strange as most service failures of turbine blades occur in creep. It is suggested that more investigations of the type undertaken here should be performed to study the effect of alloy composition on deformation mechanisms and defect energies. Studies should also be undertaken to study deformation mechanisms during creep by the TEM examination of foils manufactured from interrupted test specimens. Experiments of this type could be used to build up an overall picture of creep properties which relates alloy composition, strain rate, temperature and deformation mechanism.

Up to the present time superalloy design has been largely empirical but to gain further improvements in superalloy properties the effects of specific elements on alloy behaviour need to be studied closely if alloys with the optimum properties for their applications are to be produced. Single crystal superalloys will be useful tools in the search for improved superalloys because they can be fully homogenised, they contain very little carbon and no grain boundaries. This means that it is possible to study the effect of small changes in alloy composition on behaviour without the effects of inhomogeneities introduced by factors such as grain boundary segregation and carbide precipitation.

Appendix A. Stress-rupture Test Results

Test conditions		Alloy	Life to failure (hrs)
Stress (MPa)	Temperature (K)		
710	1023	A 1	337.2
		2	336.2
		D 1	217.1
		2	216.4
		3	194.3
		G 1	176.2
		2	136.3
430	1123	A 3	197.8
		4	217.0
		5	235.8
		D 4	118.0
		5	113.9
		6	107.8
		G 3	117.8
		4	98.5
		5	113.4
225	1223	A 6	181.0
		7	190.2
		D 7	164.9
		8	138.1
		9	130.9
		G 6	115.2
		7	100.4

Appendix B. Calculation of the Homogenisation Time Using $X=\sqrt{Dt}$

This simple calculation has been performed by approximating inhomogeneous as-cast material to a binary FCC solid solution of nickel with the most severely segregated element, in this case tungsten.

Figure B.1 shows an SEM/EDS trace of the distribution of tungsten across three dendrite arms.

According to Walsh and Donachie (1969) between 1273 and 1589K the diffusion coefficient for tungsten in nickel is:

$$D_W = 1.19\text{x}10^{-4}\exp(-0.0469c_W)\exp(\frac{-3.69\text{x}10^4}{T})\text{m}^2\text{s}^{-1} \qquad \text{eqn. B.1}$$

where T is the homogenisation temperature and c_W is the tungsten concentration.

The homogenisation temperature used is 1573K and the overall alloy tungsten content is 2·8 at.%. This gives a value of 6·77x10^{-15} m^2s^{-1} for the diffusion coefficient.

Substituting this value in $X=\sqrt{Dt}$ where X is the maximum distance a tungsten atom is required to diffuse and t is the time taken for complete homogenisation.

From figure B.1 X=32µm

$$t = \frac{X^2}{D} = 42{\cdot}02\,\text{hrs} \qquad \text{eqn. B.2}$$

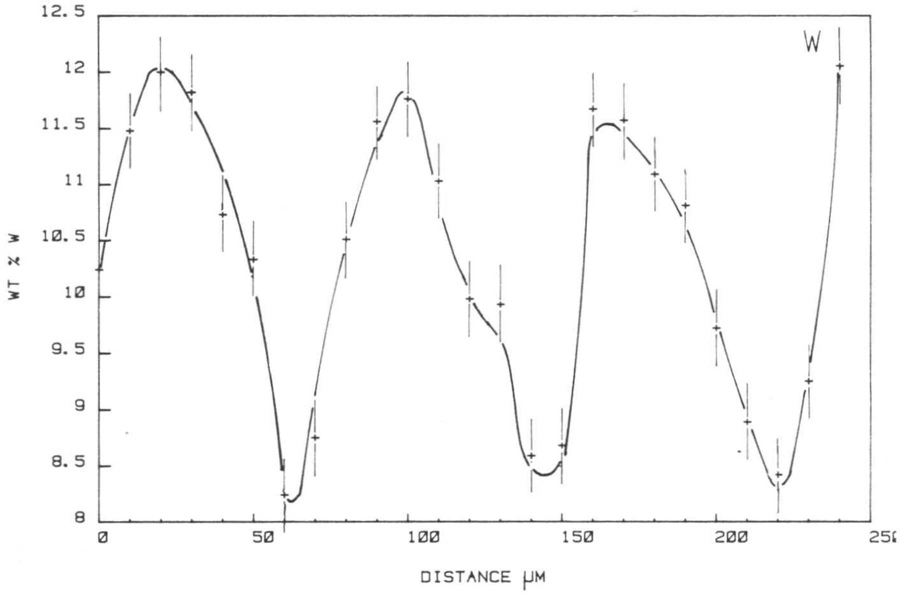

Fig. B.1. SEM/EDS analysis trace for tungsten taken across three dendrite arms of as-cast alloy A.

Appendix C. Comments on the Analysis Data Produced by the Link 860

Tables 2.1 and 2.2 show that there are considerable variations in the analysed Al contents of the γ and γ' obtained from the homogenised alloys by the Philips 400T and Link 860 analysis system. It is thought that this variation may be caused by the background subtraction performed by the Link 860. To find the background count level the system assesses the counts at either end of an analysis window which includes the peak it is analysing. It then uses these end points to calculate the background level under the peak and subtracts this from the gathered symbol to leave the counts collected from the element it is analysing.

It can be seen from figure C1 that for the alloys studied the Ta and W M_α peaks are close to the Al K_α peak and that they are situated at one end of the sampling window. The presence of the Ta and W peaks may cause the Link software to assess an incorrect Al background. Compared to Ta and W, Al is a light element and small changes in the background caused by small changes in the Ta and W may produce considerable errors in the Al content calculated by the Link.

More accurate Al data will be gained if the background assessment window is narrowed to avoid the Ta and W peaks or if the Ta and W M_α peaks are subtracted before the Al background is assessed.

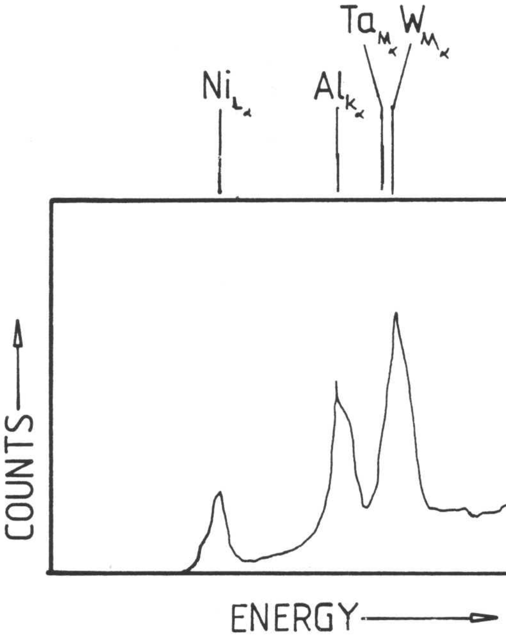

Fig. C.1. Section from an EDS spectrum gathered from the γ' of a fully homogenised thin foil of alloy A. Note the close proximity of the W and Ta M_α peaks to the Al K_α peak.

Appendix D. Calculation of the Superlattice Stacking Fault Energy from Extended Supernodes (After Rae, 1984)

Equations representing the stress field of each of the screw dislocation segments shown in figure D.1 are used to calculate the total stress field on a point O on dislocation 6. The stress field for each dislocation is calculated using a separate co-ordinate system (x_j, y_j, z_j) for each dislocation where the z_j axis lies along the dislocation line and the x_j axis is normal to the plane of the node. The stress fields due to each dislocation are then resolved on the co-ordinate system (X, Y, Z) of dislocation 6 to calculate the force on that dislocation.

The only non-zero component for the Burgers vector of a screw dislocation is b_z. Thus the only non-zero stress component is σ_{xz} (Hirth and Lothe, 1982) which will subsequently be referred to as σ_j, the stress on dislocation j:

$$\sigma_j = \frac{\mu\, b_j}{4\pi} \frac{y}{M(M+L)} \qquad \text{Eqn. D.1(a)}$$

where μ is the isotropic shear modulus taken to equal $[C_{44}(C_{11}-C_{12})/2]^{\frac{1}{2}}$, $M^2=x^2+y^2+(z-z_j)^2$, $L=z_j-z$, y and z are the co-ordinates of O relative to the axes based on the segment under consideration and z_j and z_j' are the end points of the dislocation under consideration.

It follows that:

$$\sigma_j(z_j) = \frac{\mu b_j}{4\pi}\left[\frac{y}{(y^2+(z-z_j)^2)^{\frac{1}{2}}((y^2+(z-z_j)^2)^{\frac{1}{2}}+(z_j-z))}\right] \qquad \text{Eqn. D.1(b)}$$

Consequently the stress on dislocation i from z_j to z_j' is

$$\sigma_j = \sigma_j(z_j)-\sigma_j(z_j').$$

It is assumed that dislocations 4 and 5 have infinite length. The stress fields of dislocations 7 and 8 have no component in

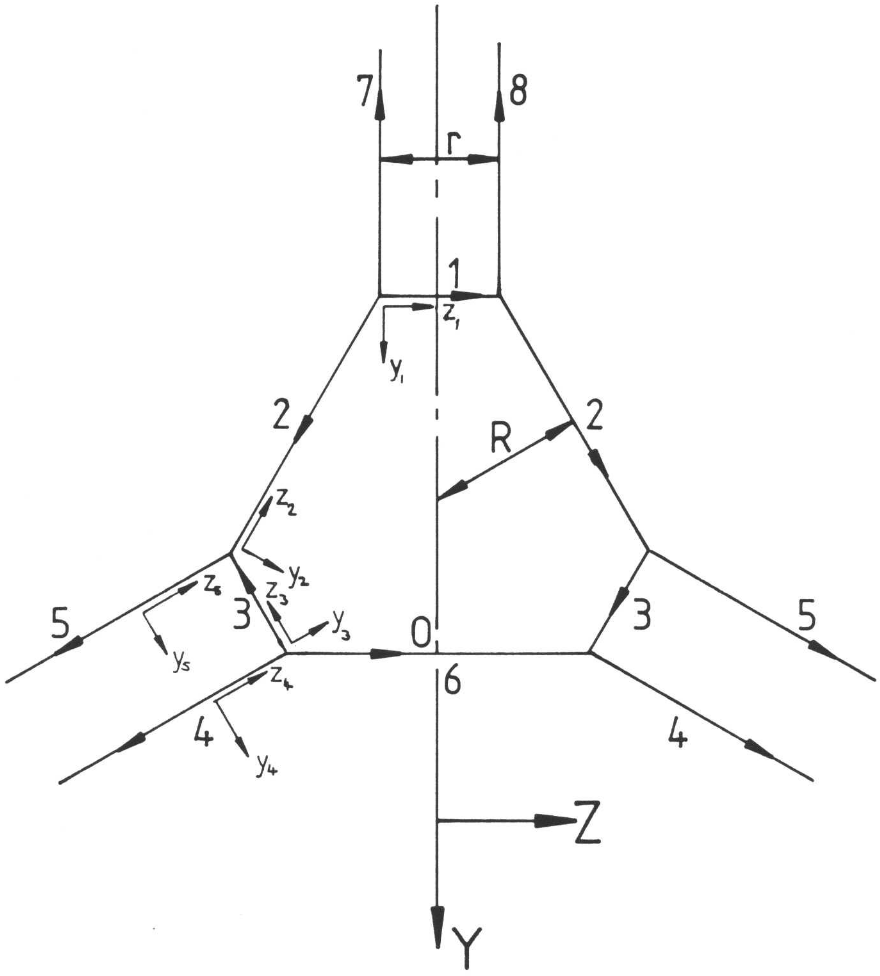

Fig. D.1. Dislocation configuration at a supernode showing the co-ordinate axes used to evaluate the stress field of each dislocation.

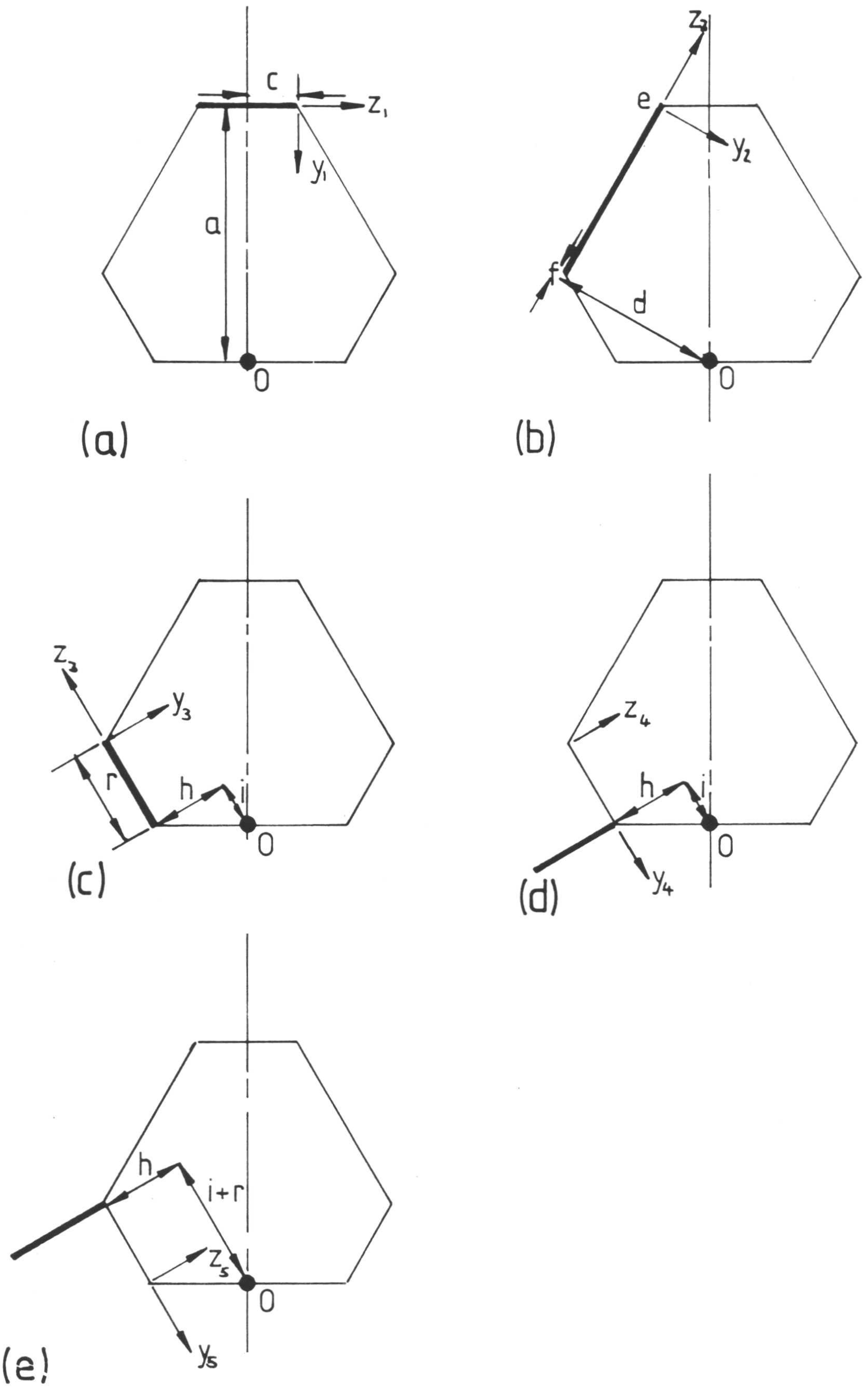

Fig. D.2. Illustration showing the co-ordinate systems and parameters used to evaluate the stress field of dislocation 1, (a); dislocation 2, (b); dislocation 3, (c); dislocation 4, (d); and dislocation 5, (e).

the Z reference direction so they have no effect on the calculation and can be ignored.

Stress on dislocation 1 (fig. D.2a)

Co-ordinates of dislocation origin:

$$x=0,\ y=a,\ z=0$$

limits:

$$z_1=-c,\ z_1'=+c$$

$$\sigma_1 = \frac{\mu b}{4\pi}\left[\frac{2c}{a(a^2+c^2)^{\frac{1}{2}}}\right] \qquad \text{eqn. D.3(a)}$$

In terms of the node dimensions R and r:

$$a = \frac{3R-\sqrt{3}r}{2} \text{ and } c = \frac{r}{2}$$

Substituting these in eqn. D.3(a) gives:

$$\sigma_1 = \frac{\mu b_1}{4\pi}\left[\frac{r}{\frac{(3R-\sqrt{3}r)}{2}(9R^2-3\sqrt{3}Rr+r^2)^{\frac{1}{2}}}\right] \qquad \text{eqn. D.3(b)}$$

Stress on dislocation 2 (fig. D.2b)

Co-ordinates of dislocation origin:

$$x=0,\ y=d,\ z=\pm f$$

limits:

$$z_2=0,\ z_2'=e$$

$$\sigma_2 = \frac{\mu b_2 d}{4\pi}\left[\frac{1}{(d^2+(e-f)^2)^{\frac{1}{2}}[(d^2+(e-f)^2)^{\frac{1}{2}}+(e-f)]} - \frac{1}{(d^2+f^2)^{\frac{1}{2}}[(d^2+f^2)^{\frac{1}{2}}-f]}\right] \qquad \text{eqn. D.4(a)}$$

In terms of the node dimensions:

$$d=\frac{3R}{2},\ e=2(\sqrt{3}R-r),\ f=\frac{(\sqrt{3}R-r)}{2}$$

Substituting these in eqn. D.4(a) gives:

$$\sigma_2 = \frac{3\mu b_2 R}{8\pi}\left[\frac{1}{(9R^2-3\sqrt{3}Rr+r^2)^{\frac{1}{2}}[(9R^2-3\sqrt{3}Rr+r^2)^{\frac{1}{2}}+\frac{3}{2}\sqrt{3}R-r]}\right.$$

$$\left.-\frac{1}{(3R^2-\sqrt{3}Rr+r^2)^{\frac{1}{2}}[(3R^2-\sqrt{3}Rr+r^2)^{\frac{1}{2}}-(\frac{\sqrt{3}}{2}R-r)]}\right] \qquad \text{eqn. D.4(b)}$$

Stress on dislocation 3 (fig. D.2c)

Co-ordinates of dislocation origin:

$x=0,\ y=h,\ z=-i$

limits:

$z_3=0,\ z_3'=r$

$$\sigma_3 = \frac{\mu b_3 h}{4\pi}\left[\frac{1}{(h^2+(r-i)^2)^{\frac{1}{2}}[(h^2+(r+i)^2)^{\frac{1}{2}}+r+i]} - \frac{1}{(h^2+i^2)^{\frac{1}{2}}[(h^2+i^2)^{\frac{1}{2}}+i]}\right] \qquad \text{eqn. D.5(a)}$$

In terms of the node dimensions:

$$h^2+(r+i)^2 = [3R^2-\sqrt{3}Rr-4r^2] \ ;$$

$$h^2+i^2 = (\sqrt{3}R-r)^2 \quad ; \quad h = \frac{3R-\sqrt{3}r}{2}$$

Substituting these in eqn. D.5(a) gives:

$$\sigma_3 = \frac{\mu b_3(3R-\sqrt{3}r)}{8\pi}\left[\frac{1}{(3R^2-\sqrt{3}Rr+r^2)^{\frac{1}{2}}\left[(3R^2-\sqrt{3}Rr+r^2)^{\frac{1}{2}}+\frac{\sqrt{3}R+r}{2}\right]} - \frac{1}{\frac{3}{2}(\sqrt{3}R-r)^2}\right] \qquad \text{eqn. D.5(b)}$$

Stress on dislocation 4 (fig. D.2d)

Co-ordinates of dislocation origin:

$x=0,\ y=i,\ z=h$

limits:

$z_4=0,\ z_4'=\infty$

$$\sigma_4 = \frac{\mu b_4 i}{4\pi} \frac{1}{(i^2-h^2)^{\frac{1}{2}}[(i^2+h^2)^{\frac{1}{2}}+h]} \qquad \text{eqn. D.6(a)}$$

but:

$$(i^2+h^2)^{\frac{1}{2}} = 2i \quad ; \quad h = \sqrt{3}i$$

In terms of the node dimensions:

$$i = \frac{(\sqrt{3}R-r}{2}$$

Substituting eqn. D.6(a) gives:

$$\sigma_4 = \frac{\mu b_4}{4\pi} \frac{1}{(\sqrt{3}R-r)(2+\sqrt{3})} \qquad \text{eqn. D.6(b)}$$

Stress on dislocation 5 (fig. D.2e)

Co-ordinates of dislocation origin:

$$x=0, \ y=(i+r), \ z=h$$

limits:

$$z_5=0, \ z_5'=\infty$$

$$\sigma_5 = \frac{+\mu b_5(i+r)}{4\pi} \left[\frac{1}{((i+r)^2+h^2)^{\frac{1}{2}}[((i+r^2)+h^2)^{\frac{1}{2}}+h]}\right] \qquad \text{eqn. D.7(a)}$$

In terms of the node dimensions:

$$i+x = \frac{\sqrt{3}R+r}{2} \quad ; \quad h = \frac{3R-\sqrt{3}r}{2}$$

Substituting in D.7(a) gives:

$$\sigma_5 = \frac{\mu b_5}{8\pi} \left[\frac{(\sqrt{3}R+r)}{(3R^2-\sqrt{3}Rr+r^2)^{\frac{1}{2}}\left[(3R^2-\sqrt{3}Rr+r^2)^{\frac{1}{2}}+\frac{3R-\sqrt{3}R}{2}\right]}\right] \qquad \text{eqn. D.7(b)}$$

Resultant resolved stress on dislocation 6

The resultant resolved force, F, on dislocation 6 is the sum of the stresses on all the component dislocation segments resolved along Z_6:

$$F = [\sigma_1+2\sigma_2\cos60-2\sigma_3\cos60+2\sigma_4\cos30+2\sigma_5\cos30].b_6$$

$$F = [\sigma_1+\sigma_2-\sigma_3+\sqrt{3}\sigma_4+\sqrt{3}\sigma_5]\cdot b_6 \qquad \text{eqn. D.8}$$

So, equating this with the SSF energy of the supernode gives:

$$\gamma_{SSF} = [\sigma_1+\sigma_2-\sigma_3+\sqrt{3}\sigma_4+\sqrt{3}\sigma_5]\cdot b_6 \qquad \text{eqn. D.9}$$

Appendix E. Anti-phase Boundary Energy Results

Alloy A (γ' Ti content = 3.9 at.%)

Dislocation Spacing (nm)	Energy (mJm^{-2})
8.4	86
6.75	107
6.56	110
10.5	69
8.36	86
8.55	85
6.35	114
9.32	78
9.42	77
9.17	78
10.39	70
9.30	78
8.78	83
9.12	80
10.61	68
7.95	91
10.11	71
12.12	60
7.21	100
9.74	74

Alloy D (γ' Ti content = 3.3 at.%)

Dislocation Spacing (nm)	Energy (mJm^{-2})
6.36	114
11.27	64
13.13	55
8.02	90
8.02	90
10.26	70
10.31	70
8.75	83
10.00	72
10.47	69

Alloy G (γ' Ti content = 2.8 at.%)

Dislocation Spacing (nm)	Energy (mJm^{-2})
7.54	96
6.70	108
6.29	115
6.29	115
12.66	57
12.66	57
8.89	81
8.51	85
9.14	79
9.14	79
9.89	73
7.44	97

Appendix F. Superlattice Stacking Fault Energy Results

Intrinsic supernodes

Alloy	Dislocation Spacing r (nm)	Internal Radius R (nm)	ρ (r/R)	Energy γ_{SISF} (mJm^{-2})
A	9	6.5	1.38	117
(γ'Ti=3.9 at.%)	9	6.5	1.38	117
	9	6.5	1.38	117
	9	6.5	1.38	117
	9	6.5	1.38	117
	9	6.5	1.38	117
	8	6.0	1.33	119
D	9	6	1.5	134
(γ'Ti=3.3 at.%)	9	6	1.5	134
	9	6.5	1.38	117
	9	6	1.5	134
	9	6	1.5	134
	9	6	1.5	134
G				
(γ'Ti=2.8 at.%)	6	5	1.2	137

Extrinsic supernodes

Alloy	Dislocation Spacing r (nm)	Internal Radius R (nm)	ρ (r/R)	Energy γ_{SESF} (mJm^{-2})
A	9	12	0.75	55
(γ'Ti=3.9 at.%)	9	14	0.64	47
	9	16.5	0.55	40
	9	14	0.64	47
	9	13.5	0.66	49
	9	14.4	0.62	45
	8	13.5	0.59	49
	8	17	0.47	39
D	9	9.5	0.95	70
(γ'Ti=3.3 at.%)	9	8.5	1.06	79
	9	9	1	74
	9	9	1	74
	9	8.5	1.06	79
	9	9	1	74
	6.5	10.5	0.62	63
	9	9	1	74
	9	8.5	1	79
G	5	7.5	0.67	88
(γ'Ti=2.8 at.%)	5	7	0.71	94
	6.5	6.5	1	100
	7	8	0.88	82
	10	7	1.43	108

Appendix G. Calculation of the Minimum Temperature at which Titanium Diffusion is Rapid Enough to Move with a Pair of $a/_3\langle 211\rangle$ Dislocations

Consider the dislocation density, ρ, to be about $10^{13}m^{-2}$, the total Burgers vector of the dislocation bounding the fault to be $\underline{b}=a\langle 110\rangle$ and the secondary creep rate, $\dot{\varepsilon}$, (measured from alloy A) to be $6x10^{-8}s^{-1}$. When the gamma prime lattice parameter is 0.358nm the magnitude of b is about $5x10^{-10}m$.

The velocity of the gliding dislocation, v, is:

$$v = \frac{\dot{\varepsilon}}{\rho b} = 1.2x10^{-11}ms^{-1}. \qquad \text{eqn. G.1}$$

So in one second the dislocations will move $1.2x10^{-11}m$.

If titanium is to pin the dislocation it must also travel $1.2x10^{-11}m$ in one second.

Now, according to Larikov et al. (1982), the diffusion coefficient for titanium diffusion in $Ni_3(Al_{0.6}Ti_{0.4})$ is:

$$D = 1.9x10^{-10}\exp\left(\frac{-17462}{T}\right)m^2s^{-1} \qquad \text{eqn. G.2}$$

By substituting this into $\sqrt{Dt}=v$ the minimum temperature at which titanium diffusion is rapid enough to move with the dislocation is found to be 630K.

REFERENCES

E. Aerts, P. Delavignette, R. Siems and S. Amelinckx, 1962, J. Appl. Phys., 33, p3078

S. Amelinckx, 1956, Phil. Mag., 1, p269

S. Amelinckx, 1979, Dislocations in Solids: Volume 2, ed. F.R.N. Nabarro, North-Holland Publ. Co., Amsterdam, p67

I. Baker, D.V. Veins and E.M. Schulson, 1984, J. Mat. Sci., 19, p1799

R. Bakish and W.D. Robertson, 1956, Acta Met., 4, p342

A. Baldan, 1983, Phys. Stat. Sol. (a), 75, p441

C.C. Bampton, I.P. Jones and M.H. Loretto, 1978, Acta Met., 26, p39

B.E.P. Beeston, I.L. Dillamore and R.E. Smallman, 1968, Met. Sci. J., 2, p12

B.E.P. Beeston and L.K. France, 1968, J. Inst. Metals, 96, p105

W. Bell, W.R. Roser and G. Thomas, 1964, Acta Met., 12, p1247

J.D. Bernal, 1969, Science in History: Volume 1, C.A. Watts and Co. Ltd., London, p220

B.A. Bilby, R. Bullough and E. Smith, 1955, Proc. Roy. Soc., A231, p263

D. Blavette and A. Bostel, 1984, Acta Met., 32, p811

L.M. Brown and R.K. Ham, 1971, Strengthening Mechanisms in Crystals, eds. A. Kelly and R.B. Nicholson, App. Sci. Publ. Ltd., London, p9

L.M. Brown and A.R. Thölen, 1964, Disc. Faraday Soc., 38, p35

T. Carnahan, B. Cullen, J. Demel, J. McIlwain, M.J. Marcinkowski, J. Munford, J. Pahlman, T. Prevender and J. Warner, 1967, Trans. Met. Soc. AIME., 239, p2014

C. Carry, C. Houis and J.L. Strudel, 1981, Mem. et Etudes Sci. Rev. de Met., 78, p139

C. Carry and J.L. Strudel, 1975, Scripta Met., 9, p731

C. Carry and J.L. Strudel, 1979, Acta Met., 25, p767

C. Carry and J.L. Strudel, 1978, ibid., 26, p859

B. Chalmers, 1954, Trans. AIMME., 200, p519

J.W. Christian and P.R. Swann, 1967, Alloying Behaviour and Effects in Concentrated Solid Solutions, ed. T.B. Masalski, Gordon and Breach, New York, p105

C.T. Chou, P.B. Hirsch, M. McLean and E. Hondros, 1982, Nature, 300, p621

L.M. Clareborough, 1971, Aust. J. Phys., 24, p79

L.M. Clareborough and A.J. Morton, 1969a, Aust. J. Phys., 22, p351

L.M. Clareborough and A.J. Morton, 1969b, ibid., 22, p371

D.J.H. Cockayne, 1973, J. Microc., 98, p116

D.J.H. Cockayne, M.L. Jenkins and I.L.F. Ray, 1971, Phil. Mag., 24, p1383

D.J.H. Cockayne, P. Pirouz, Z. Liu, G.R. Anstis and P. Karnthaler, 1984, Phys. Stat. Sol. (a), 82, p425

D.J.H. Cockayne, I.L.F. Ray and M.J. Whelan, 1969, Phil. Mag., 20, p1265

S.M. Copley and B.H. Kear, 1967, Trans. Met. Soc. AIME., 239, p984

A.H. Cottrell, 1953, Dislocations and Plastic Flow in Crystals, Oxford University Press, p172

A.G. Cullis and G.R. Booker, 1972, Proc. 5th European Congress on Electron Microscopy, Manchester, Inst. of Phys., London, p532

B.D. Cullity, 1978, Elements of X-Ray Diffraction: 2nd Edition, Addison-Wesley Publ. Co. Inc., London.

J. Czernichow, J.P. Gudas, M.J. Marcinkowski and Wen Feng Tseng, 1971, Met. Trans., 2, p2185

R.G. Davies and N.S. Stoloff, 1965, Trans. AIME., 233, p714

R.F. Decker, 1969, Steel Strengthening Mechanisms, Climax Moly. Co., Zurich, p147

R.F. Decker and J.R. Mihalisin, 1969, Trans. ASM., 62, p481

D. Driver, D.W. Hall and G.W. Meetham, 1981, The Development of Gas Turbine Materials, Applied Science Publishers, London

R.C. Ecob, R.A. Ricks and A.J. Porter, 1982, Scripta Met., 16, p1085

K. Enami and S. Nenno, 1968, J. Phys. Soc. Japan, 25, p1517

J.D. Eshelby, W.T. Read and W. Shockley, 1953, Acta Met., 1, p251

E.A. Fell, 1961, Metallurgia, 63, p157

H. Fisher and M.J. Marcinkowski, 1961, Phil. Mag., 6, p1385

P.A. Flinn, 1960, Trans. Met. Soc. AIME., 218, p145

H. Föll, C.B. Carter and M. Wilkens, 1980, Phys. Stat. Sol. (a), 58, p393

L.K. France and M.H. Loretto, 1968, Proc. Roy. Soc., A307, p83

H.J. Frost and M.F. Ashby, 1982, Deformation-Mechanism Maps, Pergammon Press, Oxford, p57

P.C.J. Gallagher, 1966, Phys. Stat. Sol., 16, p95

R. Gevers, A. Art and S. Amelinckx, 1963, Phys. Stat. Sol., 3, p1563

H. Gleiter and E. Hornbogen, 1965, Phys. Stat. Sol., 12, p251

A.F. Giamei, J.M. Oblak, B.H. Kear and W.H. Rand, 1971, Proc. 29th An. Meeting EMSA, p112

D.A. Grose and G.S. Ansell, 1981, Metall. Trans., 12A, p1631

A. Havalada, 1969a, Trans. ASM, 62, p477

A. Havalada, 1969b, ibid., 62, p581

A.K. Head, P. Humble, L.M. Clareborough, A.J. Morton and C.T. Forwood, 1973, Computed Electron Micrographs and Defect Identification, North-Holland Publ. Co., Amsterdam

P. Hirsch, A. Howie, R.B. Nicholson, D.W. Pashley and M.J. Whelan, 1977, Electron Microscopy of Thin Crystals, 2nd Edition, Butterworths, London

J.P. Hirth and J. Lothe, 1982, Theory of Dislocations, 2nd Edition, J. Wiley and Sons, New York.

E. Hornbogen and M. Mukerjee, 1964, Z. Metallk., 55, p293

L.M. Howe, M. Rainville and E.M. Schulson, 1974, J. Nuc. Mat., 50, p139

A. Howie and C.H. Sworn, 1970, Phil. Mag., 22, p861

A. Howie and M.J. Whelan, 1961, Proc. Roy. Soc., A263, p217

A. Howie and M.J. Whelan, 1962, ibid., A267, p206

W.G. Johnston and J.J. Gilman, 1960, J. Appl. Phys., 31, p632

B.H. Kear, 1966, Acta Met., 14, p659

B.H. Kear, 1974, Proc. Int. Symp. on Order-Disorder Transformations in Alloys, Tubingen, Germany, ed. H. Warlimont, Springer-Verlag, Berlin, p440

B.H. Kear, A.F. Giamei, J.M. Silcock and R.K. Ham, 1968, Scripta Met., 2, p287

B.H. Kear, G.R. Leverant and J.M. Oblak, 1969, Trans. ASM, 62, p639

B.H. Kear and J.M. Oblak, 1974, J. Phys. Coll., 35, pC7-35

B.H. Kear, J.M. Oblak and A.F. Giamei, 1970, Metall. Trans., 1, p2477

B.H. Kear and G.F. Wilsdorf, 1962, Trans. Met. Soc. AIME., 224, p382

P.M. Kelly, A. Jostsons, R.G. Blake and J.G. Napier, 1975, Phys. Stat. Sol. (a), 31, p771

J.M. Kenyon, 1983, Part II project, University of Cambridge

J.S. Koehler and F. Seitz, 1947, J. Appl. Mech., 14, pA-217

L.N. Larikov, V.V. Geichenko and V.M. Fal'chenko, 1981, Diffusion Processes in Ordered Alloys, Amerind Publ. Co. Pvt. Ltd., New Delhi, p117

G.R. Leverant, M. Gell and S.W. Hopkins, 1970, 2nd Int. Conf. on the Strength of Metals and Alloys, ASM, p1141

G.R. Leverant, M. Gell and S.W. Hopkins, 1971, Mat. Sci. Eng., 8, p125

G.R. Leverant and B.H. Kear, 1970, Metall. Trans., 1, p491

G.R. Leverant, B.H. Kear and J.M. Oblak, 1973, Metall. Trans., 4, p355

M.H. Loretto, 1964, Phil. Mag., 10, p467

M.H. Loretto, 1969a, Phil. Mag., 12, p141

M.H. Loretto, 1969b, Phys. Stat. Sol., 35, p167

M.J. Marcinkowski, 1963, Electon Microscopy and Strength of Crystals, eds. G. Thomas and J. Washburn, Interscience, New York, p333

M.J. Marcinkowski, N. Brown and R.M. Fisher, 1961, Acta Met., 9, p129

A.L. Marsh, 1906, U.K. Patent no. 2129

J.R. Mihalisin, 1969, Advances in X-Ray Analysis, 13, p598

R.F. Miller and G.S. Ansell, 1977, Met. Trans., 8A, p1979

W.I. Mitchell, 1966, Z. Metallk., 57, 586

F.R.N. Nabarro, 1967, Theory of Crystal Dislocations, Oxford University Press, p421

P.G. Nash, V. Vejus and W.W. Laing, 1982, Bulletin of Alloy Phase Diags., 3, p367

J.R. Nicholls and R.D. Rawlings, 1977, J. Mat. Sci., 12, p2456

O. Noguchi, Y. Oya and T. Suzuki, 1981, Met. Trans., 12A, p1647

R. Nordheim and N.J. Grant, 1954, Trans. AIMME., 200, p211

J.M. Oblak and B.H. Kear, 1972, Electron Microscopy and the Structure of Materials, Univ. of California Press, London, p566

J.M. Oblak, W.A. Owczarski and B.H. Kear, 1971, Acta Met., 19, p355

J.M. Oblak and W.H. Rand, 1972, Proc. 30th Annual Meeting of EMSA, p648

K. Ono and R. Stern, 1969, Trans. Met. Soc. AIME., 245, p171

E. Orowan, 1948, Symposium on Internal Stress in Metals and Alloys, Inst. of Metals, London, p451

V. Paidar, D.P. Pope and V. Vitek, 1984, Acta Met., 32, p435

H. Pak, T. Saburi and S. Nenno, 1976, Scripta Met., 10, p1081

R.M.N. Pelloux and N.J. Grant, 1960, Trans AIME., 218, p232

B.J. Piearcey, 1970, US Patent no. 3,494,709

B.J. Piearcey, B.H. Kear and R.W. Smashey, 1967, Trans. ASM, 60, p634

B.J. Piearcey and B.E. Terkelson, 1967, Trans. Met. Soc. AIME., 239, p1143

D.P. Pope and S.S. Ezz, 1984, Int. Metals Rev., 29, p136

M.V. Pridantsev, 1967, Izv. Acad. Nauk. SSSR Met., 5, p115

C.M.F. Rae, 1984, to be published

C.M.F. Rae and G.S. Hillier, 1984, to be published

I.L.F. Ray and D.J.H. Cockayne, 1970, Phil. Mag. 22, p853

I.L.F. Ray and D.J.H. Cockayne, 1971, Proc. Roy. Soc., A325, p543

I.L.F. Ray, R.C. Crawford and D.J.H. Cockayne, 1970, Phil. Mag., 21, p1027

D. Raynor and J.M. Silcock, 1970, Met. Sci. J., 4, p121

W.T. Read, 1953, Dislocations in Crystals, McGraw-Hill, New York, p207

J.E. Restall, The Development of Gas Turbine Materials, 1981, ed. G.W. Meetham, App. Sci. Publ., London, p259

R.A. Ricks, A.J. Porter and R.C. Ecob, 1983, Acta Met., 31, p42

Rolls-Royce Ltd., 1973, The Jet Engine, T.S.D. 1302

R.G. Roome, 1982, Report MEG 0645, Rolls-Royce Ltd., Derby

A.W. Ruff, 1970, Met. Trans., 2, p2391

P.L. Ryder and W. Pitsch, 1968, Phil. Mag., 18, 807

S.M.L. Sastry and B. Ramaswami, 1976, Phil. Mag. A, 33, p375

P.G. Self, M.P. Shaw and W.M. Stobbs, 1982, Phys. Stat. Sol. (a), 73, p.37

J.M. Silcock and W.J. Tunstall, 1964, Phil. Mag., 10, p361

A.E. Staton-Bevan and R.D. Rawlings, 1975a, Phil. Mag., A, 32, p787

A.E. Staton-Bevan and R.D. Rawlings, 1975b, Phys. Stat. Sol. (a), 29, p613

W.M. Stobbs, 1973, 3rd Course on Electron Microscopy in Materials Science, Erice, ECSC, Luxembourg, p591

W.M. Stobbs and C.H. Sworn, 1971, Phil. Mag., 24, p1365

H. Suzuki, 1952, Sci. Repts. Tohoku Univ., Japan, A4, p455

K. Suzuki, M. Ichihara and S. Takeuchi, 1979, Acta Met., 27, p193

R.J. Taunt, 1973, Ph.D thesis, Univ. of Cambridge

R.J. Taunt and B. Ralph, 1974, Phil. Mag., 30, p1379

S. Takeuchi and E. Kuramoto, 1973, Acta Met., 21, p415

S. Takeuchi, E. Kuramoto, T. Yamamoto and T. Taaka, 1973, Jap. J. Appl. Phys., 12, p1486

A. Taylor and R.W. Floyd, 1952, J. Inst. Metals, 81, p25

A.S. Tetelman, 1962, Acta Met., 10, p813

N. Thompson, 1951, Proc. Phys. Soc., 40, p1014

R.H. Thornton, R.G. Davies and T.L. Johnston, 1970, Met. Trans., 1, p207

J.K. Tien, B.H. Kear and G.R. Leverant, 1972, Scripta Met., p135

F.L. VerSnyder and R.W. Guard, 1960, Trans. ASM, 52, p485

F.L. VerSnyder and M.E. Shank, 1970, Mat. Sci. Eng., 6, p213

A.E. Vidoz and L.M. Brown, 1962, Phil. Mag., 7, p1167

J.M. Walsh and M.J. Donachie, 1969, Mat. Sci. J., 3, p68

C. Wells, 1981, The Development of Gas Turbine Materials, ed. G.W. Meetham, Appl. Sci. Publ., London, p207

M.J. Whelan, 1959, Proc. Roy. Soc., A219, p114

M.J. Whelan and P.B. Hirsch, 1957a, Phil. Mag., 2, p1121

M.J. Whelan and P.B. Hirsch, 1957b, ibid., 2, p1301

F. Whittle, 1930, U.K. Patent no. 347,206

M. Yamaguchi, V. Paidar, D.P. Pope and V. Vitek, 1982, Phil. Mag. A, 45, p867

M. Yamaguchi, V. Vitek and D.P. Pope, 1981, Phil. Mag. A, 43, p1027